UNIVERSITY OF MELBOURNE

# The structure of adverse and favourable pressure gradient turbulent boundary layers

by

Zambri Harun

A thesis submitted in partial fulfillment for the
degree of Doctor of Philosophy

in the
Department of Mechanical Engineering

April 2012

# Declaration of Authorship

I, Zambri Harun, declare that this thesis titled, 'The structure of adverse and favourable pressure gradient turbulent boundary layers' and the work presented in it are my own. I confirm that:

- This work was done wholly or mainly while in candidature for a research degree at this University.
- Where any part of this thesis has previously been submitted for a degree or any other qualification at this University or any other institution, this has been clearly stated.
- Where I have consulted the published work of others, this is always clearly attributed.
- Where I have quoted from the work of others, the source is always given. With the exception of such quotations, this thesis is entirely my own work.
- I have acknowledged all main sources of help.
- Where the thesis is based on work done by myself jointly with others, I have made clear exactly what was done by others and what I have contributed myself.

Signed: _____

Date: _____

# *Abstract*

A parametric study of turbulent boundary layers with pressure gradients was carried out using hotwire anemometry in order to investigate the effects of varying Reynolds number and pressure gradient strength.

The coefficient of friction is obtained from oil-film interferometry (OFI). Through this independent method, a systematic deviation from the log law which grows with pressure gradient strength is observed.

Mean statistics such as the mean velocities, turbulent intensities and turbulence production change in the outer region with pressure gradients. The large-scale features in the flow are found to be more energetic as the pressure gradient changes from favourable to adverse when Reynolds number is held constant. The large-scale features are responsible for the rise in turbulence intensities especially in the outer region. The large-scale features also causes the skewness to increase in the near-wall region. The more energetic large-scale features in the outer region have a greater 'foot-print' near the wall.

In the second part of the study, a two-point sensor analysis reveals that the turbulence in the near-wall region is found to be only weakly disturbed by the pressure gradient in contrast to recent findings, e.g. by Lee and Sung (2009). Nevertheless, the structural inclination angle increases with adverse pressure gradient, and decreases with favourable pressure gradient.

# *Acknowledgements*

Firstly I thank my supervisors, Professor Ivan Marusic and Dr. Jason Patrick Monty for giving me the opportunity to study with them, and increase my understanding of turbulent flows. Furthermore, thanks are also due to them for guiding me how on to document the findings, provide arguments and explanations. Such guides have tremendously helped in the preparation of manuscripts (papers and this thesis). I am very grateful to the University of Melbourne and its staff.

During the start of the experiment, my supervisors, together with Dr. Nicholas Hutchins, my fellow students Henry Ng and Vigneswaran Kulandaivelu (Vickey), have always been there to give advice and guidelines on measurements. Dr. Hutchins for example would spend hours at the wind tunnel or in front of a computer to solve problems or to explain turbulence arguments. Henry gave me my first lessons in hotwire anemometry. Vickey helped set up the wind tunnel until it was fully operational and ready to take measurements.

During the course of measurement, Vickey and Bagus Nugroho helped with the setting up of the pressure gradient. Together with Reza Madad, the oil-film interferometry (OFI) experimental set up and measurement were established. Dr. Kapil Chauhan provided technical advice for the OFI as well as processing photographs of fringes. Dr. Romain Mathis gave advice beyond turbulence issues: on how to manage data.

Mr. Derek Jacquest and Geoff Duke's technical expertise has greatly helped the experiment. Mr. Jacquest has helped particularly in the installation of the OFI infrastructures and the construction of the two-axis traverse. Further, he always has brilliant solutions in installing small gadgets which ultimately made the experiment easier or more automated.

This research does take a toll. My father Harun Mat Som (1924 - 2009) passed away back home in Malaysia while I was in the laboratory. He was always proud of me in whatever I was doing. My mum Ramlah Hamid keeps me going tough in this 'turbulent' time. My elder brother M. Rozaidee Harun has to takes care of a lot of issues on my behalf. My two younger brothers too Ramlan and Rohidi, have always been supportive of my plans. My wife Hashimah Hashim is now researching her PhD at the LaTrobe University and our eldest child Aiman Hakim helped us many times by looking after his two younger brothers, Daniel and Harris. I sincerely thank all my family for their support and understanding.

Without financial support, the study would not be possible. I would like to thank the government of Malaysia and the National University of Malaysia (UKM) for providing the university fees, allowances and the trusts. There have also been important financial supports from the university and supervisors' grants for research purposes.

I would also like to thank my friends for helping, sharing and sometimes teaching me. It was wonderful to learn here with them in this atmosphere. Without the help, advice and support these individuals offered, the study would not have been possible. Finally, thanks to God who creates the fascinating turbulence for the good and the bad.

...

# Contents

# List of Figures

# List of Tables

# Abbreviations

| | |
|---|---|
| 1-D | one–dimensional |
| 2-D | two–dimensional |
| 3-D | three–dimensional |
| DNS | Direct Numerical Simulation |
| F | Flatness |
| HHT | Hilbert-Huang Transformation |
| LMR | Low Momentum Region |
| LSE | Linear Stochastic Estimation |
| MPG | Mile Per Gallon |
| PDF | Probability Density Function |
| PIV | Particle Image Velocimetry |
| OFI | Oil-film Interferometry |

# Symbols

| | |
|---|---|
| $B$, | Constant in Perry et al. (1994) |
| $c_1, c_2$ | Constants in Coles (1956) |
| $C_1$ | Integral in Perry et al. (1994) |
| $C_f$ | Coefficient of friction |
| $C_K$ | Kolmogorov constant |
| $C_p$ | Coefficient of pressure |
| $D_1, D_2$ | Universal constants |
| $E_K$ | Kolmogorov-scaled energy |
| $f_s$ | Sampling frequency |
| $J$ | Universal constant in Perry et al. (1966) |
| $k_x$ | Streamwise wave number, $k_x = 2\pi f/U_c$ |
| $K$ | Acceleration parameter, $K = \nu/{U_1}^2(\mathrm{d}U_1/\mathrm{d}x)$ |
| $l^+$ | Non-dimensionalised hotwire length, $l^+ = lU_\tau/\nu$, $l$ is the sensor length |
| $L_y$ | The characteristic spanwise length scale in $R_{uu}$ |
| $L_{ymin}$ | The characteristic spanwise length scale when minima in $R_{uu}$ occur |
| $m$ | The exponent for boundary layer development in equilibrium, $U \propto x^m$ |
| $P, P_1, P_t$ | Pressure, free stream static pressure, total pressure |
| $Pr$ | Turbulence production |
| $P_x^+$ | Viscous-scaled pressure gradient parameter, $P_x^+ = \nu/(\rho U_\tau^3)(\mathrm{d}P_1/\mathrm{d}x)$ |
| $Re_\delta^\star$ | Reynolds ($Re$) number based on the displacement thickness, $Re_\delta^\star = U_1\delta^\star/\nu$ |
| $Re_h$ | $Re$ number based on channel height, $Re_h = U_{CL}h/\nu$ (h is channel height) |
| $R_{uu}$ | Correlation of streamwise velocity fluctuations |
| $R_x$ | $Re$ number based on a streamwise reference point, $R_x = xU_{in}/\nu$ |

| | |
|---|---|
| $Re_\tau$ | $Re$ number based on boundary layer thickness, $Re_\tau = U_\tau \delta / \nu$ |
| $Re_\theta$ | $Re$ number based on momentum thickness, $Re_\theta = U_1 \theta / \nu$ |
| $Re_{\lambda T}$ | $Re$ number based on the Taylor microscale, $Re_{\lambda T} = \lambda_T \sqrt{\overline{u^2}} / \nu$ |
| $S$ | Skin friction parameter, $S = U_1 / U_\tau$ |
| $S_{ij}$ | Rate of strain tensor |
| $S_k$ | Skewness |
| $\tilde{S}_k$ | Skewness reconstructed without the cross product term $\widetilde{\overline{3u_L^+ u_S^{+2}}}$ |
| $t^+$ | Non-dimensionalised time, $t^+ = t U_\tau^2 / \nu$, where $t = 1/f$ |
| $TU_1/\delta$ | Boundary layer turnover time, $T$ is time in seconds |
| $u$, $v$ and $w$ | Velocity fluctuations in x (streamwise), y (spanwise) & z (wall-normal) |
| $U$, $V$ and $W$ | Local mean velocity in x (streamwise), y (spanwise) & z (wall-normal) |
| $U_c$ | Convection velocity |
| $U_{CL}$ | Centre line velocity (channel flow) |
| $U_{in}$ | Inlet velocity |
| $U_s$ | Schofield and Perry velocity scale e.g. in Perry and Schofield (1973) |
| $U_\tau$ | Friction velocity |
| $U_1$ | Local free stream velocity |
| $w$ | Wake function |
| $W_c$ | Coles wake function |
| $z^+\|_{peak\ uv}$ | Reynolds stress peak location |
| | |
| $\alpha_1, \alpha_2$ | Variables in Barenblatt (1993)'s half power law |
| $\alpha_3$ | Variable in Stratford (1959)'s power law |
| $\beta$ | Clauser adverse pressure gradient parameter, $\beta = \delta^* / \tau_o (\mathrm{d}P_1/\mathrm{d}x)$ |
| $\delta$ | Boundary layer thickness |
| $\delta_c$ | Boundary layer thickness based on Coles' formulations |
| $\delta_s$ | Perry and Schofield length scale |
| $\delta^*$ | Displacement thickness |
| $\Delta$ | Incremental value of a quantity |
| $\epsilon$ | Energy dissipation rate |
| $\eta$ | Non-dimensionalised distance from the wall, $\eta = z/\delta$ |

| | |
|---|---|
| $\eta_K$ | Kolmogorov length scale, $\eta_K = \nu^{3/4}/\epsilon^{1/4}$ |
| $\lambda$ | Wavelength of sodium lamp light source |
| $\lambda_x$ | Streamwise wavelength, $\lambda_x = 2\pi/k_x$ |
| $\lambda_{xc}$ | Cut-off length scale |
| $\lambda_y$ | Spanwise distance or separation |
| $\lambda_T$ | Taylor microscale $\sqrt{\overline{u^2}/\overline{(\partial u/\partial x)^2}}$ |
| $\Lambda$ | A shape or type of eddy |
| $\nu$ | Kinematic viscosity |
| $\phi$ | Diameter of hotwire sensor |
| $\phi_{uu}$ | Streamwise energy spectra |
| $\psi$ | Energy deficit, energy difference |
| $\Pi$ | Coles' wake factor |
| $\rho$ | Density of fluid |
| $\tau$ | Local shear stress |
| $\tau_o$ | Wall shear stress magnitude |
| $\tau_m$ | Maximum shear stress $\tau_m = \rho uv\|_{\max}$ |
| $\theta$ | Momentum thickness |
| $\theta_{struc}$ | Structural inclination angle |
| $\Xi$ | Diagnostic function |
| $\zeta$ | Non-equilibrium parameter in Perry et al. (2002), $\zeta = S\delta(\mathrm{d}\Pi/\mathrm{d}x)$ |

*In loving memory of my father, Harun Mat Som (1924 - 2009). May god bless you. To my mother Ramlah Hamid, wife Hashimah Hashim, boys Aiman, Daniel and Harris, brother Rozaidee, Ramlan and Rohidi. Thanks for your support . . .*

# Chapter 1

# Introduction

This thesis reports on turbulent boundary layer pressure gradient studies at the University of Melbourne. Why study pressure gradient boundary layer flows? A lot of studies have been performed in zero pressure gradient (ZPG) flows, yet layers exposed to pressure gradients are the ones most likely to be encountered in many engineering applications (Dixit and Ramesh, 2010, Lee and Sung, 2009). Examples of these applications are diffusers, turbine blades and aerofoils. Turbulent flows are characterised by three-dimensional chaotic motions caused by movements of coherent eddies of different sizes and orientations. Researchers are focussing on the physics of these eddies because they are known to play a very significant role in the production of turbulence kinetic energy and are major contributors to skin friction.

The simplest and yet an important example of how such studies benefit mankind is the effect of skin friction on aeroplanes. Large airliners need to use up to 50% of their power to overcome drag due to skin friction (Ganapathisubramani et al., 2005, Stenzel et al., 2011). Airline companies quickly single out rising fuel costs as the main reason for them not meeting the balance sheet. Many airline companies take drastic actions to cut costs such as implementing staff reduction and a reorganisation of routes to increase efficiencies. Complex geometries, such as in the cases of pressure gradient flows provide useful information towards the physics of aerodynamics. Understanding the physics of aerodynamics contributes to better aeroplane designs (e.g., Rahgozar and Maciel, 2011b), which in turn helps these companies to reduce their fuel costs.

Aerodynamics affect many livelihoods outside of the airline industry as well. Cars use approximately 20% of their engine power to overcome aerodynamic drag. This figure

changes from company to company and even from one model to the others within the same manufacturer. General Motors (GM) aerodynamics studies in Advanced Material & Processes, in its January 2006 edition, reported that figure to be about 20%. Some manufacturers design hybrid systems, where the fuel-driven engine is usually shut-off after the car no longer needs a lot of power (usually from stationary to a certain desired speed) and replaced with battery power. Hybrid systems are a major area of investment for car manufacturers wishing to increase fuel efficiency.

Governments and regulating bodies too are expediting regulations, because rising fuel prices hurt everybody, individuals, private or governments. The Spanish government reduced the compulsory maximum speed limit from 120 km/h to 110 km/h on 7 March 2011, when war broke out in Northern Africa, the source of much of Spain's fuel. Aggressive driving (speeding, rapid acceleration and braking) wastes fuel. It lowers a car's fuel mileage by 33% at highway speeds and by 5% in suburban areas. Drag generally is proportional to the frontal area, the area that sees the incoming air or fluid and square of the speed (White, 1991). Returning to Spain's highway speed limit, in June of the same year, the regulation was extended because of its effectiveness in reducing vehicles' fuel consumption. Studies pointed out that this regulation only reduced fuel consumption by approximately 5%, not by the government estimate of 15% (a 15% reduction would potentially save the nation's fuel bill by €2.3bn. However, a 5% saving represents a huge sum of much needed money that could be used for other sectors of Spain's economy.

In the U.S., the President announced in July 2011 that car manufacturers had to meet tougher Corporate Average Fuel Economy (CAFE) laws regarding fuel efficiency. CAFE laws were first enacted in 1975 to improve the average fuel economy of cars and light trucks. Automakers have agreed to a 54.5 mile-per-gallon (MPG) national average fuel economy standard by 2025 (54.5 MPG is equivalent to 4.32 l/100km). The new standard is the 'single most important step' to cut U.S. dependence on foreign oil, according to the President. It will mean the average motorist can fill up every two weeks, instead of every week. Most car companies submitted their plans, especially more aerodynamic designs. The 2013 Chevrolet Malibu model will see a significant improvement in aerodynamics with a shape approaching the wind drag of the Chevy Volt extended-range electric car. The Hyundai Accent, the entry-level subcompact, gets a 2.1% improvement in fuel savings from reduced wind drag. Among other things, the car is fitted with an underbody panel to keep air from becoming trapped underneath. The new Ford Focus is 7% more fuel-efficient. Among the changes were more aerodynamic side mirrors, wheel wind deflectors, a panel underneath the front end, shutters that close behind the grille

at higher speeds and molding on the front roof pillars aimed at smoothing out air flow. The subcompact Nissan Versa, going on sale in summer 2011, is more than an inch lower than the one it replaces, to make it more aerodynamic. The new version of the Honda Civic has a rear spoiler and wheels that have a flatter surface to prevent trapped air. It gets a 3 MPG improvement (USA Today, 1 Aug. 2011). The savings from the more fuel efficient designs increase many households disposable income. More disposable income means spending on other items will increase, lifestyles change too.

Understanding the physics of friction generation and how to reduce it contributes to fuel-efficient designs. Complex car surfaces are better approximated with flows in pressure gradients, therefore better understandings in APG and FPG flows are greatly required. The two examples above of how greatly aerodynamics affect aeroplanes' and cars' performances demonstrate the importance of such applications for this study. Aerodynamic drag is also an important factor in the maritime and land transportation industries and in high-speed trains. In sports, aerodynamics have long been important features in bicycle and helmet designs, swimsuits, canoes, etc.

To summarize, aerodynamic issues exist in many aspects of life; applications from such knowledge improve individual life styles as well as the national economy. However, studies of boundary layers in pressure gradients are lacking in the literature, as expressed recently in Dixit and Ramesh (2010), Lee and Sung (2009) and Rahgozar and Maciel (2011b). Lee and Sung (2009) stressed that the efficiency of such devices is almost always determined by the APG, so the behaviour of the APG flows is of practical importance. In general, elucidating the behaviour of turbulent boundary layers exposed to pressure gradients improves its modeling (Lee and Sung, 2009) and contributes to flow control strategies (Robinson, 1991).

## 1.1 Literature review

### 1.1.1 Progress in wall turbulence

Wall-turbulence research has seen some successes in the last decade in understanding the large-scale structures of the flow. The large-scale structures reside in the outer layer consisting of the log region, in which the length scale varies almost linearly with the distance from the wall, and the wake region in which the length scale approaches the boundary-layer thickness. Both regions contain eddies ranging from as small as those

found in the buffer layer in the near-wall region, as well as the much larger eddies. The characteristics of the structures in the buffer layer such as the streaks, the low and high speed streamwise vortices, modulated in spanwise direction have been well documented (Kline et al., 1967, Robinson, 1991, Smith and Metzler, 1983). They have been linked with a sequence of events called the bursting process, in which streaks lift-up, oscillate and break down (Jeong et al., 1997, Kim et al., 1987). The mechanism by which the wall turbulence sustains itself has also been documented (Panton, 1997, Walleffe, 1997). Less is known about the structure of the outer layers than about the buffer layer, partly because it contains a wider range of scales (Adrian et al., 2000). Marusic et al. (2010a) too noted that the majority of investigations have been focussed in the near-wall region. However, there have also been earlier studies on turbulent structures in the outer layers. Kovasznay et al. (1970) and Brown and Thomas (1977) for example, showed structures which scales with the boundary layer thickness, dominated the outer layers.

Kim and Adrian (1999) proposed a model of vortex packets to explain the dominance of very low frequency energy in the log region of high Reynolds number wall-turbulence. This study was followed by similar studies highlighting large-scale structures in the outer layers (Adrian et al., 2000, Balakumar and Adrian, 2007, del Álamo et al., 2004, Ganapathisubramani et al., 2003, Guala et al., 2006, Hutchins and Marusic, 2007a, Tomkins and Adrian, 2003). As has been discussed above, the turbulent structures in the outer layers have features that scale with outer variables. The alternating regions of high and low-speed regions suggest that the large-scale features have widths that scale with the outer variables too (Ganapathisubramani et al., 2005, Hutchins et al., 2005, Monty et al., 2007). Much less is known about turbulent structure for boundary layers in pressure gradients as most previous studies have been performed in ZPG turbulence boundary layer (TBL), channel or pipe flows.

### 1.1.2 The 'active' and 'inactive motions'

Bradshaw (1967a), Lee and Sung (2009), Skåre and Krogstad (1994) and recently Monty et al. (2011) showed evidence of increased large-scales features when a TBL flow is exposed to APG. To understand the extent of the increased larger-scale structures, it is useful to revisit the 'active' and 'inactive' motions postulated by Townsend (1961). Bradshaw (1967a) further refined this hypothesis: an inner turbulence motion, say in the region $z/\delta < 0.2$, consists of an active universal component, scaling on friction velocity and wall-normal distance, which produces the shear stress, and an inactive component,

imposed by the eddies and pressure fluctuations in the outer part of the boundary layer, which does not produce shear stress near the wall and can be regarded as a quasi-steady oscillation of the inner layer flow. The inactive motions, larger, swirling and meandering eddies however produce shear stress much further in the outer region (Townsend, 1976). Supported by experimental evidence, Townsend (1976) and Bradshaw (1967b) showed that inactive motions are intense in boundary layers in the adverse pressure gradient. The latter further elaborated that there was no noticeable effect in the mean quantities in the inner layer if these very large fluctuations are imposed, since such structures do not change the universality of the smaller motions in the inner layer. Despite their passive contribution in the inner layer, the inactive motions are strong contributors to the shear stress and turbulence production in the outer layer. These effects can also be seen clearly in very large APG experiments of Skåre and Krogstad (1994) and Dengel and Fernholz (1990), where a secondary peak in turbulence production was observed in the outer region. For the purpose of this study, the small-scale and the large-scale structures, commonly associated with the active and inactive motions, are used to describe turbulent structures.

### 1.1.3 Reynolds number effects

Wei and Wilmarth (1989) reported that turbulence quantities are dependent on the Reynolds number in their turbulent channel experiments flow using a Laser Doppler Anemometer (LDA) with the Reynolds number range $3000 < Re_h < 40000$ ($Re_h$ is the Reynolds number based on channel height). The mean velocities, turbulence intensities, the Reynolds stress and energy spectra, were shown not to scale with inner variables very close to the wall. Ching et al. (1995), Johansson and Alfredsson (1983), Klewicki and Falco (1990) and DeGraaff and Eaton (2000) as was commonly assumed in the classical literature also reported in well-resolved measurements that the near-wall turbulence intensity peak location grows with the Reynolds number. In channel flow experiments by Johansson and Alfredsson (1983), skewness and flatness slightly increased when a high Reynolds number, ($Re_h$ = 129000) was compared to a low Reynolds number flow ($Re_h$ = 50000). Andreopoulos et al. (1984), Balint et al. (1991), den Toonder and Nieuwstadt (1997), Durst et al. (1998), Metzger and Klewicki (2001) have all shown Reynolds number dependencies of the skewness and flatness.

The variation in the skewness observed when the Reynolds number increases, has been shown to be associated with the large-scale structures. Metzger and Klewicki (2001)

showed that the skewness shifts upwards in the near-wall region as the Reynolds number is increased and using a high-pass filter to remove the low-frequency large-scale features showed clearly that the large-scales were responsible for the increase in the skewness.

Gad-el-Hak and Bandyopadahyay (1994)'s discussion of the Reynolds number effects was focused on the Reynolds shear stress because it is the most important dynamical quantity affecting mean motion. The major portion of the momentum transported in a two-dimensional turbulent wall-bounded flow is attributable to this quantity. In this paper, the shear stress peak locations in Wei and Wilmarth (1989) and Harder and Tiederman (1991) are shown to move away from the wall as the Reynolds numbers increase. In Sreenivasan (1989), the shear stress peak location is shown to be a strong function of the Reynolds number. By using least-square fitting from a list of compiled data, Sreenivasan (1989) demonstrated the peak location can be predicted by the Reynolds number, $z^+|_{peak\ uv} = (Re^*)^{0.75}$ for direct shear stress measurement or $z^+|_{peak\ uv} = 2(Re^*)^{0.5}$ when shear stress is computed from measured mean velocities. Here, $Re^*$ is the pipe radius or boundary layer thickness, and the '+' symbol denotes nondimensionalised unit, both with inner variables.

In sufficiently large Reynolds number ZPG TBL flows, Hutchins and Marusic (2007a) demonstrated that the large-scale features in the outer layers maintain a presence in the near-wall region. From the energy spectra analysis, Hutchins and Marusic (2007a) found that the contribution to the streamwise turbulence intensities associated with the largest-scale motions, referred to as superstructures, appears to be increasingly significant with increasing Reynolds number, and scales with outer length variable, $\delta$. The influence of the large-scale structures could be observed in the near-wall region and it seems that these features modulate the near-wall cycles. The influence of the low-wave number energy into the near-wall region is consistent with the rise in near-wall streamwise turbulence intensities (when scaled with inner variables noted in the list of papers at the start of this sub-section) to occur with increasing Reynolds numbers. Recently there have been more research identifying large Reynolds number effects in the near wall-region as a result of the interaction between the small-scale structures here and the large-scale features in the outer region.

Mathis et al. (2009) studied the relationship between the large-scale features and the small-scale near-wall cycle based on the Hutchins and Marusic (2007a) findings. Here, the influence of the large-scale boundary-layer motions on the small-scale near-wall cycle through an amplitude modulation process was studied. The Hilbert transformation was applied to the spectrally filtered small-scale component of fluctuating velocity signals,

in order to quantify the interaction and Mathis et al. (2009) showed evidence that the amplitude modulation effect becomes progressively stronger as the Reynolds number increases. Using turbulence intensities, turbulence production and energy spectra analyses, Marusic et al. (2010a) demonstrated that the energised large-scale features in the outer region (due to larger Reynolds number) become increasingly important in terms of sustaining and producing turbulence as compared to the near-wall cycle. The large-scale energy 'percolates' down to the buffer and viscous sub-layers. Hence, explaining the dependency of the near-wall turbulence intensities peak on the Reynolds number in the fully-resolved measurement discussed earlier in Ching et al. (1995), Johansson and Alfredsson (1983), Klewicki and Falco (1990), Wei and Wilmarth (1989) and DeGraaff and Eaton (2000) amongst others.

### 1.1.4 Known pressure gradient effects

The effect of pressure gradients on the turbulence statistics i.e. mean velocities, turbulence intensities, skewness, flatness, structural inclination angle and turbulence production, have been documented in APG flows in Marusic and Perry (1995), Nagano and Houra (2002), Skote and Henningson (2002), Skåre and Krogstad (1994) and in FPG flows in Fernholz and Warnack (1998), Jones et al. (2001) and Bourassa and Thomas (2009). The wake in the mean velocities and turbulence intensities grows with adverse pressure gradient parameter in the outer region. The skewness and flatness coefficients also increase in the near wall region due to the APG. From a two-point correlation, Krogstad and Skåre (1995) showed that the structure inclination angle increases with APG[1]. Krogstad and Skåre (1995) explained that the features rose up and broke down to form shorter structures. In contrast, Dixit and Ramesh (2010) showed that the angle is smaller in FPG (5-10$^o$ depending on the severity of the FPG). Relating to the APG experiment by Krogstad and Skåre (1995), Dixit and Ramesh (2010) made an analogy that, the structures are flattened and stretched in FPG (the opposite of the effects observed in APG). An increase in the streamwise integral length scale and a decrease in the wall-normal integral length scale observed in Warnack and Fernholz (1998) also imply elongation of the large-eddy structure.

The 'constants' $\kappa$ and $A$ in the log law of the wall equation (to be discussed in Chapter 3) have also been observed to be affected by pressure gradients. Krogstad and Skåre (1995), Lee and Sung (2009), Nagano et al. (1998) and Monty et al. (2011) observed

[1]The structural inclination angle is nominally 15$^o$ in ZPG TBL (Brown and Thomas, 1977, Ganapathisubramani et al., 2003, Marusic and Heuer, 2007, Robinson, 1991)

a shift-down in the mean velocity profiles from the log law of the wall. In contrast, Bourassa and Thomas (2009) and Dixit and Ramesh (2010) found a shift-up in strong FPG flows.

The turbulence production increases in APG and decreases in FPG flows (Fernholz and Warnack, 1998, Skåre and Krogstad, 1994) especially in the outer region. Nagano et al. (1992) and Skåre and Krogstad (1994) explained that the high production in the outer region was due to higher turbulent shear stresses. Lee and Sung (2009) showed that the increased outer kinetic energy and shear stress are associated with the presence of large-scale outer streaky structures. Lee and Sung (2009) used instantaneous visualisation to demonstrate the presence of a low momentum regions (LMR), which are intensified and regulated by the presence of APG. The LMRs identified here fit the descriptions of the large-scale structures with a streamwise length of $4\delta$ and width of $0.4\delta$. The average size of LMR is estimated using linear stochastic estimation (LSE), a method employed by Christensen and Adrian (2001).

The skewness is also found to increase with APG (Nagano and Houra, 2002, Skåre and Krogstad, 1994). However it has not been shown in detailed analysis that such an effect is due to the increased large-scale features in APG flows. In ZPG flows with increasing Reynolds number, Metzger and Klewicki (2001) demonstrated that it is the large-scale features that contribute to the rise of the skewness. It is useful if a similar test is performed in pressure gradient study to prove that large-scale features increase with APG.

Based on the above review, it is evident that the increased large-scale features are likely to be responsible for the rise in the turbulence intensities in the outer region, rise of the skewness, increase in the structural inclination angle and the turbulence production in APG flows. These structures break up, creating shorter structures depending on the severity of the APG (Lee and Sung, 2009). The effects on the boundary layer through the 'association' of the large-scale features is well-documented, but *not* the mechanism or physics behind it. Different researchers explained these phenomena with their own results. Skåre and Krogstad (1994) showed that the direction of the turbulent diffusion is reversed, resulting in considerable turbulent transport towards the wall in strong APG flows. Nagano et al. (1998) explained that APG causes a change in sweep and ejection motions[2]. In an APG flow, sweep motions become equivalent to that of ejections, the outward and wall-ward interactions relatively increase near the wall, reflecting a change in the coherent structures. The two examples above highlight the

[2]the sweep and ejection motions based on quadrant analysis for example in (Lu and Willmarth, 1973)

different approaches taken by different researchers in explaining these phenomena; it is hard to comprehend a mechanism that may be agreed upon by most researchers when these different explanations are compared. The physics behind these changes has never been satisfactorily explained despite much research. The difficulties in analysing APG effects are further aggravated by the fact that large-scale features also increase, as explained at the start of this paragraph[3].

This thesis too, is unable to reconcile the physics behind these changes - this will require continuous, focussed efforts and years of research, e.g. similar to efforts prior to the establishment of information regarding the near-wall streak. However through systematic studies, the author attempts to identify the differences when the large-scales effect are increased or removed from the flow. This is an analysis (pertaining to TBL pressure gradient flows) which seems to be lacking in the literature which will contribute towards greater understanding of this phenomenon.

### 1.1.5 Unknown pressure gradient effects

Effect of increasing $\beta$ or $Re$ independently

Table 1.1 lists existing studies in APG flows. Each of these studies has revealed important properties of APG flows. Column four of Table 1.1 shows the adverse pressure gradient parameter $\beta$, while column five displays the corresponding Reynolds number based on momentum thickness, $Re_\theta$. Both parameters are known to affect boundary layer (in the literature review section) and the large variations in both $\beta$ and the Reynolds number have been preferred for different analysis (e.g., Bradshaw, 1967a). As a result, the effect of increasing $\beta$ is 'contaminated' by the Reynolds number effect and vice versa. This has created a barrier in understanding the full extent of the effect purely by varying one parameter at a time.

Studying the effects of these parameters are the main highlights of this thesis, but there are also more analyses that appear to be lacking in the literature, namely the effect of sensor length, $l^+$ and the identification of the large-scale features through energy spectra analysis.

[3] Adrian et al. (2000) explained the difficulties to analyse flow structure when there are wider range of scales

| Authors | $l^+$ | $z^+_{min}$ | $\beta$ | $Re_\theta$ |
|---|---|---|---|---|
| Samuel and Joubert (1974) | 24 – 65 | 12 | 0.09 – 8 | 5000 – 30000 |
| Cutler and Johnston (1989) | 60 – 70 | 12 | 2 – 12 | 12000 – 25000 |
| Nagano et al. (1998) | 7.9 – 15.6 | 1 | 0.76 – 4.66 | 1290 – 3350 |
| Skåre and Krogstad (1994) | ≈11 | 3 | 12 – 21 | 25000 – 54000 |
| Marusic and Perry (1995) | 7 – 38 | 20 | 0 – 7 | 2200 – 19100 |
| Aubertine and Eaton (2005) | 3 – 4 | 3 | -0.4 – 2.3 | 3000 – 6300 |
| Skote et al. (1998) | DNS | DNS | 0.24 – 0.65 | 360 – 690 |
| Lee and Sung (2008) | DNS | DNS | 0.25 – 1.68 | 850 – 1400 |

TABLE 1.1: Flow and experimental parameters for existing adverse pressure gradient boundary layer data.

$l^+$ effect

Column two in Table 1.1 shows the sensor length parameter, $l^+$. Large $l^+$ causes small-scale attenuations, and in pressure gradient flow, the competing effects due to increased Reynolds number and due to increased $l^+$ discussed in Klewicki and Falco (1990) and Hutchins et al. (2009) may be aggravated. The detail of such effects is discussed in Chapter 4. At this point it is sufficient to note that the introduction of APG causes effects similar to increasing Reynolds number: when APG parameter is introduced, the measured near-wall intensities scaled with inner variables will most likely increase too, as evident in Marusic and Perry (1995), Nagano et al. (1992), Skote and Henningson (2002) and Lee and Sung (2009). However, it is not known if the other competing effect ($l^+$) acted similarly as in previous ZPG studies. Therefore, it is useful to establish the effect of $l^+$ in pressure gradient flows.

The roles of the large-scale features in pressure gradient flows

In order to identify the extent of the large-scale effect (the consequence of increasing $\beta$, as discussed in the literature review), it is necessary to remove the large-scales by using a high-pass filter. This is similar to removing the large-scales as done in the high Reynolds number data in Metzger and Klewicki (2001). As discussed earlier in Sub-Section 1.1.3, this effect is not so well explained and therefore it is imperative that such findings be highlighted in detail. The contributions of the large-scales to turbulence intensities, skewness and flatness in the outer region will also be analysed and compared with existing data.

Modulation effect

The modulation effect of the large-scales on the small-scale events shown by Mathis et al. (2009) grows with the Reynolds number. Clearly, the increased large-scales are responsible for the stronger modulation effect in the higher Reynolds number flows (Hutchins and Marusic, 2007a). The increased large-scale features in an APG flow may be assumed to increase their influence on the near-wall motions also. There is no literature on the modulation effect in pressure gradient boundary layer flows up to date. This is quite understandable since the analysis in ZPG by Mathis et al. (2009) has been documented only quite recently.

## 1.2 Motivation

A lot of effort is given to address the unknown pressure gradient effects discussed in Sub-Section 1.1.5, in particular the roles of the large-scale features. Furthermore, this thesis also compares the mean statistics of pressure gradient flows with the pipe and channel flows. This interest arises from the large-scale features study by Hutchins and Marusic (2007a) and Monty et al. (2009).

Hutchins and Marusic (2007a) showed evidence of very long meandering features that reside in the log and lower wake regions of turbulent boundary layers via spanwise rake of hotwire measurements. These features, the large-scale structures or superstructures, can commonly have lengths of up to $20\delta$, observed in flows ranging more than a decade of Reynolds numbers. Monty et al. (2007) compared turbulent pipe and channel flows at a constant Reynolds number, and the structures of fully developed turbulent pipe and channel flows were analysed with data obtained using custom-made arrays of hot-wire probes. The outcome revealed long and meandering structures of lengths up to 25 pipe radii or channel half-heights, similar to finding in ZPG boundary layer flow by Hutchins and Marusic (2007a).

Monty et al. (2009) compared ZPG, channel and pipe flows at matched conditions. Results show that mean statistics (mean velocities, turbulence intensities, skewness and flatness) in the near-wall region collapse well until $0.5\delta$. However, contrary to views from many previous findings, the energy spectra analysis showed noticeable structural differences. Further to studies in large-scale structures by del Álamo et al. (2004), Kim and Adrian (1999) and Guala et al. (2006) who found the large-scale peak in energy spectra analysis in channel/pipe flow occurs at significantly longer wavelengths than that in boundary layer flow, Monty et al. (2009) added that the energy contribution

from these large-scales continues to move to longer wavelength with distance from the wall in pipe/channel flows. The present study repeats this analysis by adding APG and FPG flows, again at matched conditions. Mean velocities, turbulence intensities, skewness, flatness, energy spectra analysis and turbulence production are compared in order to gain better knowledge of the effect of pressure gradients.

In summary, the major aims of this thesis are as follows:

1. To perform experiments on turbulent boundary layers in increasing Reynolds number while $\beta$ is constant, and in varying $\beta$ while the Reynolds number is constant. The analysis is also extended to compare with ZPG, channel and pipe flows performed by Monty et al. (2007), with the addition of boundary layer flows exposed to pressure gradients.

2. To analyse the extent of the sensor length parameter, $l^+$, effect on pressure gradient flows.

3. To analyse pressure gradient effects towards turbulence statistics (mean velocities, turbulence intensities, skewness, flatness). The energy spectra and the two-points correlations shall also be analysed to identify the extent of the large-scale features.

# Chapter 2

# Experimental set up

## 2.1 Facility

The experiments were performed in an open-return blower wind tunnel. The important features of the tunnel are a settling chamber containing a honeycomb and five screens, followed by a contraction with area ratio of 8.9:1, which leads into an initial inlet section area of 940 × 375 mm. This facility was previously used by Marusic and Perry (1995) and Jones et al. (2001).

### 2.1.1 Traverse construction

The two-axis traverse is one of the important element for this measurement. Figure 2.1 shows the perspective view of the traverse. The entire traverse could be moved along the wind tunnel's streamwise direction. There are four wheels, two on each side of the traverse. The base plate is made of solid rectangular aluminum (labeled as traverse body in the figure). On this plate, there are two main components i.e. traverse one and traverse two. Traverse one is stationary, therefore a hotwire sensor attached to it only performs wall-normal measurements. Traverse two moves in both the wall-normal and spanwise directions. Stiffening metal is fixed to each traverse to ensure deflections caused by forces associated with air speed or other sources were minimised.

The two-axis system is designed especially for the two-sensor measurement discussed in Chapter 5. A close-up, front view of the two sensors is shown in Figure 5.2.

For the spanwise direction, two rails and their accessories and a slot on the base plate had to be constructed. The spanwise movement is driven by a motor-ball screw couple. Spanwise horizontal slots have to be made at the locations where measurements are to be performed. To ensure that there is minimum air leakage, a slot cover is provided for each slot. Foam seals are fitted into these slots to minimize air leakage.

### 2.1.2 Wind tunnel layout

The adjustable section drawing for the wind tunnel is shown in Figure 2.2. For this investigation a new, flexible test section ceiling is made from acrylic and hung by ball screws such that its height is easily adjusted; the adjustable length is 4.2 m. Butterfly screws were attached to the ball screws to adjust the ceiling heights. There are more of these features (ball screw, butterfly screws and stiffening spanwise metal across the acrylic ceiling) than shown in Figure 2.2 to achieve the desired pressure gradient setting.

The smooth wind tunnel floor is made up of a single sheet of acrylic laminate bonded to a 12 mm thick chipboard sheet and attached to the main frame of the test section. Oil film interferometry (OFI) infrastructure could also be observed in Figure 2.2 fixed on the acrylic laminate - thick chipboard sheet. Pressure taps (for the measurements of coefficient of pressure) were along the centre line of the smooth wall. The first few pressure taps were spaced 120 mm apart, mostly in the ZPG development region. The other pressure taps were spaced 40 mm apart.

For all data presented in the thesis, the section heights are 375 mm at the trip wire ($x = 0$ m), 400 mm at $x = 3$ m and 550 mm at $x = 5$ m for APG (or 270 mm for FPG). The geometry is shown in Figure 2.4. At no location is the boundary layer thickness greater than 20% of the tunnel height, ensuring that the boundary layers on the floor and ceiling of the tunnel do not influence each other. To maintain a constant adverse pressure gradient, the cross-sectional area of the tunnel increases nominally exponentially. However, to maintain a constant favourable pressure gradient, the cross-sectional area of the tunnel decreases approximately linearly.

A front view of the wind tunnel is shown in Figure 2.3. There are five plugs in the wind tunnel installed for the present study. The first plug is located furthest upstream, this is station 1. The fifth plug, station 5, is closest to the camera. A transparent glass plug is installed at station 5 and is lit by a sodium light from underneath. These plugs and the settings are for the oil-film interferometry (OFI) method discussed in Section

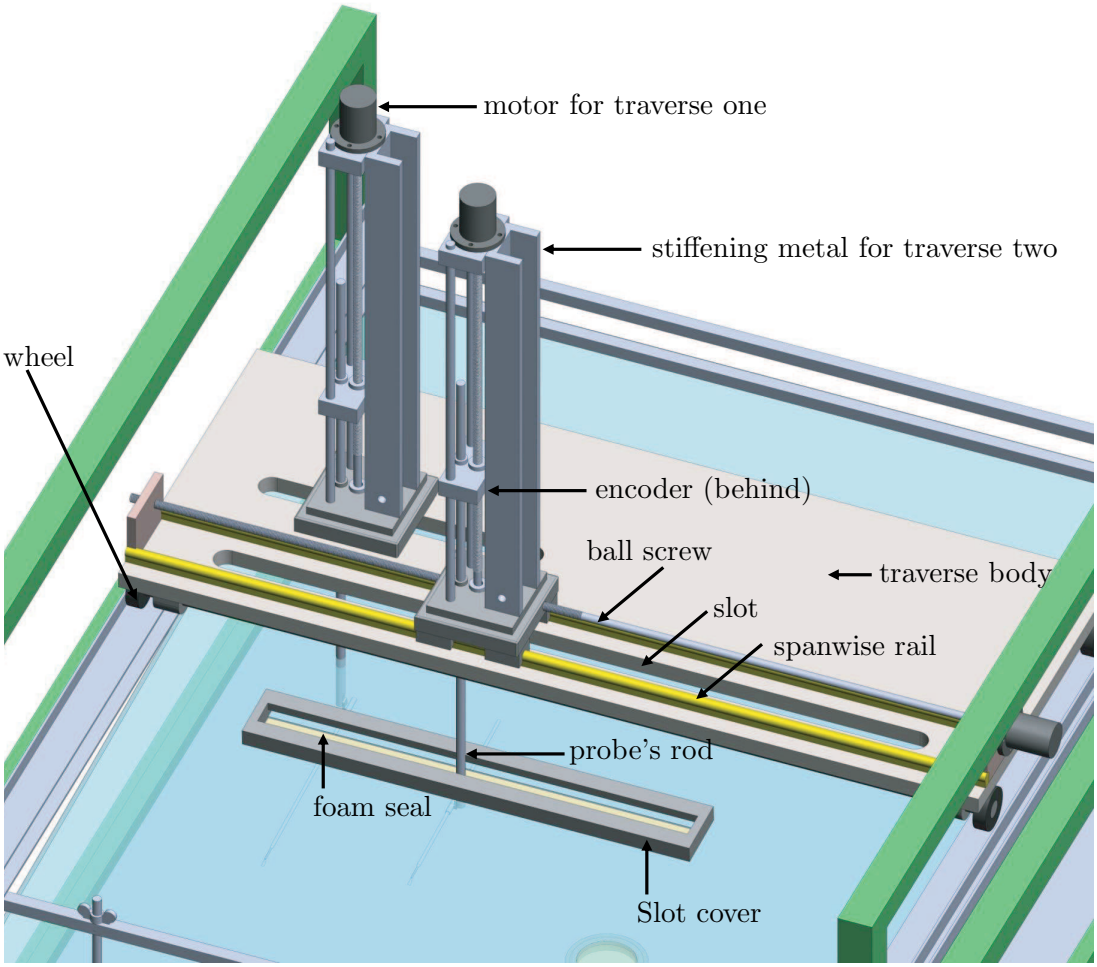


FIGURE 2.1: Traverse perspective view.

2.3. There is only one glass plug; interchangeable all throughout the five stations. The detailed construction of the OFI infrastructure is shown in Section 2.3.

## 2.2 Pressure gradient

The wind tunnel is divided into four sections: the inlet, the ZPG, APG (or FPG) and outlet sections. Modifications have been made to the wind tunnel ceiling to get smooth pressure gradients. The pressure gradient was carefully adjusted so that the coefficient of pressure defined in equation 2.1 set to be within ±0.01 throughout the velocities tested. Here $P$ is the static pressure measured by the wall tappings, $P_t$ is the reference total pressure, $P_0$ is the reference static pressure and $U_1$ is the local free-stream velocity.

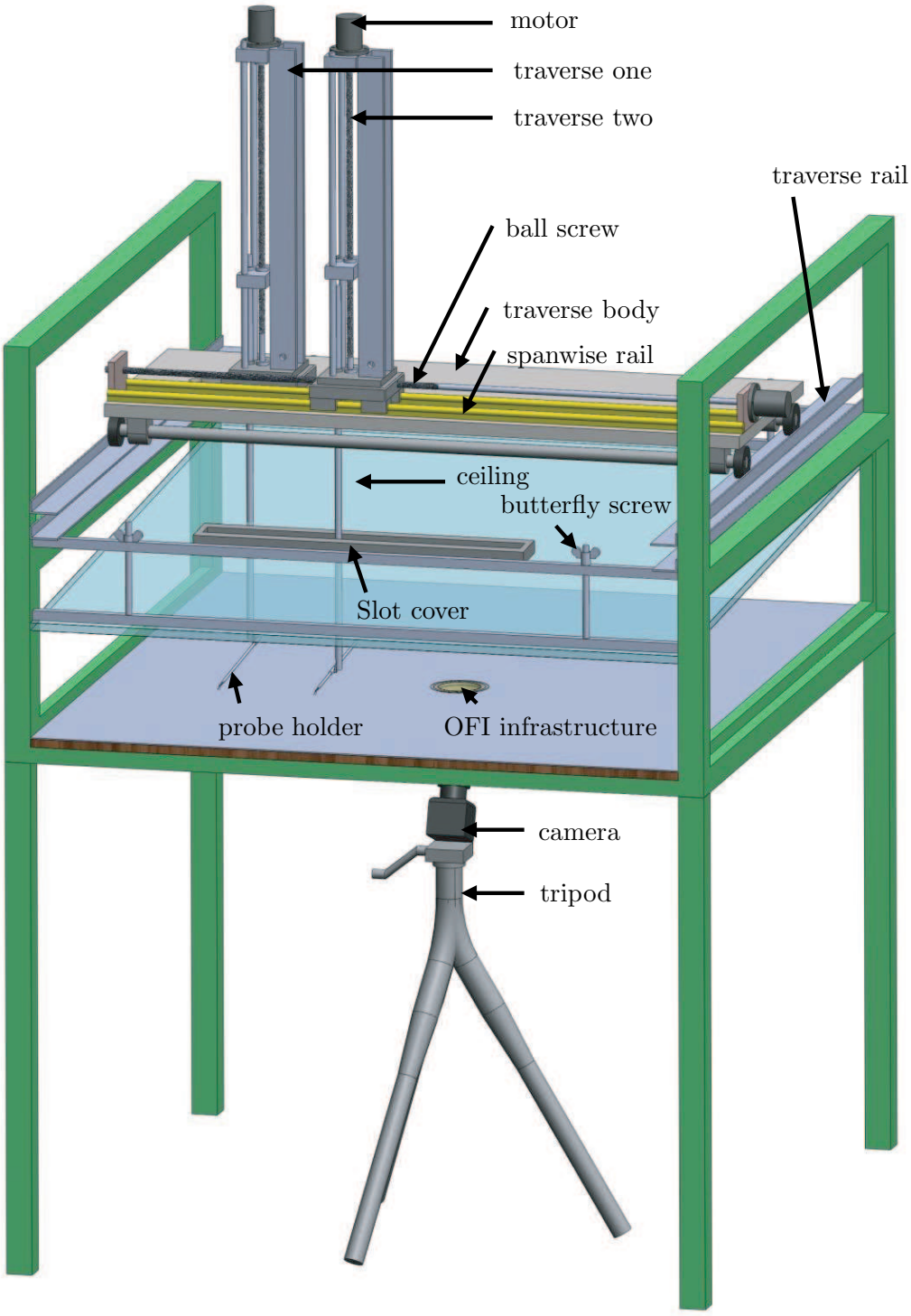


FIGURE 2.2: Wind tunnel perspective view.

FIGURE 2.3: Front view of wind tunnel

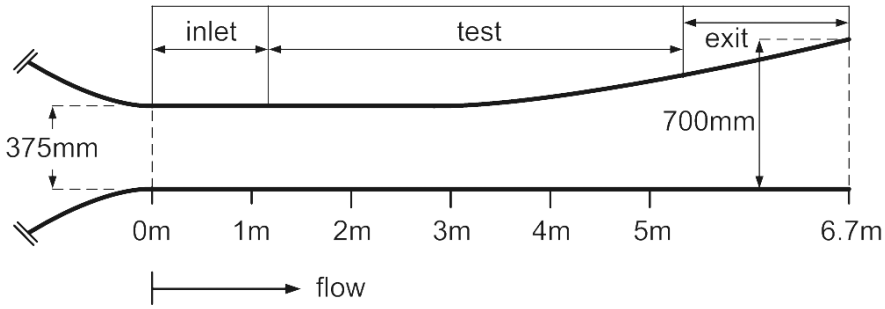


FIGURE 2.4: Illustration of the wind tunnel geometry

$$C_P = \frac{P - P_0}{P_t - P_0} = \frac{P - P_0}{\frac{1}{2}\rho {U_{in}}^2} = 1 - \left(\frac{U_1}{U_{in}}\right)^2 \tag{2.1}$$

Figure 2.5 shows $C_P$ plotted against streamwise position (m). The first 10 pressure taps are in the inlet section. The figure shows that the next 15 pressure taps are in the zero pressure gradient region. The long ZPG section is to ensure that the flow is stable

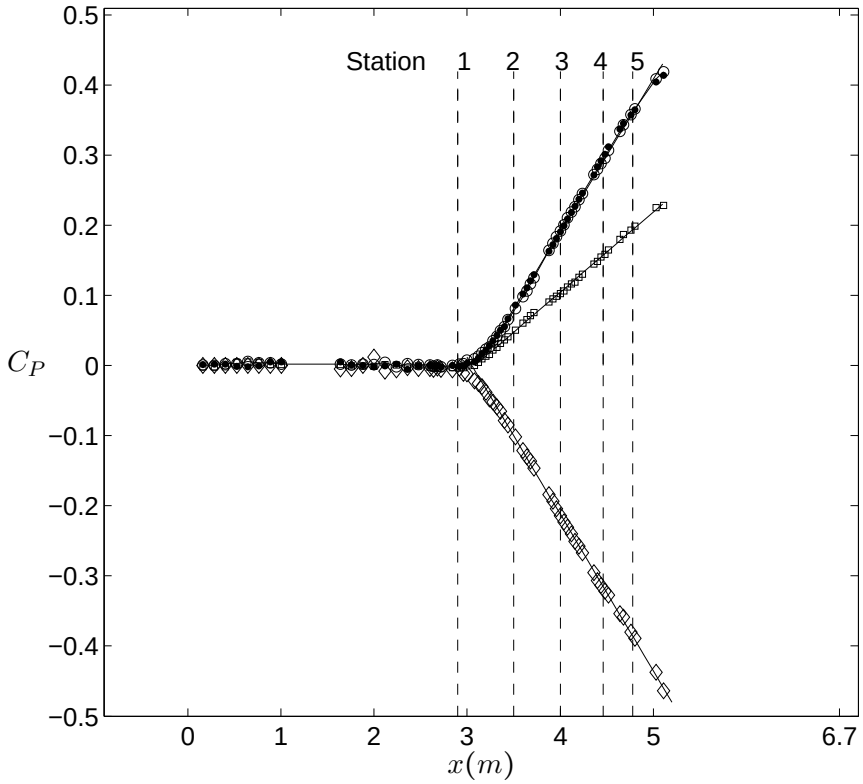


FIGURE 2.5: Coefficient of pressure $C_P$. ○: $U_{in}$ = 15.9 m/s, •: $U_{in}$ = 10.5 m/s for APG and □: $U_{in}$ = 10.5 m/s for mild APG. ⋄: $U_{in}$ = 10.5 m/s for FPG.

before any pressure gradient is introduced. For the APG case, two inlet velocities $U_{in}$ = 10.5 m/s and 15.9 m/s are tested. The $C_P$ obtained from the two inlet velocities collapses well. It can be shown that $C_P$ does not change with any inlet velocities within the velocity range of the experiment performed, i.e. 8 m/s $\lesssim U_{in} \lesssim$ 22 m/s.

To address any history effects, another $C_P$ based on a totally different wind tunnel ceiling setting was measured. In this case, a milder adverse pressure gradient was obtained, shown by the □ symbol. A detailed discussion regarding the effect of history is in Chapter 6. For the FPG cases, the ceiling setting was also set for a mild pressure gradient. The minimum $C_P$ in figure 2.5 is $C_P \approx -0.48$. The mild pressure gradients in these experiments are necessary to avoid any sudden change in the flow which may introduce changes in the flow structures.

## 2.3 Oil-film interferometry

The determination of the wall shear stress is crucial to the studies of wall-bounded flows. This quantity is especially important because of the scaling laws used to describe the velocity profiles of such flows. Many turbulence statistics, such as the mean velocity profiles and energy spectra, are non-dimensionalised by friction velocity, $U_\tau$. The friction velocity is defined as $U_\tau = \sqrt{\tau_o/\rho}$, where $\tau_o$ is the wall shear stress and $\rho$ is the density of the fluid and in this case, air.

A typical method to obtain wall shear stress is the Preston tube (Preston, 1954), it relies on the law of the wall calibrations. The Clauser chart method (Clauser, 1954) assumes the validity of the log law and requires knowledge of the universal constants. Recent findings in APG studies reveal that there is a deviation from the log law (Lee and Sung, 2009, Skote and Henningson, 2002), and the same applies to highly FPG studies (Bourassa and Thomas, 2009, Dixit and Ramesh, 2010). Therefore, it is crucial that an independent study to determine $U_\tau$ is adopted for the current pressure gradient study.

The Oil Film Interferometry (OFI) method is a direct method, requiring no calibration within the experiment. It is based solely on the thinning rate of a thin oil film and the forces imparted on the film as flow passes over it. The oil film interferometer can be used to obtain the wall shear stress without detailed knowledge or assumptions about the flow field (Ng et al., 2007).

OFI was used independently to determine skin friction coefficient $C_f$. The OFI measurement took place at the position where a hot-wire anemometer measurement was performed to the accuracy of 1 mm in the streamwise direction. 20 cSt and 200 cSt Dow Corning 200 Fluid, silicon-based oils were dropped onto a transparent, flat, fine surface glass flush-fit to the wind tunnel wall. Temperature and pressure were sampled while pictures of fringes on the droplet were taken using a Nikon D90 camera attached to a computer. The equipment list used for OFI measurement is shown in Appendix A.1.

The main cause for inaccuracy in OFI measurement is the temperature dependence of the oil viscosity (Zanoun et al., 2003). Therefore, the oil viscosity needs to be experimentally calibrated. Dow Corning 200 Fluid, can be obtained in many different viscosities. For these experiments the 20 and 200 cSt oils were used. The 20 cSt oil was found to be sufficient for the shear stress magnitudes in the APG experiment, while the 200 cSt oil was suitable for the FPG experiment. The calibration details for both silicone oils are shown in Appendix A.2.

Oil-film interferometry is based on the relationship between the thinning rate of the oil film and three main forces that may act upon it: gravity, pressure and shear forces. When the oil film is sufficiently thin, the effect of gravity and pressure forces becomes negligible and the thinning rate of the oil film is assumed to be linear.

Tanner and Blows (1976) found that the thinning rate of an oil film, could be applied in a simple relationship, to the measurement of shear stress, by using the thin oil film equation developed by Squire (1961). Further work was subsequently done by Tanner (1977a,b) and modifications to the equation were made in Monson (1983), Monson and Higuchi (1981). A review of the many methods is given by Naughton and Sheplak (2003). The wall shear relationship with the acting force is given by

$$\tau_o = \mu_{oil} \frac{\Delta x}{\Delta t} \frac{2\sqrt{n_{oil}^2 - n_{air}^2 sin^2\theta}}{\lambda}, \tag{2.2}$$

where $\theta$ is the illumination incident angle, $n_{oil}$ and $n_{air}$ are refractive indices of oil and air and $\lambda$ is the wavelength of the light source ($\lambda = 589.9$ nm for the sodium lamp that was used). $\Delta x$ is the fringe displacement found by the Huang Hilbert Transform (HHT) method discussed by Chauhan et al. (2010) and $\Delta t$ is the time between two successive pictures of fringes.

A detailed sketch of the OFI viewing port from Figure 2.3 is shown in Figure 2.6. The illustration at the top shows how the infrastructure is fixed to the wind tunnel base floor. The bottom contains the sectional view. There are three main parts: the glass plug, main frame and stiffening ring. Only one plug contains the transparent material to allow viewing from the bottom. The rest of the plugs are completely made from aluminum. This is because it is quite expensive to produce so many glass plugs, and glass is harder to maintain as well (glass surface can easily chip and scratch when in contact with sharp objects).

During installation, the main frames were glued with epoxy resin to the wind tunnel structure (floor). The top ring of the main frame has to be flush with the wind tunnel floor, therefore surface flatness equipment, such as small rectangular metal bars were used for visual inspection. Residues of the epoxy either on the wind tunnel surface or on the OFI infrastructures were completely removed using cleaning chemicals.

During operation, the glass plug (and all other solid plugs) and the main frame in Figure 2.6 has to be flush with the wind tunnel floor surface before measurement could

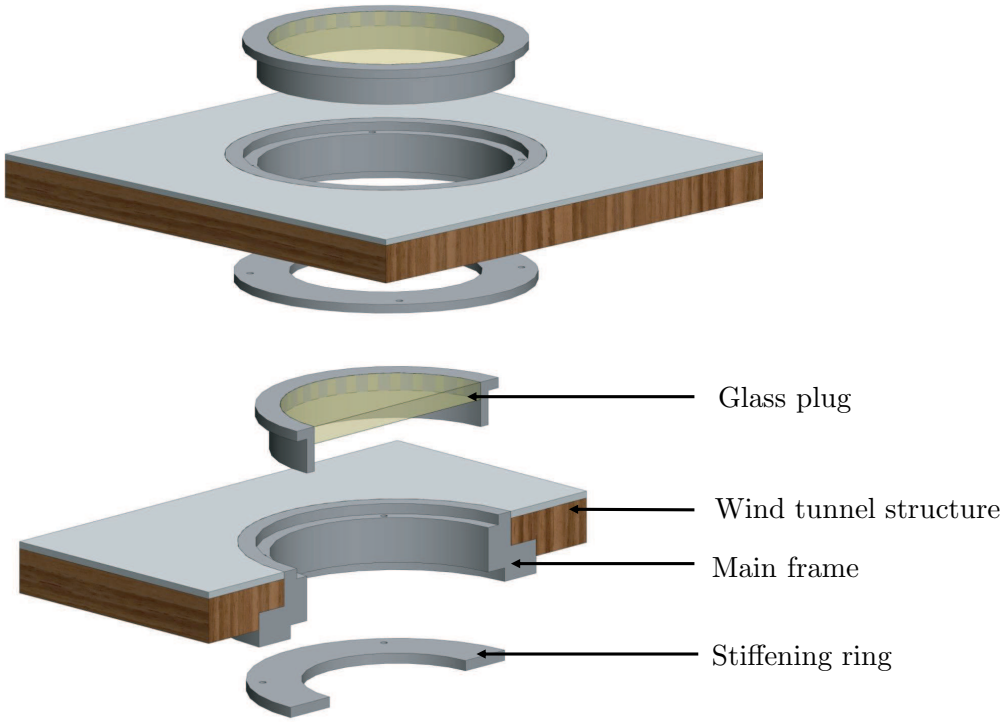


FIGURE 2.6: Oil-film interferometry infrastructure. Top figure shows the blown-out structure of the equipment and bottom figure shows the cross-section.

be performed. Adjusting bowel screws fixed into the main support were used to adjust the levels of the plugs. Finally, stiffening rings at the bottom of the installation were used to tighten all plugs.

Figure 2.7 shows transparent glass with a high-pressure sodium lamp lit from underneath, this lamp produced the yellowish colour. This type of lamp was used because of the characteristic wavelength of the light source. This picture was taken immediately after a measurement was performed, so there were still traces of fringes from two drops of silicone oils. Note that one of the sheared oil films (the upper) almost touched the edge of the transparent glass and the aluminium ring. This is acceptable even if the sheared oil film touched the aluminum ring, as the ring is still part of the removable plug, whereas if the sheared oil traveled beyond the aluminum ring, pictures taken after that were not considered. If the sheared oil went beyond the aluminum and touched the aluminum frame (the lower), the data from this particular oil drop would be discarded. The surface tension of the oil film might be altered once the oil film crossed the

FIGURE 2.7: Equipment for Oil-Film Interferometry: transparent glass plug on wind tunnel wall

plug-frame boundary; the oil might fill the tiny gap within the boundary.

Figures 2.8($a$) and ($b$) show samples of OFI fringes developed on the transparent plug. Figure 2.8 ($a$) is a typical 20 cSt oil drop sheared in the APG experiment. A 20 cSt oil drop spreads within less than one minute. The oil drop is also sheared easily and fringes can develop within three to four minutes. The air velocity in the wind tunnel has to be increased mildly as bubbles may develop on the fringes. Bubbles act much like foreign materials as they affect the fringe development and subsequent $\Delta x/\Delta t$ in equation 2.2. Oil drops were sheared faster in FPG studies; so there was a smaller window for measurement. Therefore, a higher viscosity oil was needed. A 200 cSt oil was used for FPG study. Figure 2.8($b$) shows typical 200 cSt drops on the transparent glass. The smaller spread within a given time allows more pictures to be taken at one run. The time to shear the fringes for the higher viscosity oil is approximately three times as long for an arbitrary distance $\Delta x_o$ than with the lower viscosity oil. Therefore, the time between two successive pictures of fringes, $\Delta t_o$, for the 200 cSt oil could be made three times longer for the same resolution i.e. $\Delta x_o/\Delta t_o$. $\Delta t$ is one of the three

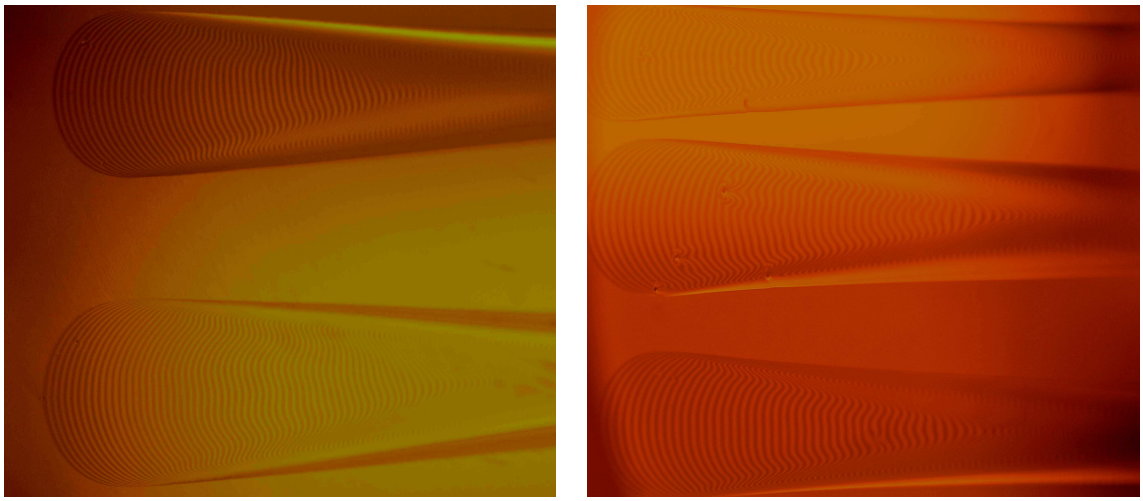

$(a)$ $(b)$

FIGURE 2.8: Fringes on transparent plug $(a)$ typical fringes from two drops of 20 cSt $(b)$ fringes from three drops 200cst.

important parameters in an OFI measurement. The others being free stream velocity and oil viscosity. All parameters are related and need to be balanced (Chauhan et al., 2010). (Chauhan et al., 2010) explained that short acquisition times would require a relatively low viscosity oil so that enough linear change in fringe spacing could be observed to determine the slope, which is not easily achieved in an experiment. By using the HHT, such problems are eliminated as the HHT is able to extract fringe spacing even from short signal length or interferograms with few visible fringes.

Figure 2.9$(a)$ shows a close-up, processed, black and white version of the bottom sheared oil in Figure 2.8$(a)$. This is a good quality picture of fringes. Figure 2.9$(b)$ shows the same from the second sheared oil (located in the middle) in Figure 2.8$(b)$. There are four dots on the fringes. These dots are not foreign materials, but air bubbles that developed when the air velocity was being ramped up aggresively. A small amount of bubbles like this do not usually affect the calculated $\Delta x/\Delta t$. This can be verified by comparing the other calculated $\Delta x/\Delta t$ from the top and bottom sheared oil in Figure 2.8$(b)$. However, larger bubbles or more bubbles may affect such calculations and these pictures were discarded. Once an OFI experiment was set up, it could be repeated easily, therefore it was usually better to discard pictures containing bubbles like in Figure 2.8$(b)$.

More about the OFI method used, background and calibration can be found in Madad et al. (2010), Ng et al. (2007) and Chauhan et al. (2010).

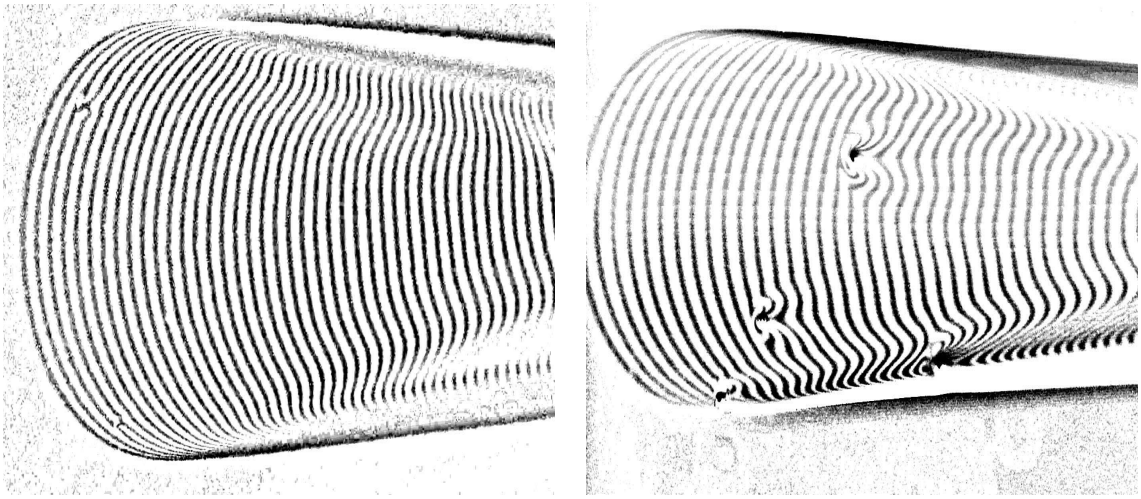

(*a*) (*b*)

FIGURE 2.9: Fringes on transparent plug (*a*) typical fringes from one drop 20 cSt (*b*) fringes from three drops 200 cSt.

## 2.4 The green boundary layer wind tunnel

Figure 2.10 shows a photograph of the green boundary layer wind tunnel. It has been painted green, therefore it is named the 'green tunnel'. Data collected from this tunnel have been used to test the validity of the Townsend (1976) attached-eddy hypothesis model in non-equilibrium adverse pressure gradient flows (Marusic and Perry, 1995). Later, FPG data obtained from this tunnel was used to evaluate an extended model, so that this model covers flows at arbitrary pressure gradients (Perry et al., 2002). The evolution of turbulent boundary layers in sink flows was also studied using data from this wind tunnel (Jones et al., 2001).

The setting up of this wind tunnel was done in early 2009. The works included replacing the wind tunnel ceiling with about 4 m long new pieces of 10 mm acrylic for the test section and a 1.5 m long 12 mm thick wooden ceiling for the inlet section. The reason for the change; the older ceiling, also made from acrylic, had a wavy profile. The waviness was picked up by the flow resulting in a wavy coefficient of friction. By mid 2009, the required pressure gradient profile was set up. By the end of 2009, most of the single hotwire measurement measurements in APG had been performed. The work for the OFI was started just before 2010 and was completed in three months.

For the spanwise measurements to take place, air-tight (spanwise) slots were required. The traverse too, had to be installed with a second axis. It had a positional encoder

FIGURE 2.10: Picture of the green tunnel.

installed for the first axis (vertical direction). Not to increase wind tunnel down-time, the construction of the traverse took place simultaneously with the installation of OFI infrastructure. The extra body of the traverse, including the stiffening metal ribs made the new traverse to weigh a little bit less than 50 kg.

In late 2010, most of APG measurement were completed. Since the traverse and OFI method have been set up, only the coefficient of pressure needed to be set up to achieve the required degree of FPG. The FPG experiments were carried out by the end of 2010.

## 2.5 Experimental parameters

Table 2.1 displays all parameters for the entire experiment. $U_{in}$ is the inlet velocity, taken at the position of the trip wire ($x$ = 0 m in Figure 2.4). $Re_\tau = \delta U_\tau/\nu$ is the Reynolds number based on the boundary layer thickness, where the boundary layer thickness is calculated by the method in Perry et al. (2002). $Re_\theta = \theta U_1/\nu$ is the Reynolds number based on the momentum thickness. $\delta^*$ is the displacement thickness, defined in (3.12) and $\theta$ is the momentum thickness defined in (3.17). $\Pi$ is the Cole's wake factor (Coles, 1956). However, since the friction velocity is obtained from the OFI method, there is a difference in the calculated values of $\Pi$. The difference is illustrated in Figure 3.7. The pressure gradient parameter, $\beta$ is defined as

$$\beta = \frac{\delta^*}{\tau_o}\frac{\mathrm{d}P_1}{\mathrm{d}x}, \tag{2.3}$$

and acceleration parameter, $K$ is defined as

$$K = \frac{\nu}{{U_1}^2}\frac{dU_1}{dx}. \tag{2.4}$$

| Symbol | $U_{in}$ m/s | $U_1$ m/s | $x$ m | $Re_\tau$ | $Re_\theta$ | $\delta$ m | $\delta^*$ m | $\theta$ m | $\Pi$ | $\beta$ | $K$ $\times 10^{-7}$ | $\nu/U_\tau$ $\mu m$ | $d$ $\mu m$ | $l^+$ | $t^+$ | $TU_1/\delta$ |
|---|---|---|---|---|---|---|---|---|---|---|---|---|---|---|---|---|
| Constant $Re_\tau \approx 3000$ in Adverse, Zero and Favourable PG | | | | | | | | | | | | | | | | |
| ⊡ | 22.3 | 20.00 | 4.00 | 3200 | 12030 | 0.077 | 0.0134 | 0.0093 | 1.38 | 1.74 | -1.05 | 24.6 | 2.5 | 30 | 0.52 | 25000 |
| △ | 21.6 | 21.57 | 2.90 | 3010 | 5900 | 0.059 | 0.0088 | 0.0059 | 0.64 | ZPG | ZPG | 19.6 | 2.5 | 30 | 0.70 | 30000 |
| ⊕ | 16.5 | 18.12 | 4.00 | 3100 | 6450 | 0.066 | 0.0069 | 0.0054 | 0.31 | -0.42 | 7.7 | 21.3 | 2.5 | 30 | 0.67 | 21800 |
| APG measurements | | | | | | | | | | | | | | | | |
| Constant $Re_\tau \approx 1900$ in APG | | | | | | | | | | | | | | | | |
| ▷ | 14.4 | 14.24 | 2.90 | 1820 | 5020 | 0.052 | 0.0075 | 0.0055 | 0.60 | ZPG | ZPG | 28.7 | 2.5 | 17 | 0.38 | 21800 |
| ⋄ | 13.4 | 12.70 | 3.50 | 1880 | 6090 | 0.061 | 0.0100 | 0.0072 | 0.82 | 0.91 | -1.40 | 32.5 | 2.5 | 15 | 0.28 | 31000 |
| o | 12.3 | 11.10 | 4.00 | 1990 | 6860 | 0.079 | 0.0142 | 0.0097 | 1.20 | 1.67 | -1.91 | 41.2 | 2.5 | 16 | 0.19 | 21900 |
| □ | 12.0 | 10.10 | 4.46 | 1980 | 8310 | 0.093 | 0.0196 | 0.0128 | 1.65 | 2.81 | -2.37 | 47.0 | 2.5 | 17 | 0.14 | 18400 |
| ∗ | 12.2 | 9.78 | 4.78 | 1970 | 9440 | 0.104 | 0.0242 | 0.0151 | 1.95 | 4.54 | -2.73 | 52.7 | 2.5 | 16 | 0.11 | 22500 |
| Constant $\beta \approx 1.6$ in APG | | | | | | | | | | | | | | | | |
| ⟁ | 10.9 | 9.84 | 4.00 | 1750 | 6390 | 0.078 | 0.0148 | 0.0099 | 1.33 | 1.63 | -2.09 | 44.7 | 2.5 | 15 | 0.14 | 19000 |
| ⊗ | 13.0 | 11.72 | 4.00 | 2010 | 7320 | 0.076 | 0.0138 | 0.0094 | 1.33 | 1.60 | -1.74 | 37.9 | 2.5 | 16 | 0.20 | 23000 |
| ⊛ | 16.3 | 14.71 | 4.00 | 2400 | 8960 | 0.073 | 0.0133 | 0.0092 | 1.37 | 1.60 | -1.38 | 31.0 | 2.5 | 17 | 0.31 | 24000 |
| Constant $\beta \approx 4.3$ in APG | | | | | | | | | | | | | | | | |
| ⊞ | 10.0 | 8.00 | 4.78 | 1730 | 7620 | 0.108 | 0.0242 | 0.0150 | 2.00 | 4.16 | -3.37 | 61.1 | 2.5 | 16 | 0.08 | 18000 |
| ⊠ | 15.9 | 12.93 | 4.78 | 2500 | 11640 | 0.102 | 0.0226 | 0.0143 | 2.05 | 4.27 | -2.10 | 40.8 | 2.5 | 17 | 0.19 | 16000 |
| ⊙ | 21.4 | 17.13 | 4.78 | 3510 | 16260 | 0.106 | 0.0225 | 0.0146 | 2.02 | 4.37 | -1.53 | 30.2 | 2.5 | 16 | 0.34 | 19600 |
| ⊛ | 23.9 | 19.10 | 4.78 | 3890 | 18500 | 0.104 | 0.0224 | 0.0146 | 2.10 | 4.39 | -1.35 | 26.8 | 2.5 | 17 | 0.42 | 24200 |

*continued on next page*

*continued from previous page*

| Symbol | $U_{in}$ m/s | $U_1$ m/s | $x$ m | $Re_\tau$ | $Re_\theta$ | $\delta$ m | $\delta^*$ m | $\theta$ m | $\Pi$ | $\beta$ | $K$ $\times 10^{-7}$ | $\nu/U_\tau$ $\mu m$ | $d$ $\mu m$ | $l^+$ | $t^+$ | $TU_1/\delta$ |
|---|---|---|---|---|---|---|---|---|---|---|---|---|---|---|---|---|
| $K \approx 1.4 \times 10^{-7}$ in APG | | | | | | | | | | | | | | | | |
| + | 13.0 | 12.19 | 3.50 | 1950 | 6050 | 0.066 | 0.0103 | 0.0073 | 0.85 | 0.94 | -1.44 | 33.7 | 2.5 | 15 | 0.26 | 29000 |
| × | 16.0 | 14.38 | 4.00 | 2470 | 8860 | 0.077 | 0.0135 | 0.0093 | 1.21 | 1.52 | -1.42 | 30.3 | 2.5 | 17 | 0.28 | 23900 |
| ◁ | 19.5 | 16.41 | 4.46 | 3270 | 14070 | 0.095 | 0.0194 | 0.0128 | 1.70 | 3.06 | -1.40 | 29.1 | 2.5 | 17 | 0.30 | 26600 |
| ⋆ | 22.5 | 18.00 | 4.78 | 3560 | 17070 | 0.107 | 0.0227 | 0.0147 | 1.90 | 4.73 | -1.47 | 30.0 | 2.5 | 17 | 0.31 | 26500 |
| $U_{in} \approx 15.9$ m/s in APG | | | | | | | | | | | | | | | | |
| ⟠ | 15.9 | 15.68 | 2.90 | 2330 | 6560 | 0.061 | 0.0087 | 0.0064 | 0.71 | ZPG | ZPG | 26.2 | 2.5 | 18 | 0.44 | 20500 |
| ⟡ | 15.9 | 15.13 | 3.50 | 2670 | 8540 | 0.076 | 0.0120 | 0.0085 | 0.99 | 1.16 | -1.18 | 28.4 | 2.5 | 17 | 0.37 | 20500 |
| ⟐ | 15.9 | 14.42 | 4.00 | 2380 | 8590 | 0.076 | 0.0136 | 0.0094 | 1.32 | 1.58 | -1.47 | 32.0 | 2.5 | 15 | 0.31 | 22600 |
| ◈ | 15.9 | 13.42 | 4.46 | 2500 | 10550 | 0.090 | 0.0184 | 0.0122 | 1.78 | 2.76 | -1.78 | 36.0 | 2.5 | 14 | 0.24 | 23500 |
| ⊠ | Same as in constant $\beta \approx 4.3$ | | | | | | | | | | | | | | | |
| Varying $l^+$ in APG | | | | | | | | | | | | | | | | |
| ⊙ | 21.3 | 19.15 | 4.00 | 3100 | 11480 | 0.078 | 0.0136 | 0.0092 | 1.37 | 1.72 | -1.11 | 25.2 | 5.0 | 41 | 0.52 | 24600 |
| ⊡ | 21.8 | 19.67 | 4.00 | 3180 | 11770 | 0.076 | 0.0133 | 0.0092 | 1.35 | 1.66 | -1.06 | 23.9 | 5.0 | 31 | 0.48 | 25000 |
| ▪ | 21.7 | 19.54 | 4.00 | 3130 | 11490 | 0.075 | 0.0132 | 0.0092 | 1.37 | 1.60 | -1.08 | 24.0 | 2.5 | 21 | 0.55 | 26000 |
| Milder $dC_p/dx = 0.114$ | | | | | | | | | | | | | | | | |
| ⧈ | 9.25 | 8.69 | 4.78 | 1820 | 6053 | 0.093 | 0.0150 | 0.0105 | 0.95 | 0.81 | -1.21 | 47.8 | 2.5 | 16 | 0.13 | 6100 |

*continued on next page*

*continued from previous page*

| Symbol | $U_{in}$ m/s | $U_1$ m/s | $x$ m | $Re_\tau$ | $Re_\theta$ | $\delta$ m | $\delta^*$ m | $\theta$ m | $\Pi$ | $\beta$ | $K$ $\times 10^{-7}$ | $\nu/U_\tau$ $\mu m$ | $d$ $\mu m$ | $l^+$ | $t^+$ | $TU_1/\delta$ |
|---|---|---|---|---|---|---|---|---|---|---|---|---|---|---|---|---|
| FPG measurements | | | | | | | | | | | | | | | | |
| $U_{in} \approx 10.5$ m/s in FPG | | | | | | | | | | | | | | | | |
| ✡ | 10.5 | 10.46 | 2.90 | 1600 | 4300 | 0.062 | 0.0089 | 0.0064 | 0.63 | ZPG | ZPG | 38.8 | 2.5 | 14 | 0.21 | 14000 |
| ▽ | 10.5 | 11.67 | 3.50 | 1750 | 4380 | 0.059 | 0.0079 | 0.0058 | 0.48 | -0.52 | 1.34 | 33.4 | 2.5 | 15 | 0.28 | 24300 |
| ◈ | 10.5 | 11.98 | 4.0 | 2100 | 4430 | 0.065 | 0.0074 | 0.0056 | 0.30 | -0.43 | 1.17 | 31.7 | 2.5 | 14 | 0.30 | 15000 |
| ⊕ | 10.5 | 12.53 | 4.46 | 2300 | 4870 | 0.070 | 0.0079 | 0.0060 | 0.30 | -0.42 | 1.04 | 30.6 | 2.5 | 16 | 0.33 | 16000 |
| ◫ | 10.5 | 13.07 | 4.78 | 2290 | 4500 | 0.066 | 0.0069 | 0.0053 | 0.20 | -0.33 | 0.95 | 28.7 | 2.5 | 17 | 0.37 | 15700 |
| Varying $l^+$ in FPG | | | | | | | | | | | | | | | | |
| ◎ | 17.0 | 18.67 | 4.00 | 2870 | 6690 | 0.063 | 0.0076 | 0.0057 | 0.38 | -0.47 | 0.78 | 22.1 | 5.0 | 48 | 0.65 | 23600 |
| ⊕ | Same as in AZF PG | | | | | | | | | | | | | 31 | | |
| • | 16.4 | 18.03 | 4.00 | 3100 | 6130 | 0.066 | 0.0067 | 0.0051 | 0.31 | -0.40 | 0.77 | 21.4 | 1.5 | 21 | 0.67 | 21800 |
| –. | 20.9 | 20.92 | 2.90 | 3000 | 8920 | 0.065 | 0.0088 | 0.0065 | 0.75 | ZPG | ZPG | 20.6 | 2.5 | 31 | 0.72 | 27000 |

TABLE 2.1: Experimental parameters for pressure gradient study using hotwire anemometers. All data from the University of Melbourne.

Three types of hotwire anemometer were used, namely the AA Lab Systems AN-1003, DISA and the Melbourne University Constant Temperature Anemometer (MUCTA). The hotwire probes were all operated with a constant temperature mode with an overheat ratio of 1.7 - 1.8. The indicated frequency response to the systems to 0.3 kHz - 2.0 kHz square-waves varied from 70 kHz to 130 kHz. Most of the measurements used 2.5 $\mu$m diameter wollaston wires. However, to compare with existing data such as that used in Monty et al. (2009), 5 $\mu$m wires were used. Most of the time, the AA Lab was used, however for the 1.5 $\mu$m wires, the DISA and MUCTA systems had to be used as it was not possible to balance the AA Lab anemometer.

Hot-wire signals were sampled using a Data Translation data-acquisition board. The sampling frequency, $f_s$, was set at 50 kHz and a low-pass filter was set at 25 kHz unless otherwise stated. The platinum sensing element was fabricated on boundary layer-type probe-body geometry, Dantec 55P05 or 55P15 with prong spacings of 3 mm and 1.25 mm. Wollaston wires were soldered to the prong tips and etched to give a platinum sensing element of physical length $l$. The viscous scale non-dimensional length of the platinum sensing element is given by $l^+ = lU_\tau/\nu$. The ratio of the sensing element to its diameter was $l/d > 200$ (Bruun, 1995, Ligrani and Bradshaw, 1987).

The hot wires were statically calibrated *in situ* against a Pitot-static tube pair before and after each boundary-layer traverse. Third-order polynomial curves were fitted to the calibration data. Atmospheric conditions were monitored continuously throughout the experiments, using a calibrated thermocouple and an electronic barometer (144S-BARO, Sensortechnics). Uncertainties due to temperature drift were accounted for by using a linear interpolation for temperature correction using the pre and post-experiment calibrations. However, such temperature correction procedure was applied to less than 10% of the data, because temperature drifts were not usually significant ($\approx 0.8^oC$ at worst).

The non-dimensional sample interval is given by $\Delta t^+ = \Delta t U_\tau^2/\nu$ where $\Delta t = 1/f_s$. The total length in seconds of the velocity sample at each wall-normal measuring position is given by $T$, non-dimensionalised to give boundary-layer turnover times $TU_1/\delta$. In order to obtain converged statistics, $TU_1/\delta$ has to be large. According to Guala et al. (2006), Hutchins and Marusic (2007a), Kim and Adrian (1999) and Monty et al. (2009), the large-scale features in wall-bounded turbulent flows can exceed $20\delta$, therefore a minimum of hundreds of these events are expected to past the probe for converged statistics. The current experiment where the boundary layer thickness is in the region of 50 mm $< \delta <$ 100 mm and with the streamwise velocities 10 m/s $< U_1 <$ 25 m/s, normally required

| Source | Uncertainty |
|---|---|
| Pressure transducer | ±0.15% |
| Temperature | ±0.1% |
| Atmospheric pressure | ±0.1% |
| Friction velocity, $U_\tau$ | ±1% |
| Pitot probe uncertainty during calibration | ±0.5% |
| Wire size, $l$ | ±0.04 mm |
| Initial wall normal position | ±0.025 mm |
| Inner scaled mean velocity, $U^+$ | $\pm \approx 2\%$ |
| Inner scaled mean velocity, $\overline{u^2}^+$ | $\pm \approx 4\%$ |

TABLE 2.2: Uncertainty estimates.

sampling time of $100 < T < 300$ in seconds (the sampling time is used for the boundary layer turnover $TU_1/\delta$). Hence, for a typical 50-point wall-normal measurement, three hours were needed for a complete measurement.

To maintain similar convergence for the two points spanwise measurements, a much longer time was required. For the spanwise measurement, in addition to the two to three-hour boundary layer measurement, the spanwise measurements were added at four pre-selected wall-normal locations. At each wall-normal location, 40 spanwise measurement were recorded. The entire course of measurement sometimes exceeded 10 hours. Temperature drifts for this experiment were not significant. If there was a change of temperature of $\Delta T > 0.5^o$C in the course of the experiment, a temperature compensation correction would be applied. The temperature compensation correction was based on the pre and post calibration temperatures. Given the pre and post calibration curves and their respective temperatures, new sets of calibration curves were obtained from linear interpolations based on the temperature of each wall-normal position.

### 2.5.1 Uncertainty estimates

During experiments, there are a list of experimental uncertainties which can cause errors in many of the parameters shown in Table 2.1. These errors are described in Table 2.2.

The method used in the uncertainty analysis is similar to the one in Kline and McClintock (1953). The hotwire uncertainties are consistent with findings from the well-calibrated hotwire study by Bruun (1995). The estimated errors are also consistent with recent experiments by Hultmark et al. (2010) and Ng et al. (2011).

# Chapter 3

# Mean statistics

This chapter discusses the background theory before presenting the mean statistics. This chapter mainly discusses the coefficient of friction, the mean velocities, turbulence intensities, shape factor, skewness, flatness and turbulence production. The mean velocities and turbulence intensities are scaled with friction velocity or free stream velocity to test the relevance of these scalings. The deviations from the log law as observed by Bourassa and Thomas (2009), Nagano et al. (1998), Skåre and Krogstad (1994) and Dixit and Ramesh (2010) will be shown. The development of the wake region too will be explained using the diagnostic function. The amplified wake of the mean velocity profile, the easily recognised feature of an APG flow has been documented by Nagano et al. (1998), Samuel and Joubert (1974) and Aubertine and Eaton (2005). The relationship between pressure gradient parameter and the wake has been proposed by Perry et al. (2002). While these studies have undoubtedly contributed to better understanding in pressure gradient flows, the two important parameters in pressure gradient flows, the pressure gradient parameter, $\beta$ and the Reynolds numbers, $Re_\tau$, varied. Here, in one set of the data, the effect of the pressure gradient on the mean velocities and turbulence intensities profiles is analysed when the Reynolds number is constant. The effect of increasing the Reynolds number when there is a pressure gradient (also constant), will also be shown in another set of data. This achieves one of the major aims of the thesis, to isolate the effect of these two important parameters in pressure gradient flows.

The section on the shape factor (3.12) is a continuation of the work by Monkewitz et al. (2008) on the mean flow similarity laws in ZPG TBL. The skewness and flatness, Section 3.13, attempts to highlight the effect of pressure gradients when the large-scales are removed from the flow using a filtering method, similar to the analysis performed by

Metzger and Klewicki (2001) addressing the effect of very high Reynolds number flow. It is known that the large-scale features are energised in APG (Bradshaw, 1967a, Lee and Sung, 2009, Monty et al., 2011, Skåre and Krogstad, 1994), so it is suspected that the large-scale features are responsible for the increased skewness in APG flows (Nagano and Houra, 2002, Skåre and Krogstad, 1994), an analysis that has not been documented in detail. Understanding the roles of the large-scales is another main aim of the thesis.

The analysis for the turbulence production (Section 3.15) considers data from three pressure gradient cases at a constant Reynolds number. This analysis arises from recent literature by Marusic et al. (2010a) who attributed that as the Reynolds number increases, the large- scales become important in terms of sustaining and producing turbulence. This analysis is repeated in pressure gradient flows, where the detail of such analysis seems to be not so well documented. This chapter contains some new information regarding the effect of pressure gradients, attempting to answer the aims outlined at the start of the thesis i.e. to identify the effect of the two important parameters $\beta$ and the Reynolds number, to analyse the effect of the large-scale features on turbulent statistics and to compare mean statistics of pressure gradient boundary layer flows.

## 3.1 Coefficient of friction

The scaling used for most analyses are based on internal variables, friction velocity $U_\tau$ and kinematic viscosity $\nu$. Therefore it is important to employ a proper analysis to calculate $U_\tau$. The friction velocity is obtained from the coefficient of friction, where the latter is defined as

$$C_f = \frac{\tau_o}{\frac{1}{2}\rho U_1^2} = 2\frac{U_\tau^2}{U_1^2}, \tag{3.1}$$

which is measured using the oil-film interferometry method described in Section 2.3. It is important to note that there is a difference between $U_\tau$ measured with OFI and that determined by the Clauser method using the mean velocity profile. Figure 3.1 displays the coefficient of friction plotted as a function of the pressure gradient parameter, $\beta$ (the Reynolds number is maintained constant). Note that the skin friction determined from the Clauser chart method agrees with that obtained from oil-film interferometry *only* for zero and mild adverse pressure gradient boundary layer flows. Beyond $\beta \approx 2$, the difference between the methods becomes significant (up to approximately 10% difference in $C_f$). This suggests that the Clauser chart is invalid for moderate to strong

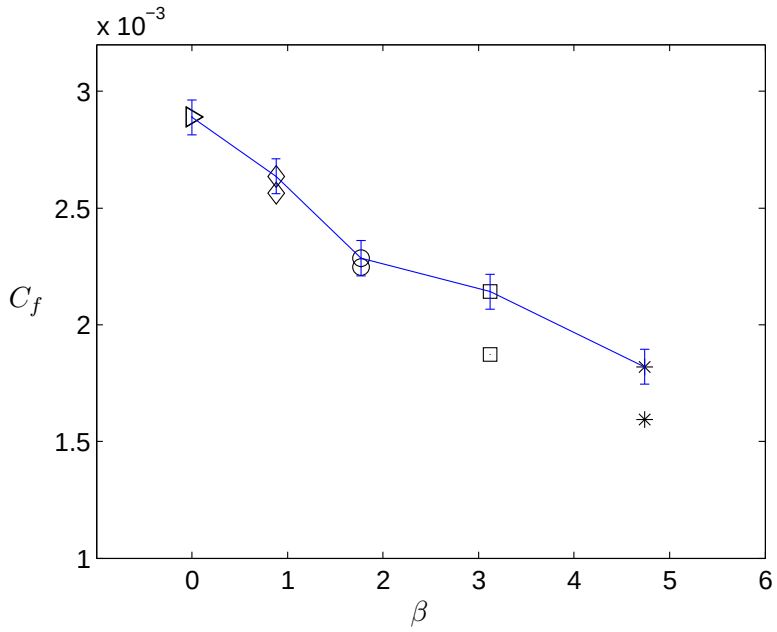


FIGURE 3.1: Coefficient of friction for constant $Re_\tau \approx 1900$. The solid line connects $C_f$ obtained directly by OFI. The error bars of 2.5% for the OFI method are shown. Symbols: ($\triangleright$) Station 1, ($\diamond$) Station 2, (o) Station 3, ($\square$) Station 4, ($*$) Station 5, for other details, refer to Table 2.1. Symbols not connected with the solid line represent $C_f$ obtained from Clauser chart.

adverse pressure gradients. The use of $C_f$ obtained from the Clauser chart could lead to inaccurate conclusions about the applicability of scaling arguments for pressure gradient boundary layers. Throughout this thesis, $U_\tau$ is determined by oil-film interferometry except in the cases of the zero pressure gradient data of Hutchins et al. (2009) where the Clauser method was used.

Figure 3.2 shows the coefficient of friction plotted as a function of the Reynolds number when the pressure gradient parameter, $\beta$ is maintained constant. The figure shows that there is almost a constant shift between $C_f$ measured by OFI compared to $C_f$ obtained from the Clauser chart method, with a percentage difference of approximately 10 – 15%. In ZPG boundary layer flows, Coles (1962), Fernholz and Finley (1996) and DeGraaff and Eaton (2000) have shown skin friction as a decreasing exponential function of the Reynolds number based on momentum thickness, $Re_\theta$. Nagib et al. (2007) compiled ZPG TBL data and showed a collapse of $C_f$ which decreased as a function of the Reynolds numbers based on numerous skin friction - Reynolds number relationships. In channel flow too, Ng et al. (2007) have also shown skin friction that decays exponentially with the Reynolds number (based on channel height). The existing studies cited have the

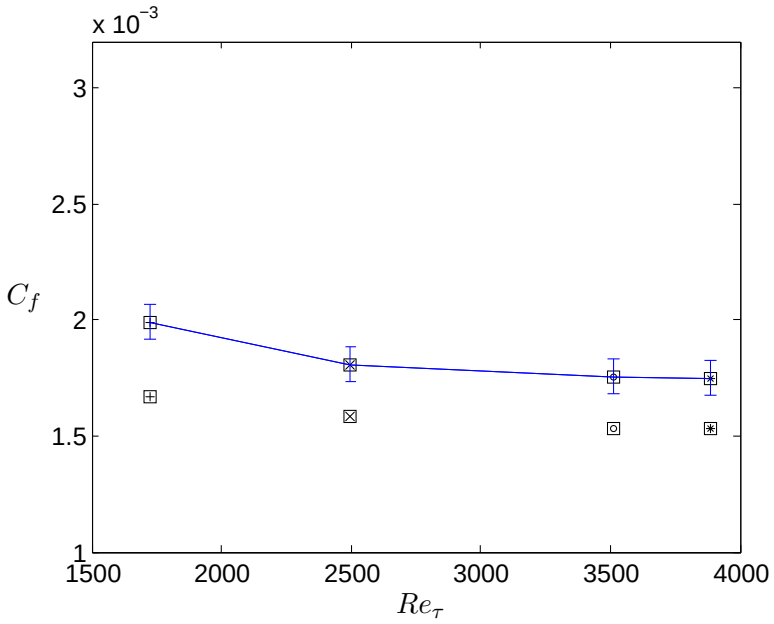


FIGURE 3.2: Coefficient of friction for constant $\beta \approx 4.3$. The solid line connects $C_f$ obtained directly by OFI. The error bars of 2.5% for the OFI method are shown. Symbols not connected with the solid line represent $C_f$ obtained from Clauser chart. Refer to table 2.1 for symbols.

Reynolds numbers in the order of $10^4$. There is also a trend here that $C_f$ in a constant pressure gradient $\beta$ decreases with the Reynolds number. An experiment in APG with skin friction determined from a much higher Reynolds number should be carried out to confirm this trend.

In the current FPG experiments, there is only a small difference between $C_f$ obtained from OFI and that determined from the Clauser chart method. The significant difference found in strong FPG by Bourassa and Thomas (2009), Fernholz and Warnack (1998) and Dixit and Ramesh (2010) is not observed due to the relatively mild pressure gradients employed here.

## 3.2 The law of the wall

In this section, a background theory of turbulent boundary layer flows is presented. The background theory starts with the development of the law of the wall and the law of the wake (Coles, 1956). For general two-dimensional turbulent wall-shear flow, the velocities in the streamwise and wall-normal directions are given by $u(x, z)$ and $v(x, z)$. The flow

exerts a wall shear stress, $\tau_o$ on a smooth impermeable wall at rest at $z = 0$. Assuming a fluid with constant density, the friction velocity is given by

$$U_\tau = \sqrt{\tau_o/\rho} \tag{3.2}$$

Ludwig Prandtl of Göttingen, Germany published a paper in 1904 suggesting that flow over a solid boundary may be separated into two regions. The first region is concerned with the flow outside of the boundary layer which may be considered inviscid. In the second region, closer to the wall, Prandtl assumed that only wall variables give rise to the flow and significantly influenced by viscosity. The flow in this region is a function of wall-normal distance, $z$, friction velocity, $U_\tau$ and kinematic viscosity, $\nu$. By dimensional analysis the relationship is shown as

$$\frac{U}{U_\tau} = f_1\left(\frac{zU_\tau}{\nu}\right). \tag{3.3}$$

Here, $f_1$ is a universal function that is independent of the large-scale characteristics of the flow. This is called 'Prandtl's law of the wall'. Similarly, in the region beyond the viscous buffer layer, the mean streamwise velocity is observed to follow, what is called the 'velocity defect law'

$$\frac{U_1 - U}{U_\tau} = f_2\left(\frac{z}{\Delta}\right). \tag{3.4}$$

Here $\Delta$ is the boundary layer thickness and $f_2$ is a function dependent on $z/\Delta$ for a given turbulent shear flow. Following for example Millikan (1938), assuming there is a region in the turbulent shear flow where both (3.3) and (3.4) are valid, equating gradients of velocity i.e the derivatives of (3.3) and (3.4) produces

$$\frac{\partial}{\partial z}\left(\frac{U}{U_\tau}\right) = \frac{U_\tau}{\nu} f_1'\left(\frac{zU_\tau}{\nu}\right) = -\frac{1}{\Delta} f_2'\left(\frac{z}{\Delta}\right), \tag{3.5}$$

Integration then yields

$$\frac{U}{U_\tau} = \frac{1}{\kappa}\ln\left(\frac{zU_\tau}{\nu}\right) + A, \tag{3.6}$$

called the classic logarithmic law of the wall, and

$$\frac{U_1 - U}{U_\tau} = -\frac{1}{\kappa}\ln\left(\frac{z}{\delta}\right) + B. \tag{3.7}$$

called the logarithmic velocity defect law. Here, $\kappa$ is the von Kármán constant, $A$ is a universal constant and $B$ is a large-scale characteristic constant that depends on flow geometry and pressure gradients. The classic logarithmic law of the wall, in this thesis called the 'log law' for simplicity, has been widely accepted until now. The 'constants' $\kappa$ and $A$ have been reviewed many times. For example, Coles (1962) suggested $\kappa = 0.41$ and $A = 5$. With an abundance of experimental and numerical data to support it, the explicit form of the log law remains as it is. Detailed discussion about the dependence of these constants on flow geometry is discussed in Section 3.12.

Returning to (3.6) and (3.7), the region of overlap increases directly with the Reynolds number ($\delta U_\tau/\nu$), however in adverse pressure gradient (APG), the logarithmic region is shorter, the immediate result of an increasing wake region.

## 3.3 Alternatives to log law

Although the log law has been accepted almost universally, the velocity scale in the logarithmic velocity defect law has been questioned, especially at low to moderate Reynolds number. Changing outer flow scale invalidates the derivations above, (3.5 to 3.7). An alternative form to characterise the behaviour of the mean velocity is called the power law:

$$\frac{U}{U_\tau} = \alpha_1\left(\frac{zU_\tau}{\nu}\right)^{\alpha_2}. \tag{3.8}$$

The power law has been used for example in Barenblatt (1993) and George and Castillo (1997). There are also other forms of the power law. A lot of previous studies have focused on boundary layer flows in equilibrium, i.e. these profiles are assumed to be independent of streamwise distance. For boundary layers held at incipient separation, Stratford (1959) reported that the mean velocity near the wall did not contain a logarithmic region but could be related with the half-power law equations as follows:

$$U = D_1(\alpha_3 z)^{1/2} + D_2(\alpha_3 \nu)^{1/3} \tag{3.9}$$

where $\alpha_3 = (1/\rho)\mathrm{d}P_1/\mathrm{d}x$ is the local kinematic pressure gradient and $D_1$ and $D_2$ are absolute constants. Perry et al. (1966) proposed the 'half-power law' for APG flows. It was postulated that a sufficiently developed APG flow could be divided into three regions. Region 1 is close to the wall, and Prandtl's law of the wall (3.3) is applicable. Region 2 is in the logarithmic region, therefore the log law (3.6) is applicable. Provided that the flow has sufficiently developed, for a large wall distance, region 3 is described by

$$\frac{U}{U_\tau} = J\left(\frac{\alpha_3 z}{U_\tau}\right)^{1/2} + \frac{\Delta U_2}{U_\tau}\left(\frac{U_\tau^3}{\alpha_3 \nu}\right), \tag{3.10}$$

called the half power law. Here $J$ is a universal constant, $\alpha_3$ is the as defined in (3.8), $\Delta U_2$ is a function of integration which is independent of $z$, $\Delta U_2/U_\tau$ is referred to as the 'slip function'. The slip function represents the non-dimensional velocity of slip at the wall if this equation is extrapolated to the wall. Perry et al. (1966) presented APG data in support of this formulation.

With a wide range of APG data, Perry and Schofield (1973) and Schofield (1981) successfully established the Schofield-Perry mean velocity and velocity defect equations. As an adverse pressure gradient increases indefinitely, the local coefficient of friction (and friction velocity, $U_\tau$ too) approaches zero while $\Pi$ and $\beta$ approach infinity. The log region thins and vanishes and near-wall variables become inappropriate (White, 1991). Therefore it is natural to replace $U_\tau$ with a velocity scale that could describe the flow better. Schofield-Perry proposed a profile correlation $U(z)$ which near separation, varied approximately with $z^{1/2}$. This relationship had been earlier predicted analytically by Mellor and Gibson (1966). Schofield-Perry showed that an APG flow could be divided into two main regions, the outer flow and the inner flow. The outer flow is described by the velocity defect law

$$\frac{U_1 - U}{U_s} = 1 - 0.4\left(\frac{z}{\delta_s}\right)^{1/2} - 0.6\sin\left(\frac{\pi}{2}\frac{z}{\delta_s}\right), \tag{3.11}$$

where $\delta_s = 2.86\delta^* U_1/U_s$ is the integral layer thickness, later called the Schofield-Perry boundary layer thickness and $U_s$ is the Schofield and Perry velocity scale. The displacement thickness, $\delta^*$ is defined as

$$\delta^* = \int_0^\delta \left(1 - \frac{U}{U_1}\right) dz. \tag{3.12}$$

Schofield-Perry's inner flow is described by inner law in the form

$$\frac{U}{U_1} = 0.47\left(\frac{U_s}{U_1}\right)^{3/2}\left(\frac{z}{\delta^*}\right)^{1/2} + 1 - \frac{U_s}{U_1}, \tag{3.13}$$

where $\delta_s = 2.86\delta^*(U_1/U_s)$. The ratio $U_s/U_1$ is determined from a mean velocity profile by using a 'half power chart' similar to the Clauser chart i.e. $U_\tau/U_1$ is analogous to $U_s/U_1$. An example is shown in Figure 3.3($a$). Note the half power abscissae, $(z/\delta^*)^{1/2}$. To demonstrate the effect of varying $U_s$, by using an initial pre-selected trial value of $U_s = 7.2$, the result of evaluated (3.13) is shown by the dash-dotted line. The trial value of $U_s$ is increased by a fixed value of 0.5 and these are shown by evaluated (3.13) denoted by the dotted lines. In the region of $0.1 < (z/\delta^*)^{1/2} < 1.0$, using the 'accepted' $U_s$, the data are supposed to collapse with (3.13), shown by the solid line. This is the region selected in most of the analysis in Perry and Schofield (1973), Schofield (1981), Schofield and Perry (1973).

As shown in Figure 3.3($a$), the data does not collapse well with the approximating method chosen here, where $U_s = 8.7$ is indicated by the solid line. A similar trend could be found in Schofield and Perry (1973) when the data from Ludwieg & Tillman (Fig. 15 and Fig. 16) were used, when $\tau_m/\tau_o < 1.5$, where the maximum shear stress is obtained from the local shear stress profile $\tau_m = \rho uv|_{\max}$ and $\tau_o$ is calculated from (3.2). For these formulations to work, there needs to be sufficient maximum shear stress to the wall-shear stress ratio i.e. $\tau_m/\tau_o > 1.5$. This ratio is met in the current APG data, where $\tau_m/\tau_o \approx 3.0$[1]. There is no obvious reason to explain why the current data does not collapse well with the Schofield-Perry formulations (as shown in Schofield and Perry (1973) with a similar $\tau_m/\tau_o$ ratio), however the data collapses well when a multiplier of 0.52 is used to replace 0.47 in (3.13). $U_s$ for the other data were also obtained from this method resulting in different $U_s$ for each data.

[1]The $uv$ term is approximated by formulation described in Perry et al. (2002)

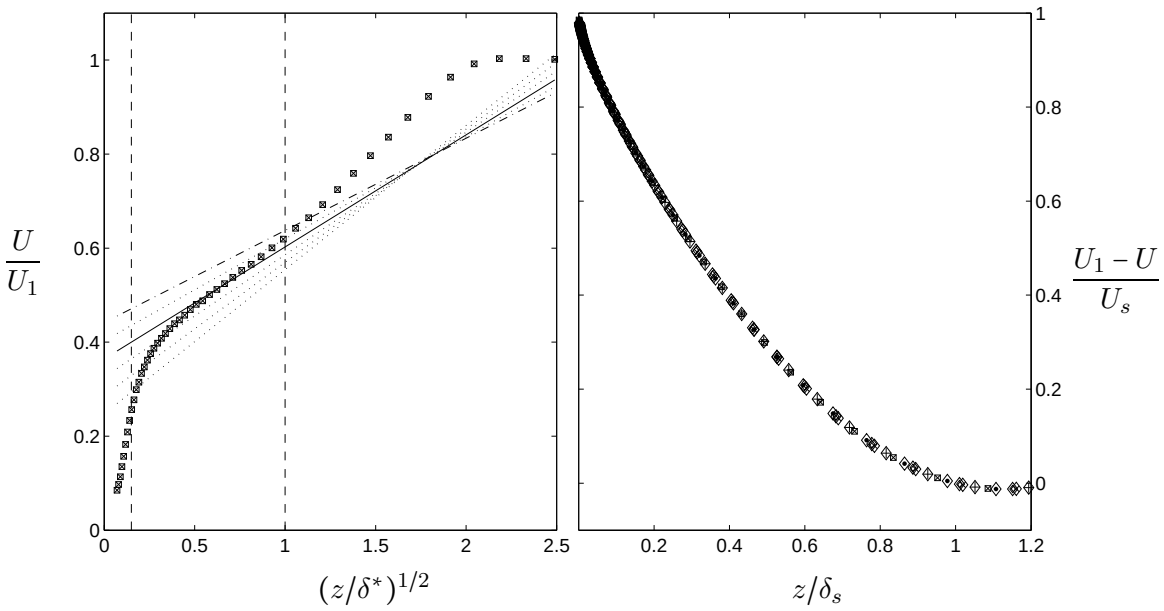


FIGURE 3.3: Half-power formulations by Perry and Schofield (1973). ($a$) Inner law, solid line denotes (3.13) with accepted $U_s$ = 8.7. The vertical dashed lines are $(z/\delta^*)^{1/2}$ = 0.1 and $(z/\delta^*)^{1/2}$ = 1.0. The other lines are results from varying $U_s$, explained in the text. The data is taken from constant $U_{in} \approx$ 15.9 m/s with $\beta \approx 4.4$, $x$ = 4.78m. ($b$) Defect law from (3.11). Symbols: ⊕ $x$ = 2.90m (ZPG), ⊗ $x$ = 3.50m, ◇ $x$ = 4.00m, ◈ $x$ = 4.46m and ⊠ $x$ = 4.78m, refer to Table 2.1 for more details.

A velocity defect governed by (3.11) for all of the data at constant $U_{in} \approx$ 15.9m/s is shown in Figure 3.3($b$). Note that, in this set of data, the pressure gradient parameter increases from $\beta$ = 0 (ZPG) at station one, ($x$ = 2.90m) to $\beta \approx 4.4$ at station five, ($x$ = 4.46m). A collapse can be seen by using this formulations across the pressure gradient parameter, $\beta$.

Schofield claimed that the formulations represented in (3.11) and (3.13) applied to all adverse pressure gradient boundary layers including those at the verge of separation, regardless of whether the boundary layers were in the state of equilibrium or not. However, Dengel and Fernholz (1990)'s data did not confirm these formulations except for one point. Furthermore, Dengel and Fernholz (1990) said that these formulations were 'not particularly good approximation for the other profiles', referring to a great percentage of their data. This might be why the current data (Figure 3.3($a$)) does not collapse with the Schofield-Perry formulations. However, as has been noted earlier, small modifications could be introduced to make the formulations work.

## 3.4 Coles' law of the wall and law of the wake

Based on a large number of mean flow profiles, Coles (1956) proposed that the mean velocity could in general be described by the 'law of the wall' (3.6) and the 'law of the wake' as follows

$$\frac{U}{U_\tau} = \frac{1}{\kappa}\ln\left(\frac{zU_\tau}{\nu}\right) + A + \frac{\Pi}{\kappa}W_c\left(\frac{z}{\delta_c}\right), \tag{3.14}$$

where $W_c(z/\delta_c)$ is Coles' universal wake function, $\Pi$ is the wake strength which depends on the streamwise flow development, and $\delta_c$ is the boundary layer thickness determined by such formulation i.e. the boundary layer based on Coles wake formulation. For $w(0) = 0$, $w(1) = 2$, ($w(z/\delta_c)$ is the wake function) and $\int_0^2 (z/\delta_c)\mathrm{d}w = 1$. Equation 3.14 can be related to the wake parameter $\Pi$ by the local skin friction coefficient $C_f = 2(U_\tau/U_1)^2$. The equation could be related to the displacement thickness $\delta^*$ by (Coles, 1956)

$$\kappa\frac{\delta^* U_1}{\delta_c U_\tau} = 1 + \Pi, \tag{3.15}$$

and to the momentum thickness $\theta$ by

$$\frac{\kappa^2}{2}\frac{\delta^* - \theta}{\delta_c}\frac{U_1^2}{U_\tau^2} = 1 + c_1\Pi + c_2\Pi^2, \tag{3.16}$$

where $c_1$ and $c_2$ are constants of order unity. The momentum thickness $\theta$, the thickness of a layer of fluid, of velocity $U$, for which the momentum flux is equal to the deficit of momentum flux through the boundary layer is determined by

$$\theta = \int_0^\delta \frac{U}{U_1}\left(1 - \frac{U}{U_1}\right)dz. \tag{3.17}$$

Coles (1956) further demonstrated that (3.14) and (3.15) together with the identity

$$\left(\frac{\delta^*}{\delta_c}\right)\left(\frac{U_1}{U_\tau}\right) = \left(\frac{\delta^* U_1}{\nu}\right)\Big/\left(\frac{\delta_c U_\tau}{\nu}\right), \tag{3.18}$$

are sufficient to determine all five of the dimensionless parameters $U_1/U_\tau$, $\delta^*/\delta_c$, $\delta_c U_\tau/\nu$, $\delta^* U_1/\nu$ and $\Pi$ when any two parameters are known. For example, if the two known quantities are $U_1/U_\tau$ and $\delta^* U_1/\nu$ as in many boundary layer flow cases, substituting these known quantities into (3.15) leads to $\delta_c = \kappa\delta^* U_1/(1+\Pi)/U_\tau$. Further substituting this expression ($\delta_c$) to (3.14), leads to a simple equation for $\Pi$;

$$2\Pi - \ln(1+\Pi) = \kappa\frac{U_1}{U_\tau} - \kappa A - \ln\left(\frac{\delta^* U_1}{\nu}\right) - \ln\kappa. \tag{3.19}$$

Coles (1956) suggested that the functional form of the wake function in (3.14) takes the form

$$w\left(\frac{z}{\delta_c}\right) = 1 - \cos\left(\pi\frac{z}{\delta_c}\right). \tag{3.20}$$

Expressions (3.14) and (3.20) have been quite successful in describing mean velocity profiles. However, the slope of the profile at $z = \delta_c$ is non-zero. A further modification by Perry and Li (1990) leads to

$$\frac{U}{U_\tau} = \frac{1}{\kappa}\ln\left(\frac{zU_\tau}{\nu}\right) + A + \frac{\Pi}{\kappa}W_c\left(1 - \cos(B\pi\frac{z}{\delta_p})\right), \tag{3.21}$$

where $B$ is equal to the ratio $\delta_p/\delta_c$ and is a function of only $\Pi$. The new boundary layer thickness now, $\delta_p$ is calculated by the integral method

$$\delta_p = \frac{\delta^*}{C_1}\frac{U_1}{U_\tau} = \frac{\Pi + 3/4}{\kappa}, \tag{3.22}$$

where

$$C_1 = \int_0^\infty \frac{U_1 - U}{U_\tau}\mathrm{d}\eta, \tag{3.23}$$

where $\eta = z/\delta_p$. The velocity defect is in the form

$$\frac{U_1 - U}{U_\tau} = -\frac{1}{\kappa}\ln\eta + \frac{\Pi}{\kappa}\{\cos(B\pi\eta) - \cos(B\pi)\}. \tag{3.24}$$

## 3.5 Modification to Coles' Laws

Townsend (1976) postulated the existence of 'attached eddies' in boundary layer flows that represent the large-scale organised flow. This was further supported by Head and Bandyopadhyay (1981)'s smoke flow visualisation experiment, where a ZPG boundary layer was observed to possess a large population of identifiable hairpin type, resembling attached eddies. Perry and Chong (1982) have shown that many aspects of the near-wall turbulent statistics, such as mean velocities, turbulent intensities and even spectra, may be predicted by calculations, by assuming a population of hairpin or horseshoe or $\Lambda$ vortices with $45^{o}$ inclination against the wall. Perry et al. (1994) proposed a closure scheme for boundary layers in arbitrary pressure gradients for cases where the streamwise derivatives of the Coles' wake factor was not very large. Later, Perry and Marusic (1995) proposed a wall-wake model for boundary layers in equilibrium using the conventional mean velocity formulations by Coles, as well as momentum equations and convolution integrals; the momentum equations and convolution integral are based on attached eddies hypothesis. Further supported by non-equilibrium layers experimental data, Marusic and Perry (1995) found that the wall-wake model was in agreement with their APG data. The formulations were extended to cover relaxing, developing states and flow approaching equilibrium sink flow in Perry et al. (2002).

The usual boundary layer mean momentum equation is given by (Pope, 2000, Rotta, 1962)

$$U\frac{\partial U}{\partial x} + W\frac{\partial U}{\partial z} = -\frac{1}{\rho}\frac{\mathrm{d}P_1}{\mathrm{d}x} + \frac{1}{\rho}\frac{\partial \tau}{\partial x} \tag{3.25}$$

where $\tau$ is the local shear stress, and

$$\frac{\tau}{\rho} = -\overline{uw} + \nu\frac{\partial U}{\partial z}. \tag{3.26}$$

Here, $\nu\partial U/\partial z$ is the viscous contribution and $\overline{-uw}$ is the Reynolds shear stress and $W$ is the local mean normal to the wall velocity. The mean continuity equation is given by

$$\frac{\partial U}{\partial x} + \frac{\partial W}{\partial z} = 0. \tag{3.27}$$

and if $U_1$ is the free stream velocity, then

$$-\frac{1}{\rho}\frac{\mathrm{d}P_1}{\mathrm{d}x} = U_1\frac{\partial U_1}{\partial x}. \tag{3.28}$$

As was shown by Perry et al. (2002), the log law, (3.14) was used for the purpose of computing the total shear stress and overall momentum balance, and was assumed to be valid until the near-wall region[2]. For a range of Reynolds numbers, this approximation was in good agreement with developing and sink flow layers as well (Jones et al., 2001). When Coles' wake formulation is a function of the distance $z/\delta_c = \eta$ and wake parameter $\Pi$, Coles' velocity defect law can be expressed as

$$\begin{aligned}\frac{U_1 - U}{U_\tau} &= -\ln(\eta) + \frac{\Pi}{\kappa}W_c(1,\Pi) - \frac{\Pi}{\kappa}W_c(1,\Pi) \\ &= f(\eta,\Pi).\end{aligned} \tag{3.29}$$

Therefore,

$$U = U_1 - U_\tau f(\eta,\Pi) \tag{3.30}$$

Upon substituting (3.30) in (3.27), an expression for the normal velocity $W$ is obtained in terms of the other mean flow and their streamwise derivatives. The terms for $U$ and $W$ along their derivatives can be substituted into (3.25). This term is integrated using (3.28) as the boundary conditions, Perry et al. (2002) have shown that there are four non-dimensional parameters which describe the state of the boundary layers

$$\Pi, \quad S = \frac{U_1}{U_\tau}, \quad \beta = \frac{\delta^*}{\tau_o}\frac{\mathrm{d}P_1}{\mathrm{d}x}, \quad \zeta = S\delta_c\frac{\mathrm{d}\Pi}{\mathrm{d}x} \tag{3.31}$$

Here, $S$ is a skin friction parameter, $\beta$ is the Clauser (1954) pressure gradient parameter and $\zeta$ is non-equilibrium parameter. Perry et al. (2002) further used formulation by Jones et al. (2001) to derive functions that predict the wall shear stress, which is shown below:

[2] in Perry et al. (2002) $W_c(z/\delta_c,\Pi)$ is used instead of $W_c(z/\delta_c)$ in (3.14)

$$\frac{U}{U_\tau} = \overbrace{\underbrace{\frac{1}{\kappa}\left(\frac{zU_\tau}{\nu}\right) + A}^{\text{log law of the wall}} + - \frac{1}{3\kappa}\eta^3}^{\text{Pure wall flow}} + \overbrace{\frac{\Pi}{\kappa} 2\eta^2(3-2\eta)}^{\text{Pure wake component}} \quad . \tag{3.32}$$

The above is also called the modified Coles' law.

To understand the development of these important parameters, let's consider current APG data with $C_P$ shown in Figure 2.5. The constant $U_{in} \approx 15.9$ m/s case is chosen so that the value of $\zeta$, which contains the $\mathrm{d}\Pi/\mathrm{d}x$ term, could be calculated. The other flow cases where $U_{in}$ was not constant, could not be used to calculate $\zeta$ (except for the constant $U_{in} \approx 10.5$ for the FPG case). Figure 3.4($a$) shows the mean velocity profiles for the constant $U_{in} = 15.9$ m/s. The symbol $\oplus$ represents the ZPG data. This data was acquired at 'Station 1' (refer to the wind tunnel illustration in Figure 2.4 and $C_P$ in Figure 2.5), located 2900 mm ($60\delta$) from the trip wire. This station is also the last section before any pressure gradient is introduced. The solid line indicates the log law of the wall, (3.6), with $\kappa = 0.41$, $A = 5.0$. To facilitate better viewing (because of overcrowding of data), the mean velocity data points in Figure 3.4($a$) in the near-wall and logarithmic regions have been down-sampled (every 2 points are taken out from 3 data points). In the log region, taken as $50 \lesssim z^+ \lesssim 0.15Re_\tau$, $U^+$ of the ZPG data collapses with the log law of the wall. In the outer region, the ZPG data has a wake parameter value of $\Pi = 0.6$, as would normally be expected from ZPG boundary layer data (e.g. DeGraaff and Eaton, 2000, Monkewitz et al., 2008, Robinson, 1991, Spalart, 1986). The next data is shown by the symbol $\otimes$ where the flow is already in the APG section. This is at 'Station 2' with the pressure gradient parameter $\beta \approx 1.1$. The subsequent data are exposed to stronger $\beta$. It can be observed that there is a deviation from the log law of the wall in the log region as $\beta$ increases. The log region for the stronger APG is shorter, shown by the 'peeling-off' that occurs at a closer distance to the wall (the wake region occurs at a lower wall-normal height). This will be discussed in more details in Section 3.6. In the outer region, the wake parameter also increases with $\beta$.

The turbulence intensities, $\overline{u^2}/U_\tau^2$ profiles are shown in Figure 3.4($b$). In the near-wall region, the magnitude of the near-wall turbulence intensities increases with $\beta$. The near-wall peak generally occurs at $z^+ \approx 15$; the dashed-dotted line in this figure denotes $z^+ = 15$. The same trend follows in the outer region. The effect of APG to mean velocities, turbulence intensities and other statistics are discussed in more detail in

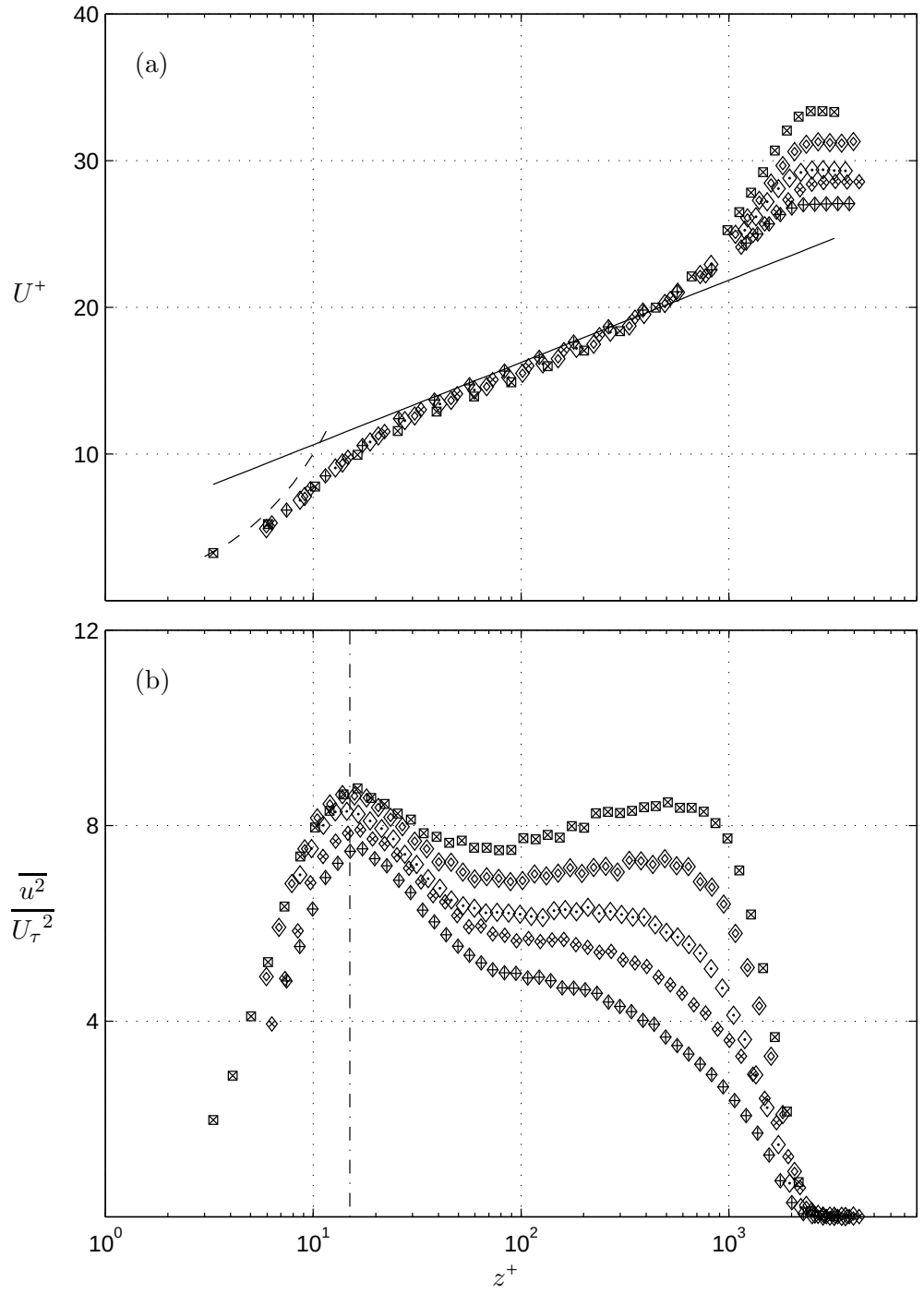


FIGURE 3.4: Mean statistics for adverse pressure gradient boundary layers with constant $U_{in} \approx 15.9$ m/s. (a) Mean velocity and, (b) turbulence intensity profiles. Symbols: ⊕ $x$ = 2.90m (ZPG), ⊗ $x$ = 3.50m, ◇ $x$ = 4.00m, ◈ $x$ = 4.46m and ⊠ $x$ = 4.78m, refer to Table 2.1 for more details. The solid line shows (3.6) with $\kappa = 0.41$, $A = 5.0$, the dashed line shows $U^+ = z^+$ and the dashed-dot line indicates $z^+ = 15$.

Sections 3.6 - 3.9. As the emphasis in this section is on the development of the turbulent boundary layer along the streamwise direction, it is sufficient for now to note that the wake in the mean velocity and the outer region of the turbulence intensities profiles in Figures 3.4($a$) and ($b$) are in agreement with existing studies i.e. the wake increases with $\beta$ (Aubertine and Eaton, 2005, Bradshaw, 1967a, Marusic and Perry, 1995, Nagano et al., 1992, Samuel and Joubert, 1974) and Lee and Sung (2009).

Figure 3.5($a$) shows the mean velocity profiles for the FPG cases for constant $U_{in}$ = 10.5 m/s. To avoid overcrowding of data points in the plot, every two out of three data points are removed. The ZPG data is not shown here, therefore the first point is at Station 2 with symbol ✡ followed with data from the subsequent stations. It can be observed that in the log region (taken to be $50 \lesssim z^+ \lesssim 0.15Re_\tau$), all profiles collapse with the log law of the wall, in contrast to the APG cases with constant $U_{in}$, discussed previously. The log region grows with streamwise distance, although this trend is not so easily seen as in the APG cases. In the outer region, the wake parameter, $\Pi$ decreases gradually with streamwise distance. Experiments performed by Jones et al. (2001) show a similar trend, i.e. decreasing $\Pi$ with streamwise distance. The turbulence intensities, $\overline{u^2}/U_\tau^2$ profiles are shown in Figure 3.5($b$). It can be observed that the near-wall peak in turbulence intensities decreases with streamwise distance. In general, the FPG cases shown here agree with typical existing data (e.g. Bourassa and Thomas, 2009, Jones et al., 2001).

The analysis of the four parameters in (3.31) which describes the state of a turbulent flow is now continued, using the current APG cases (with $U_{in}$ = 15.9 m/s) and the FPG case (with $U_{in}$ = 10.5 m/s) shown in Figure 3.5. Furthermore, the existing data of Marusic and Perry (1995) (10 m/s and 30 m/s) and Jones et al. (2001) (5 m/s with acceleration parameter, $K = 3.59\times10^{-7}$ and 10 m/s with $K = 2.70\times10^{-7}$) are also added. The four parameters are shown in Figure 3.6. In the abscissae, $R_x = xU_{in}/\nu$, where $x$ is measured from the trip point. $S$ in the current APG experiment is observed to follow the trend in Marusic and Perry (1995), i.e. $S$ increases with the distance from the trip wire. However as $R_x$ increases, $S$ in the current experiment gets even larger because of a smaller $U_\tau$ obtained from the OFI method (Marusic and Perry (1995) used the Clauser chart method). Similar effects, and the validity of the Clauser chart have been discussed in Chapter 2 (in Section 2.3, the Clauser chart method is found to be invalid as $\beta$ grows). In the current FPG experiment, $S$ decreases with increasing $R_x$, contrary to Jones' experiments.

Both the current APG experiment and Marusic and Perry (1995) experiment show increasing $\Pi$ with $R_x$. However, at larger $R_x$ values, $\Pi$ in Marusic and Perry (1995) is

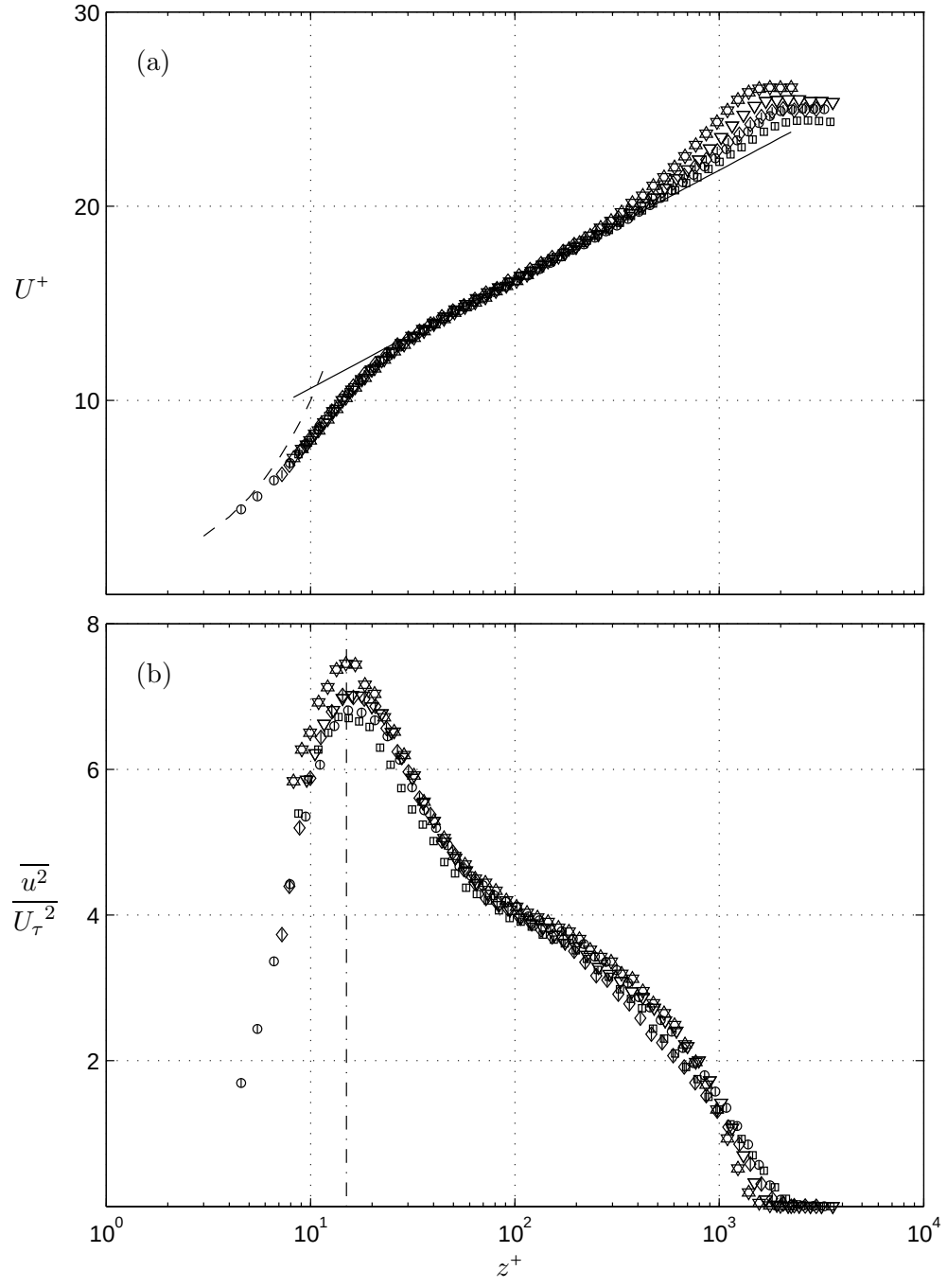


FIGURE 3.5: Mean statistics for adverse pressure gradient boundary layers with constant $U_{in} \approx 10.5$ m/s. (a) Mean velocity and, (b) turbulence intensity profiles. Symbols: ✡, ▽, ◈, ⊕ and ⊞ refer to Table 2.1 for more details. The solid line shows equation 3.6 with $\kappa = 0.41$, $A = 5.0$, the dashed line shows $U^+ = z^+$ and the dashed-dot line indicates $z^+ = 15$.

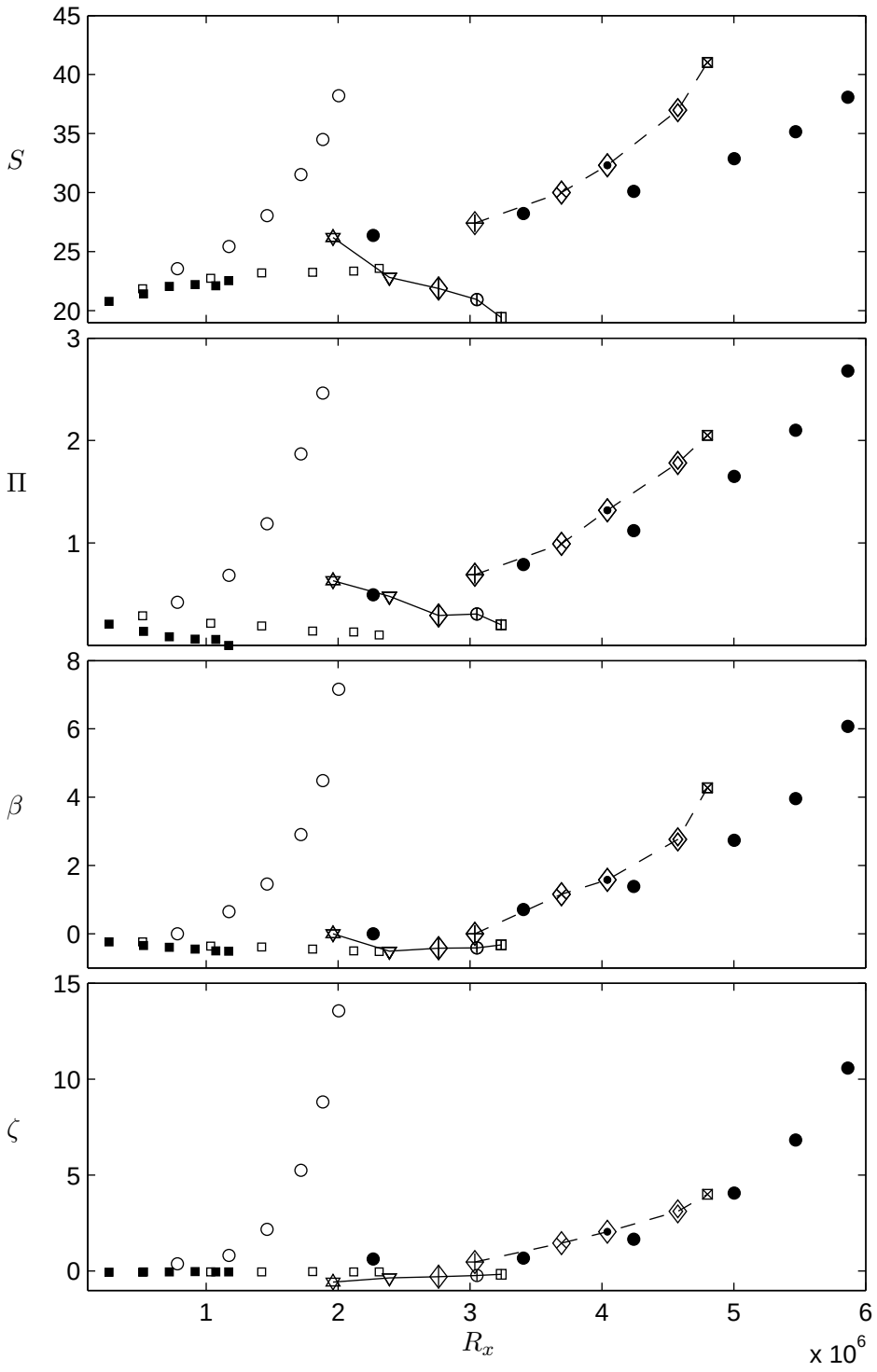


FIGURE 3.6: The non-dimensionalised parameters that describe the state of boundary layers. ○: Marusic and Perry (1995) 10m/s, •: Marusic and Perry (1995) 30m/s, ■: Jones et al. (2001) 5m/s ($K = 3.59\times10^{-7}$), □: Jones et al. (2001) 10m/s ($K = 2.70\times10^{-7}$). The symbols ⊕, ⊗, ◇, ◈, ⊠ represent the current APG experiment at $U_{in}$ = 15.9 m/s. The symbols ✡, ▽, ⌖, ⊕ and ⊞ represent current the FPG experiment at $U_{in}$ = 10.5 m/s. For visualisation purposes, the dashed lines connect the current APG quantities and the solid lines connect the current FPG quantities.

larger. This is due to the greater pressure gradient parameter $\beta$, a direct consequence of steeper roof gradient or $\mathrm{d}P_1/\mathrm{d}x$. For the FPG cases, the current experiment shows a decreasing $\Pi$ with growing $R_x$, similar to Jones et al. (2001). The current experiment starts at ZPG, therefore a greater value of $\Pi = 0.6$ is observed, and from this point onwards, $\Pi$ gradually decreases. Note that the values of the acceleration parameter, $K$ in Jones et al. (2001) are fixed with inlet velocities throughout $R_x$. However in the current FPG experiment, the acceleration parameter starts at $K = 0$ (ZPG), reaching maximum value quite rapidly and gradually decreasing from this point onwards.

For the current APG experiment, $\beta$ increases very rapidly with $R_x$. The same is also observed in Marusic and Perry (1995) data. For the FPG cases, $\beta$ only decreases slightly with $R_x$ for Jones et al. (2001) experiment and for the current experiment, $\beta$ is constant throughout all stations. The last term, $\zeta$ increases very rapidly with $R_x$ for both velocity cases in Marusic and Perry (1995) and considerably smaller for the current APG data (in comparison with Marusic and Perry (1995)). However, $\zeta$ is invariant with $R_x$ in all of the FPG cases considered here. This is clearly due to the fact that the variation in $\Pi$ is small for the FPG cases ($\zeta$ is a function of $\mathrm{d}\Pi/\mathrm{d}x$). The calculations of boundary layer thickness $\delta$, the wake parameter $\Pi$ throughout the thesis are based on the these formulations (Perry et al., 2002).

In Perry et al. (2002), $\delta$ is calculated by (3.22). The wake factor $\Pi$ here is calculated from

$$\Delta\left(\frac{U}{U_\tau}\right) = \frac{2\Pi}{\kappa}, \tag{3.33}$$

where the $\Delta(U/U_\tau)$ is the maximum deviation from the linear-logarithmic region in the mean velocity profile. Note that in Jones et al. (2001) and Perry et al. (2002), the maximum deviation from the log law is determined by $\Delta(U/U_\tau)$ (I), illustrated in Figure 3.7. However, in the current analysis where the mean velocity is scaled with friction velocity obtained from the OFI method, the maximum deviation from the linear-logarithmic region in the mean velocity profile is $\Delta(U/U_\tau)$ (II). The values of $\kappa$ and $A$ are also different, as they are based on the OFI analysis. The different methods here cause different values of $\Pi$ and subsequent different values of $S$, $\beta$ and $\zeta$. Both analyses assume the log region to be $50 < z^+ < 0.15Re_\tau$.

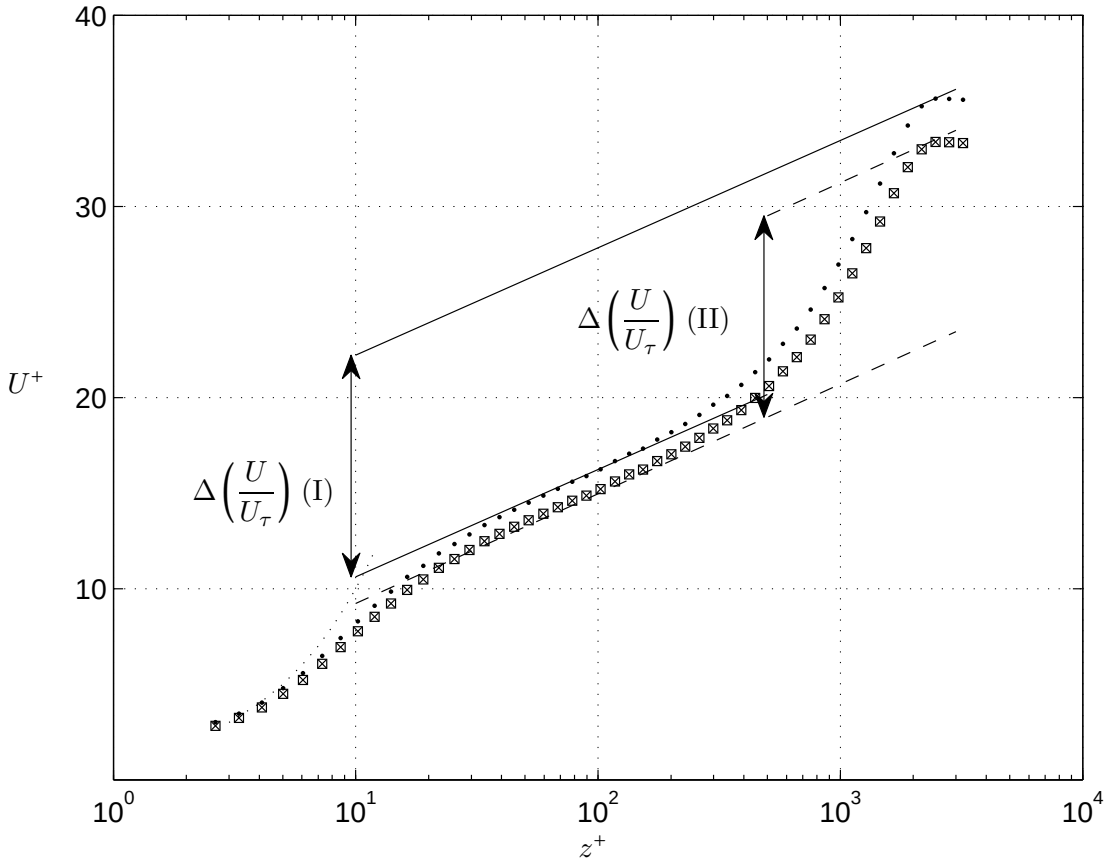


FIGURE 3.7: Method for determining Π. The data is taken from $U_{in} \approx 15.9$ m/s at $x = 4.78$ m denoted by ⊠ scaled with $U_\tau$ obtained from OFI, while the same data is scaled with $U_\tau$ obtained from the Clauser chart denoted by the dotted symbol. $\Delta U/U_\tau$ (I) is based on Perry et al. (2002) (3.22) where $\kappa = 0.41$ and $A = 5$. $\Delta U/U_\tau$ (II) is based on maximum deviation from the linear-logarithmic region in the mean velocity profile used in the current analysis, where $\kappa = 0.4009$ and $A = 3.4751$.

## 3.6 The development of the log region

The APG and FPG data displayed in Figures 3.4($a$) and 3.5($a$) appear to show a varying log region depending on the pressure gradient. However, so far this observation is only based on visual inspection of the peeling-off location from the log-linear region in the mean velocity profiles. To evaluate more accurately the extent of the overlap region and the log scaling of the mean velocity, it is helpful to employ the diagnostic function

$$\Xi = z^+ \frac{\mathrm{d}U^+}{\mathrm{d}z^+}. \tag{3.34}$$

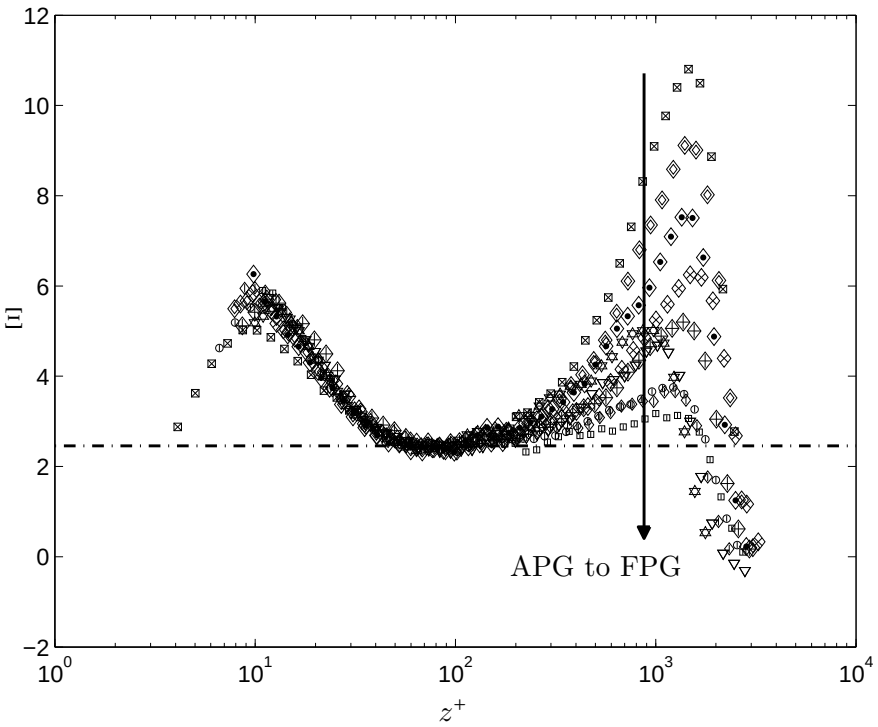


FIGURE 3.8: Diagnostic function for $U_{in} \approx 15.9$ m/s in APG and constant $U_{in} \approx 10.5$ m/s in FPG. Symbols are the same as in Figure 3.4. Dashed-dotted line shows $\kappa = 0.41$.

The log region of a velocity profile occurs in the range of $z^+$ for which $\Xi$ is constant. In fact, it can be shown by differentiating (3.6) that $\Xi = 1/\kappa$ in this region.

Figure 3.8 shows the diagnostic function of the APG and FPG cases. The linear region for the strong APG case is the shortest and the rise in the outer region for this case is also the largest. In contrast, as the APG reduces to ZPG and subsequently to FPG, the linear region grows. This is clear evidence that APG shortens, while FPG stretches, the log region. Similar analyses have been performed e.g. in Jones et al. (2001) and Bourassa and Thomas (2009), indicating a longer log region that increases with the degree of FPG.

## 3.7 Mean velocity and turbulence intensity profiles for adverse, zero and favourable pressure gradients

The analysis starts by comparing one case each from relatively mild adverse and favourable pressure gradients ($\beta \approx 1.7$ and -0.4), with a zero pressure gradient case at matched $Re_\tau \approx 3000$. This comparison is intended to provide clear and simple evidence of the effects of pressure gradient on the mean statistics, similar to the analyses of mean velocities and turbulence intensities profiles of ZPG TBL, channel and pipe flows, shown in Monty et al. (2007). The comparison of three boundary layers subjected to pressure gradients is one of the main foci of this study.

Figure 3.9($a$) displays the inner-scaled mean velocity profiles for all boundary layer flows. In the wake region ($z/\delta > 0.15$), the APG mean velocity rises higher than that in the ZPG case, typical of adverse pressure gradient boundary layers. The 'strength' of the wake is commonly quantified by the Coles wake parameter, $\Pi$ (essentially a measure of the maximum deviation from the log law). Calculation of $\Pi$ requires the explicit knowledge of the log law that describes the mean velocity data in the overlap region. That is, the constants $\kappa$ and $A$ in $U^+ = 1/\kappa \log(z^+) + A$ must be known. The classical values for the smooth wall, zero pressure gradient boundary layer are $\kappa = 0.41$ and $A = 5.0$, which leads to a value of $\Pi \approx 0.6$ for the ZPG case. However, it is not trivial to determine $\Pi$ for the APG case, since an examination of the logarithmic region in Figure 3.9($a$) reveals that the APG mean velocity drops below the classical log law. Nevertheless, the wake factor increases with APG. This is obtained from analysis of the mean velocity profile with the values $\kappa$ and $A$ in the log law equation obtained from oil-film interferometry (OFI) as discussed in Section 2.3. The increased $\Pi$ in APG has also have been well documented in other APG studies (Lee and Sung, 2008, Marusic and Perry, 1995, Nagano et al., 1998).

By visual inspection of Figure 3.9($a$), it appears that there is a difference in the extent of the logarithmic region for the three flows. The logarithmic layer is most commonly considered as the region of $100 < z^+ < 0.15Re_\tau$, however, numerous studies challenge this (for example, Bourassa and Thomas (2009), Nagib and Chauhan (2008), Österlund and Johansson (2000), Zagarola and Smits (1998)). For the ZPG case presented here, the logarithmic region appears to begin at $z^+ \approx 70$ and extends to $z^+ \approx 0.15Re_\tau$, which is slightly more extensive than generally accepted. Although the log region for the FPG case begins at approximately the same location, the log region extends all the way towards $z^+ \approx 0.5Re_\tau$. The longer log region in FPG has been observed by Jones et al.

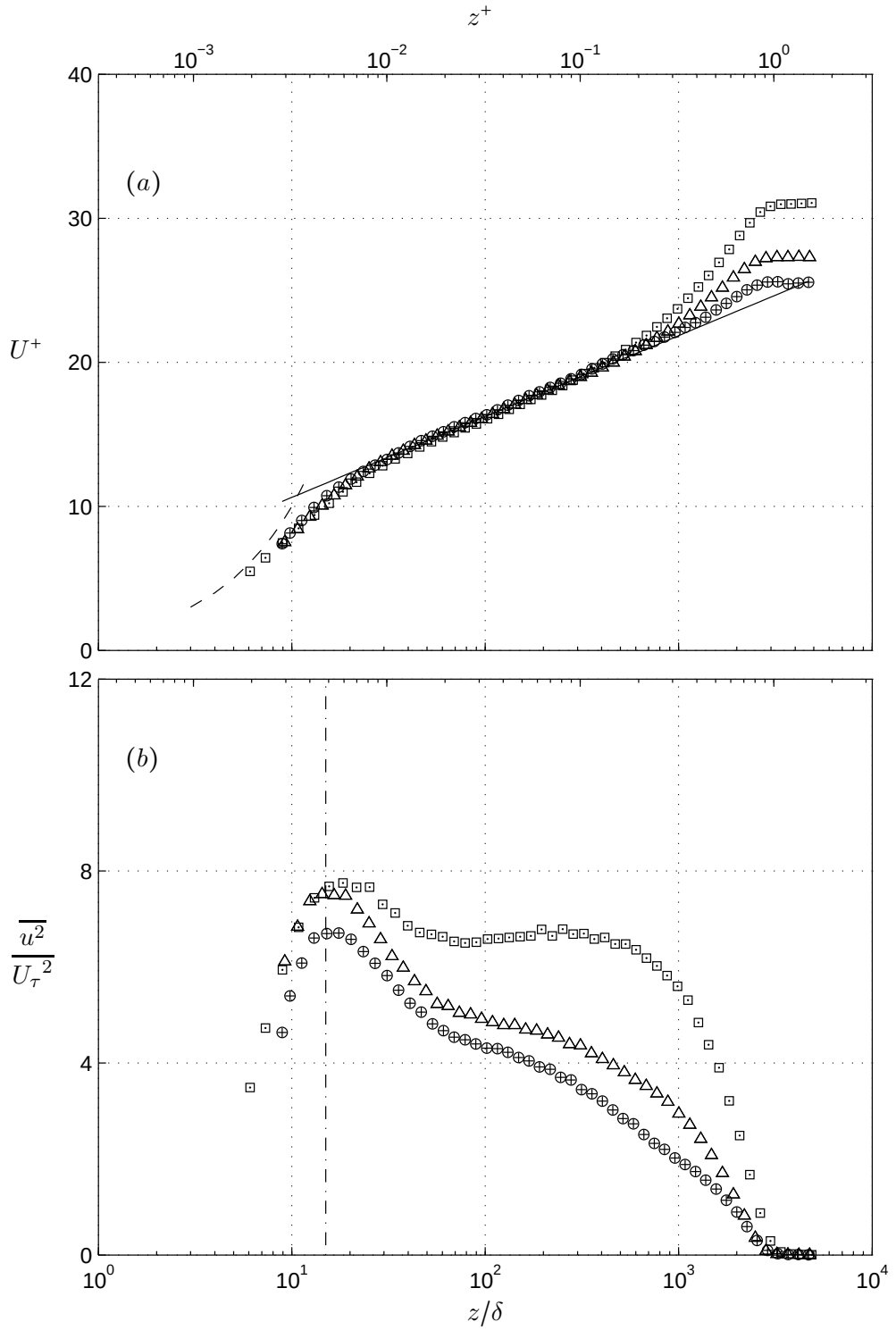


FIGURE 3.9: Comparison of APG, ZPG and FPG flows at matched $Re_\tau \approx 3000$ ($a$) Mean velocity profiles ($b$) Broadband turbulence intensity profiles. Symbols: (⊡) APG (△) ZPG and (⊕) FPG, for other parameters refer to Table 2.1. The solid line shows log law (3.6) with $\kappa = 0.41$, $A = 5.0$, dashed line shows $U^+ = z^+$ and dashed-dotted line $z^+ = 15$.

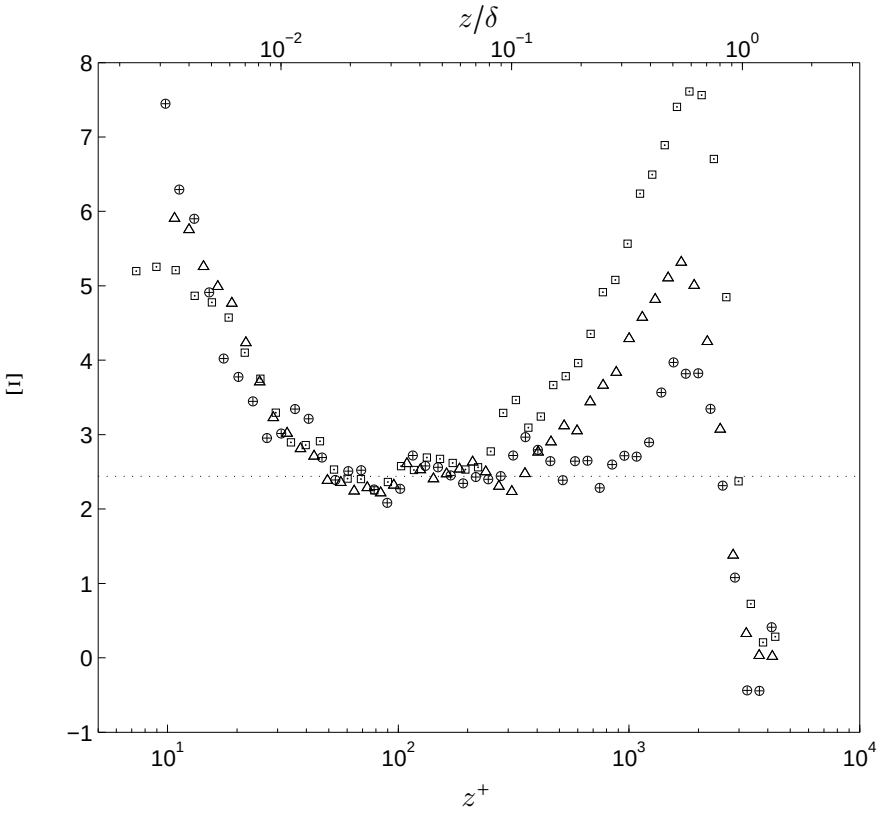


FIGURE 3.10: Diagnostic function for adverse, zero and favourable pressure gradient flows at matched $Re_\tau \approx 3000$. For symbols, refer to Figure 3.9. Dotted line shows $\kappa = 0.41$.

(2001) and Bourassa and Thomas (2009). Figure 3.10 shows diagnostic function for the three pressure gradient cases at constant Reynolds number data. This figure shows that the log region is the longest for the FPG case and shortest for the APG case as expected.

It is also evident that all three cases agree well until $z^+ \approx 200$, from which point there is a deviation of the APG data followed by ZPG data at $z^+ \approx 400$. The diagnostic function data are noisy (inherent in the spatial differentiation of experimental data), nevertheless, it could be argued that the wake region of the APG flow has begun as early as $z^+ = 250$ ($z/\delta = 0.07$). Thus there is a very narrow logarithmic region in APG flow at this pressure gradient and Reynolds number. The values of $\kappa$ could change depending on the length of log region employed in the diagnostic function analysis. Monty et al. (2011) showed the sensitivity of the employed log region towards the value of $\kappa$, nevertheless by employing a log region of $70 < z^+ < 0.15Re_\tau$, the value of $\kappa$ equals 0.37. A lower $\kappa$ for the APG case is in agreement with Nickels (2004), Skåre and Krogstad (1994) and Nagib and Chauhan

(2008). The value of $\kappa$ from the analysis with longer log region for ZPG and FPG data is 0.41. Similar values of $\kappa$ in both ZPG and FPG are explained by the mild favourable pressure gradient in the experiment.

There is an increasing attention given to the scaling of the streamwise turbulence intensity near the wall in canonical turbulent shear flows (for example, DeGraaff and Eaton, 2000, Hutchins et al., 2009, Marusic et al., 2010a,c, Metzger et al., 2001, Smits et al., 2011). In the case of boundary layers subjected to pressure gradients, far less reliable data (covering the range of pressure gradients and the Reynolds numbers) is available to enable the formulations of scaling arguments for the turbulence intensities. Figure 3.9($b$) presents turbulence intensities for adverse, zero and favourable pressure gradient cases at $Re_\tau \approx 3000$. The etched portion of the hotwire sensor has been fixed at $l^+ \approx 30$. The specifically matched $Re_\tau$ and $l^+$ are required to allow a valid comparison in the turbulence intensities analysis. Klewicki and Falco (1990) and Hutchins et al. (2009) demonstrated that in ZPG flows, the scatter in viscous-scaled turbulence intensity in the near-wall region is due in large part to the competing effects of the Reynolds number and non-dimensionalised hotwire length. That is, as the Reynolds number is increased, large-scale structures contribute to an increase in turbulence intensity, however as $l^+$ is increased, the small-scale fluctuations become increasingly attenuated, thus causing a decrease in turbulence intensity. The effect of $l^+$ in pressure gradient is discussed in Section 3.11. For this reason, it is necessary to match $l^+$ when turbulence intensities analysis is performed.

It is immediately clear that the turbulence intensity is highest throughout the flow for the APG case followed by ZPG and FPG flows. The biggest difference occurs in the outer region, where a secondary hump is observed in the APG data. No secondary hump is observed in the ZPG case despite some persistence in the outer region ($z/\delta \approx 0.3$). In the FPG case, the turbulence intensity decays almost monotonically through the logarithmic region. It is not possible to collapse these profiles with a unique velocity scale; thus scaling arguments alone will not be able to explain the different statistics in pressure gradients. The magnitude of the secondary hump is related to energy associated with the large-scale structures of the flow and a detailed explanation of energy distribution is provided in Chapter 4.

To demonstrate that the rise in energy in the outer region is not due simply to a scaling argument, the turbulence intensity profiles have been plotted scaled with $U_1$ in Figure 3.11. In the near-wall region, the intensity is now lowest in the APG case and increases as the pressure gradient changes sign. However, scaling with $U_1$ in the near-wall region

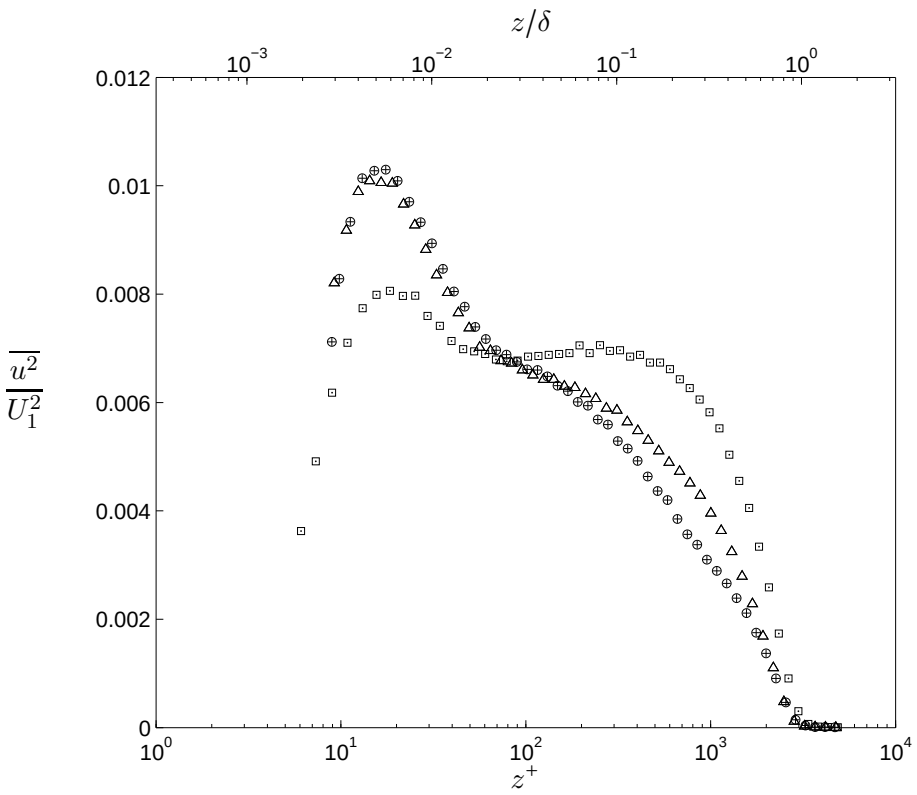


FIGURE 3.11: Broadband turbulent intensity profiles for APG, ZPG and FPG data at $Re_\tau \approx 3000$ scaled with local free-stream velocity, $U_1$. For symbols, refer to Figure 3.9.

is not appropriate since $U_1$ is not a relevant velocity scale so far from the free stream. In Figure 3.11, the vertical dash-dotted line indicates $z^+ = 100$, if we consider the outer region taken from this line towards the edge of the boundary layer, it can be observed that the intensity still rises with pressure gradient.

## 3.8 Mean velocity and turbulence intensity profiles for constant Reynolds number $Re_\tau \approx 1900$

In the literature review section of this thesis, as well as at the start of this chapter, the author has highlighted the need to isolate the competing effects of the increased Reynolds number and pressure gradient parameter. The variations of these parameters shown in Table 1.1 make it difficult to state the relative importance of each parameter. The uncertainties are analysed in this section when the Reynolds number remains constant while $\beta$ varies.

Figure 3.12($a$) shows the mean velocity profiles for adverse pressure gradient boundary layers with matched Reynolds number, $Re_\tau \approx 1900$, varying $\beta = 0 - 4.54$ and varying $K = 0 - 2.8 \times 10^{-7}$. Each data set was acquired at a different streamwise location, and it should be noted that a unique inlet free stream velocity is required to match $Re_\tau$, see Table 2.1 in Chapter 2. In the outer region, it is obvious that the adverse pressure gradient causes the wake of the mean velocity profile to increase. The wake factor $\Pi$ for the ZPG case is 0.6, as would normally be observed in ZPG boundary layer flows (Coles, 1962, DeGraaff and Eaton, 2000, Spalart, 1986).

In the region, ($z/\delta \gtrsim 0.15$), it can be clearly observed that the peel-off from the log region occurs at a distance closer to the wall for APG cases. In fact there is a systematic change for the peel-off locations; APG causes the peel-off locations nearer to the wall. A closer peel-off location suggests a shorter log region (if the log region starts at approximately same location). This effect can be observed in Figure 3.14. This figure shows that the log region is gets with APG ($70 < z^+ < 0.15Re_\tau$ for ZPG to $70 < z^+ < 90$ for $\beta \approx 4.3$ case). Figure 3.14 demonstrates that APG shortens the log region, and if sufficient APG is applied to the boundary layers, it is possible to have no log region at all.

Returning to Figure 3.12($a$) and focusing on the log region, there is a systematic deviation from the log law (downward) as pressure gradient is increased. Furthermore, the log region appears to reduce in size with increasing pressure gradient, consistent with the observation from the diagnostic function. Skåre and Krogstad (1994) proposed that the shift-down from the log law was due to the increased Reynolds number. In this experiment, the Reynolds number was maintained constant while the pressure gradient was increased, thus any Reynolds number effect was isolated, so the reduction in scaled mean velocity must be due to pressure gradient.

In the near-wall region ($5 < z^+ < 15$), the mean velocity profiles are similar across all pressure gradients. This behaviour was also reported by Krogstad and Skåre (1995) and Nickels (2004). The latter showed that, in the region of $z^+ < 10$, the mean velocity data of adverse, zero and favorable pressure gradients collapses under inner-scaling (comparison was made with data of Nagano et al. (1992) and Spalart (1986)).

Figure 3.12($b$) shows the broadband turbulence intensity profiles for matched $Re_\tau \approx 1900$. Recall that the non-dimensionalised sensor length is maintained constant at $l^+ = 16 \pm 1$ for constant $Re_\tau$ experiments to ensure similar spatial resolution effects. As noted earlier, the effect of an adverse pressure gradient is to increase the turbulence intensity throughout the layer. Figure 3.12($b$) shows just how the turbulence intensity

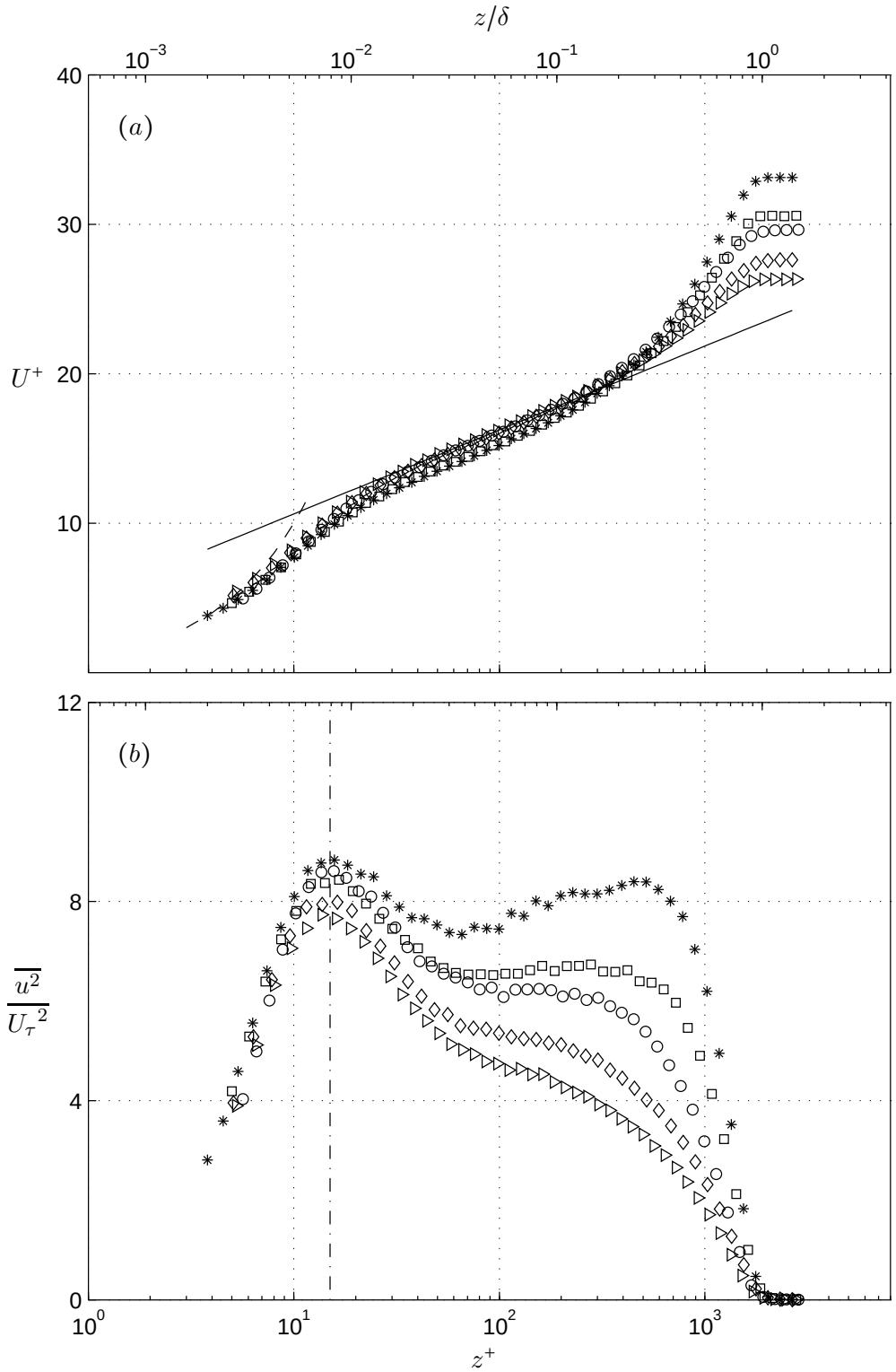


FIGURE 3.12: Mean statistics for adverse pressure gradient boundary layers with $Re_\tau \approx 1900$. $(a)$ Mean velocity and, $(b)$ turbulence intensity profiles. Symbols: ($\triangleright$) ZPG, ($\diamond$) $\beta = 0.91$, (o) $\beta = 1.67$, ($\square$) $\beta = 2.81$, ($*$) $\beta = 4.54$, for other details, refer to Table 2.1. The solid line shows log law (3.6) with $\kappa = 0.41$, $A = 5.0$, the dashed line shows $U^+ = z^+$ and the dashed-dotted line indicates $z^+ = 15$.

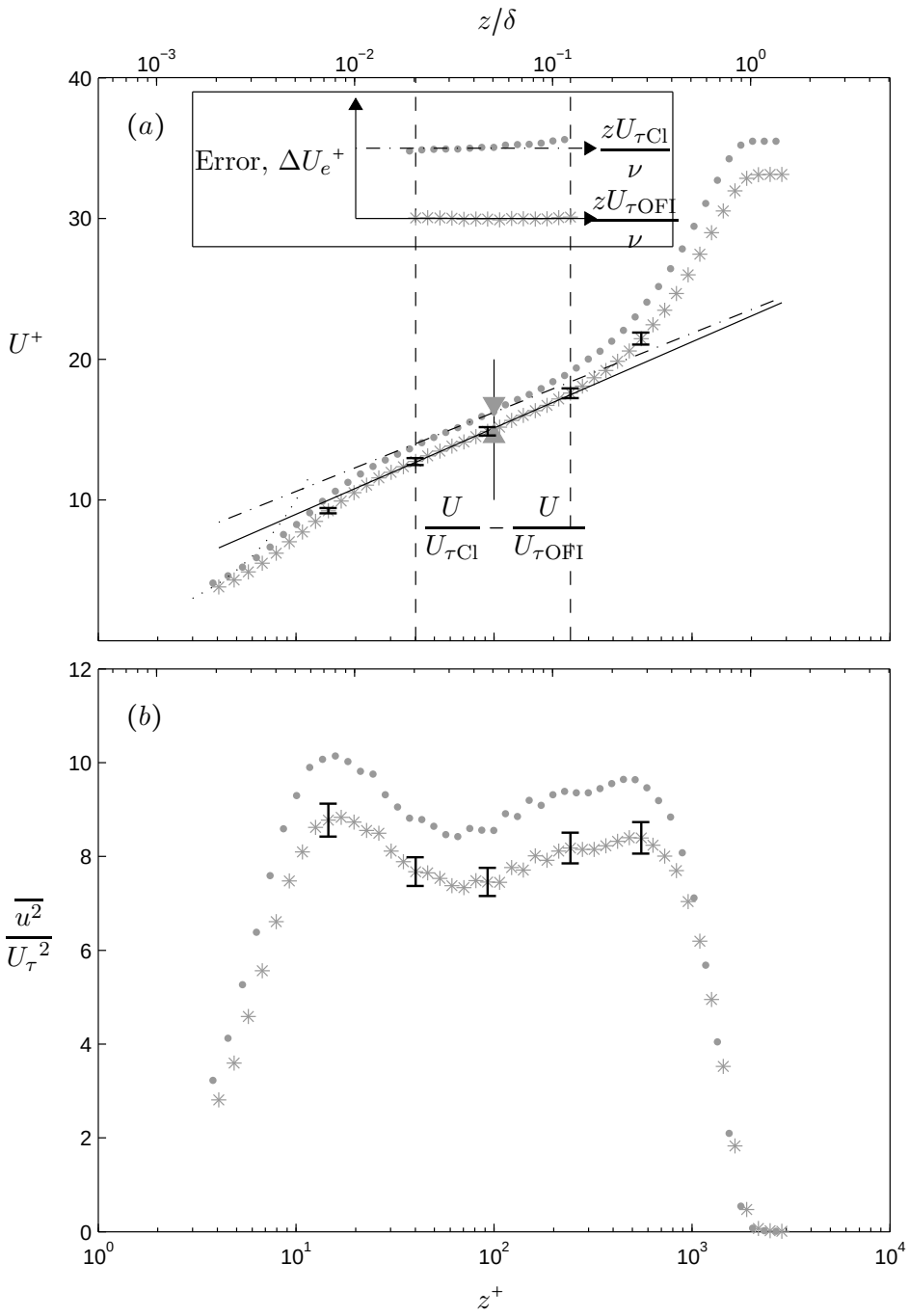


FIGURE 3.13: Error analysis for $\beta$ = 4.54, $Re_\tau \approx 1900$. $(a)$ Mean velocity. The error bars indicate ±2. Symbol: $(*)$ mean velocity scaled with $U_{\tau\mathrm{OFI}}$ and $(\bullet)$ mean velocity scaled with $U_{\tau\mathrm{Cl}}$. Dotted line denotes $U^+ = z^+$, dashed-dotted line shows log law (3.35) solid line indicates (3.36). Vertical dashed lines denote $z^+ = 40$ and $z/\delta = 0.12$ (approximate logarithmic region). In the inset, dashed line denotes error $(\Delta U_e{}^+)$ between $U/U_{\tau\mathrm{Cl}}$ and (3.35). Solid line denotes error between $U/U_{\tau\mathrm{OFI}}$ and (3.36). $(b)$ Turbulence intensity profiles. The error bars indicate ±4. The wall-normal positions where these error are shown: $z^+ \approx 15$, $z^+ \approx 40$, $z^+ \approx 100$, $z/\delta \approx 0.12$ and $z/\delta \approx 0.3$.

profile grows with increasing pressure gradient. For the inner region, the peak value of turbulence intensity rises weakly from ~ 7.8 – 9. In the outer region, however, the turbulence intensity increases sharply as the pressure gradient increases. Because the intensity in the outer region rises faster than in the inner region, at $\beta = 4.54$ (the strongest pressure gradient) the intensity in the outer region almost reaches the near-wall peak value. This leads to the 'double-hump' shape of the turbulence intensity profile and a further increase in $\beta$ would undoubtedly lead to a primary peak in the outer region. Clearly, then, there is a notable change in shape of the profile with $\beta$, which affirms that the adverse pressure gradient causes a change in the distribution of energy in a turbulent boundary layer. This change can be described as a relocation of the dominant energetic motions from the near-wall region to the outer region.

To illustrate the deviation of the mean velocity profile from the log law in Figure 3.12, the data with the largest pressure gradient ($\beta = 4.54$) is shown in Figure 3.13. A large pressure gradient parameter is chosen because the deviation is largest. In Figure 3.13, the deviation at $z^+ = 100$ is shown by the difference between the two arrows indicated by $(U/U_{\tau\mathrm{Cl}} - U/U_{\tau\mathrm{OFI}})$ where $U/U_{\tau\mathrm{Cl}}$ is evaluated using the log law (3.6), subscript 'Cl' stands for the Clauser chart method. $U/U_{\tau\mathrm{OFI}}$ is evaluated by using $\kappa = 0.3758$ and $A = 2.8563$ obtained from the OFI method. This is summarised as follows

$$\frac{U}{U_{\tau\mathrm{Cl}}} = \frac{1}{0.4100}\log\left(\frac{zU_{\tau\mathrm{Cl}}}{\nu}\right) + 5.0000, \quad U_{\tau\mathrm{Cl}} = 0.2760 \tag{3.35}$$

$$\frac{U}{U_{\tau\mathrm{OFI}}} = \frac{1}{0.3758}\log\left(\frac{zU_{\tau\mathrm{OFI}}}{\nu}\right) + 2.8563, \quad U_{\tau\mathrm{OFI}} = 0.2957 \tag{3.36}$$

In both analyses, the curve fit is performed to the logarithmic region $40 < z^+ < 0.12Re_\tau$ of the mean velocity. These differences is later called the deviation from the log law. A few selected positions are shown to highlight the deviation from the log law in Table 3.1.

It is evident from Table 3.1 that the deviation from the log law for APG with $\beta = 4.54$ is $(U/U_{\tau\mathrm{Cl}} - U/U_{\tau\mathrm{OFI}}) > 1$ for most of the logarithmic region. At the approximate start of the log region $z^+ = 40$, $(U/U_{\tau\mathrm{Cl}} - U/U_{\tau\mathrm{OFI}}) \approx 1.3$. At the end of the outer region $z/\delta = 0.12$ ,$(U/U_{\tau\mathrm{Cl}} - U/U_{\tau\mathrm{OFI}}) \approx 0.93$, however the classical value of $\kappa = 0.41$ and $A = 5$ do not fit the data well as there is an increasing positive deviation of the data from the log law at this position. In fact, at both ends of the selected log region, the errors

| $z$ position | $z^+ = 40$ | $z^+ = 100$ | $z/\delta = 0.12$ |
|---|---|---|---|
| $\frac{U}{U_{\tau\mathrm{Cl}}} - \frac{U}{U_{\tau\mathrm{OFI}}}$ | 1.3258 | 1.1226 | 0.9252 |

TABLE 3.1: Deviation from the log law for data in Figure 3.13.

($\Delta {U_e}^+ = U/U_{\tau\mathrm{Cl}}$ - (3.35)), are large, i.e. negative error at $z^+ = 40$ and positive error at $z/\delta = 0.12$. Such deviation is shown more clearly in the inset of Figure 3.13, located at the top portion of the inset. Note that the horizontal axis is $zU_{\tau\mathrm{Cl}}/\nu$. This deviation is caused by the slope of the line which is $1/\kappa = 1/0.41$.

Obviously, when $\kappa$ and $A$ are obtained directly from the curve fit to the mean velocity profile, the error is much less. This is shown by the bottom plot of the inset, where ($\Delta {U_e}^+ = U/U_{\tau\mathrm{OFI}}$ - (3.36)). Note also the horizontal axis is $zU_{\tau\mathrm{OFI}}/\nu$ which is slightly different from $zU_{\tau\mathrm{CL}}/\nu$, arising from larger value of $U_{\tau\mathrm{OFI}}$ than the value $U_{\tau\mathrm{Cl}}$[3]. As observed in Figure 3.12, the deviation from the log law is expected to be smaller when pressure gradient is smaller. The deviation is negligible in the case of ZPG flow in Figure 3.12.

It is helpful to understand the extent of the deviation from the log law in comparison with the experimental uncertainties and errors. The accumulated errors in the friction velocity discussed in Table 2.2 (uncertainty estimates) is approximately ±2%. Error bars in Figure 3.13($a$) shows the experimental uncertainties i.e. ±2% of the scaled mean velocity. It is evident from this figure that the deviation from the log law is much greater than the experimental uncertainties. The same analysis is performed to the scaled turbulence intensities. Similarly, it is found that ±4% of the turbulence intensities due to experimental uncertainties is much smaller than the deviation due to $U_\tau$ obtained from the Clauser chart.

Scaling using the friction velocity $U_\tau$ has been used to characterise the effect of pressure gradient. Another scaling using the free-stream velocity $U_1$ can also be used to demonstrate the characteristics of the structures in the outer region and this is shown in Figure 3.15 at matched $Re_\tau \approx 1900$. Figure 3.15 shows that the newly scaled turbulence

[3]The difference in $U_\tau$ from these two methods, related with the coefficient of friction, can be observed in the coefficient of friction distribution in Figure 3.1

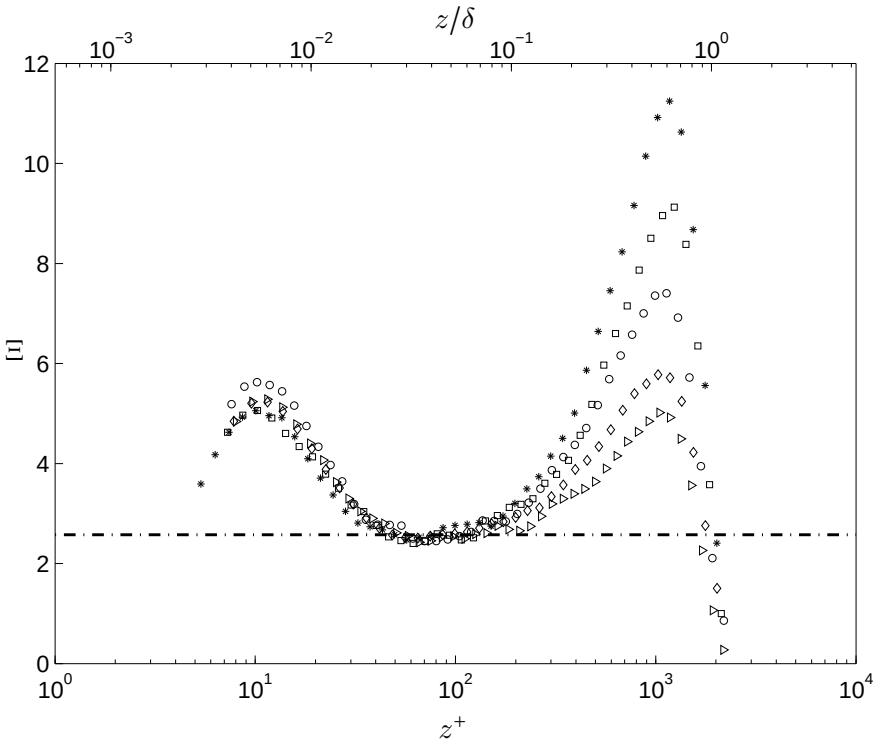


FIGURE 3.14: Diagnostic function for increasing pressure gradient flows at matched $Re_\tau \approx 1900$. For symbols, refer to Figure 3.12. Dashed-dotted line shows $\kappa = 0.41$.

intensity increases with APG in the outer region towards the edge of the boundary layer ($z/\delta$ >0.3), consistent with the results if scaling with friction velocity $U_\tau$ as was used as in Figure 3.12. Nearer to the wall, in contrast to the $U_\tau$ scaling, the turbulence intensities in Figure 3.15 decrease with APG. Such scaling suggests that turbulence intensities decrease with pressure gradient for $z^+$ <100. The results in Figure 3.15 highlight that the absolute values of the turbulence intensities tend to decrease with increasing pressure gradient in the inner region of the boundary layer, as found by Nagano et al. (1998). However the scaling using $U_1$ in the near-wall region should be read with caution because $U_1$ is not a relevant scale in the region near the wall.

Different velocity scalings have been used with some success. Zagarola and Smits (1998) developed a new scaling theory in turbulent pipe flow. The new scaling velocity has the form of $(U_{CL}-U)/u_o$, where $u_o$ is the velocity scale in the outer region. This formulation works particularly well with high Reynolds number data. Zagarola and Smits (1998) proposed that for boundary layers, $u_o = U_1\delta^*/\delta$, here $\delta^*$ is displacement thickness.

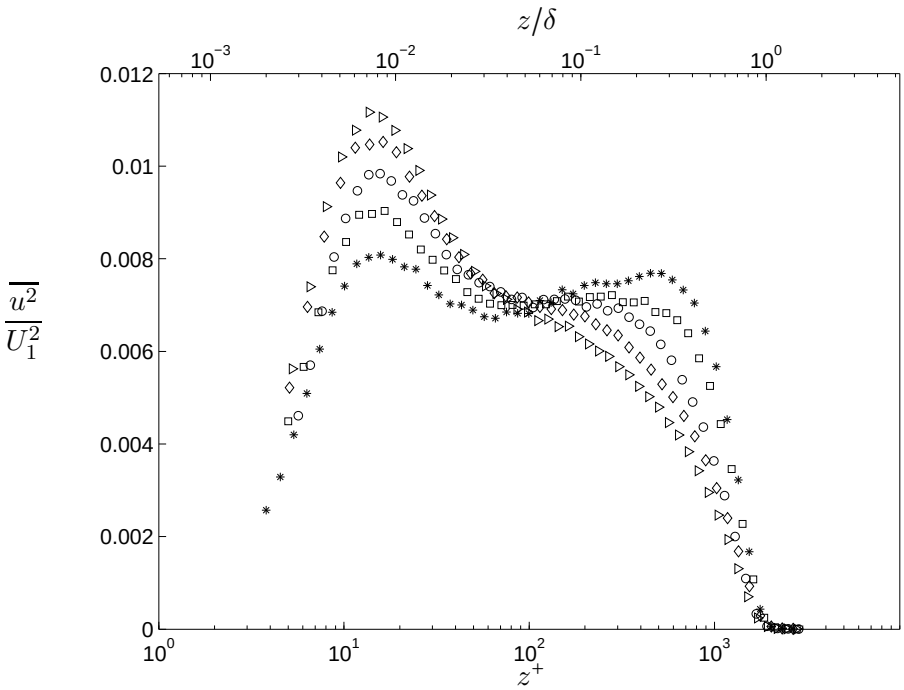


FIGURE 3.15: Broadband turbulent intensity profiles for ZPG and APG data at $Re_\tau \approx$ 1900 scaled with free-stream velocity, $U_1$. For symbols, refer to Figure 3.12.

In turbulent boundary layers with pressure gradients, Castillo and George (2001) developed a new pressure gradient parameter $\Lambda = \delta/(\rho U_1^2 \mathrm{d}\delta/\mathrm{d}x)\mathrm{d}P_1/\mathrm{d}x =$ constant. There appeared to be three different values of $\Lambda$ representing three different pressure gradient cases, the APG, ZPG and FPG flow. It was shown that the boundary layer thickness follows a power law relation of the free stream velocity, $\delta \sim U_1^\Lambda$. Velocity defect profiles scaled with $(U_1\delta^*/\delta)$ (originally from Zagarola and Smits (1998)) from the three pressure gradient cases were shown to collapse i.e. $(U_1 - U)/(U_1\delta^*/\delta)$ collapse when plotted against $z/\delta$. Similar study was also performed in Maciel et al. (2006) where the mean velocity defect profile appeared to be self-similar. However, throughout the remainder of this thesis, only friction velocity scaling will be considered, since the focus will be on identifying changes in the flow caused by pressure gradient relative to the zero pressure gradient case.

This section reveals the effect of pressure gradient when Reynolds number remains constant. In summary, the mean velocity profiles show increasing deviations from the log law when the layer is exposed with greater APG. The log region shortens, causing the peel-off to occur closer to the wall. The magnitude of the wake increases too. Correspondingly, the turbulence intensity increases in the outer region. Now, the effect

of pressure gradient can conclusively be ascertained as the Reynolds number has not changed, addressing the lack of information in Table 1.1 and answering part of the research aims pertaining to the effect of pressure gradient in isolation of the Reynolds number effect.

## 3.9 Mean velocity and turbulence intensity profiles for constant pressure gradient parameter, $\beta$

The analysis in this section is based on two data sets with constant pressure gradient parameter, $\beta \approx 1.6$ and $\beta \approx 4.3$. In Section 3.8, it has been shown that if the Reynolds number is constant, pressure gradient causes the wake parameter $\Pi$ to increase, turbulence intensities to form a second hump in the outer region, and the log region to shorten. There is also a further deviation from the log law (among other effects). Now, the focus is to isolate the pressure gradient effect and to vary the Reynolds number, also in accordance with the main aim of the research. This is similar to performing increasing Reynolds number in ZPG flows, but with a non-zero pressure gradient that is kept constant.

Figure 3.16($a$) shows the mean velocity profiles for $\beta \approx 1.6$ with varying $Re_\tau$ = 1700 – 2400. The Reynolds number range is smaller because it was difficult to acquire data with similar parameter ($\beta \approx 1.6$, $l^+ \approx 16$). The mean velocity profiles collapse in the inner and logarithmic regions for all Reynolds numbers. It is difficult to observe any deviation from the log law in the log region. In the outer region, the difference in the mean velocity profiles across the Reynolds number is small. However, observations reveal the mean velocities for the higher Reynolds number data to have longer log regions, therefore, wake regions for this data occur at larger $z^+$.

Figure 3.16($b$) shows the collapse in turbulence intensity profiles in the near-wall region. The turbulence intensity profiles increases with the Reynolds number at the start of the log region ($z^+ > 70$). There is a lack of data at higher Reynolds number to draw any conclusive observations. Reynolds number range needs to be large, e.g. $2000 < Re_\tau < 10000$, in order to observe changes in the turbulence intensities profiles, however, it was not possible in the current boundary layer wind tunnel.

As discussed earlier, $\beta \approx 1.6$ is too weak to observe any deviation from the log law and other properties such as the length of the log region and the rise of turbulence intensities in the outer region. Therefore, a larger $\beta$ is needed. At $\beta \approx 4.3$, changes

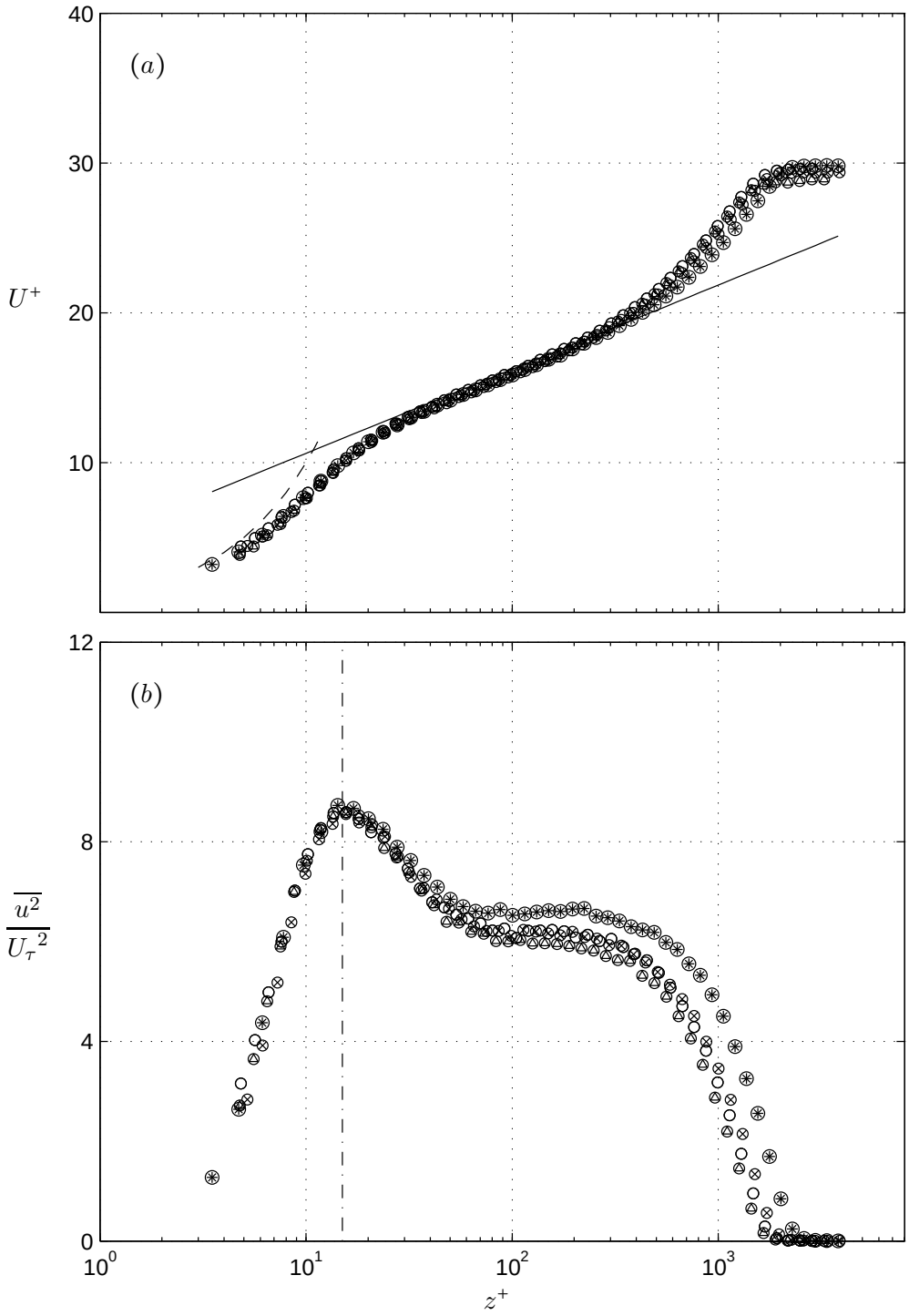


FIGURE 3.16: Mean statistics for adverse pressure gradient boundary layers with $\beta \approx 1.6$. $(a)$ Mean velocity and, $(b)$ turbulence intensity profiles. Symbols: ($\triangle$) $Re_\tau = 1750$, (o) $Re_\tau = 1990$, ($\otimes$) $Re_\tau = 2010$ and ($\circledast$) $Re_\tau = 2400$, for other details, refer to Table 2.1. The solid line shows log law (3.6) with $\kappa = 0.41$, $A = 5.0$, the dashed line shows $U^+ = z^+$ and the dashed-dotted line indicates $z^+ = 15$.

related to the pressure gradient are expected to be more visible. Figure 3.17($a$) displays the mean velocity profiles for $\beta \approx 4.3$ with varying $Re_\tau = 1770 - 3880$. The mean velocity profiles collapse in the inner and logarithmic regions for all Reynolds numbers. These do not, however, collapse onto the classical log law (3.6), which is shown in the figure for comparison. It can be observed that there an approximately constant shift-down from the log law, i.e. the value of $\kappa$ remains similar but the value of $A$ changes. The constant shift-down here is expected from the earlier study with $\beta$ varying. This can also be related to the constant shift-up between the values of the coefficient of friction determined from OFI against that obtained from the Clauser chart (Figure 3.2). The curve fit to the traditional logarithmic region of the mean velocity profile $70 < z^+ < 0.15Re_\tau$ using friction velocity $U_\tau$ obtained from OFI yields an average value of $\kappa = 0.36$ and $A = 2.2$. Deviation from the log law has been documented in Krogstad and Skåre (1995), Nagano et al. (1992) and Lee and Sung (2008).

In the previous section, the measurements performed at a constant Reynolds number with variable $\beta$ showed a gradual downward shift of the mean velocity profiles in the traditional log region as the strength of the APG was increased. This has also been documented in Monty et al. (2011). In this set of data, having constant $\beta \approx 4.3$, it appears that it is pressure gradient alone that causes deviation from the log law of the wall - not the Reynolds number. However, the Reynolds number range is relatively small, so higher Reynolds number studies should be carried out to confirm this result. This result has been published in Harun et al. (2010b).

It is difficult to determine the constants in the log law that best describe the overlap region of the mean velocity. Again, the diagnostic function is employed to give further insight into the logarithmic behaviour. Figure 3.18 shows the diagnostic function for constant $\beta \approx 4.3$ data. As expected, the diagnostic function shows the velocity profiles peeling up at larger wall-normal position from the logarithmic law as the Reynolds number increases. It can be observed that there is no log region for the lowest Reynolds number data ($Re_\tau = 1730$). Even at the highest Reynolds number ($Re_\tau = 3890$), it could be argued that the wake region still begins as early as $z^+ = 100$ (there is also a weak trend that the edge of the outer region occurs at larger $z^+$ with larger $Re_\tau$). This supports the earlier conjecture that the logarithmic region is diminished by the adverse pressure gradient, such that there is almost no evidence of logarithmic behaviour.

The major conclusion from this section is that $\beta$ causes a shift-down in the mean velocity profile regardless of the Reynolds number. From the diagnostic function analysis, it is again $\beta$ that causes the log region to shorten. Unlike in ZPG flows, Reynolds number

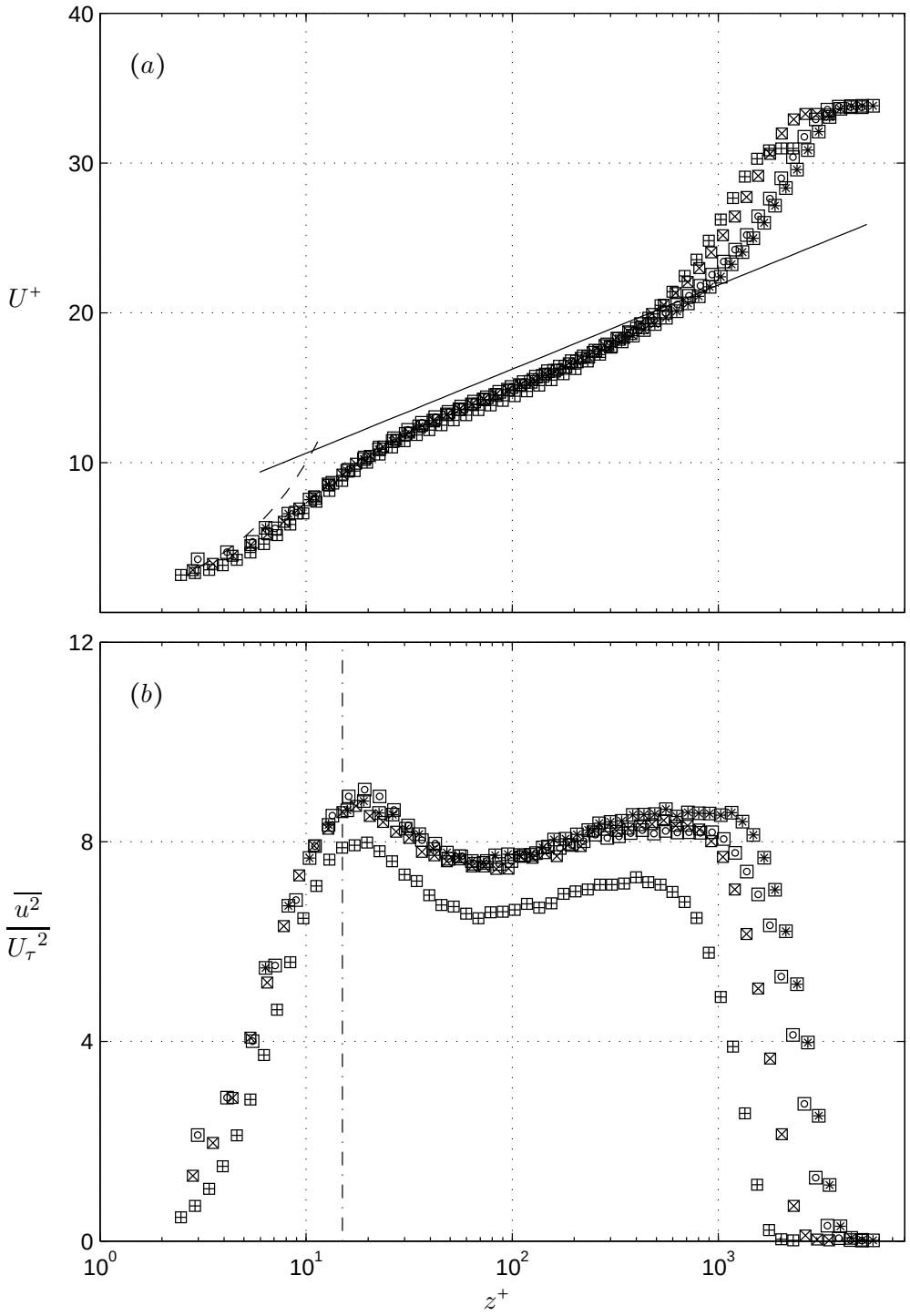


FIGURE 3.17: Mean statistics for adverse pressure gradient boundary layers with $\beta \approx 4.3$. ($a$) Mean velocity and, ($b$) turbulence intensity profiles. Symbols: (⊞) $Re_\tau = 1730$, (⊠) $Re_\tau = 2500$, (⊡) $Re_\tau = 3510$ and (⊛) $Re_\tau = 3890$, for other details, refer to Table 2.1. The solid line shows log law (3.6) with $\kappa = 0.41$, $A = 5.0$, the dashed line shows $U^+ = z^+$ and the dashed-dotted line indicates $z^+ = 15$.

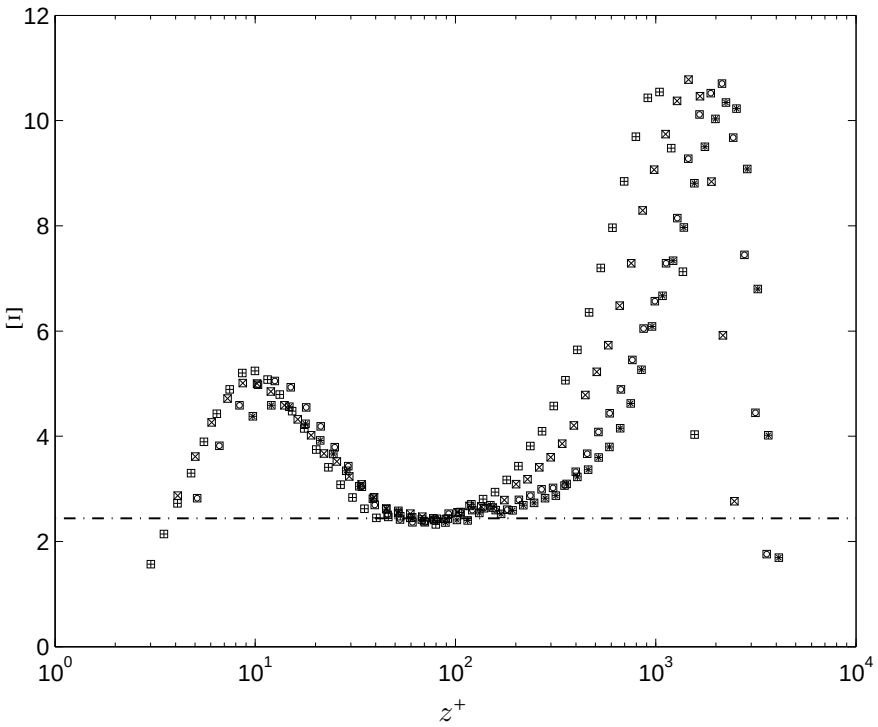


FIGURE 3.18: Diagnostic function for increasing pressure gradient flows at matched $\beta \approx 4.3$. For symbols, refer to Figure 3.17. Dashed-dotted line shows $\kappa = 0.41$.

here does not seem to make the log region longer (when scaled with inner variables). The results of this section addresses another issue pertaining to the effect of the Reynolds number in a constant APG condition. The lack of literature regarding a constant $\beta$ data is now addressed and in particular, Table 1.1 can now be furnished with constant $\beta$ data.

## 3.10 Mean velocity and turbulence intensity profiles for constant $K \approx$ -1.4×$10^{-7}$

The analysis of mean velocities and turbulence intensities for constant acceleration parameter, $K$, set of data is not specifically the aim of this thesis. However, this section is provided to understand the general behaviours in such conditions. The free stream velocity from this section is used in the analysis of the shape factor in Section 3.12, where pressure gradient effect is analysed indirectly.

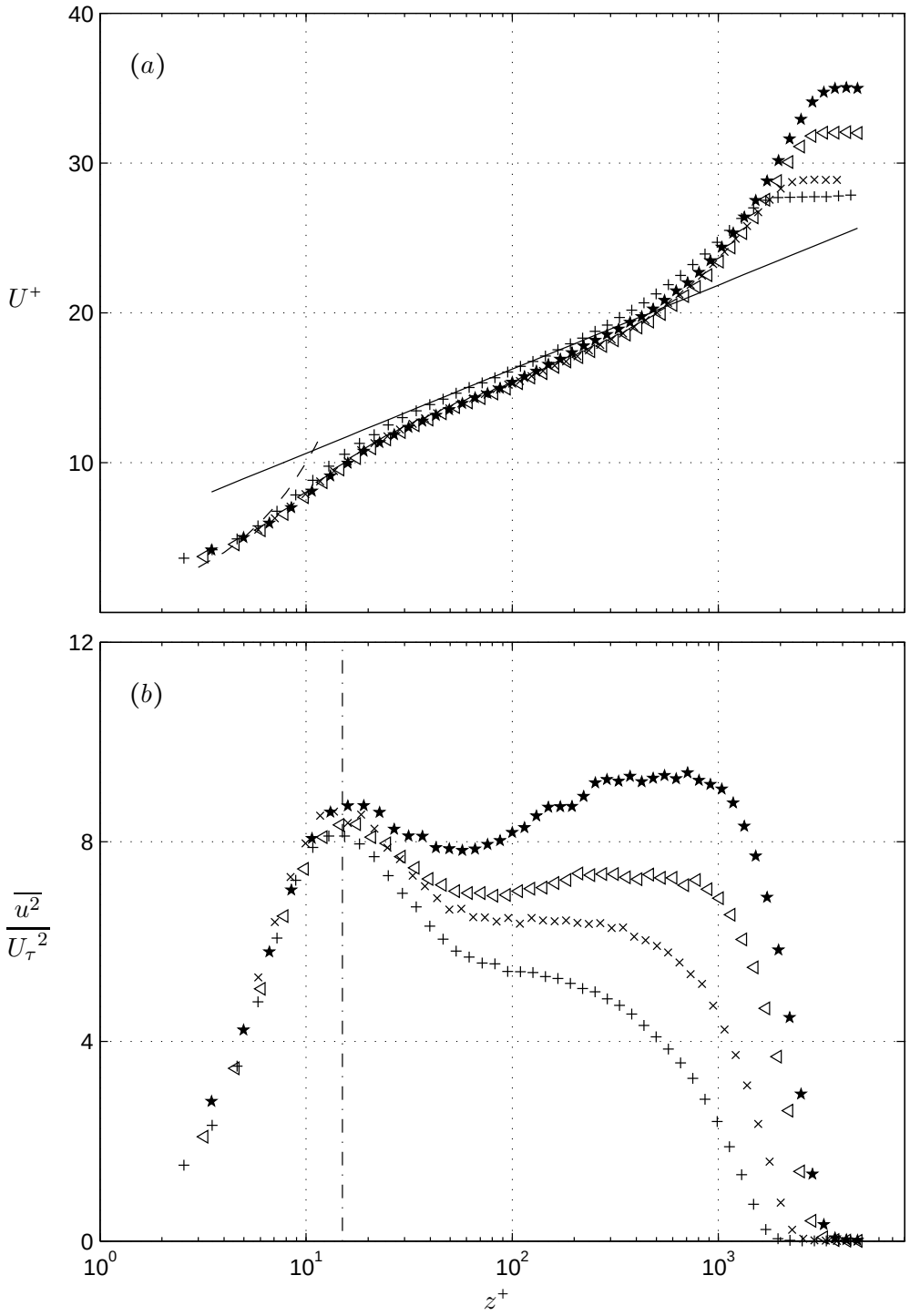


FIGURE 3.19: Mean statistics for adverse pressure gradient boundary layers with $K \approx$ -1.4×10$^{-7}$. ($a$) Mean velocity and, ($b$) turbulence intensity profiles. Symbols: (+) $Re_\tau$ = 1950 $\beta$ = 0.94, (×) $Re_\tau$ = 2470 $\beta$ = 1.52, (◁) $Re_\tau$ = 3270 $\beta$ = 3.06 and (⋆) $Re_\tau$ = 3560 $\beta$ = 4.73, for other details, refer to Table 2.1. The solid line shows log law (3.6) with $\kappa = 0.41$, $A = 5.0$, the dashed line shows $U^+ = z^+$ and the dashed-dotted line indicates $z^+ = 15$.

Figure 3.19($a$) shows the inner-scaled mean velocity profiles for a constant $K \approx$ -1.4×10$^{-7}$. The Reynolds numbers in this set of data range from 1950 < $Re_\tau$ < 3560 and the pressure gradient from 0.94 < $\beta$ < 4.73. The most observable trend is the deviation from the log law as the Reynolds number increases. In the outer region, the wake also increases dramatically with the Reynolds number. This is similar to the effect of the pressure gradient parameter on constant Reynolds number boundary layers discussed in Section 3.8, however, since the Reynolds number is also increasing here, the wake region begins at larger $z^+$ as the Reynolds number increases (for higher Reynolds number data).

Figure 3.19($b$) displays turbulence intensities for constant $K \approx$ -1.4×10$^{-7}$. The most notable difference is the wake in the outer region. The magnitude of the outer peak is greater than that of the inner peak; a greater effect of the pressure gradient when the Reynolds number is large, here $\beta$ = 4.73 (when compared with the largest $\beta$ ($\beta$ = 4.54) in constant Reynolds number flow, discussed in Section 3.8).

Scaling with inner variables shown in Figure 3.19($a$)and 3.19($b$) suggest that $K$ might not be a useful parameter because no collapse of mean velocity or turbulence intensities is observed.

## 3.11 Mean velocity and turbulence intensity profiles for varying $l^+$ at $Re_\tau \approx$ 3000 in APG and FPG

The effect of spatial resolution on turbulence intensities, skewness and flatness in the near-wall region due to the attenuation of small-scale fluctuations is substantial if the hotwire sensor length is large (Ligrani and Bradshaw, 1987). Johansson and Alfredsson (1983) added that the skewness of the time derivative of the longitudinal velocity was very sensitive to spatial averaging, because the small-scale ejection events (positive $v$, negative $u$) are attenuated more than the larger-scale sweeps (negative $v$, positive $u$). Hutchins et al. (2009) reassessed spatial resolution effect and proposed that the near-wall peak turbulent intensities could be described by a newly established empirical relationship, a function of $l^+$ and $Re_\tau$. Hutchins et al. (2009) also explained that the 'outer hump' in the turbulence intensities is only a symptom of the spatial resolution issue, which could be observed when $l^+ \gtrsim 60$.

Before analysing the spatial resolution effects in boundary layer with pressure gradients, we review the spatial resolution effect in the near-wall region for any turbulent wall-bounded flow. Andreopoulos et al. (1984), Antonia et al. (1994) and Durst et al. (1998)

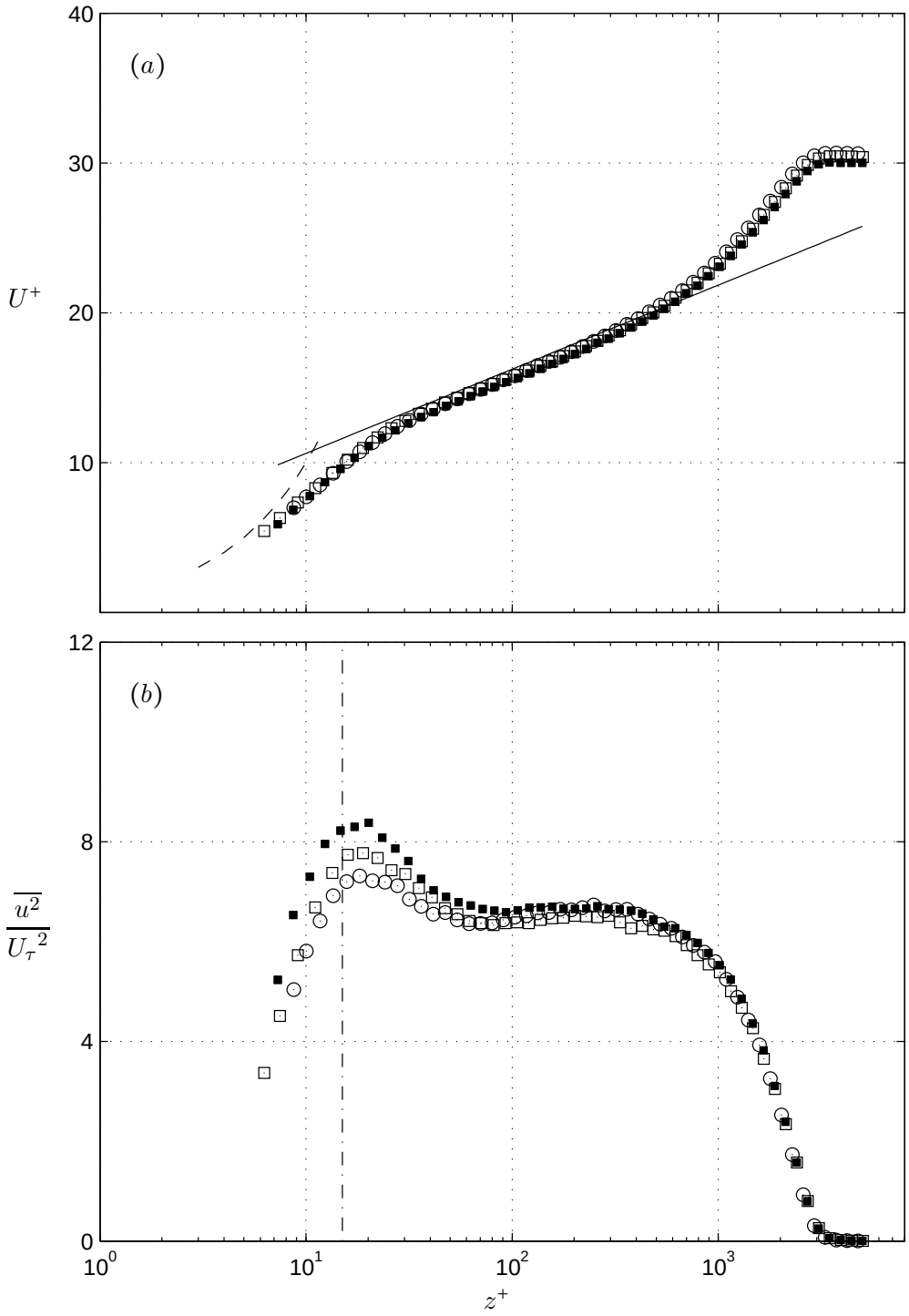


FIGURE 3.20: Mean statistics for adverse pressure gradient boundary layers with varying $l^+$ at $Re_\tau \approx 3000$ in APG, $\beta \approx 1.6$. $(a)$ Mean velocity and, $(b)$ turbulence intensity profiles. Symbols: (⊙) $l^+$ = 41, (⊡) $l^+$ = 31 and (▪) $l^+$ = 21, for other details, refer to Table 2.1. The solid line shows log law (3.6) with $\kappa = 0.41$, $A = 5.0$, the dashed line shows $U^+ = z^+$ and the dashed-dotted line indicates $z^+ = 15$.

have shown in their measurements that the near-wall peak in turbulence intensities (scaled with inner variable), $\overline{u^2}/{U_\tau}^2|_m$, decreases with Reynolds number. Similar results led Mochizuki and Nieuwstadt (1996) to conclude inaccurately that $\overline{u^2}/{U_\tau}^2|_m$ decreases with Reynolds number. Klewicki and Falco (1990), Ligrani and Bradshaw (1987) and Hutchins et al. (2009) explained that the spatial resolution effect is due to attenuations of the small-scale fluctuations, in agreement with many results (Ching et al., 1995, DeGraaff and Eaton, 2000, Johansson and Alfredsson, 1983, Wei and Wilmarth, 1989). However, as shown in Section 1.1 (the effect of pressure gradient), following Krogstad and Skåre (1995), Nagano et al. (1992) and Lee and Sung (2009), $\overline{u^2}/{U_\tau}^2|_m$ also increases with the APG parameter $\beta$. This is assumed when Reynolds number differences are not large compared with the increased magnitude of $\overline{u^2}/{U_\tau}^2|_m$. Evidence observed in Figure 3.12($b$), when Reynolds number and $l^+$ remain constant, further confirms that $\overline{u^2}/{U_\tau}^2|_m$ increases with $\beta$. Hutchins et al. (2009) noted that their analysis does not differentiate between data from internal or external geometries. The growing evidence that the large-scale features in the log and wake regions of internal flows are different from those of ZPG TBL seen in Abe et al. (2004), Guala et al. (2006), Hutchins and Marusic (2007a), Kim and Adrian (1999), Tomkins and Adrian (2003) and Monty et al. (2007) indicate that the near-wall structure may also be different. Hutchins et al. (2009) added that there should be attempts to differentiate these data, if there is sufficient data. It is obvious now that at least data for TBL exposed with pressure gradient should be treated differently as $\overline{u^2}/{U_\tau}^2|_m$ changes with pressure gradients when Reynolds number and $l^+$ remain constant (Figures 3.9($b$) and 3.12($b$)).

To analyse spatial resolution effects, a varying sensor length measurement was performed: $20 \lesssim l^+ \lesssim 40$ in an APG flows with $\beta \approx 1.6$ at $Re_\tau \approx 3000$. The mean velocity profiles are shown in Figure 3.20($a$) and are expected to collapse. The turbulence intensities are shown in Figure 3.20($b$). Turbulence intensities collapse in the outer region; however, $\overline{u^2}/{U_\tau}^2$ shows differences in the near-wall region, $\overline{u^2}/{U_\tau}^2$ is greatest for measurement recorded with the smallest sensor length, $l^+ \approx 20$.

The mean velocity profiles for the FPG boundary layers at $K \approx 0.77 \times 10^{-7}$ ($\beta \approx -0.45$) are shown in Figure 3.21($a$). The mean velocity profile for a ZPG boundary layer at $Re_\tau \approx 3000$ is also shown for reference (symbol: • with connecting lines). Again, turbulence intensities collapse in the outer regions. In the near-wall region, $\overline{u^2}/{U_\tau}^2$ is highest when the sensor length used is the smallest.

The trend of the turbulence intensities in the APG and FPG flows are expected. To understand the extent of spatial resolution effect in pressure gradient flows, we consider

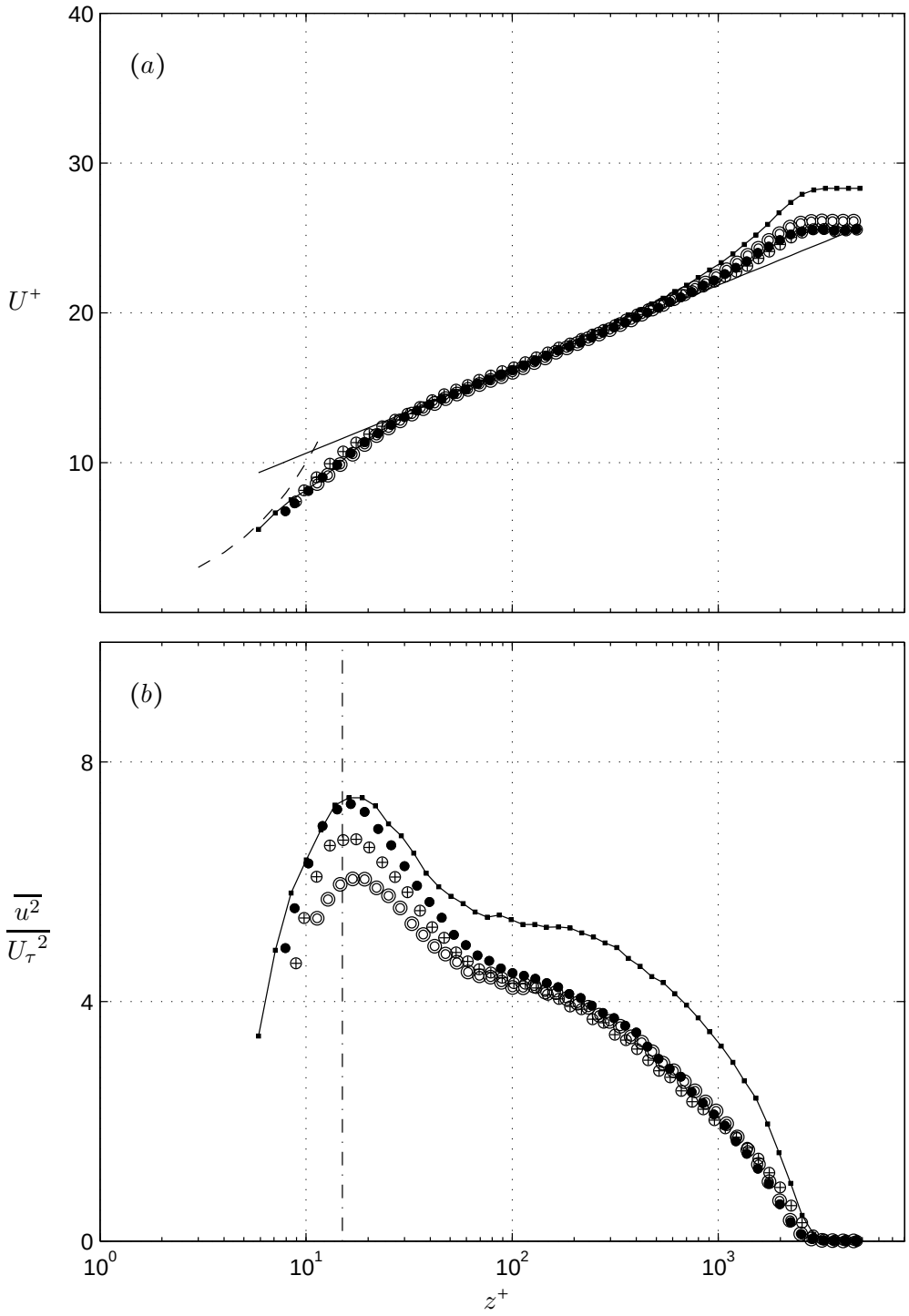


FIGURE 3.21: Mean statistics for favourable pressure gradient boundary layers with varying $l^+$ at $Re_\tau \approx 3000$ in FPG, $K \approx 0.77 \times 10^{-7}$ ($\beta \approx -0.45$). ($a$) Mean velocity and, ($b$) turbulence intensity profiles. Symbols: (◎) $l^+ = 48$, (⊜) $l^+ = 31$, (•) $l^+ = 21$ and compared with ZPG case denoted by connected dot symbol ('.') $l^+ = 31$, for other details, refer to Table 2.1. The solid line shows log law (3.6) with $\kappa = 0.41$, $A = 5.0$, the dashed line shows $U^+ = z^+$ and the dashed-dotted line indicates $z^+ = 15$.

the near-wall turbulence intensities peak $\overline{u^2}/{U_\tau}^2|_m$ for the ZPG, APG and FPG. In ZPG, $\overline{u^2}/{U_\tau}^2|_m \approx 8.0$ at $Re_\tau = 2820$ and at $l^+ = 22$ (Figure 10 in Hutchins et al. (2009)), the near-wall peak gradually increases to $\overline{u^2}/{U_\tau}^2|_m \approx 8.5$ as the Reynolds number increases to approximately 20000. $\overline{u^2}/{U_\tau}^2|_m$ increases further for higher Reynolds numbers (Marusic et al., 2010a). In APG, $\overline{u^2}/{U_\tau}^2|_m \approx 8.5$ at $Re_\tau \approx 3000$ at similar sensor length, $l^+ \approx 20$ (Figure 3.20($b$)). In the same way, $\overline{u^2}/{U_\tau}^2|_m \approx 7.5$ in FPG at the same matched conditions 3.21($b$)).

Results of detailed analysis of why peak energy is different for APG, ZPG and FPG is shown in Section 4.3, Chapter 4. At this point, it is sufficient to note that small-scale attenuations occur for boundary layers subjected to pressure gradients as well, similar to the effect demonstrated by Hutchins et al. (2009) in ZPG boundary layers.

## 3.12 Shape factor

The 'constants' $\kappa$ and $A$ in the log law (3.6) have been reviewed many times. For example, Coles (1962) suggested $\kappa = 0.41$ and $A = 5$, however high Reynolds number experiments by Nagib et al. (2004), Österlund (1999) have established that $\kappa = 0.384$. Nagib et al. (2007) and Chauhan et al. (2009) established $A = 4.17$ when using $\kappa = 0.384$. Nagib and Chauhan (2008) demonstrated variations in both 'constants' $\kappa$ and $A$ in canonical flows for channel, pipe and boundary layer flows. Moreover the latter suggest that $\kappa$ exhibits dependence not only on the pressure gradient but also on the flow geometry. In Section 3.8, it was shown that at a constant Reynolds number, there is a downward deviation of the mean velocity profile from the log law that systematically grows with $\beta$ (Figure 3.12). It was also shown that at $Re_\tau \approx 1900$ and $\beta \approx 4.54$, the scaled mean velocity is pushed down by $\Delta U^+ \approx 1$ in the log region if $\kappa$ and $A$ obtained from the OFI method were used, compared to $\kappa$ and $A$ obtained from the Clauser chart method (Figure 3.13).

It is useful to confirm the non-universality of $\kappa$ from other methods. Another method to determine $\kappa$ has been established by Monkewitz et al. (2008) by relating $H$ with $\kappa$. Monkewitz et al. (2008) developed a relationship between $H$ and the Reynolds number based on displacement thickness, $Re_{\delta^*}$; the shape factor continually decreases with increasing $Re_{\delta^*}$. The formulation for the shape factor as a function of $Re_{\delta^*}$ determined by Monkewitz et al. (2008) can be written as

$$
\begin{aligned}
H &= \left(1 - \frac{I_{WW}}{U_1^+}\right)^{-1} \\
&= \left(1 - \frac{I_{WW}}{\kappa^{-1}\log(Re_{\delta^*}) + C}\right)^{-1}, \qquad (3.37)
\end{aligned}
$$

where

$$
I_{WW} = \int_0^\infty ({U_1}^+ - U^+)^2 d\eta.
$$

Here $\eta = z/\Delta$ and $\Delta = \delta^* U_1^+$, $C$ must be determined by curve-fitting $(U_1^+, Re_{\delta^*})$ data. It has been shown that $I_{WW} = 7.11$ in zero pressure gradient boundary layers. Therefore, by knowing $H = \delta^*/\theta$, (3.37) could be rearranged to obtain the value of $\kappa$.

This section also aims to analyse the behaviour of the shape factor in TBL with pressure gradients. The behaviour of the shape factor, $H$, with varying Reynolds numbers has recently been shown by the work of Monkewitz et al. (2008) for zero pressure gradient flows. However, with the presence of pressure gradients, the upstream history has a complex effect on the mean velocity and so the effect on the shape factor is not so well understood. It has been shown that the shape factor increases with $\beta$ (Nagano et al., 1992, Skåre and Krogstad, 1994, Spalart and Watmuff, 1993). Therefore, in TBL with pressure gradients, $H$ is dependent on both Reynolds number and on the pressure gradient parameter; this further complicates analysis. Many investigations allow both $\beta$ and $Re_\tau$ to vary between experiments (as shown in the survey of existing data in Table 1.1). It is difficult to analyse the behaviour of $H$ unless a wide range of pressure gradient $\beta$ and Reynolds number $Re_\tau$ data is available. In this parametric study, the constant $\beta$ and constant $Re_\tau$ data are very helpful in the investigation of pressure gradient effects on shape factor.

To evaluate this analysis in the presence of pressure gradients, constant Reynolds number data ($Re_\tau \approx 1900$) with increasing pressure gradient is used. Furthermore, the constant $\beta \approx 1.6$ and 4.3 data are also used, shown in Figure 3.22. For the constant $Re_\tau$ experiments (note that $Re_{\delta^*}$ does not necessarily remain constant when $Re_\tau$ is kept constant), the shape factor increases sharply as pressure gradient increases. In contrast, the constant $\beta \approx 1.6$ and 4.3 data decrease with increasing Reynolds number, as is the case for zero pressure gradient boundary layers. The trend here suggests that $I_{WW}$ increases with pressure gradient parameter $\beta$. That means any adverse pressure gradient only causes a vertical shift as shown in Figure 3.22. It is possible to calculate $I_{WW}$ for the constant $\beta$ data from the velocity profiles because they exhibit Reynolds number

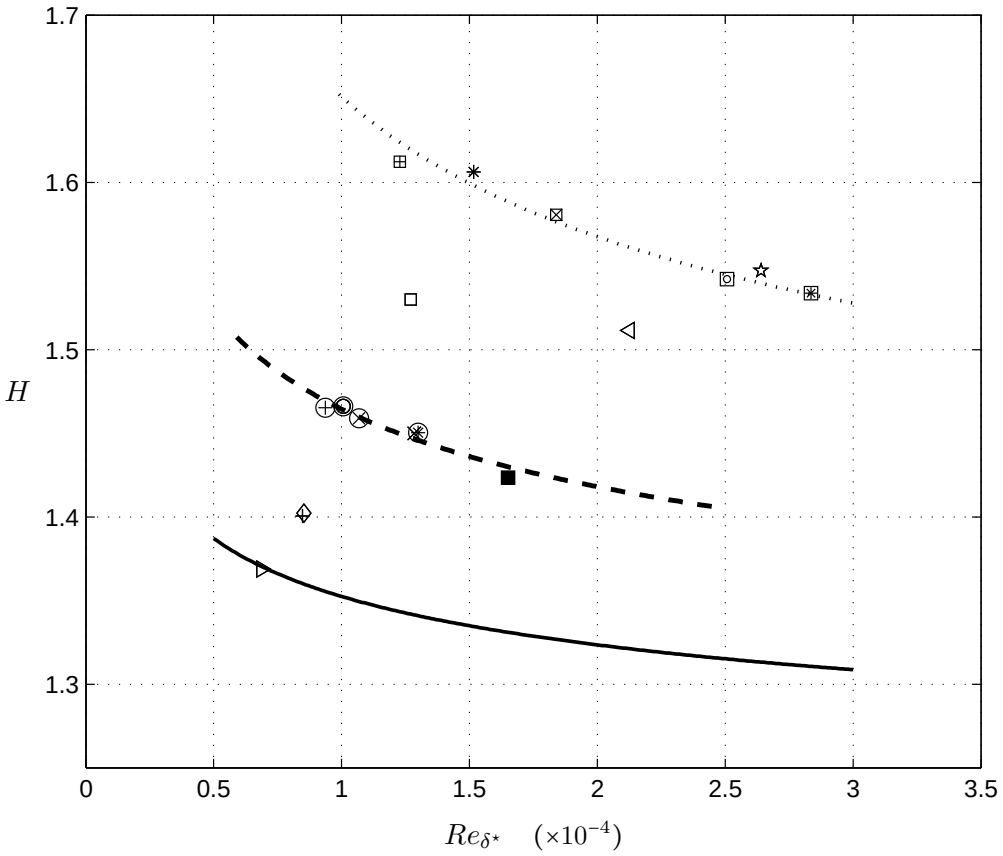


FIGURE 3.22: Shape factor, $H$ vs $Re_{\delta^\star}$ for constant $Re_\tau$, constant $\beta$ data and constant $K$ data. The solid line represents $H$=(1- $I_{WW}/(\kappa^{-1}\log(Re_{\delta^\star})$+C))$^{-1}$ established by Monkewitz et al. (2008) with existing constants for ZPG. The dashed and dotted lines represent the same function, however with proposed constants for $\beta \approx 1.6$ and 4.3 respectively, shown in Table 3.2. For symbols, refer to Table 2.1. ■ is additional data not shown in Table 2.1 included to have bigger Reynolds number, this data was performed at station three, with parameters $U_1 = 19$ m/s and $\beta = 1.6$.

similarity over the range studied (although not shown, velocity defect profiles collapse throughout the logarithmic and outer regions when $\beta$ is held constant).

The ZPG data collapses with the $I_{WW}$ formulation by Monkewitz et al. (2008), represented by the solid line in Figure 3.22. This should be sufficient to indicate that the current ZPG data follows the prediction of the composite profile studies. The average value of $I_{WW}$ in (3.37) are 9.28 and 12.6 obtained from the constant $\beta \approx 1.6$ and 4.3 data respectively. The corresponding formulations by Monkewitz et al. (2008) (3.37) are shown by the dashed line and dotted line respectively.

Note that the symbols ⊞, ⊠, ⊡ and ⊛ are from the constant $\beta \approx 4.3$ data and the additional data with symbols $*$ and $\star$ have similar magnitude of $\beta$. These data appear

| | (Monkewitz et al.) ZPG | $\beta \approx 1.6$ | $\beta \approx 4.3$ |
|---|---|---|---|
| $\kappa$ | 0.384 | 0.32 | 0.32 |
| $C$ | 3.3 | 1.0 | 2.3 |
| $I_{WW}$ | 7.11 | 9.28 | 12.6 |

TABLE 3.2: Summary of constants in Eq. 3.37 for ZPG and APG cases for $\beta \approx 1.6$ and $\beta \approx 4.3$.

to lie within the formulation by Monkewitz et al. (2008) (dotted line). Similarly, the same can be explained for the constant $\beta \approx 1.6$ data with the corresponding dashed line predicted by (3.37).

The values of $\kappa$ and $C$ are provided in Table 3.2. The values of $\kappa$ for constant $\beta$ data are about the same and lower than the value for ZPG. Their respective values for $C$ are also lower than that in ZPG. Lower $\kappa$ values than the nominal ZPG case for constant $\beta$ data have also been observed from the OFI method (via curve fitting of the mean velocity profile). It should be noted that, due to the limited data available, the values of the three parameters determined ($\kappa$, $C$ and $I_{WW}$) are estimates only. Nevertheless, the formulation for $H$ follows the data very well (the dashed and dotted lines in Figure 3.22).

The author attempted to repeat the analysis with FPG data (at constant $\beta \approx -0.5$), however the same trend could not be produced. This could be due to the limited data either in terms of the Reynolds number range or the degree of the favourable pressure gradient. Therefore, the evidence presented here suggests that the functional form of $H$ with the Reynolds number is only valid in ZPG and APG flows.

This section demonstrates that the analysis of mean flow similarity laws (Monkewitz et al., 2008) can be extended in APG flows. This analysis however, would not be possible without the constant $\beta$ set of data (with increasing Reynolds number) discussed in Section 3.9. As mentioned earlier, the analysis is based on limited data and a small range of Reynolds number[4]. Therefore, it is recommended that this analysis be expanded covering more data and a larger Reynolds number range. The section also confirms the proposal that $\kappa$ is not universal - it is also a function of the pressure gradient.

[4]The analysis performed by Monkewitz et al. (2008) was based on more than 300 mean velocity profiles and larger Reynolds number range (twice the order of the Reynolds number in the current experiment.)

## 3.13 Skewness and flatness

As mentioned in the literature review, the skewness increases when a layer is exposed to APG (Nagano and Houra, 2002, Skåre and Krogstad, 1994). In ZPG flows, Metzger and Klewicki (2001) demonstrated that it is the large-scale features that contribute to the rise of the skewness. This section is provided to repeat Metzger and Klewicki (2001)'s analysis, because it is demonstrated that the large-scale features also increase because of APG (Lee and Sung, 2009, Rahgozar and Maciel, 2011a, Skåre and Krogstad, 1994). Analysing the large-scale features' contribution towards the skewness is one of the major aims. This section also provides the general behaviours of the skewness and the flatness when the pressure gradient is varied.

The skewness, $S_k$, and flatness, $F$, factors are defined as:

$$S_k = \frac{\overline{u^3}}{\overline{(u^2)}^{3/2}}, \qquad F = \frac{\overline{u^4}}{\overline{(u^2)}^2}. \tag{3.38}$$

The third moment of a turbulent statistic, such as $\overline{u^3}$ scaled by $\overline{(u^2)}^{3/2}$, describes the skewness $S_k$, or asymmetry of the probability distribution of $u$. The function is symmetric about the origin, $S_k = 0$, if $\overline{u^3} = 0$. A positive value of $S_k$ implies that large positive values of $u$ are more frequent than large negative values. $S_k = 0$ for a Gaussian distribution. The fourth moment, or flatness, $F$, of the $u$ distribution is given by $\overline{u^4}$ scaled with $\overline{(u^2)}^2$, and is a measure of the frequency of occurrence of events far from the axis. If these are relatively frequent, $F$ will take greater values than the Gaussian value of 3 (Fernholz and Finley, 1996).

Figure 3.23($a$) shows the skewness of streamwise velocity fluctuations for adverse, zero and favourable pressure gradients at $Re_\tau \approx 3000$. A large difference between the three pressure gradient cases can be observed. The entire skewness profile is lifted up for the APG case and shifted down for the FPG case. For FPG, skewness is negative, starting at $z/\delta = 0.008$ and remaining negative for the entire boundary layer. Skewness for APG remains positive from the near-wall region towards the wake region ($z/\delta \approx 0.3$), while skewness for the ZPG case is between the APG and FPG cases. Thus there is a difference in skewness caused by the pressure gradient. However, the sensor length $l^+$, does cause differences in the near-wall region. Johansson and Alfredsson (1983) showed that skewness varied with sensor length i.e. $S_k \approx -0.2$ for $l^+ = 14$; however this changed to $S_k \approx 0$ for $l^+ = 32$ in the near-wall region ($20 \lesssim z^+ \lesssim 30$) at $Re_h \approx 50000$ in turbulent

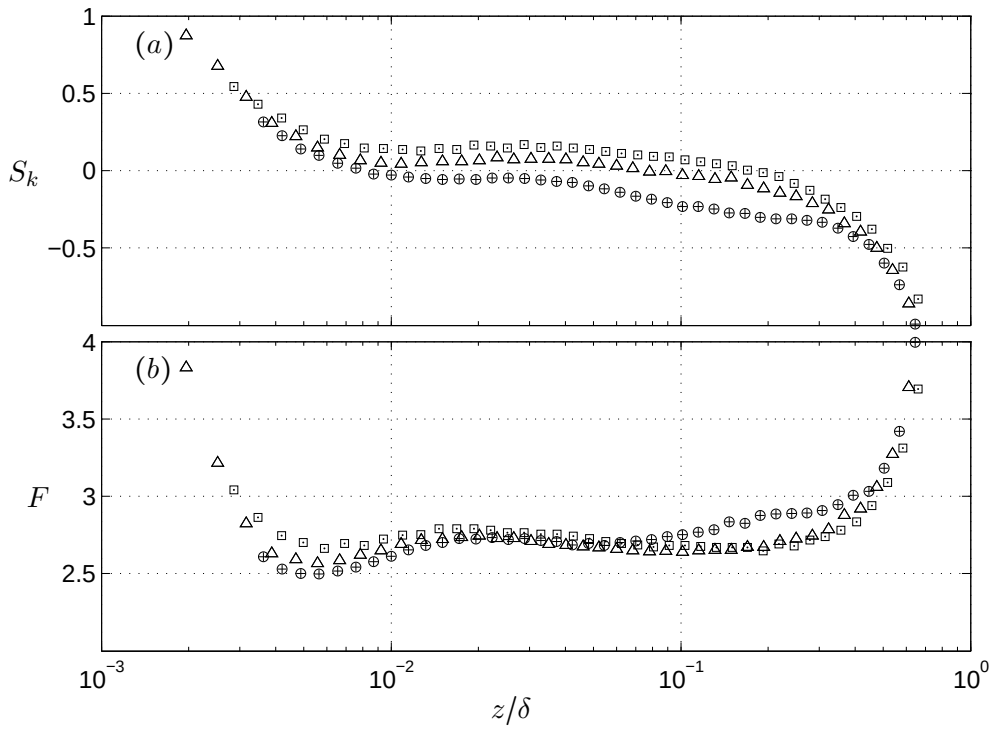


FIGURE 3.23: (a) Skewness $S_k$ and (b) flatness $F$ for adverse, zero and favourable pressure gradients at $Re_\tau \approx 3000$. Symbols: (⊡) APG, (△) ZPG and (⊕) FPG. For other details, refer to Table 2.1.

channel flow experiments ($Re_h$ is Reynolds number based on channel height). This effect (due to changing $l^+$) has been ruled out here, since $l^+$ is constant in the current data ($l^+ \approx 30$). Johansson and Alfredsson (1983) compared two flows at relatively high but different Reynolds number, $Re_h \approx 50000$ and $Re_h \approx 129000$, at constant $l^+ = 33 - 34$, and showed that there was a slight difference in $S_k$. Therefore, the Reynolds number also does cause a difference in $S_k$. The data for this thesis' comparison was acquired at a constant Reynolds number and $l^+$, thus neither Reynolds number nor $l^+$ effects apply here and the focus is solely on the pressure gradient.

Figure 3.23($a$) shows that the pressure gradient increases the skewness over the whole boundary layer, as was also reported by Nagano and Houra (2002), Skåre and Krogstad (1994). A large deviation from the Gaussian distribution ($S_k = 0$) is expected for the APG case (Dengel and Fernholz, 1990). For the inner region, Nagano and Houra (2002) suggested that the rise in skewness is caused by 'structural changes in the near-wall' region due to the pressure gradient. Johansson and Alfredsson (1982) showed that in the near-wall region in channel flow, 'a positive skewness reflects the presence of high shear events imposed on a background of lower turbulence level'. Here, it is proposed

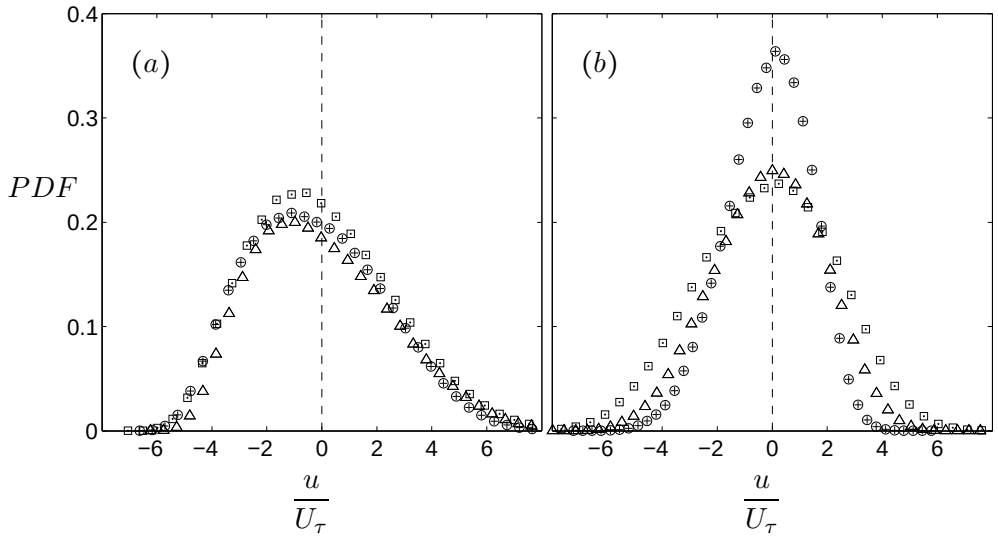


FIGURE 3.24: Probability density function (PDF) at $(a)$ $z^+ \approx 15$ and, $(b)$ $z/\delta \approx 0.3$ for adverse, zero and favourable pressure gradients at $Re_\tau \approx 3000$. Symbols: (⊡) APG, (△) ZPG and (⊕) FPG. For other details, refer to Table 2.1.

that, for high Reynolds numbers ($Re_\tau \gtrsim 2000$), the change in skewness with pressure gradient is due to the increased large-scale influence in the near-wall region that was found earlier to be associated with increased $\beta$.

Figure 3.23($b$) shows the flatness of streamwise velocity fluctuations for adverse, zero and favourable pressure gradients at $Re_\tau \approx 3000$. Again, noticeable differences can be observed between the cases, especially in the near-wall region ($z/\delta \lesssim 0.08$) and much further out in the outer region, ($z/\delta \gtrsim 0.1$). In the near-wall region, the APG case has the lowest value of $F$.

As shown in Figure 3.23($a$), APG causes the skewness profile to lift upwards, in contrast FPG causes the profile to shift downwards. It would be informative to learn about the distribution of the fluctuating velocities, $u$. Figures 3.24($a$) and ($b$) show representative probability density function (PDF) plots for adverse, zero and favourable pressure gradients at $Re_\tau \approx 3000$. Figure 3.24($a$) shows the PDF in the near-wall region, $z^+ \approx 15$. No substantial differences between the three cases can be observed in this figure. However, in the outer region, at $z/\delta \approx 0.3$, shown in Figure 3.24($b$), dramatic changes can be observed across the three cases. The PDF of fluctuating velocities for FPG has the smallest band, and for APG the greatest band.

Metzger and Klewicki (2001) compared low Reynolds number laboratory data with that from a high Reynolds number atmospheric surface layer. At lower Reynolds numbers,

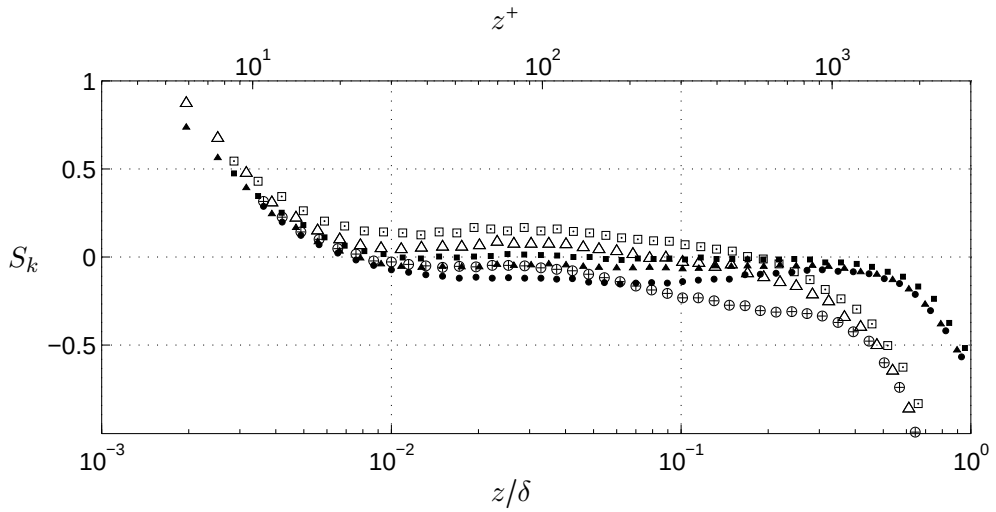


FIGURE 3.25: Skewness $S_k$ for adverse, zero and favourable pressure gradients at $Re_\tau \approx 3000$. Symbols: (⊡) APG, (△) ZPG and (⊕) FPG. Filtered data ($\lambda_x/\delta < 1$) symbols: (■) APG, ZPG (▲) and FPG (●).

it was found that in the inner region of $10 < z^+ < 100$, the skewness was negative, while for the high Reynolds number geophysical flow, the skewness remained positive in the same region. Upon applying a high-pass filter to the streamwise velocity component to separate low-frequency, large-scale motions, it was concluded that the increased energy of large-scale structures caused the increase in skewness from a negative to a positive value. In this study, a high-pass filter was applied to the adverse, zero and favourable data, using a cut-off wavelength of $\lambda_{xc} = \delta$. The selection of cut-off wavelength is discussed in detail in Chapter 4.

The skewness profiles of the filtered data from the adverse, zero and favourable at $Re_\tau \approx 3000$ is shown in Figure 3.25. It can be observed that the skewness profiles for all three cases are shifted down for the region $z^+ < 100$, which is similar to the observations in the study by Metzger and Klewicki (2001). The most distinguishing features of Figure 3.25 are in the outer region. The difference in the outer region, almost arbitrarily selected at $z/\delta = 0.3$, is very large ($S_k \approx -0.15$ for APG and $S_k \approx -0.35$ for FPG). Interestingly, the filtered data shows a resemblance to a Gaussian distribution ($S_k \approx 0$) for all three cases. The effect of a high-pass filter in this region is to increase the values of $S_k$, contrary to the effect of filtering in the near-wall region. Returning to Figure 3.23($a$), the increased skewness in the near-wall region can now be confirmed to be associated with the large-scale features in APG flows.

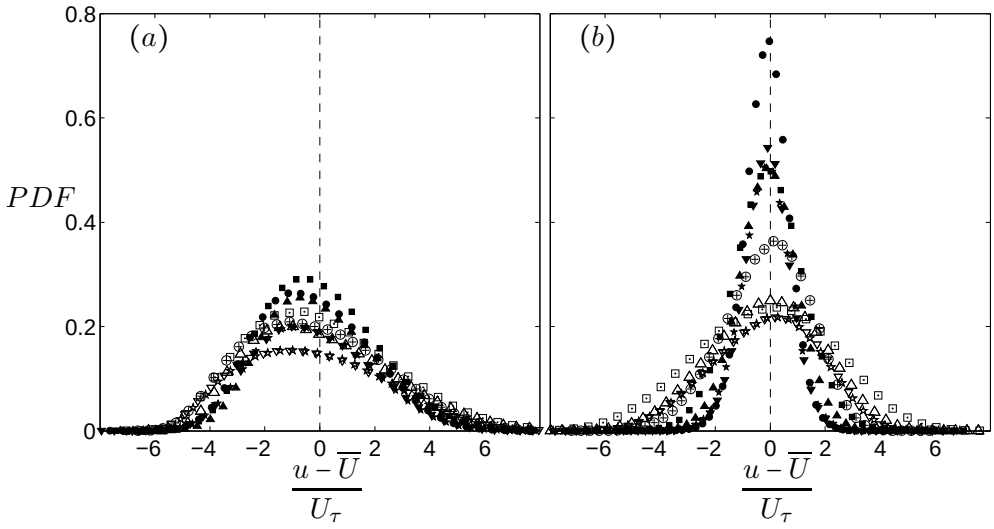


FIGURE 3.26: Probability density function (PDF) at $(a)$ $z^+ \approx 15$ and, $(b)$ $z/\delta \approx 0.3$ for adverse, zero and favourable pressure gradients at $Re_\tau \approx 3000$. Symbols: (⊡) APG, (△) ZPG and (⊕) FPG. Filtered data ($\lambda_x/\delta < 1$) symbols: (■) APG, ZPG (▲) and FPG (●).

Metzger and Klewicki (2001) explained that a high-pass filter procedure systematically eliminates any additive effect of large-scale, low-frequency motions on measured statistics. In the near-wall region, small-scales are predominant. Therefore, the effect of high-pass filtering is caused only by the large-scales' influence onto the small-scales. However, in the outer region, small-scales co-exist among and within large-scales. A high-pass filter has a far-reaching effect when the large-scale components are removed. Figures 3.26 show PDFs of the filtered data at $z^+ \approx 15$ and $z/\delta \approx 0.3$ for the three pressure gradient cases. In the near-wall region, the high-pass filtered data is slightly less skewed (towards positive velocities), resulting in lower positive skewness values in Figure 3.26$(a)$. These effects are however quite small. In the outer region, high-pass filtered data not only causes the skewness to increase (from large negative towards zero), but also causes the PDF width to thin i.e. the standard deviations are reduced. This suggests that the large-scales are responsible for the negative skewness (this is in contrast with the effect of large-scales in the near-wall region where $S_k$ rises with increasing small- and large-scale interactions).

Figure 3.27$(a)$ shows the skewness of streamwise velocity fluctuations for varying adverse pressure gradients. For the zero pressure gradient case, the skewness is negative in the lower part of the traditional logarithmic region, $0.01 < z/\delta < 0.03$. Further from the wall ($0.03 < z/\delta < 0.15$), the PDF of streamwise velocity closely follows a Gaussian distribution

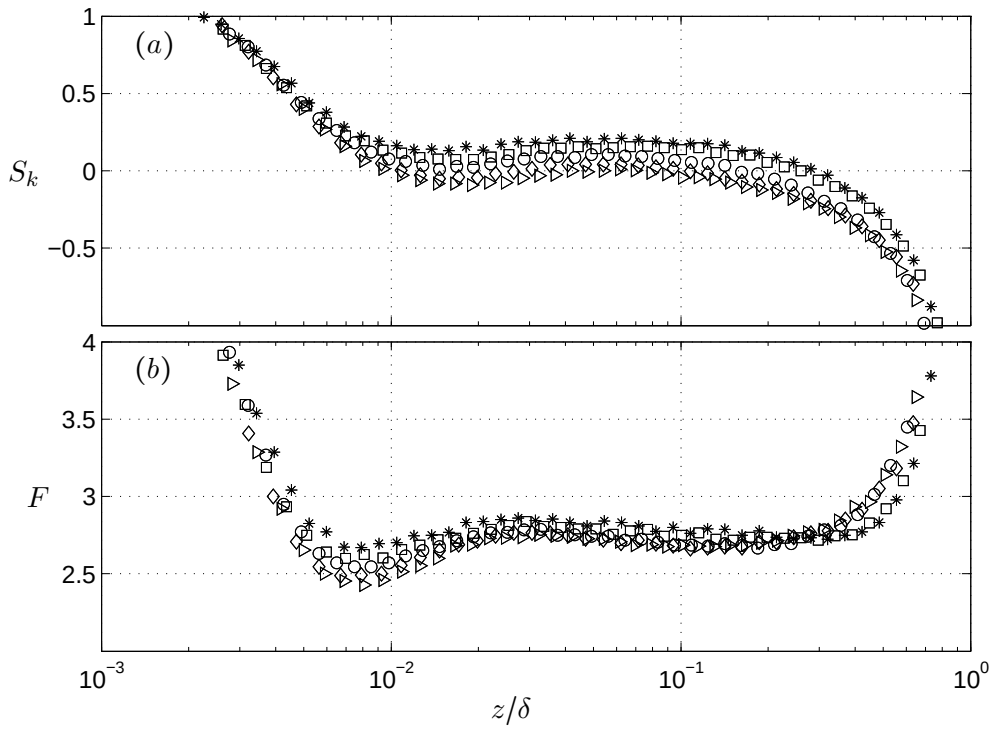


FIGURE 3.27: $(a)$ Skewness $S_k$ and $(b)$ flatness $F$ for constant $Re_\tau \approx 1900$. Symbols: $(\triangleright)$ ZPG, $(\diamond)$ $\beta \approx 0.9$, (o) $\beta \approx 1.6$, $(\square)$ $\beta \approx 2.8$ and $(*)$ $\beta \approx 4.4$. For other details, refer to Table 2.1.

(i.e., $S_k \approx 0$). These trends are consistent with previous findings (for example, Balint et al., 1991).

Figure 3.27$(b)$ shows the flatness, $F$, of the streamwise velocity fluctuations for the constant $Re_\tau$ data. The zero pressure gradient flow has the lowest value of flatness in the near-wall region and, in general, the flatness increases with pressure gradient. In the outer region, the flatness is nearly invariant with pressure gradient. A rise in flatness is often attributed to a rise in intermittency (Dengel and Fernholz, 1990). This interpretation leads to the conclusion that there is a weakly increasing intermittency in the near-wall region of the boundary layer as the pressure gradient increases.

Figures 3.28 show the skewness $(a)$ and flatness $(b)$ of streamwise fluctuating velocity for the constant pressure gradient parameter, $\beta \approx 4.3$ data with varying $Re_\tau$. As with the lower-order statistics, the skewness collapses for all Reynolds numbers in the logarithmic and outer regions (the deviation near the wall is due to outer scaling of the wall-normal coordinate, $z$). The invariance of skewness with Reynolds number shows that the Reynolds number range is not great. At this pressure gradient, the skewness

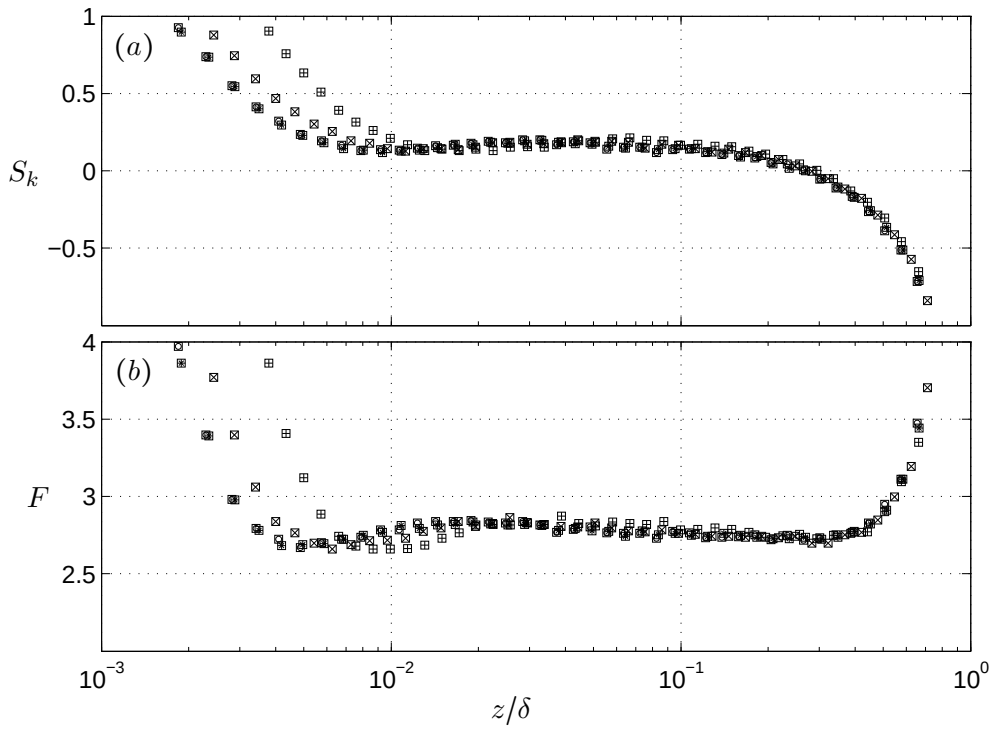


FIGURE 3.28: (a) Skewness $S_k$ and (b) flatness $F$ for constant $\beta \approx 4.3$. Symbols: (⊞) $Re_\tau \approx 1700$, (⊠) $Re_\tau \approx 2500$, (⊡) $Re_\tau \approx 3500$, (⊛) $Re_\tau \approx 3900$.

remains positive through most of the layer, consistent with the data in Figure 3.27($a$). Similarly, flatness collapses for all of the constant pressure gradient data in the logarithmic and outer regions and, as with the skewness, a relatively constant deviation from a Gaussian distribution of velocity in the logarithmic and outer regions is observed.

The skewness analysis suggests that the interactions of the small-scales in the inner region with the large-scales in the outer region cause the $S_k$ to deviate in a positive direction from the Gaussian distribution. This is similar to the trend of increasing $S_k$ with Reynolds number, attributed to a higher degree of interactions between the small- and large-scales (Metzger and Klewicki, 2001). The large-scales are directly responsible for the positive skewness in the outer region. The effect of a high-pass filter in the outer region brings $S_k$ closer towards Gaussian distribution, suggesting the large-scales are responsible for negative skewness in this region. The flatness increases with the pressure gradient parameter in the near-wall region however this effect reduces in the outer region.

## 3.14 Skewness relationship with amplitude modulation

Mathis et al. (2009) and Marusic et al. (2010b) have shown that the skewness is related to the amplitude modulation of the near-wall, small-scale motions by the large-scale structures. These studies also report the rise in skewness with higher Reynolds numbers for ZPG flows and show that this is explained by the increased amplitude modulation. The behaviour of the skewness observed in Figure 3.27($a$) indicates that the large-scales are not only increasing in strength, but are also increasingly amplitude modulating the small-scales as the pressure gradient increases.

Schlatter and Örlü (2010) critically argued against the amplitude modulation parameter proposed by Mathis et al. (2009) because of the similarity of the amplitude modulation's coefficient with the skewness coefficient. Mathis et al. (2011) expanded $S_k$ using a decomposed signal such that $u^+ = u_L^+ + u_S^+$, where subscripts $L$ and $S$ denote large and small scale components, therefore

$$S_k = \frac{\overline{u^{+3}}}{\left(\overline{u^{+2}}\right)^{3/2}} = \frac{\overline{u_L^{+3}} + \overline{3u_L^{+2}u_S^+} + \overline{3u_L^+u_S^{+2}} + \overline{u_S^{+3}}}{\left(\overline{u^{+2}}\right)^{3/2}}, \tag{3.39}$$

can be simplified as

$$S_k = \widetilde{\overline{u_L^{+3}}} + \widetilde{\overline{3u_L^{+2}u_S^+}} + \widetilde{\overline{3u_L^+u_S^{+2}}} + \widetilde{\overline{u_S^{+3}}}, \tag{3.40}$$

where $\widetilde{\overline{ab}} = \overline{ab}/\left(\overline{u^{+2}}\right)^{3/2}$. Mathis et al. (2011) has chosen a cut-off filter of $\lambda_x^+ = 7000$, however, in this analysis, the cut-off filter is $\lambda_x^+ \approx Re_\tau = 3000$. The cut-off filter selection is discussed in Energy Spectra, Section 4.1.

The skewness and each term of decomposed skewness factors for an APG turbulent boundary layer flow at $Re_\tau \approx 3000$ and $\beta \approx 1.7$ is shown in Figure 3.29. The small-scales term $\widetilde{\overline{u_S^{+3}}}$ and cross-term $\widetilde{\overline{3u_L^+u_S^{+2}}}$ appear to account for the majority of the $S_k$ up to $z^+ \approx 30$. Mathis et al. (2011) also found these two terms to be important contributors to $S_k$ in ZPG boundary layer flow. However, much smaller contribution from $\widetilde{\overline{3u_L^+u_S^{+2}}}$ is observed in Mathis et al. (2009) when compared with current APG data.

The larger cross product term $\widetilde{\overline{3u_L^+u_S^{+2}}}$ coefficient in Figure 3.29 (which is in APG), than observed in Mathis et al. (2011) (in ZPG) needs further analysis. Therefore, it is helpful

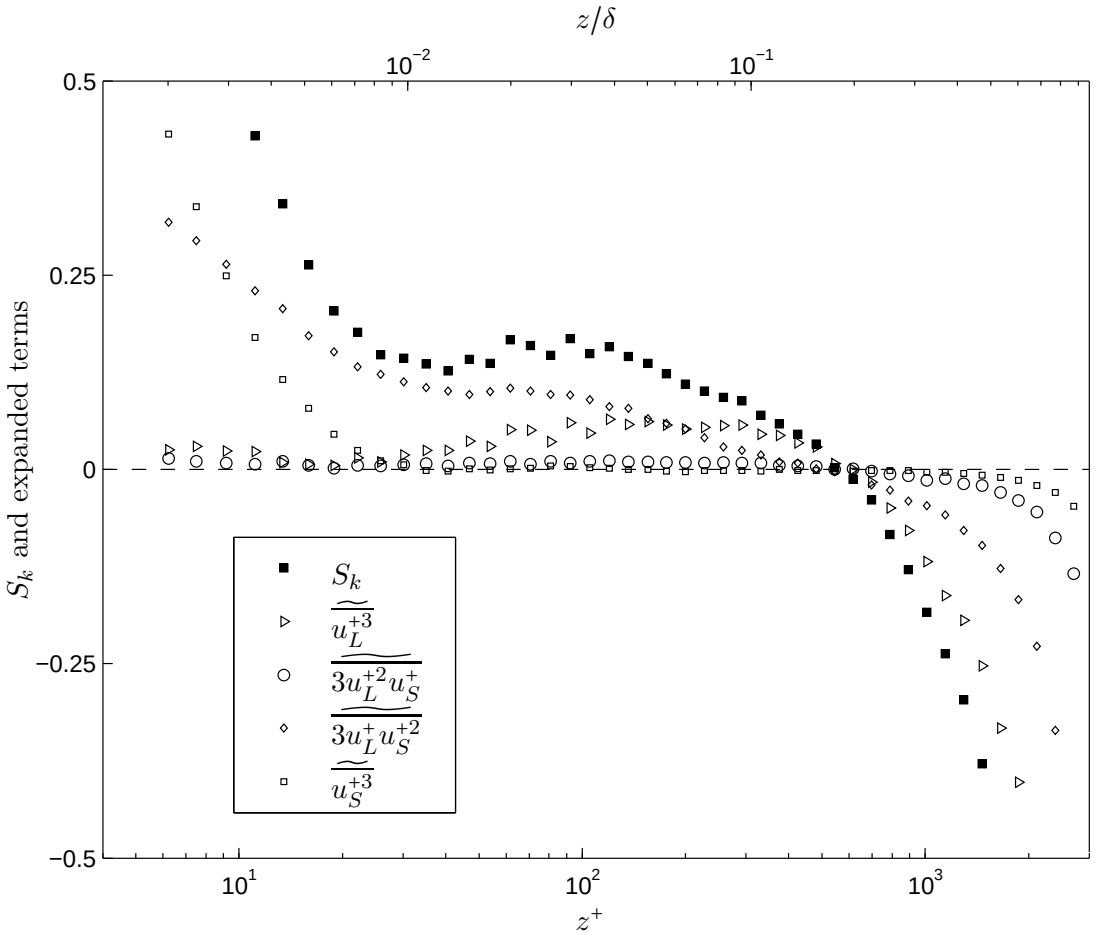


FIGURE 3.29: Skewness $S_k$ for APG at $Re_\tau \approx 3000$. The skewness factors are expanded following $u^+ = u_L^+ + u_S^+$. The expanded terms are shown in (3.40).

to compare this term from all pressure gradient cases. We analyse these two significant terms which are $\widetilde{u_S^{+3}}$ and $\widetilde{3u_L^+u_S^{+2}}$.

Figure 3.30($a$) displays the small-scales term $\widetilde{u_S^{+3}}$ of the expanded $S_k$ for APG, ZPG and FPG at $Re_\tau \approx 3000$. The term $\widetilde{u_S^{+3}}$ is slightly larger in APG than in ZPG and than in FPG in the log region $40 \lesssim z^+ \lesssim 0.15Re_\tau$. In the outer region, the small-scales $\widetilde{u_S^{+3}}$ term's contribution to $S_k$ collapses for all pressure gradient cases.

Figure 3.30($b$) displays the cross product term $\widetilde{3u_L^+u_S^{+2}}$ for APG, ZPG and FPG at $Re_\tau \approx 3000$. The cross product term $\widetilde{3u_L^+u_S^{+2}}$ is larger for APG than for ZPG and FPG. This could be related to the fact that there are more large-scales in the near wall region as the boundary layer is exposed to APG (Krogstad and Skåre, 1995, Lee and Sung, 2009, Monty et al., 2011). In ZPG, Mathis et al. (2011) proposed that the cross product

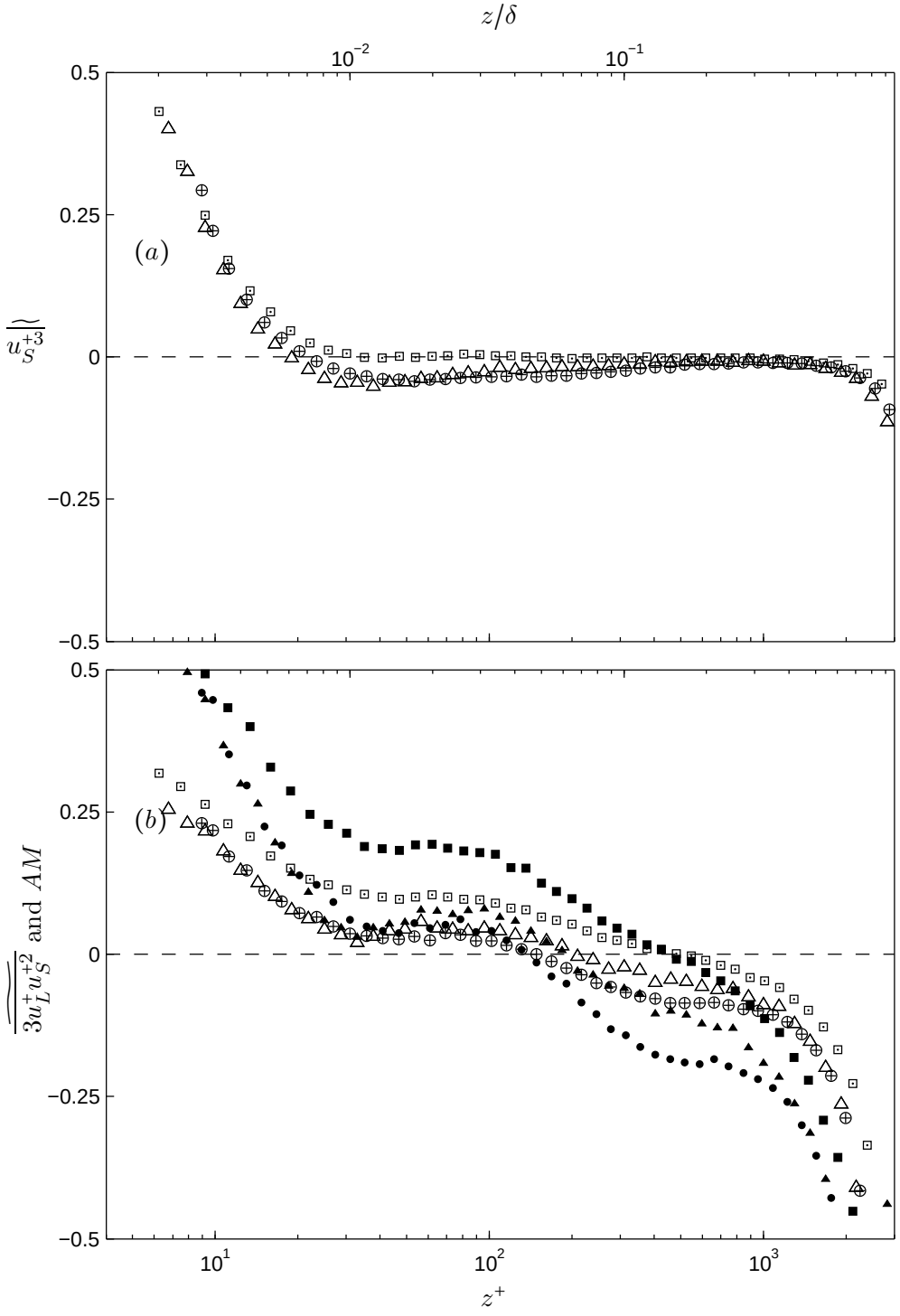


FIGURE 3.30: Skewness terms and amplitude modulation $AM$ comparison of APG, ZPG and FPG flows at matched $Re_\tau \approx 3000$ (a) the small-scale term $\widetilde{\overline{u_S^{+3}}}$ and (b) the cross product term $\widetilde{\overline{3u_L^+u_S^{+2}}}$. Symbols: (⊡) APG (△) ZPG and (⊕) FPG skewness terms. The $AM$ are denoted by the solid symbols: (■) APG, (▲) ZPG and (●) FPG. The skewness is expanded as explained in Figure 3.29.

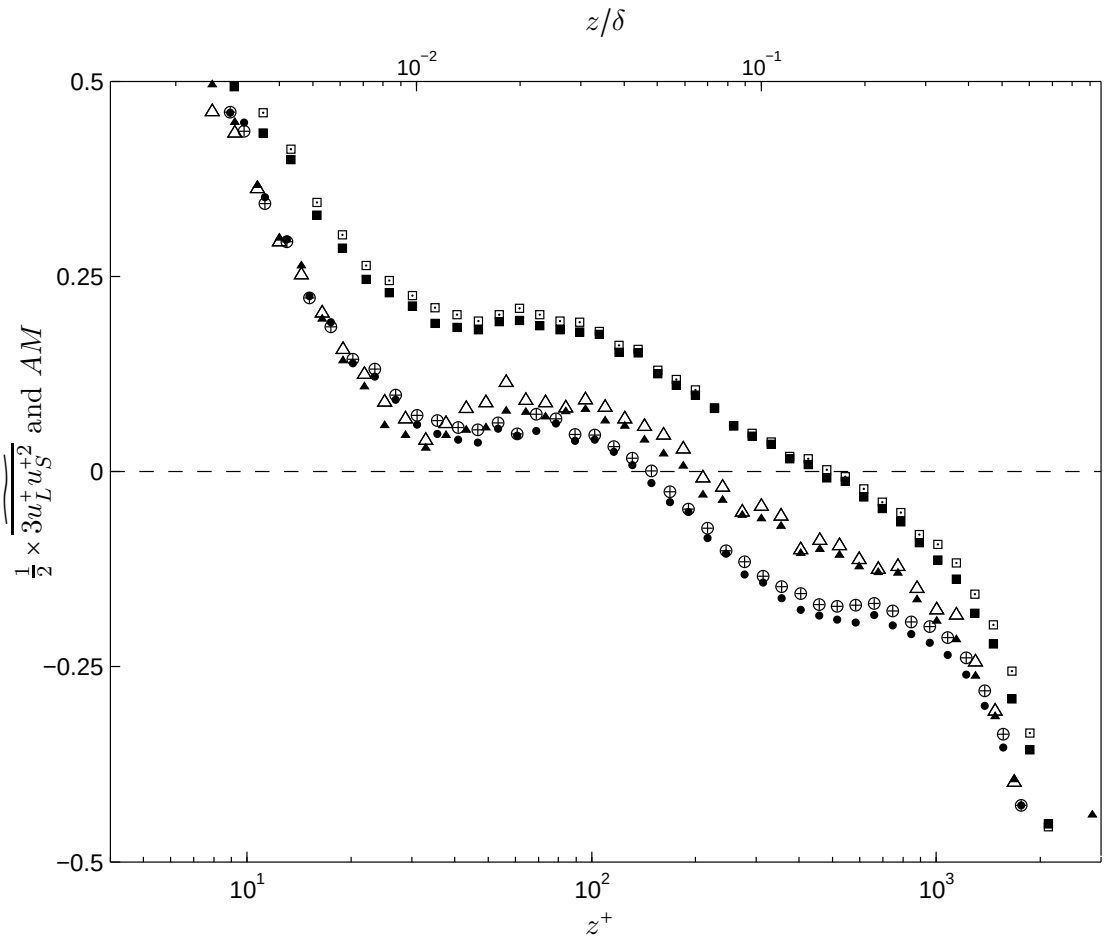


FIGURE 3.31: Skewness terms $2\times\widetilde{3u_L^+u_S^{+2}}$ and amplitude modulation $AM$ comparison of APG, ZPG and FPG flows at matched $Re_\tau \approx 3000$. Symbols: (⊡) APG (△) ZPG and (⊕) FPG skewness terms. The $AM$ are denoted by the solid symbols: (■) APG, (▲) ZPG and (●) FPG.

term $\widetilde{3u_L^+u_S^{+2}}$ to be an alternative to the amplitude modulation scheme by Mathis et al. (2009) because of their robustness over a wide range of Reynolds numbers $2800 < Re_\tau < 19000$. The term $\widetilde{3u_L^+u_S^{+2}}$ in the current ZPG data also bears a resemblance to the $AM$ coefficient (calculated by the method used in Mathis et al. (2009)) in Figure 3.30($b$).

However, $\widetilde{3u_L^+u_S^{+2}}$ coefficients are obviously much smaller than $AM$ for the APG case in $z^+ \lesssim 0.15Re_\tau$. The most important observation here is that $\widetilde{3u_L^+u_S^{+2}}$ share the same resemblance of the $AM$ for all three pressure gradients cases.

In order to collapse $AM$ and $\widetilde{3u_L^+u_S^{+2}}$ terms in Figure 3.30($a$), another plot is displayed in Figure 3.31, however the cross product term's multiplier 3 is changed i.e. $2\times\widetilde{3u_L^+u_S^{+2}}$. Now it can be seen that $AM$ and $2\times\widetilde{3u_L^+u_S^{+2}}$ collapse for all the pressure gradient cases.

Figure 3.32 shows the reconstruction of the skewness without the cross term $\widetilde{3u_L^+u_S^{+2}}$, i.e. $\tilde{S}_k = \widetilde{u_L^{+3}} + \widetilde{3u_L^{+2}u_S^+} + \widetilde{u_S^{+3}}$. For ZPG, $\tilde{S}_k$ in the log region $40 \lesssim z^+ \lesssim 0.15Re_\tau$ approaches 0, similar to the results by Mathis et al. (2011). However, for the APG case $\tilde{S}_k$ coefficients are larger. The contribution can be observed in Figure 3.29 to come from the term $\widetilde{u_S^{+3}}$ for the region $z^+ \lesssim 30$ and from the term $\widetilde{u_L^{+3}}$ in the log region $40 \lesssim z^+ \lesssim 0.15Re_\tau$. In contrast, the $\tilde{S}_k$ coefficient for the FPG case is much smaller than the ZPG and APG cases.

For completeness, the same procedure to decompose the fluctuating velocity into small- and large-scale components can be performed for the flatness. Following the notation in (3.40), the expanded terms can be shown as

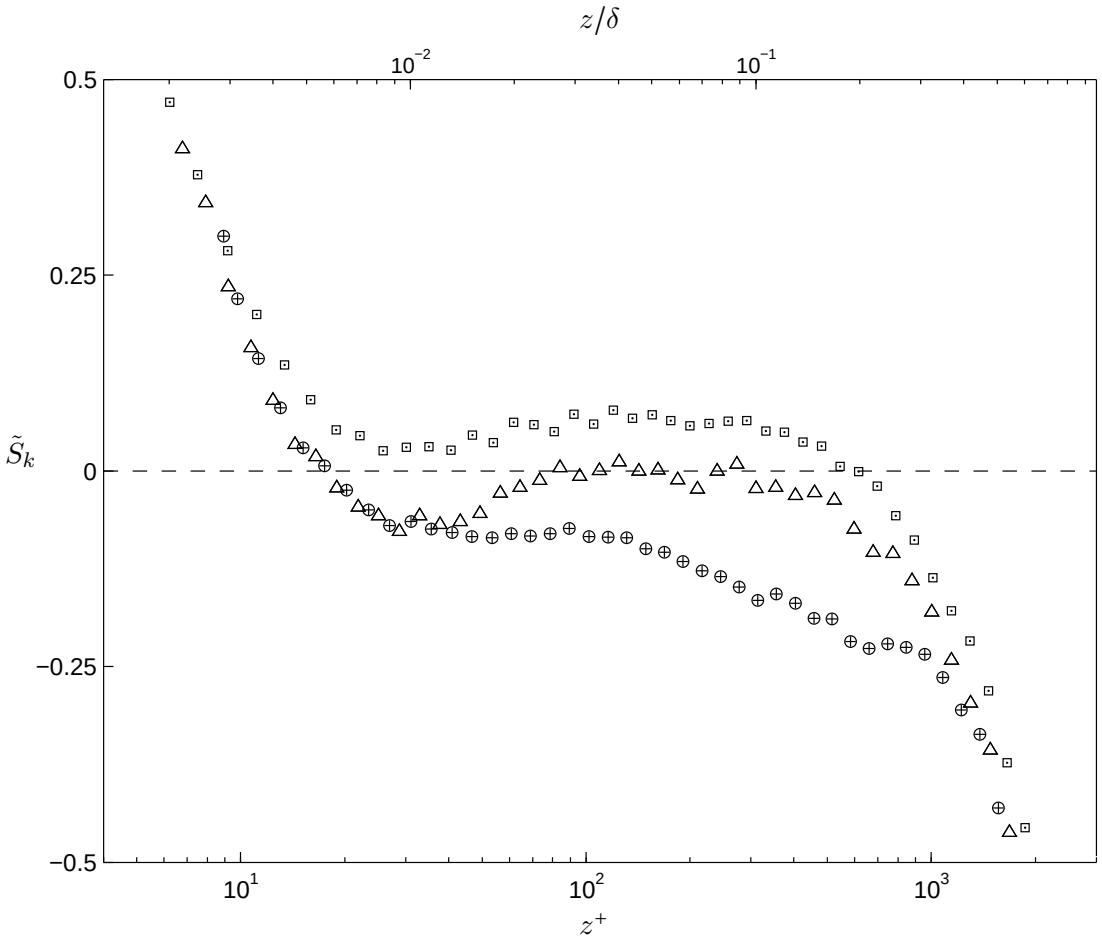


FIGURE 3.32: Skewness terms reconstruction without cross term $\widetilde{3u_L^+u_S^{+2}}$ i.e. $\tilde{S}_k = \widetilde{u_L^{+3}} + \widetilde{3u_L^{+2}u_S^+} + \widetilde{u_S^{+3}}$ for APG, ZPG and FPG flows at matched $Re_\tau \approx 3000$. Symbols: (⊡) APG (△) ZPG and (⊕) FPG skewness terms.

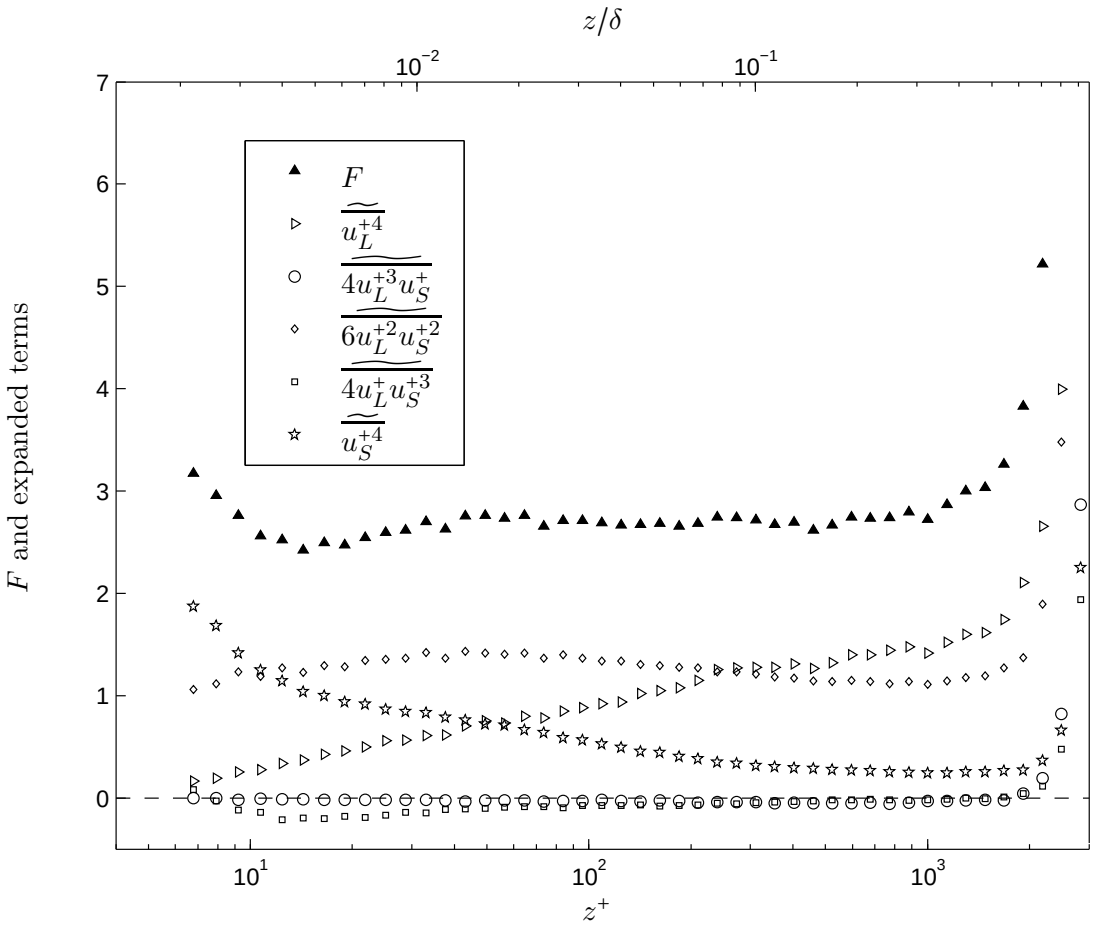


FIGURE 3.33: Flatness $F$ for APG at $Re_\tau \approx 3000$. The Flatness factors are expanded following $u^+ = u_L^+ + u_S^+$. The expanded terms are shown in (3.41).

$$F = \widetilde{\overline{u_L^{+4}}} + \widetilde{\overline{4u_L^{+3}u_S^+}} + \widetilde{\overline{6u_L^{+2}u_S^{+2}}} + \widetilde{\overline{4u_L^+u_S^{+3}}} + \widetilde{\overline{u_S^{+4}}}, \tag{3.41}$$

where $\widetilde{\overline{ab}} = \overline{ab}/\left(\overline{u^{+2}}\right)^2$. The flatness and each term of decomposed flatness factor for APG turbulent boundary layer flow at $Re_\tau \approx 3000$ and $\beta \approx 1.7$ is shown in Figure 3.33. The small-scales term $\widetilde{\overline{u_S^{+4}}}$ decreases with increasing wall-normal distance and in contrast the large-scales term $\widetilde{\overline{u_L^{+4}}}$ increases with wall-normal distance. Both cross products $\widetilde{\overline{4u_L^{+3}u_S^+}}$ and $\widetilde{\overline{4u_L^+u_S^{+3}}}$ are almost negligible however the $\widetilde{\overline{6u_L^{+2}u_S^{+2}}}$ terms is consistently a significant contributor to $F$ for the entire boundary layer thickness.

## 3.15 Turbulence production

When the large-scale features are removed from the flow, the positive deviation in the skewness in APG flow as compared with the ZPG flow in the near-wall region is reduced (Figure 3.25). This is the first evidence in the thesis to demonstrate that the APG causes large-scale features to increase. Marusic et al. (2010a) showed that the large-scale features in the logarithmic region in high Reynolds number ZPG TBL flows become increasingly important in terms of sustaining and producing turbulence, as compared to the near-wall cycle. In this section, turbulence production is analysed to demonstrate the influence of the large-scale features (now known as a consequent of increasing APG) on turbulence production. This section is therefore important to address the aim of the thesis.

DeGraaff and Eaton (2000) showed a collapse of turbulence production for ZPG and mild FPG cases in the near-wall region. However Bourassa and Thomas (2009) clearly indicated that turbulence production is higher for the ZPG case (X/L=-2.5) across the boundary layer as compared with the FPG/highly accelerated flow cases. The same trend was observed in Aubertine and Eaton (2005), where turbulence production seems to increase with APG across the entire boundary layer. Bradshaw (1967a) observed that turbulence production increased especially in the outer regions, he attributed that the large eddies (inactive motion) increase in strength relative to the rest of the turbulence as APG level increases. Nagano et al. (1992) showed that turbulence production decreases with APG, just the opposite to the other APG many studies. The conflicting trends found in the literature could be due to scaling issues, as turbulence production has been normalised with a range of scalings.

There could also be Reynolds number effects, as these experiments or simulations were performed at different Reynolds numbers. The Reynolds number effect is known to alter turbulence energy production in the outer region (Marusic et al., 2010c). Therefore, to evaluate the pressure gradient effect, the Reynolds number has to be constant. The constant Reynolds number set of data with $Re_\tau \approx 3000$ for the APG, ZPG and FPG flows data is considered in turbulence production analysis.

The general equation for turbulence production is given by

$$Pr = -\overline{u_i u_j}\ \overline{S_{ij}}, \qquad \overline{S_{ij}} = \frac{1}{2}\left(\frac{\partial U_i}{\partial x_j} + \frac{\partial U_j}{\partial x_i}\right), \tag{3.42}$$

where $u_i$ are the fluctuating velocity components. Subscripts '$i$' and '$j$' denote all possible velocity components. $\overline{S_{ij}}$ is known as the rate of strain tensor and $U_i$ is the mean velocity component (Pope, 2000). Here, the mean spanwise velocity is zero, which reduces the general equation considerably so that the turbulence production, $Pr^+$ scaled with inner variables, can be written as

$$Pr^+ = -\overline{uw}^+ \frac{\partial \overline{u}^+}{\partial z^+} - \overline{u^2}^+ \frac{\partial U_1^+}{\partial x^+} + \overline{w^2}^+ \frac{\partial U_1^+}{\partial x^+}. \tag{3.43}$$

where $w$ is the fluctuating velocity in the wall-normal direction. Since all experiments performed in this study used only single hotwire sensors, the wall-normal component of velocity $w$, is missing. To proceed however, it is sufficient to accept that $\overline{w^2}^+$ is O(1) for all wall distances in the energy-containing region, i.e. $1 < z^+ < \delta^+$ (Kunkel and Marusic, 2006). It is instructive to consider the orders of magnitude of each term in equation (3.43): the first term, $-\overline{uw}^+ \partial \overline{u}^+ / \partial z^+$ is O($10^{-1}$), while $-\overline{u^2}^+ \partial U_1^+ / \partial x^+$ and $\overline{w^2}^+ \partial U_1^+ / \partial x^+$ are O($10^{-4}$), thus the second and third terms are negligible. Since $w$ was not measured, $\overline{uw}^+$ in the first term of equation (3.43) was estimated from formulations described in Perry et al. (2002). Figure 3.34($a$) shows the Reynolds shear stress, $\overline{uw}^+$ profiles for each pressure gradient. Given that this plot is only an estimation, we simply note here that the APG case has much higher $\overline{uw}^+$ magnitude, while the $\overline{uw}^+$ profile in the FPG case is only slightly lower than for ZPG. It is certainly the outer region that distinguishes the three pressure gradient cases as earlier observed in the streamwise turbulence intensity profiles. The increased Reynolds shear stress trend in the outer region is well in agreement with the increasingly adverse pressure gradient results of Bradshaw (1967a), Nagano et al. (1992) and Lee and Sung (2009) and on the other hand, it is expected that the opposite would hold i.e. a decrease in Reynolds shear stress in the outer region for an increasingly favourable pressure gradient, as in Jones et al. (2001).

The estimated turbulence production, $Pr^+(z^+)$, is shown in Figure 3.34($b$). Turbulence production is highest in the near-wall region as shown by experimental and numerical studies. For example, Robinson (1991) summarised that the thin, near-wall buffer region is the most important zone of the boundary layer in terms of the production of turbulence energy. In the near-wall region, there is almost no observable change across the three cases. In previous FPG studies, in contrast, it has been shown that a high acceleration parameter $K$ acts to reduce turbulence production in the near-wall region (Bourassa

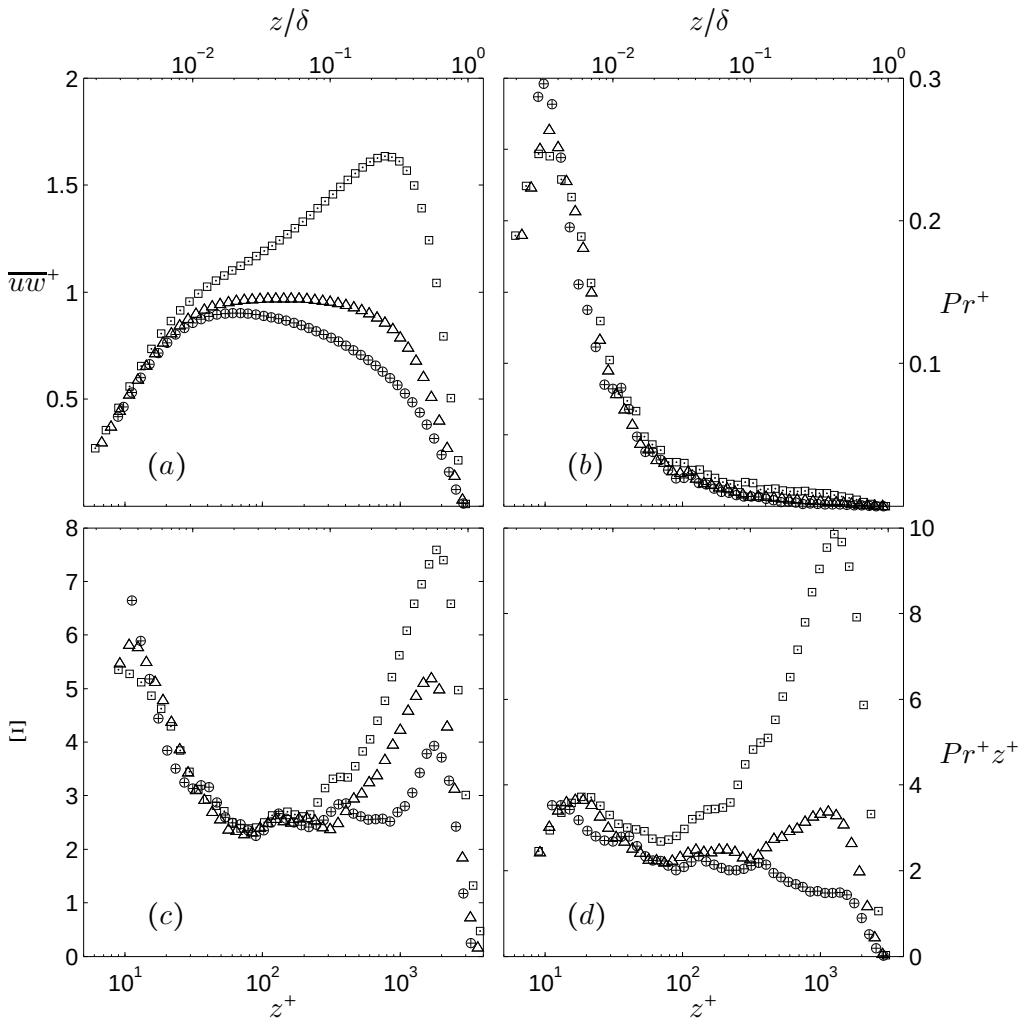


FIGURE 3.34: Profiles of $(a)$ Reynolds shear stress, $\overline{uw}^+$, $(b)$ estimated turbulence production, $Pr^+$, $(c)$ diagnostic function, $\Xi$ and $(d)$ pre-multiplied turbulence production, $Pr^+z^+$ at $Re_\tau \approx 3000$. Symbols: (⊡) APG (△) ZPG and (⟁) FPG.

and Thomas, 2009, Fernholz and Warnack, 1998). Similarly, Skote et al. (1998) also found that $Pr^+$ increases in APG cases (when compared with a ZPG case). Near the wall, Fernholz and Warnack (1998) stressed that 'there is a strong absolute increase of production term in the near-wall region during acceleration'. However, DeGraaff and Eaton (2000) found that $Pr^+$ collapses across all acceleration parameters except for the lowest Reynolds number data (attributed to a low Reynolds number effect). It is possible that the 'changes' in $Pr^+$ in the near-wall region documented in many of the previous studies are due to the Reynolds number effects, as many of them were performed at relatively low Reynolds numbers. Another possible reason why no difference between

pressure gradients was observed in the near-wall region is that the pressure gradients in the current study are mild, i.e. $\partial U_1^+/\partial x^+ < \mathrm{O}(10^{-4})$. For comparison, $\partial U_1^+/\partial x^+$ in Nagano et al. (1998) for the strong APG cases is five times bigger than in our APG case and $\partial U_1^+/\partial x^+$ in Bourassa and Thomas (2009) at position $x/L = 0.25$ (strong FPG case) is one order of magnitude larger than the current FPG case.

Considering the outer region in the FPG case, Fernholz and Warnack (1998) and Bourassa and Thomas (2009) have shown that a high acceleration parameter, $K$ acts to reduce turbulence production. In the outer region of the APG case, there is an increase in turbulence production with pressure gradient strength (Aubertine and Eaton, 2005, Nagano et al., 1992, Skote et al., 1998, Skåre and Krogstad, 1994). It is noted that Nagano et al. (1992) and Skåre and Krogstad (1994) have used outer scaling when presenting production statistics, however a rise (with pressure gradient) in the outer region in those studies is still observed if inner scaling is used. In the current data, only a slightly different shape is observed if $\delta$ is used as the length scale, thus for the rest of this section, the discussion is based on inner-scaled quantities. Figure 3.35 shows turbulence production scaled with $\delta$ (and $U_\tau$).

Marusic et al. (2010a) have shown that the $Pr^+$ representation of Figure 3.34($b$) visually underestimates the importance of the contribution in the log region when using semi-logarithmic axes. Instead, Marusic et. al. propose that one should plot $Pr^+z^+$ on these axes since the total production can be written as

$$Pr^+_{tot} = \int_0^{\delta^+} Pr^+ \, dz^+ = \int_0^{\delta^+} Pr^+ z^+ \, d(\log z^+). \tag{3.44}$$

Therefore, on a plot of $Pr^+z^+$ *versus* $\log z^+$, equal areas represent equal contributionc to the total production. In ZPG or in mild pressure gradient cases where the second and third terms in equation (3.43) can be neglected, the contribution to the bulk production can be written as

$$Pr^+z^+ = -\overline{uw}^+ \frac{\partial U^+}{\partial z^+} z^+ = -\overline{uw}^+ \Xi. \tag{3.45}$$

It is now seen that the pre-multiplied form of the production is simply the Reynolds shear stress, $-\overline{uw}^+$ multiplied by the diagnostic function, $\Xi = z^+\partial U^+/\partial z^+$. The diagnostic

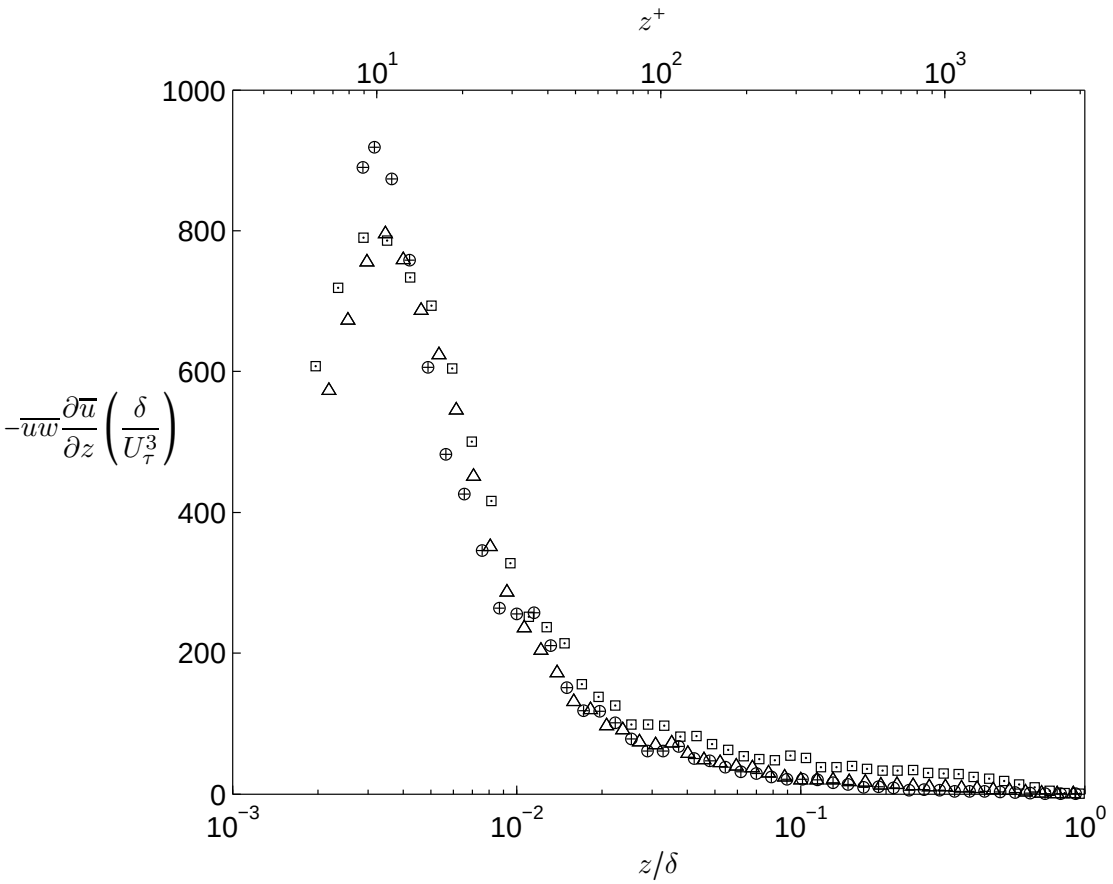


FIGURE 3.35: Turbulence production, $-\overline{uw}\ \partial\overline{u}/\partial z(\delta/U_\tau^3)$ at constant $Re_\tau \approx 3000$ for AZF PGs. Symbols: (⊡) APG (△) ZPG and (⊕) FPG.

function profiles for all pressure gradient cases are shown in Figure 3.34($c$) and the pre-multiplied turbulence production $Pr^+z^+$ profiles are shown in Figure 3.34($d$). It can be observed from the velocity profiles in Figure 3.9($a$) that the inflection in the wake of the velocity profile causes a peak in $\Xi$ in the outer region. This peak, combined with the peak in $\overline{uw}^+$, gives a large contribution to $Pr^+z^+$ in the outer region; the APG case, therefore, exhibits the largest $Pr^+z^+$, followed by the ZPG and FPG cases.

In the near-wall region, $Pr^+z^+$ is observed to be almost invariant with pressure gradient. The reason for this invariance can now be explained. $\Xi$ will change only weakly with pressure gradient near the wall (negligible change for weak pressure gradients such as these), so long as Prandtl's law of the wall holds. The Reynolds shear stress near the wall also does not change much compared with the outer region for these pressure gradient strengths. To understand this, consider the two main contributors to the near-wall

motions; small-scales from the near-wall cycle and the 'foot-print' of the large-scales which acts to modulate the small-scales. Now, the large-scale structures themselves do not contribute directly to $\overline{uw}^+$ near the wall in contrast to $\overline{u^2}^+$ (they are 'inactive' is this sense). It will be shown in the next chapter that there is considerably more energy in the large-scales in the APG flow, however, there is no evidence of changes to the small-scales near the wall. As such, the small-scales may experience more or less modulation with pressure gradient (due to energy difference in the large-scales), but the mean $\overline{uw}^+$ will be insensitive to the pressure gradient.

The results from this analysis reveal that the APG does not cause significant change towards the turbulence production in the near-wall region. The statistical analyses indicate that it is again the outer region that contains the distinguishing features for the three pressure gradient cases either in the turbulence production plot or in the pre-multiplied turbulence production plot (Figures 3.34($b$) or ($d$)). The stronger influence of the APG on turbulence production in the outer region as compared with the near-wall region is in agreement with such an effect in the mean velocity and turbulence intensity profiles seen in Figures 3.9, and in the skewness and flatness profiles in 3.23 (even though quite significant change is observed in the near-wall region of the skewness). This phenomenon can be related to the fact that the large-scale features increase in the outer region[5]. This relationship is however not an explicit one, as the large-scale features are not identified in this section. The flow structures can be identified using the energy spectra analysis. Chapter 4 attempts to provide some insights into the structures that contribute to the change in spectral statistics with different pressure gradients as observed above.

[5]large-scale features are associated with the outer region (Adrian et al., 2000, Hutchins and Marusic, 2007a)

# Chapter 4

# Energy distribution

This chapter analyses the energy spectra of TBL flows exposed to pressure gradients. The spectra indicate the energy associated with different length-scales, which can be used to infer characteristics of the structures of the flow. This chapter also analyses the effect of hotwire sensor length on the spectra. Finally, a comparison of energy distribution of APG, ZPG and FPG flows are shown to demonstrate the effect of pressure gradients at the same Reynolds number and sensor length parameter as in Monty et al. (2009)'s ZPG TBL, channel and pipe flows comparison. Therefore, this chapter is important to address the aims of the thesis i.e. to identify pressure gradient effect on the flow structures.

Via a two-sensor correlation study, Skåre and Krogstad (1994) showed that the APG shortens the large-scale structures in the outer region. In contrast, in FPG flows, the structure gets flattened and longer with stronger FPG (Bourassa and Thomas, 2009). The behaviour of the turbulence characteristics in terms of energy distribution when exposed to different pressure gradients in the outer region is not only relatively well documented, but the trends of such behaviour are found to be similar across different studies.

However, there is still conflicting information about the effect of pressure gradients in the near-wall region. Lee and Sung (2009) showed that the streak spacing quadruples to $\lambda_y^+ = 400$ in mild pressure gradient. This is quite a significant change, as streak spacing is known to be nominally $\lambda_y^+ \approx 100$ in ZPG (Kline et al., 1967) and slightly longer in FPG, $\lambda_y^+ > 100$ (Bourassa and Thomas, 2009). Prior to Lee and Sung (2009)'s study, the streak spacing was also found to be longer in the APG, e.g. $\lambda_y^+ \approx 130$ in Skote and

Henningson (2002). The effect of pressure gradient on streak spacing will be discussed in detail in Chapter 5, however the information above highlights the disparity in the literature. These streaks interact with features in the outer portion of the flow, and it is felt that this process plays a dominant role in turbulence production (Kline et al., 1967). Therefore, any remarkable change in streak spacing indicates major structural change in the near-wall region and it is the intention here to evaluate such change in an energy spectral density study.

This chapter consists of two relevant main topics: the energy spectra and scale decomposition. To limit the extent of the discussion without missing any important issue, only the comparison of adverse, zero and favourable pressure gradients at constant Reynolds number ($Re_\tau \approx 3000$) and at an increasing pressure gradient, constant Reynolds number ($Re_\tau \approx 1900$), are used. This chapter also attempts to evaluate the relationship between the rise in the mean velocity and turbulence intensity profiles in the outer region with the increased large-scale features. A scale decomposition analysis is also used to demonstrate the increased large-scale features. The extent of the small-scale attenuation due to large $l^+$ in pressure gradient flows is also analysed.

## 4.1 Energy spectra

A useful way to study and compare the energy content is to present the energy distribution in the form of a pre-multiplied energy spectra map for the streamwise velocity fluctuation, as published by del Álamo and Jiménez (2003) and Hutchins and Marusic (2007a). The map displays contours of the pre-multiplied Power Spectral Density ($k_x\phi_{uu}/U_\tau^2$) plotted against wall-distance $z^+$ and non-dimensional wavelength $\lambda_x^+$. Here $k_x = 2\pi f/U_c$ is the wave-number, $f$ is the frequency and $U_c$ is the convection velocity, taken to be the local mean velocity (invoking Taylor's frozen turbulence hypothesis). In many cases, when the Reynolds number ($Re_\tau$) is constant, another axis with outer scaling is shown ($\lambda_x/\delta$ and $z/\delta$). These representations are simply a reflected mirror image of conventional $k_x\phi_{uu}/{U_\tau}^2$ versus $\log(k_x\delta)$ (in comparison with $k_x\phi_{uu}/{U_\tau}^2$ versus $\lambda_x/\delta$ plot), and the equal area under the curve represents equal contribution to energy (refer to Hutchins and Marusic, 2007b, Nickels et al., 2005).

In ZPG flow, there is a highly energetic peak in the near-wall region occurring at $z^+ \approx 15$ and $\lambda_x^+ \approx 1000$, called the 'inner peak'. The inner peak is due to the inner wall cycle of streaks and quasi-streamwise vortices (Kline et al., 1967). The energy shifts to a larger

wavelength, growing with the distance from the wall. Hutchins and Marusic (2007b) showed that there is a second peak in the boundary layer spectra map at $z^+ \approx 0.06\delta$, corresponding to superstructures of wavelength $\lambda_x/\delta \approx 6$. Mathis et al. (2009) later refined the location of this peak to be Reynolds number dependent, $z^+ \approx (15Re_\tau)^{1/2}$.

The current data were carefully acquired with the non-dimensionalised sensor length remaining constant at $l^+ \approx 30$, to account for the attenuation in turbulence intensities due to spatial resolution uncertainties in the near-wall region. The Reynolds number was also kept constant to isolate any potential Reynolds number effects.

Figures 4.1($a$) to ($c$) show such maps for all three flows; ($a$) for APG, ($b$) for ZPG and ($c$) FPG cases. The overall shape of the three maps remain similar, however, there are substantial differences appearing in the outer region. At first glance, for all the maps, a similar highly energetic peak can be observed near the wall at $z^+ \approx 15$, centred around $\lambda_x^+ \approx 1000$ (marked by the symbol '×'). This is the 'inner peak', the well-known near-wall cycle energetic signature described earlier.

In these figures, the contours denote iso-pre-multiplied energy, $k_x\phi_{uu}/U_\tau^2$. Contour levels are from 0.16 to 1.6 in steps of 0.16. Some contour lines are highlighted with their magnitudes indicated; these lines are intercepted with '+' signs. The white dash-dotted lines indicate $\lambda_x/\delta = 1$. The 'outer peak' for the ZPG case reported by Hutchins and Marusic (2007b) and Mathis et al. (2009) is denoted by the symbol '▲', located at $z^+ \approx (15Re_\tau)^{1/2}$ at wavelength $\lambda_x/6 \approx \delta$. It can be seen in Figure 4.1($b$) that this peak occurs at a slightly lower wall-normal distance and a shorter wavelength. This is indicated by the location of maximum energy in this region i.e. contour line $k_x\phi_{uu}/U_\tau^2 = 1.12$. The outer peak for the APG case is not clearly seen from the contour map, however an outer hump can clearly be observed (because of the rather wider region in which these features become energetic). It will be shown later that the peak in the APG case occurs at $z/\delta \approx 0.3$ at wavelength $\lambda_x/\delta \approx 3$, this is denoted by the symbol '■'. The existence of this peak is observed to be weak in FPG. This suggests that one of the effects of the adverse pressure gradient is to significantly strengthen the large-scale motions.

It can be observed that in the ZPG case, the contour line that corresponds to $k_x\phi_{uu}/U_\tau^2 = 1.6$ overlaps the $\lambda_x/\delta = 1$ line, while in the FPG case, the same energy is shifted away from this line (towards smaller wavelengths). Thus, there is evidence of more large-scale contribution in the near-wall towards turbulence intensities for the APG case. Nonetheless, the location of the near-wall peak is approximately the same for other cases. For the APG case, in Figure 4.1($a$), the near-wall peak in the $k_x\phi_{uu}/U_\tau^2$ may

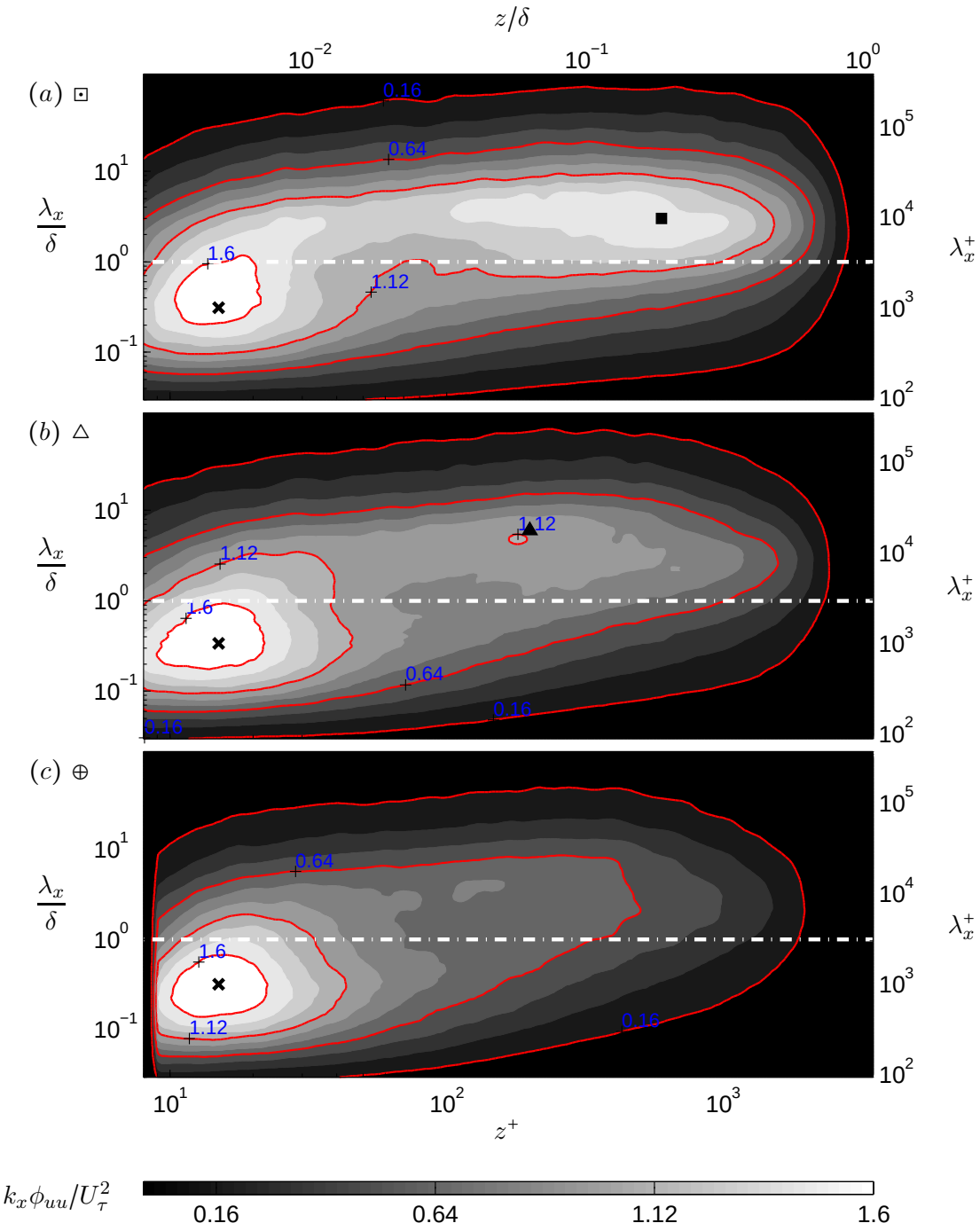


FIGURE 4.1: Pre-multiplied energy spectra of streamwise velocity fluctuation $k_x\phi_{uu}/U_\tau^2$ at constant $Re_\tau \approx 3000$ and $l^+ \approx 30$ for different pressure gradients. Contour levels are from 0.16 to 1.6 in steps of 0.16. The symbol '×' denotes the location of ($z^+$ = 15, $\lambda_x^+$ = 1000), '▲' denotes the location of $z^+ = (15Re_\tau)^{1/2}$, $\lambda_x/\delta$ = 6 and '■' denotes the location of $z/\delta$ = 0.2, $\lambda_x/\delta$ = 3.

occur at wavelength longer than $\lambda_x^+ \approx 1000$. This is one of the foci of the thesis, to be revisited in Section 4.3.

It is known that as the pressure gradient parameter $\beta$ gets larger, the boundary layer is getting close to separation from the wall. Near separation, the coefficient of friction, $C_f$, value is very small, and at incipient separation, before reversed flow is encountered, $C_f$ is zero. Therefore as $\beta$ increases to very large values, there is less energy in the near-wall region. In a mild pressure gradient flow such as in this experiment, friction velocity $U_\tau$ decreases with increasing APG (refer to Figure 3.1), since the spectral energy density results are scaled with $U_\tau$ (to compare the small– and the large-scale features), the larger-scale features in the APG case are observed to have increased relative to the ZPG case. Therefore, it shall be noted that when a reference is made to the strengthened or energised large-scale motions due to APG, it means the large-scale energy increases relative to the small-scale energy. This description is used throughout the thesis.

Figures 4.2($a$) - 4.2($c$) show a repeat of Figures 4.1($a$) - 4.1($c$), with only contours. These contours are finer than in Figures 4.1($a$) - 4.1($c$) i.e. the contour levels are 0.12 to 1.8 in steps of 0.12. The darkened contour lines for every three steps are shown for better comparison of these figures. The darkened contour line $k_x\phi_{uu}/U_\tau^2 = 1.44$ in the near-wall region for the APG flow extends further beyond $\lambda_x/\delta = 1$ when compared with the ZPG and FPG cases. As shown in Figures 4.1($a$) - 4.1($c$), this effect is due to the increased larger-scale features in the near-wall region.

To observe the differences caused by pressure gradient, it is useful to subtract the extra energy due to APG as compared with the ZPG flow. In contrast, the difference between ZPG and FPG can also be shown by subtracting the energy of the FPG flow from the energy in the ZPG flow. The general equation for this calculation is

$$\frac{\psi_{uu}|_{PG}}{U_\tau^2} = \frac{k_x[(\phi_{uu})|_{PG} - (\phi_{uu})|_{ZPG}]}{U_\tau^2}. \tag{4.1}$$

The energy difference between the APG and ZPG flows $\psi_{uu}|_{APG}/U_\tau^2$ is shown in Figure 4.2($d$) and $\psi_{uu}|_{FPG}/U_\tau^2$ is shown in Figure 4.2($e$). It can be seen that a significant amount of energy is added in the outer region for the APG flow and in contrast, energy is reduced for the FPG flow in this region. Interestingly, the peak energy difference occurs at approximately the same location $z/\delta \approx 0.2$ - 0.3, and the same wavelength $\lambda_x/\delta \approx 2$ - 3, for both APG and FPG cases. Even though the additional large-scale

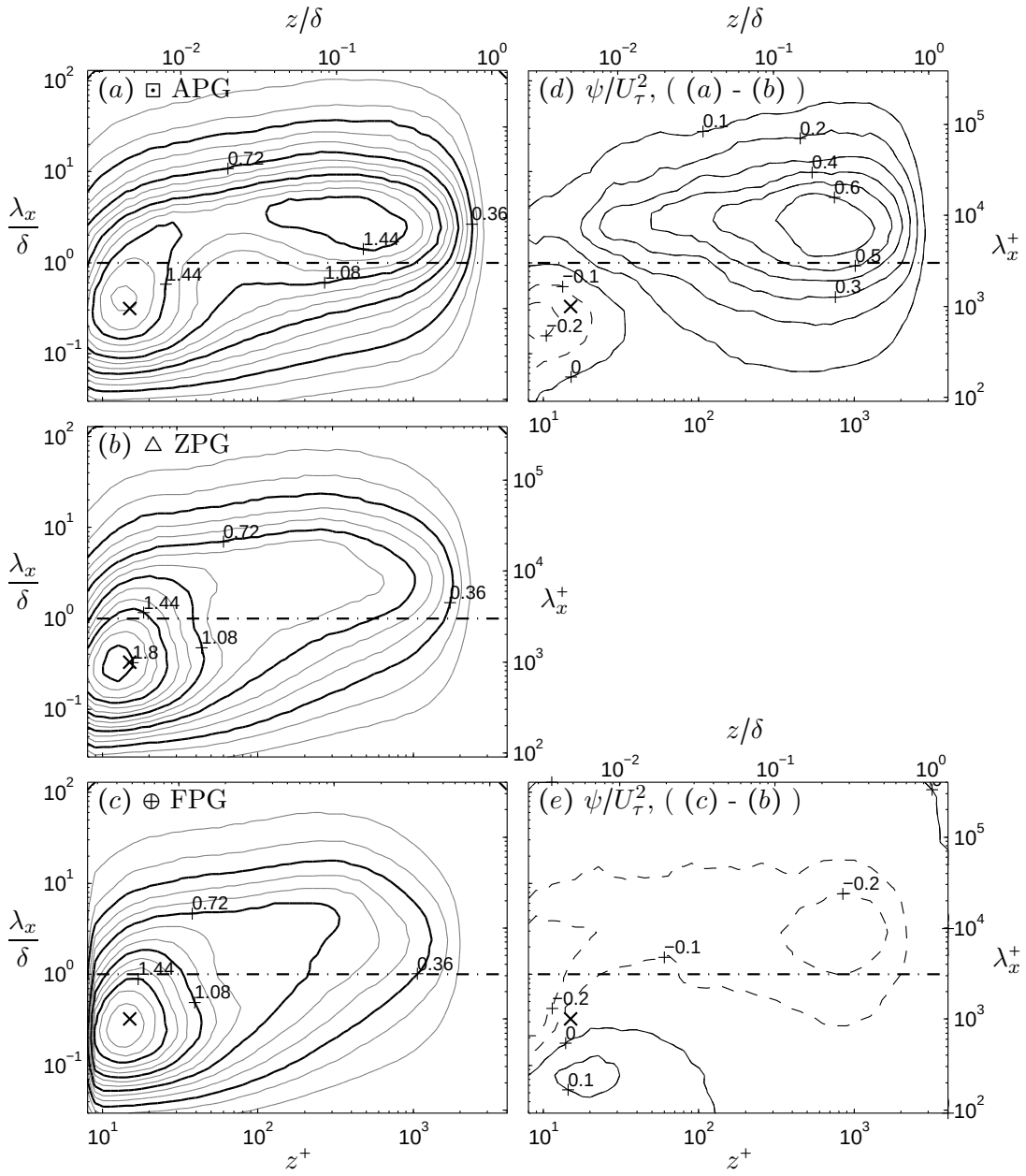


FIGURE 4.2: Plots $(a)$ to $(c)$: pre-multiplied energy spectra of streamwise velocity fluctuation $k_x\phi_{uu}/U_\tau^2$ at constant $Re_\tau \approx 3000$ for the APG, ZPG and FPG flow. Contour levels are from 0.12 to 1.8 in steps of 0.12. Contour lines are darkened and contour values are shown every three steps (0.36, 0.72, 1.08, 1.44 and 1.8). Plots $(d)$ and $(e)$: missing energy, $\psi_{uu}/U_\tau^2$. Contour levels are from -0.2 to 0.6 in steps of 0.1 (dashed contours indicate negative values). All contour values are indicated. The symbol '×' denotes the location of $z^+ = 15$, $\lambda_x^+ = 1000$, dashed-dotted lines denote $\lambda_x/\delta = 1$.

energy is centred in the outer region, there is also significant additional energy in the near-wall region for the APG case.

From the overall picture of the energy content of the three flows given in Figure 4.1, it is evident that the most significant differences appear in the outer part of the boundary layers, although there are some discrepancies remaining close to the wall (clearly evident in the total streamwise energy plot of Figure 3.9($b$)). To further analyse the effect of pressure gradients on energy distribution, it is helpful to compare energy spectra for each pressure gradient case at selected wall-normal locations. The wall-normal locations chosen are ($a$) $z^+ \approx 15$, ($b$) $z^+ \approx 100$, ($c$) $z^+ \approx (15Re_\tau)^{1/2}$, and ($d$) $z/\delta \approx 0.3$.

The pre-multiplied spectra scaled with friction velocity, $k_x\phi_{uu}/U_\tau^2$ at each wall-normal location are shown in Figures 4.3($a$) to ($d$). In the near-wall region, (Figure 4.3($a$)), all flows show a similar energy distribution with the inner peak clearly visible at $\lambda_x^+ \approx 1000$. It can be seen that the intensity of the inner peak is of the same magnitude (within experimental uncertainties), suggesting that the small-scale features remain mostly unaffected by the pressure gradient. However, there is a rise of the energy in the larger wavelengths ($\lambda_x > \delta$) as the pressure gradient turns sign from FPG to APG. This is an evidence of the strengthening of the 'footprint' of the large-scales as described by Hutchins and Marusic (2007a) as the adverse pressure gradient increases.

At $z^+ \approx 100$ shown in Figure 4.3($b$), the large-scale structures clearly dominate the flow in the APG case as compared with the ZPG case. The most energetic structures here are at $\lambda_x/\delta \approx 6$. The large-scale structures are energised in APG however the small-scale motions are only weakly energised with the changing pressure gradient. For the FPG case, it seems that the contributions from the small- and large scale features are about balanced resulting in a almost flat $k_x\phi_{uu}/U_\tau^2$ for $0.5 \lesssim \lambda_x \lesssim 6$.

In the geometric centre of the log region, $z^+ \approx (15Re_\tau)^{1/2}$ as shown in Figure 4.3($c$), the large-scale structures have a clear peak wavelength of $\lambda_x/\delta \approx 6$, the same as found previously (Hutchins and Marusic, 2007a, Mathis et al., 2009). The $\lambda_x/\delta = 6$ line is shown by the solid vertical line in this figure. However, in the APG case, the most energetic structures seem to occur at $\lambda_x/\delta \approx 3$, (half as long as in the ZPG case), shown by the vertical dashed-dotted line. The large-scale motions' signature is not clearly seen in the FPG case. Shorter structures observed in the outer region in the APG case is consistent with finding by Skåre and Krogstad (1994). This figure suggests that the higher turbulence intensities in the outer region due to increasing pressure gradient seen in Figure 3.9($b$), come from the enhanced energy of the large-scale features.

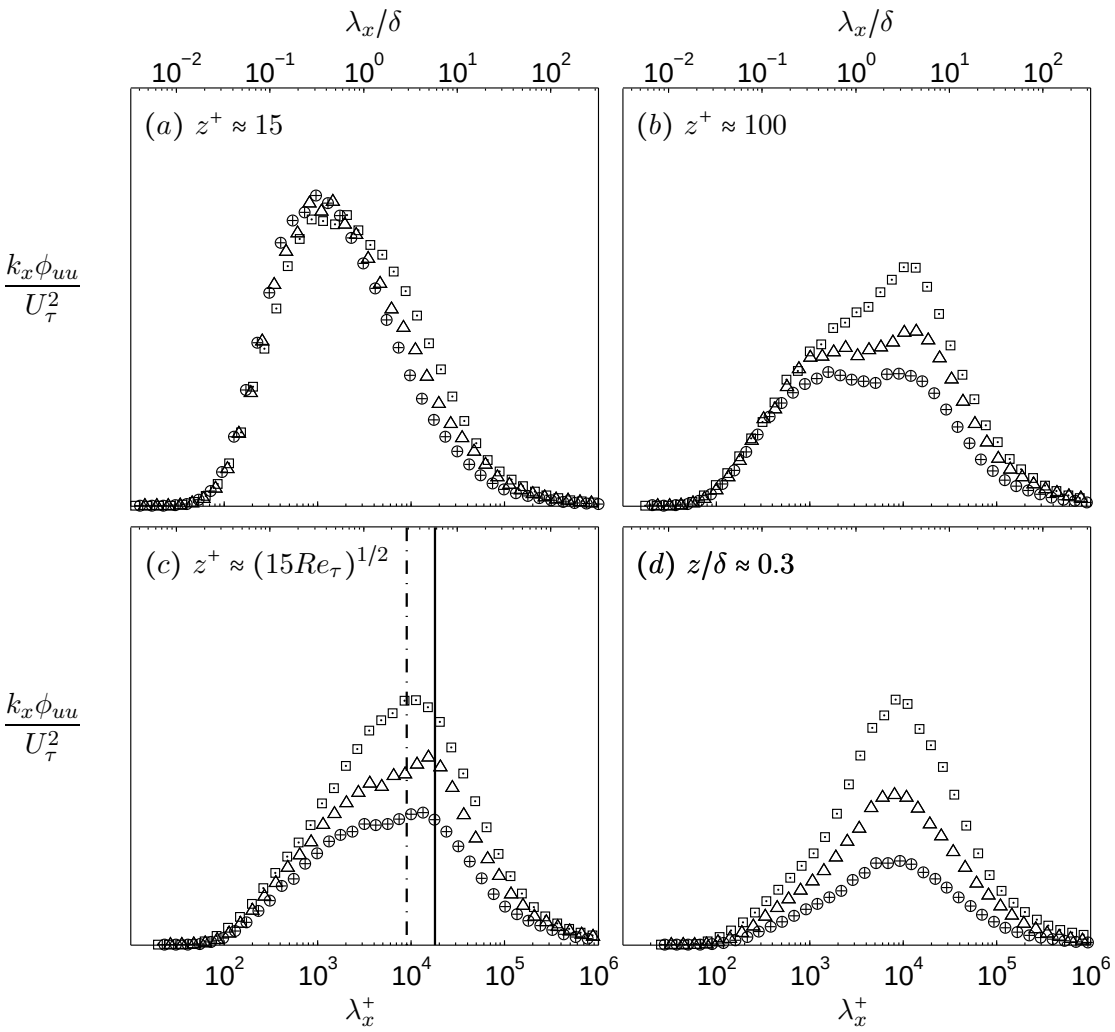


FIGURE 4.3: Pre-multiplied energy spectra, $k_x\phi_{uu}/U_\tau^2$ at constant $Re_\tau \approx 3000$ and $l^+ \approx 30$ at four selected wall-normal locations, $(a)$ $z^+ \approx 15$, $(b)$ $z^+ \approx 100$, $(c)$ $z^+ \approx (15Re_\tau)^{1/2}$, and $(d)$ $z/\delta \approx 0.3$. (⊡) APG (△) ZPG and (⊕) FPG. The solid line indicates $\lambda_x/\delta = 6$ and dashed dotted line indicates $\lambda_x/\delta = 3$.

There is definitely more energy in the outer region in the APG case than in the ZPG and FPG cases. Figure 4.3$(d)$, shows that the energy for the APG at $z/\delta \approx 0.3$ is strongly intensified; the magnitude of the energy in the APG case is double that of the FPG case across all wavelengths. The most energetic structures in this region centre at $\lambda_x/\delta \approx 3$, invariant with the pressure gradient. It has been shown that the dominant mode in the outer region in channel and pipe flows is similar (Balakumar and Adrian, 2007, Monty et al., 2011), and this mode is termed the 'large-scale motion' (LSM). In APG, the LSM is strongly energetic, the 'outer peak' with the wavelength signature $\lambda_x/\delta \approx 6$ may still

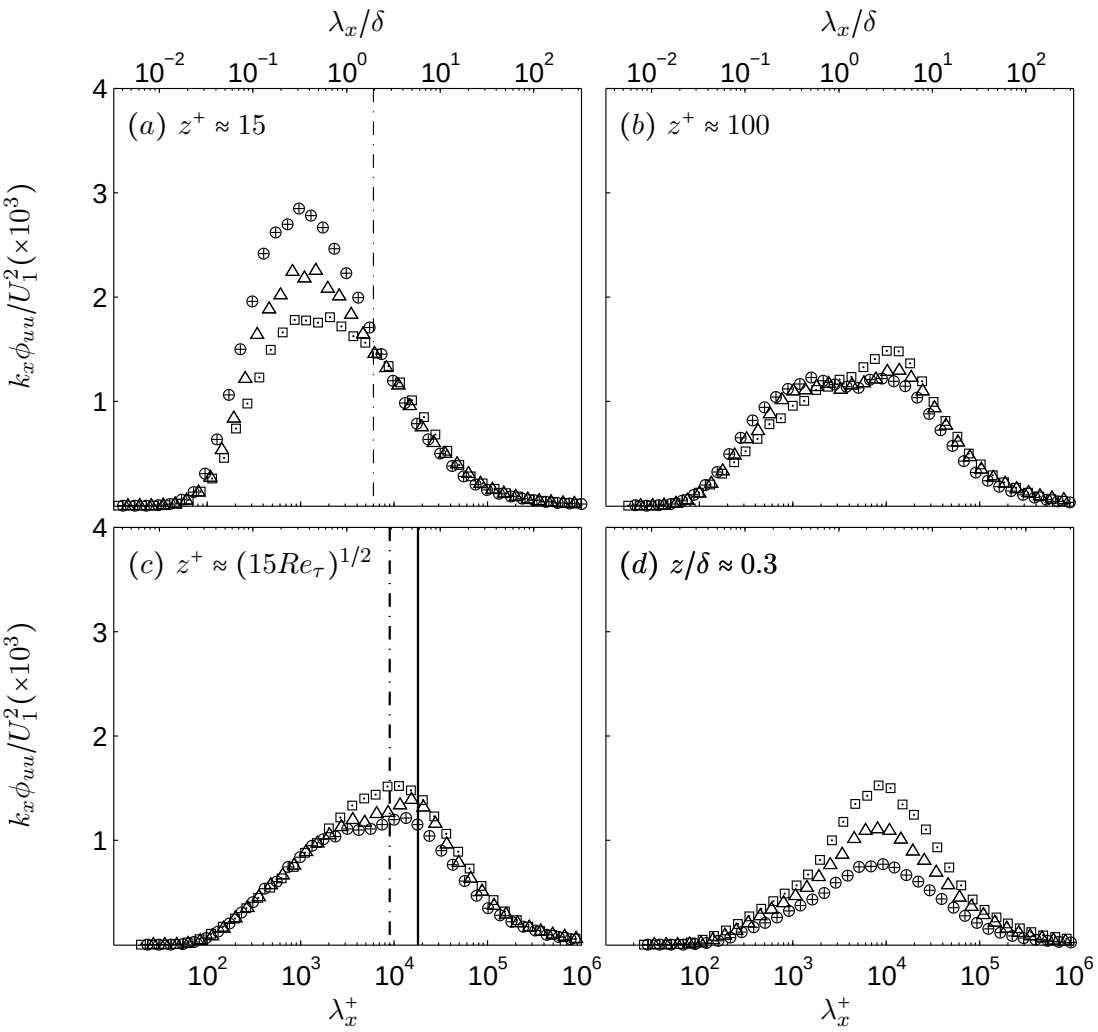


FIGURE 4.4: Pre-multiplied energy spectra of streamwise velocity fluctuation scaled with free stream velocity $k_x\phi_{uu}/U_1^2$ at constant $Re_\tau \approx 3000$ and $l^+ \approx 30$ at selected wall-normal location. (⊡) APG (△) ZPG and (⊕) FPG. The dashed dotted line indicates $\lambda_x/\delta = 2$

exist in the log region, however being 'swamped' by the LSM. There seems to be two energetic modes overlapping in these regions, the LSM (strong both in log and outer regions) and the $\lambda_x/\delta \approx 6$ structures (only strong in the log region).

Since it is not clear how turbulent fluctuations scale in pressure gradients, a second scaling is tried here. The energy distribution is now scaled with the free stream velocity, $U_1$, as shown in Figures 4.4($a$) to ($d$). In the near-wall region, $z^+ \approx 15$, energy is closer across the three flows for large wavelengths; this is shown by the dashed-dotted line $\lambda_x/\delta = 2$ in Figure 4.4($a$). Note that a different convection velocity is used to scale

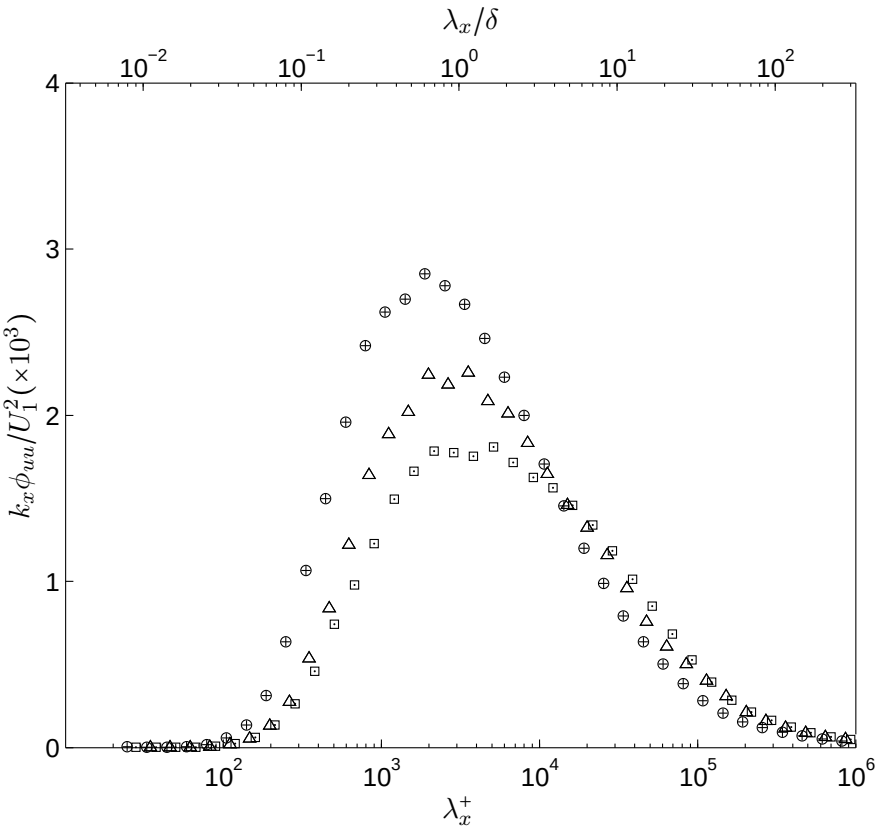


FIGURE 4.5: Pre-multiplied energy spectra of streamwise velocity fluctuation $k_x\phi_{uu}/U_1^2$ at constant $Re_\tau \approx 3000$ and $l^+ \approx 30$ at $z^+ \approx 15$ using convection velocity of $U_c = 0.82U_1$. (⊡) APG (△) ZPG and (⊕) FPG.

energy in the near-wall region. When convection velocity is taken as $U_c = 0.82U_1$ (Dennis and Nickels, 2008) shown in Figure 4.5, again a similar effect as in Figure 4.4($a$) can be observed for large wavelengths. Therefore the trend observed for the large-scale in Figure 4.4($a$) is not simply due to the scaling used.

At $z^+ \approx 100$, shown in Figure 4.4($b$), there is a little more energy in the larger-scales in the APG case. This is indicated by the slight increase in energy at $\lambda_x/\delta \approx 6$. As the distance increases further away in the log region, the large-scales are more energetic relative to the small-scales especially in the APG case. A milder effect can be observed in the ZPG and FPG cases as well, this is shown in Figure 4.4($c$). In the outer region, the small-scales are weaker for all three pressure gradient cases, the large-scales dominate the flow. This is shown in Figure 4.4($d$).

Both scaling with friction velocity $U_\tau$ and free stream velocity $U_1$, consistently indicate that energy increases in the outer region are due to the increased large-scale content.

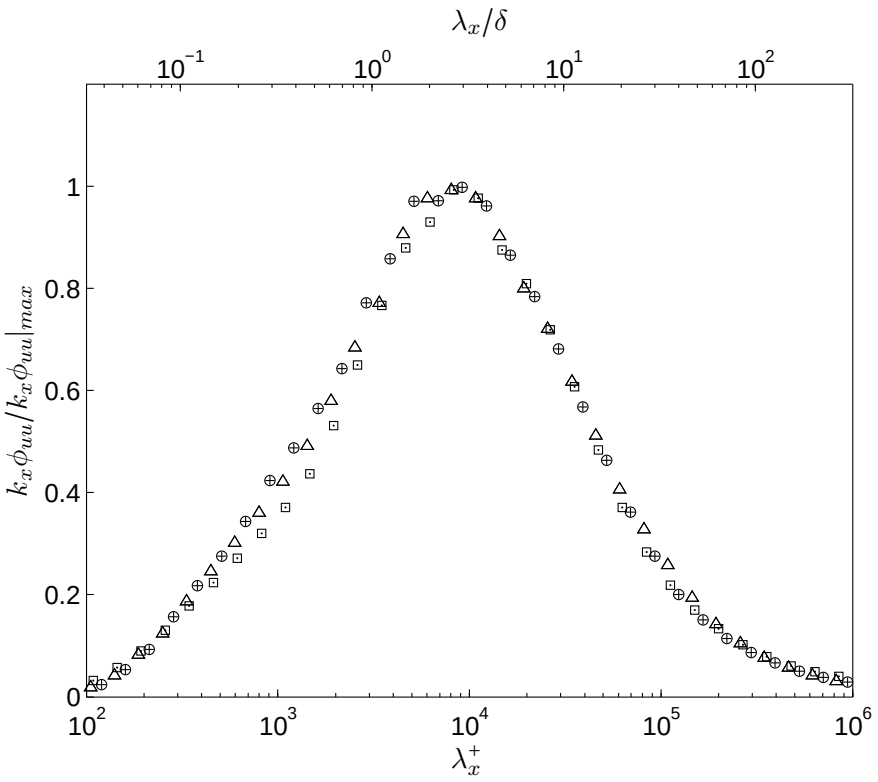


FIGURE 4.6: Pre-multiplied energy spectra of streamwise velocity fluctuation $k_x\phi_{uu}/k_x\phi_{uu}|_{max}$ at constant $Re_\tau \approx 3000$ and $l^+ \approx 30$ at $z/\delta \approx 0.3$. (⊡) APG (△) ZPG and (⊕) FPG.

This energy, centred at $\lambda_x/\delta \approx 3$, is not only prominent in the turbulent boundary layer flows, but as mentioned earlier, also in pipe and channel flows. As can be seen in Figure 4.3($d$), the peak energy in the ZPG and FPG cases is reduced compared with APG, however, distributions appear similar. To check this, it is useful to plot the energy spectra scaled with its maximum magnitude, $k_x\phi_{uu}/k_x\phi_{uu}|_{max}$. The pre-multiplied energy spectra of streamwise velocity fluctuation $k_x\phi_{uu}/k_x\phi_{uu}|_{max}$ for APG, ZPG and FPG cases is shown in Figure 4.6. This figure shows that the distribution of energy in the outer region ($z/\delta = 0.3$) is the same for all three pressure gradient cases.

The energy spectra analysis shows that the most influenced features in boundary layers subjected to different pressure gradients are the large-scales, in the outer region. Large-scale motions are energised with APG and in contrast they are attenuated in FPG. It is important to understand the contributions from the small– and large-scale features due to the introduction of pressure gradient in more detail. In fact it is possible to

perform such an analysis by adopting a separation of scales procedure. Such separation of features is discussed in the following section.

## 4.2 Scale decomposition

This section attempts to highlight the effect of pressure gradients on the small– and large-scale features via scale decomposition. The decomposition method is similar to that proposed by Hutchins and Marusic (2007b) and Mathis et al. (2009), a cut-off wavelength is defined based on an analysis of the pre-multiplied energy spectra map of the streamwise velocity component. A cut-off length-scale equal to the thickness of the boundary layer ($\lambda_{xc} = \delta$) was chosen. This cut-off length scale was used by Mathis et al. (2009) in the quantification of amplitude modulation of the small-scales of wall-turbulence in zero pressure gradient boundary layers. These lines are shown in Figures 4.1($a$) to ($c$). It can be observed in these figures that there may be an insufficient scale separation at these Reynolds numbers particularly in FPG. For example, there is significant large-scale component ($\lambda_x/\delta > 1$) that actually contributes to the inner peak. However the 'leak' here is considered too small to affect any significant outcome.

Figure 4.7 shows the decomposed turbulence intensity profiles (from Figure 3.9($b$)) for the three pressure gradient flows. It is observed that the energy from the large-scales is dominant in the outer region for all three cases. However the large-scale energy contribution for the APG case is much higher throughout the flow, particularly in the outer region (where a secondary peak in the broadband turbulence intensities is present). Although there is also increased energy in the small-scales in the outer region of the APG boundary layer, it is the large-scale energy increase that is the major contributor to the high turbulence intensities in this region. The large-scale component is also energised in the log region and down to the near-wall region in the APG case. Since the small-scale component is almost invariant with the pressure gradient, it is the difference in the large-scale content that is the greater contributor in the near-wall region as well. The insignificant change in the small-scale component in the inner region ($z^+ \lesssim 50$) suggests that the near-wall cycle remains similar despite the pressure gradient introduction. Hutchins and Marusic (2007a) reported that the increased magnitude of the broadband turbulence intensities at $z^+ \approx 15$ is due to greater influence of the large-scales or the 'foot print' in ZPG. Monty et al. (2011) proposed that foot-print is stronger with APG, as observed here. The increase of the near-wall turbulence intensity in the APG case is due to the increased influences and other activities of the large-scale structures in the

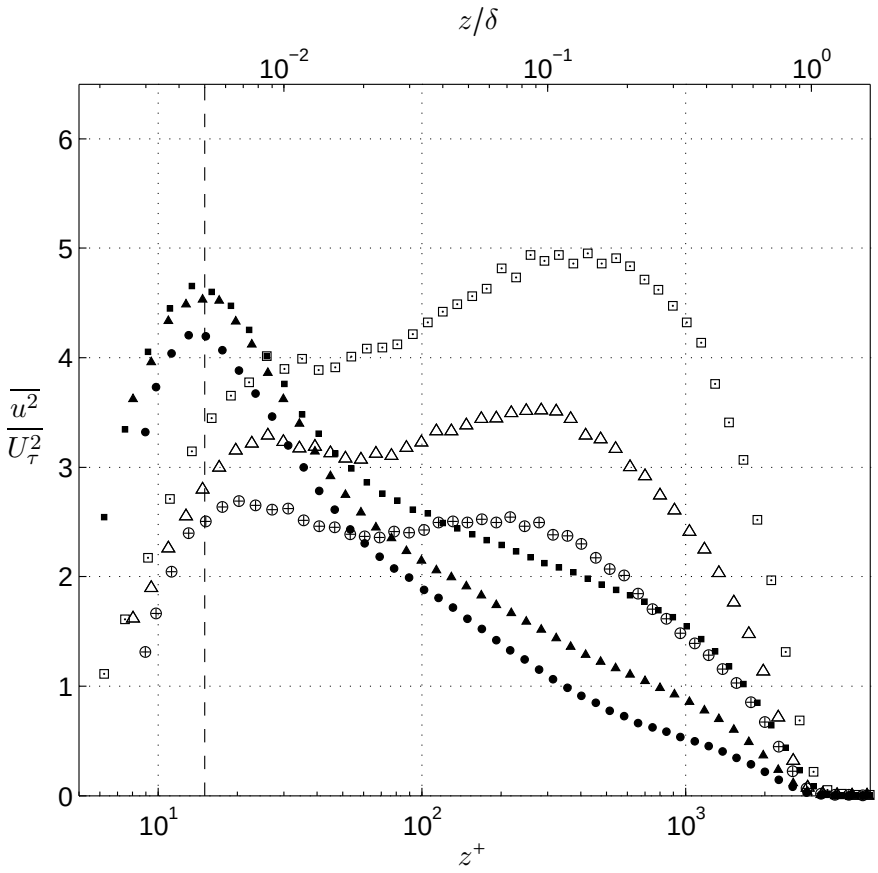


FIGURE 4.7: Decomposition of the broadband turbulence intensity profiles $\overline{u^2}/{U_\tau}^2$ into a small- and a large-scale components for constant $Re_\tau \approx 3000$ and $l^+ \approx 30$. Small-scale components ($\lambda_x/\delta < 1$) symbols: (■) APG, (▲) ZPG and (●) FPG. Large-scale components ($\lambda_x/\delta \geq 1$) symbols: (⊡) APG, (△) ZPG, (⊕) FPG. Dashed-dotted line denotes $z^+ = 15$.

near-wall region, and the converse: the reduction in the near-wall turbulence intensity for the FPG case seen in Figure 3.9($b$) is associated with reduction of such activities of the large-scale structures.

The near-wall turbulence intensity peak is not only related to the effect caused by the large-scales in the near-wall region (the effect of large-scales increases with Reynolds number), it is also directly associated with the attenuation of the small-scales due to large non-dimensionalised hotwire sensor length, $l^+$. Therefore, a closer look at $l^+$ and influences of pressure gradient on energy spectra is required.

## 4.3 The effect of sensor length

It is certainly exciting to observe the 'longer' features than the nominal value of $\lambda_x^+ \approx 1000$ detected for the inner peak in the APG case shown in Figure 4.1($a$). If this is true, there may be structural changes in this most important region of the boundary layer (Kline et al., 1967), this will be addressed in this section. Before proceeding into the details of experimental set-up and analysis of this section, it is helpful to review important features of the $l^+$ effect in ZPG boundary layers.

Ligrani and Bradshaw (1987) explained that turbulence intensities become increasingly attenuated as the hotwire sensor length $l^+$ increases. Therefore, $l^+ \approx 20 - 25$ was suggested so that turbulence intensities are sufficiently resolved in this region. Using the scale decomposition method and energy spectra analysis as described in the previous sections, Hutchins et al. (2009) elaborately explained that the large-scale contribution to turbulence intensities for the entire ZPG boundary layer collapses at a given Reynolds number, invariant with $l^+$ in ZPG. However, the small-scale contribution in the near-wall region decreases with increasing $l^+$. The argument is that as $l^+$ increases, the small-scale structures which advect past the wire, are thin enough relative to the wire length, this causes the signal triggered by such advections to be averaged with the rest of the sensor length. This has caused attenuations to the small-scale fluctuations, resulting in under-resolved turbulence intensities in the near-wall region. While the effects of $l^+$ have been studied in great length in ZPG, there has been no such study in boundary layers with pressure gradients. This has left experimenters (and even researchers in computational studies focusing on spatial resolution) to assume that recommendations from $l^+$ studies in ZPG flows are also valid for pressure gradient flows. However, cautions shall be exercised because the large-scale features in the near-wall region detected by a given $l^+$, previously invariant in ZPG, have now varied with pressure gradient (as shown in Section 3.13, Lee and Sung, 2009, Skåre and Krogstad, 1994).

Hutchins et al. (2009) established an empirical equation determining the relationship between the magnitude of the near-wall peak in the turbulence intensities as a function of $l^+$ and Reynolds number. However, in pressure gradient flows, the magnitude of the near-wall peak is also a function of the pressure gradient parameter $\beta$, shown in Monty et al. (2011). Even though no explicit form was established, the latter has conclusively shown that the near-wall turbulence intensities peak increases with $\beta$ when $l^+$ and Reynolds number remain constant. Thus, the empirical relationship proposed by Hutchins et al. (2009) fails to predict the behaviour of turbulence intensities with

the presence of a pressure gradient[1]. It has been shown in Figures 4.7($a$)-($d$) that the presence of large-scales is responsible for the rise in the turbulence intensities for the entire boundary layer profile. This phenomenon has warranted a closer look at the effect of $l^+$ and pressure gradient on turbulence intensities. To perform this analysis, comparisons of varying $l^+$ in a constant Reynolds number and constant pressure gradient are needed, as well as increasing Reynolds number experiments performed at different pressure gradients (similar to testing $l^+$ in ZPG). While it is relatively easy to perform varying $l^+$ with constant Reynolds number, the effect of varying Reynolds number could not be performed here due to laboratory limitations. The Reynolds number needs to be very large, for example $Re_\tau \approx 6000$ for any significant behaviour to be observed. This is not possible to achieve with the current wind tunnel set-up.

Figure 4.8 shows the decomposed turbulence intensity profiles for varying $l^+$ for the APG case ($\beta \approx 1.6$) at $Re_\tau \approx 3000$. Clearly, the small– and large-scale contributions to $\overline{u^2}/{U_\tau}^2$ collapse in the outer region, are invariant with $l^+$. In the near-wall region, there is a trend of a decreasing small-scale contribution with increasing $l^+$, in agreement with Hutchins et al. (2009).

To clearly observe the energy distribution due to the varying $l^+$, it is helpful to look at the spectra map of these cases. Figures 4.9($a$) - ($c$) show the spectra map at Reynolds number ($Re_\tau \approx 3000$) with varying $l^+$. Contour levels are from 0.12 to 1.8 in steps of 0.12. For every three steps, the contour is highlighted with thicker lines. The values of these thicker lines are indicated on the plots; the corresponding line is intercepted by the symbol '+'. In the outer region, the magnitudes of $k_x\phi_{uu}/U_\tau^2$ are about the same across $l^+$. Among the three cases, it can be seen in Figure 4.9($a$) that the $l^+ \approx 20$ case has the highest $k_x\phi_{uu}/U_\tau^2$'s near-wall peak magnitudes. This is indicated by the contour line $k_x\phi_{uu}/U_\tau^2 = 1.8$ in Figure 4.9($a$) (Figures ($b$) and ($c$) do not have the contour line $k_x\phi_{uu}/U_\tau^2 = 1.8$). This effect can be observed in Figure 4.8 too; moving from FPG to APG shows a larger wall-normal distance where this peak occurs. Now the relationship between pressure gradient and the location of the near-wall peak highlighted at the start of this section is established, i.e. APG causes the near-wall peak to occur at longer wavelength.

It is interesting to learn that the location of inner peak has 'changed' in the case of $l^+ \approx 40$. This is in fact different from the observations in the ZPG case, where the most energetic structures in the near-wall region remain at the same wavelength, i.e.

[1]Demonstration of how the prediction by Hutchins et al. (2009) should distinguish data from TBL exposed to pressure gradient is shown in Section 3.11.

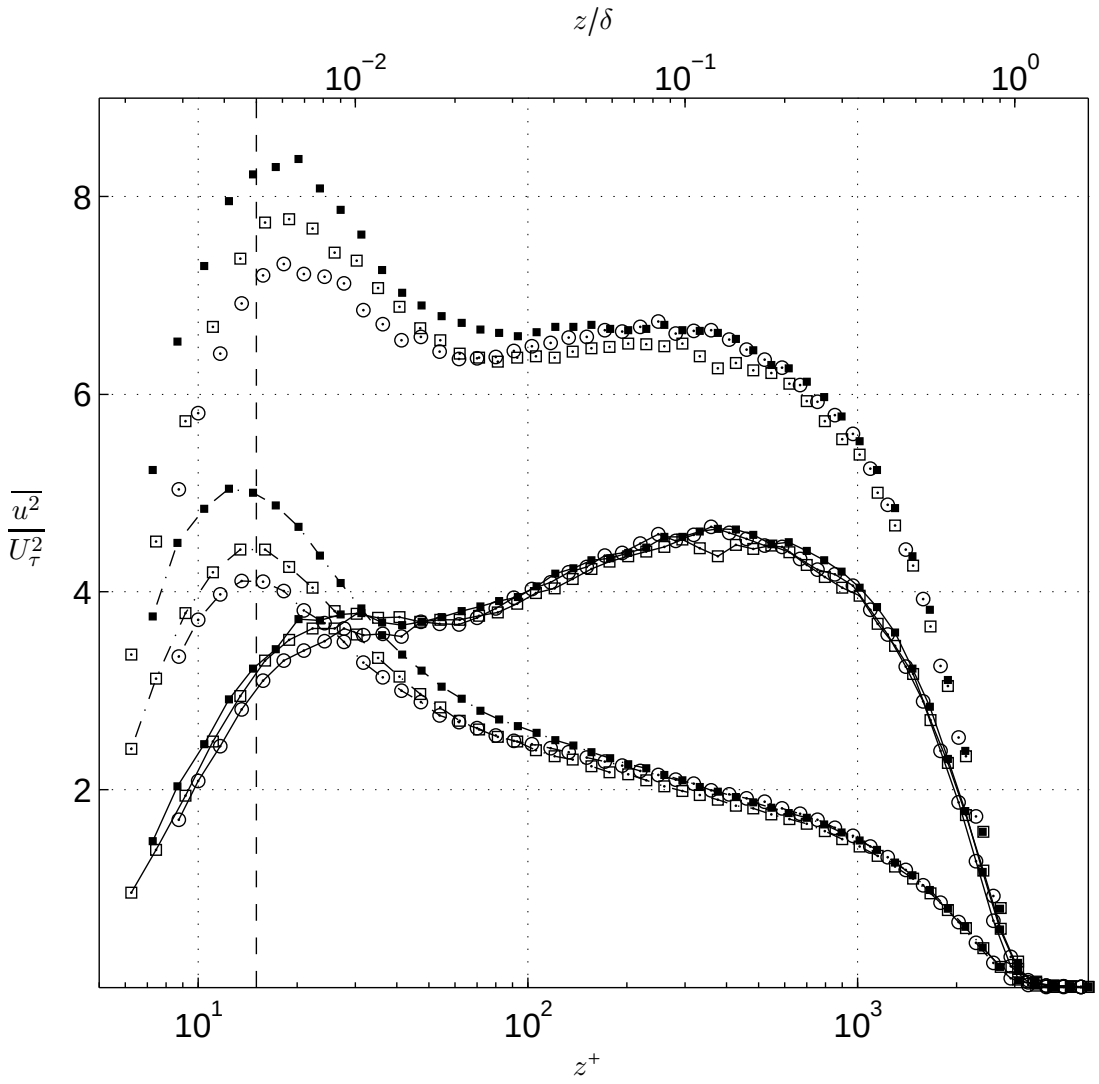


FIGURE 4.8: Decomposition of the broadband turbulent intensity profile $\overline{u^2}/{U_\tau}^2$ into a small- and a large-scale components at $Re_\tau \approx 3000$ for APG with varying $l^+$. Symbols: (▪) $l^+ \approx 20$, (⊡) $l^+ \approx 30$ and (⊙) $l^+ \approx 40$. Small-scale components ($\lambda_x/\delta < 1$) are denoted by dashed-lines and large-scale components ($\lambda_x/\delta \geq 1$) are denoted by solid lines. Dashed-dotted line denotes $z^+ = 15$.

($\lambda_x \approx 1000$) across $l^+$ (Hutchins et al., 2009). Note that in Figure 4.1($a$), the greatest contour line value is $k_x\phi_{uu}/U_\tau^2 = 1.6$, less than specified here (in Figure 4.9, the greatest contour line value is $k_x\phi_{uu}/U_\tau^2 = 1.8$). Therefore, in Figure 4.1($a$), the inner peak falls within a wider region of iso-$k_x\phi_{uu}/U_\tau^2 = 1.6$ and consequently, it seems that the near-wall peak is marginally disturbed by the pressure gradient. In Figure 4.9($a$), the symbol 'o' refers to $\lambda_x^+ = 1500$ and $z^+ = 15$, an approximate centre of $k_x\phi_{uu}/U_\tau^2 = 1.44$. Note that

this is not only observed in Figure 4.9($c$) - the same trend could also be sensed in Figure 4.9($b$). The centre of iso–$k_x\phi_{uu}/U_\tau^2 = 1.68$ (contour value not shown) occurs at a slightly longer wavelength $\lambda_x^+ > 1000$.

As pointed out by Hutchins et al. (2009), there is an attenuation of the small-scale fluctuations in the near-wall region as $l^+$ increases. In APG, this is further complicated by the significant rise of longer structures in this region. To evaluate this, the energy spectra in the longer $l^+$ cases could be subtracted from the energy spectra in the $l^+ \approx 20$ case to create energy deficit:

$$\frac{\psi_{uu}|_m}{U_\tau^2} = \frac{k_x[(\phi_{uu})|_{l^+\approx 20} - (\phi_{uu})|_{l^+=m}]}{U_\tau^2}. \tag{4.2}$$

The energy deficit for $l^+ \approx 30$ is shown in Figure 4.9($d$). There is an energy deficit from the small-scale fluctuations originating from the near-wall region. The deficit consists of structures well shorter than $\lambda_x/\delta = 1$ (albeit that a little loss of signatures for features longer than $\lambda_x/\delta = 1$ could be observed). Figure 4.9($e$) displays energy deficit for case $l^+ \approx 40$. As expected, there is a great deficit of shorter structures centred at $\lambda_x^+ \approx 1000$ in the near-wall region. This is in agreement with Hutchins et al. (2009) and Chin et al. (2011). However, unlike in the ZPG cases in these citations, the effect of large $l^+$ not only reduces the near-wall turbulence intensities, it also causes the large-scales to superficially dominate the flow. The immediate, preliminary conclusion from these observations is that the near-wall peak occurs with longer structures (as seen in Figure 4.9($c$)).

This effect is shown more clearly in Figures 4.10($a$) to ($d$). Figure 4.10($a$) shows pre-multiplied energy spectra for different $l^+$ in the near-wall region, $z^+ \approx 15$. The $\lambda_x/\delta = 1$ lines in Figures 4.9 is shown again in Figure 4.10($a$) by the dashed-dotted line. Note that the contribution of the large-scales ($\lambda_x/\delta \gtrsim 1$) collapses across $l^+$. The $\lambda_x^+ = 1000$ is shown by the solid line. It is now obvious that the peak for the case $l^+ \approx 20$ occurs at $\lambda_x^+ = 1000$, however, as $l^+$ grows, the peak seems to shift to longer length scales. Figures 4.10($b$) to ($d$) exhibit similar small– and large-scales contribution for the outer regions, similar to results in the varying $l^+$ case in Hutchins et al. (2009). Therefore, the preliminary conclusion from Figure 4.9($c$), in which the most energetic features have a length scale of $\lambda_x^+ \approx 1500$ is indeed inaccurate. The 'change' of the near-wall peak location in turbulence intensities (Figure 4.8) for large $l^+$ can now be explained; it is due to spatial resolution issues.

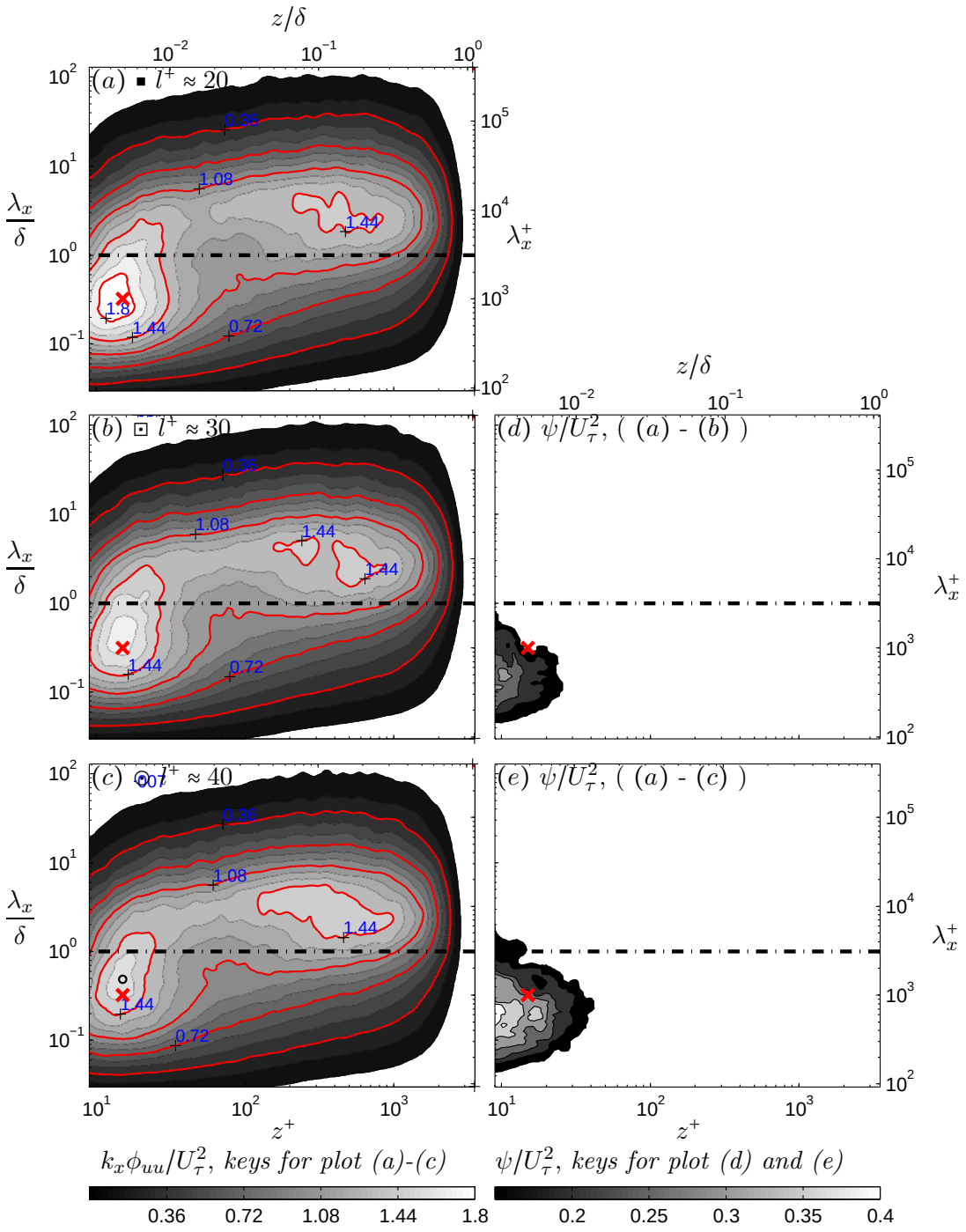


FIGURE 4.9: Plots $(a)$ -$(c)$: pre-multiplied energy spectra of streamwise velocity fluctuation $k_x\phi_{uu}/U_\tau^2$ at constant $Re_\tau$ for the APG, ($\beta \approx 1.6$) with varying $l^+$. Contour levels are from 0.12 to 1.8 in steps of 0.12. Plots $(d)$ and $(e)$: missing energy, $\psi_{uu}/U_\tau^2$. The symbol '×' denotes the location of $z^+ = 15$, $\lambda_x^+ = 1000$, dashed-dotted lines denote $\lambda_x/\delta = 1$.

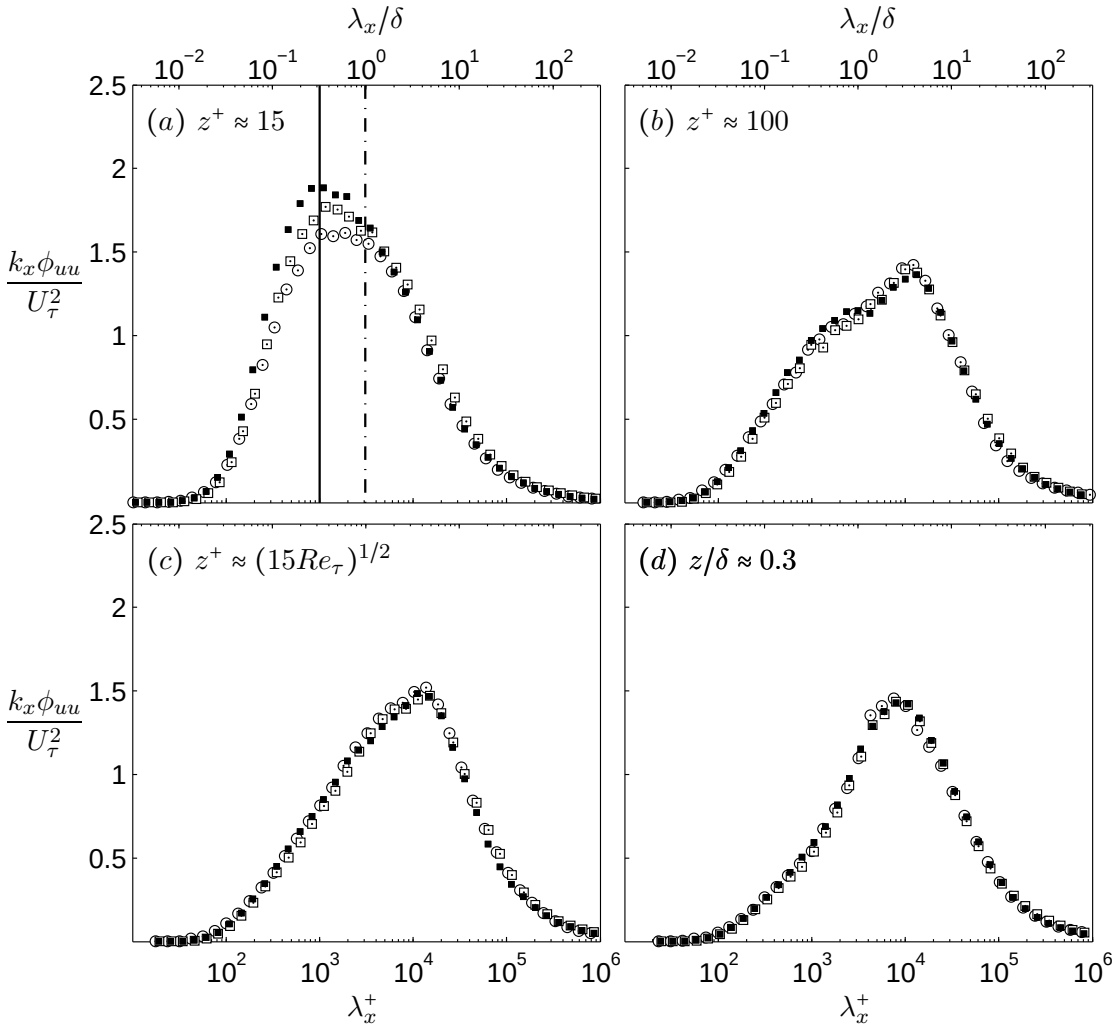


FIGURE 4.10: Pre-multiplied energy spectra, $k_x\phi_{uu}/U_\tau^2$ at constant $Re_\tau \approx 3000$ for the APG, ($\beta \approx 1.6$) with varying $l^+$ case at four selected wall-normal locations, ($a$) $z^+ \approx 15$, ($b$) $z^+ \approx 100$, ($c$) $z^+ \approx (15Re_\tau)^{1/2}$, and ($d$) $z/\delta \approx 0.3$. Symbols: (▪) $l^+ \approx 20$, (⊡) $l^+ \approx 30$ and (⊙) $l^+ \approx 40$. Solid line denotes $\lambda_x^+ = 1000$ and dashed-dotted line denotes $\lambda_x/\delta = 1$.

The same procedure of varying $l^+$ in constant Reynolds number is repeated for the FPG case. Figure 4.1($c$) (spectra map for FPG case) does not exhibit any particular deviation from the ZPG case, except that the outer peak is significantly diminished. Figure 4.11 shows the decomposition of the small– and large-scales for varying $l^+$ for the FPG case ($\beta \approx -0.4$, $K \approx 0.78 \times 10^{-7}$), at constant Reynolds number, $Re_\tau \approx 3000$ with a cut-off filter $\lambda_{xc} = 1$. As expected, this figure shows the collapses of small– and large-scale contributions in the outer regions. The collapse of the large-scale contribution in the near-wall region is remarkable. Note that the largest sensor length here is $l^+ \approx 48$ (as

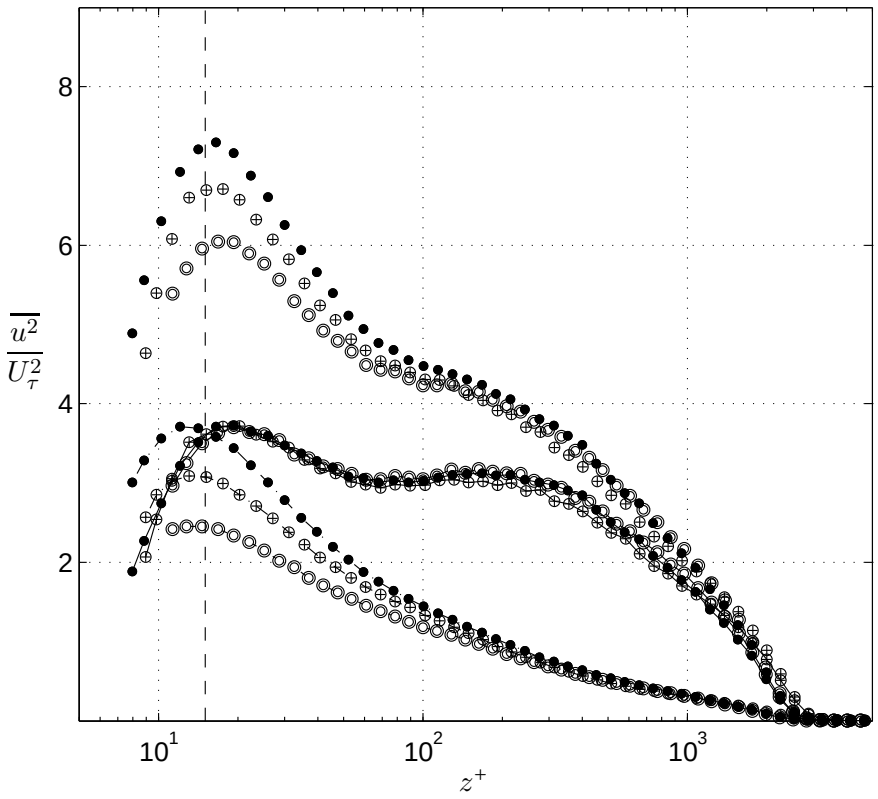


FIGURE 4.11: Decomposition of the broadband turbulent intensity profile $\overline{u^2}/{U_\tau}^2$ into a small- and a large-scale components at $Re_\tau \approx 3000$ for the FPG case ($\beta \approx -0.4$, $K \approx 0.78 \times 10^{-7}$), with varying $l^+$. Symbols: ($\circledcirc$) $l^+ \approx 48$, ($\oplus$) $l^+ \approx 30$ and ($\bullet$) $l^+ \approx 20$. Small-scale components ($\lambda_x/\delta < 1$) are denoted by dashed-lines and large-scale components ($\lambda_x/\delta \geq 1$) are denoted by solid lines. Dashed-dotted line denotes $z^+ = 15$.

compared with the largest $l^+$ in the APG cases, $l^+ \approx 40$). Thus, a greater effect of the small-scale attenuation could be observed. It is also interesting to note that the small-scale contribution to the turbulence intensities for any $l^+$ is: $\overline{u^2}/{U_\tau}^2 < 4$ while for the APG cases, the small-scales contribution is: $\overline{u^2}/{U_\tau}^2 > 4$. The $l^+$ in both the APG and FPG cases are similar ($l^+ \approx 20$, $l^+ \approx 30$, except for the largest one, $l^+ \approx 40$ in the APG case, against $l^+ \approx 48$ in the FPG case).

Now that the effect of large $l^+$ in the near-wall region is known, it is imperative that an accurate experiment and assessment be performed at small $l^+$. Analysis at the smallest $l^+$ here, ($l^+ \approx 20$) will therefore provide a better result in observing the behaviour of the small-scale features in the near-wall region. Figures 4.12($a$) and ($b$) show pre-multiplied $k_x\phi_{uu}/U_\tau^2$ at constant $Re_\tau \approx 3000$ and $l^+ \approx 20$ for the APG case and FPG case respectively. Note that, for the APG case, Figure 4.1($a$) is reproduced in Figure 4.12($a$)

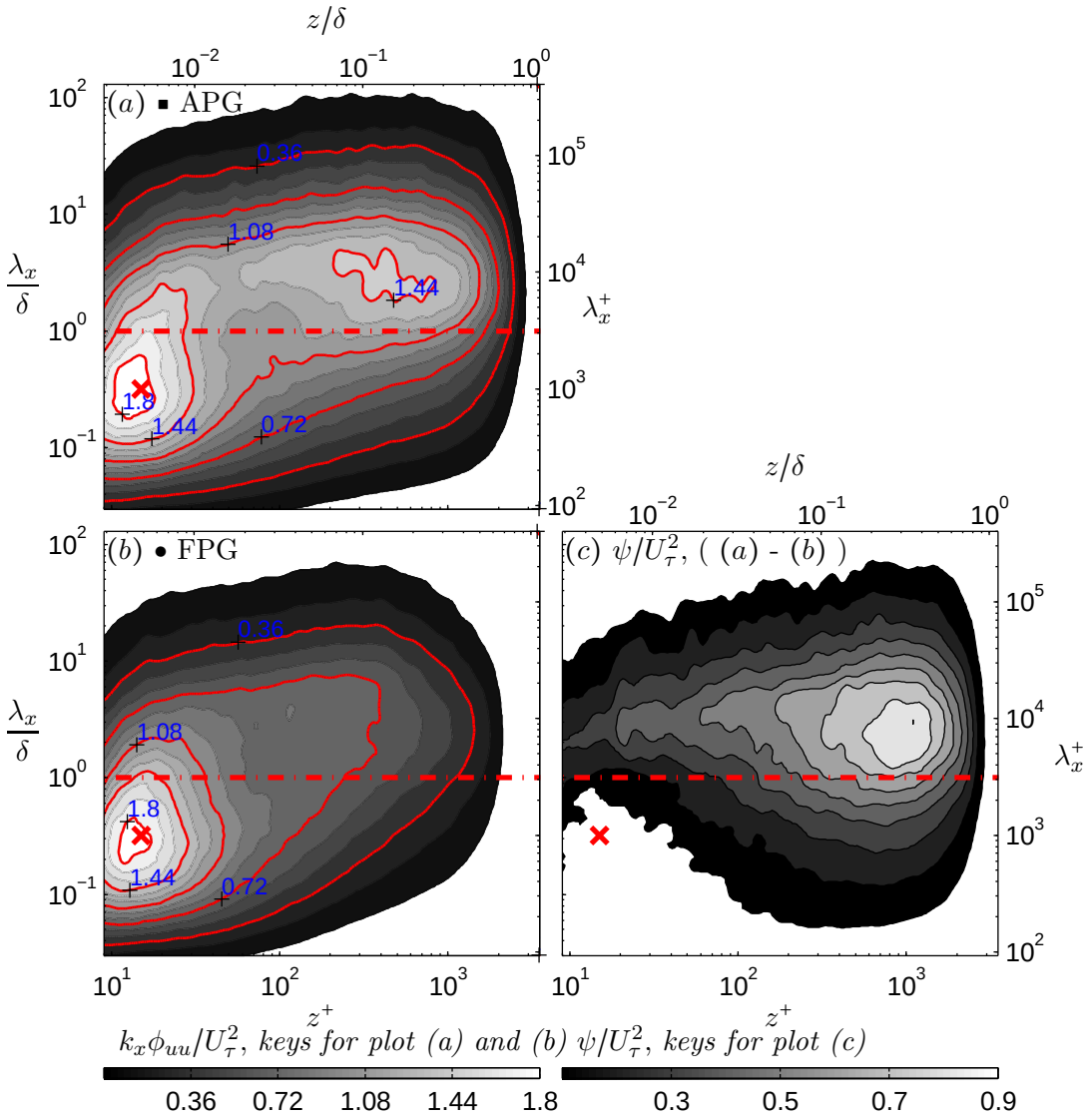


FIGURE 4.12: Pre-multiplied energy spectra of streamwise velocity fluctuation $k_x\phi_{uu}/U_\tau^2$ at constant $Re_\tau \approx 3000$ and $l^+ \approx 20$ for the APG case $(a)$ and for the FPG case $(b)$. Contour levels are from 0.12 to 1.8 in steps of 0.12. Energy difference, $\psi_{uu}/U_\tau^2$ $(c)$. Contour levels are from 0.1 to 0.9 in steps of 0.10. The symbol '×' denotes the location of $z^+ = 15$, $\lambda_x^+ = 1000$, dashed-dotted lines denote $\lambda_x/\delta = 1$.

to facilitate visual comparison with the FPG case. The near-wall peak for both APG and FPG flows occurs at $z^+ \approx 15$, $\lambda_x^+ \approx 1000$. However, as expected, the large-scale structures are more energised in the APG case. This is shown by the contour line $k_x\phi_{uu}/U_\tau^2 = 1.44$ that crosses the $\lambda_x/\delta = 1$ line in the APG case (the same contour line barely crosses the $\lambda_x/\delta = 1$ in the FPG case). The resulting energy difference, $\psi_{uu}/U_\tau^2$ is shown in Figure 4.12$(c)$. Note that the contour line for energy difference starts at $\psi_{uu}/U_\tau^2 = 0.1$.

The key for $\psi_{uu}/U_\tau^2 = 0.0 - 0.1$ is not shown to avoid too much of darker colour in the plots, not to avoid any noise inherited from such calculation. The energy deficit analysis in the region where the near-wall peak occurs (marked with '×' in Figure 4.12($c$)) is small ($\psi_{uu}/U_\tau^2 < 0.1$). Therefore, it is clear now that the energy difference in the near-wall region is negligible. These results confirm two main issues. Firstly, the selection of $l^+ \gtrsim 30$ will cause a near-wall peak to occur with a superficially longer wavelength, $\lambda_x^+ > 1000$. Secondly, changing pressure gradients such as these ($-0.4 < \beta < 1.7$) do not significantly change the structure in the near-wall region.

In summary, these analyses have shown that the small-scale attenuation in the near-wall not only produces a lower near-wall peak magnitude in turbulence intensities, it also superficially causes the inner peak to occur at a longer length scales than the nominal value of $\lambda_x^+ \approx 1000$. The insignificant effect across the pressure gradient observed in energy spectra analysis in the near-wall region is in contrast to recent findings by Lee and Sung (2009), Skote and Henningson (2002). Such disparity warrants a closer look especially into the structure of the streaks in this region; this shall be analysed in Chapter 5 (Streamwise velocity correlation). A further observation arising from this analysis is that the empirical form in Hutchins et al. (2009) fails to predict the behaviour of near-wall turbulence intensities at large $l^+$ in APG flows.

## 4.4 The rise of large-scales in APG

Section 4.1 shows that large-scale structures are more energised in APG. The pressure gradient parameter for the APG case in Section 4.1 is mild, i.e. $\beta \approx 1.7$. In the literature, experiments in APG have been carried out with a wide range of $\beta$, as discussed in Chapter 1. Some of these existing experiments discussed the increased large-scale structures, such as Skåre and Krogstad (1994) and Lee and Sung (2009). However, the cited experiments did not address the rise of the large-scales with a specific pressure gradient parameter, in fact, no study explicitly addresses this relationship.

The data from constant Reynolds number, ($Re_\tau \approx 1900$), with increasing pressure gradient parameter, $\beta$ have been used to analyse this effect. It is stressed here that $l^+ = 16 \pm 1$. This is important, as the near-wall small-scale attenuation is reduced, as discussed in Section 4.3. Figures 4.13($a$) to ($d$) show the pre-multiplied energy spectra of streamwise velocity fluctuation $k_x\phi_{uu}/U_\tau^2$ at constant $Re_\tau \approx 1900$ at selected heights from the wall with varying $\beta$.

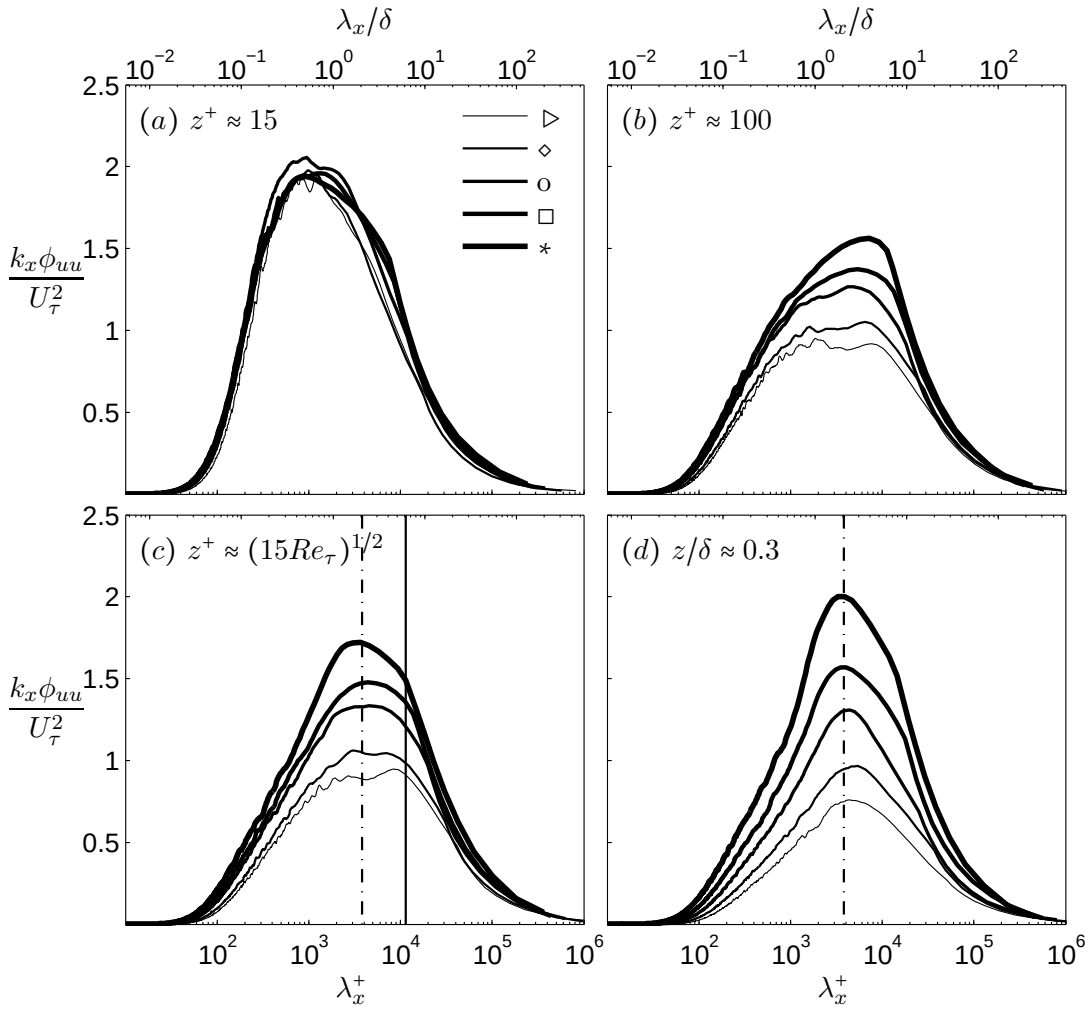


FIGURE 4.13: Pre-multiplied energy spectra of streamwise velocity fluctuation $k_x\phi_{uu}/U_\tau^2$ at constant $Re_\tau \approx 1900$ at selected heights from the wall. $\beta$ increases with line in increasing thickness. Symbols: ($\triangleright$) ZPG, ($\diamond$) $\beta = 0.91$, (o) $\beta = 1.67$, ($\square$) $\beta = 2.81$, ($*$) $\beta = 4.54$. Solid line denotes $\lambda_x/\delta = 6$ and dashed-dotted line denote $\lambda_x/\delta = 2$.

In the near-wall region, ($z^+ \approx 15$), shown in Figure 4.13($a$), $k_x\phi_{uu}/U_\tau^2$ increases from the ZPG case towards strong APG cases. The near-wall peak occurs at $\lambda_x^+ \approx 1000$ for all matched $Re_\tau$ data. The large-scale structures are observed to be energised slightly as $\beta$ is increased[2]. This is shown by the increasing large-scale contribution ($\lambda_x/\delta \gtrsim 1$). This confirms the finding based on Figure 4.3($a$)[3].

[2]The attenuation for small-scale fluctuations is greatly reduced here, thus it can be observed that the most energetic length for the near-wall region is $\lambda_x^+ \approx 1000$ for all cases.

[3]Based on the spectra map comparison of APG, ZPG and FPG at $Re_\tau \approx 3000$, there is a rise of energy in the larger wavelength as the pressure gradient turns sign from FPG to APG.

In Figure 4.13($b$) at $z^+ \approx 100$, the pre-multiplied energy $k_x\phi_{uu}/U_\tau^2$ reduces for all flows. As $\beta$ increases, the structures with greater energy have become more concentrated at $\lambda_x/\delta \approx 3$. At low $\beta$, $k_x\phi_{uu}/U_\tau^2$ has the shape of a plateau, showing that the energy contributions from the small– and large-scales are balanced. At greater $\beta$, the large-scale features have become more energised.

Figure 4.13($c$) shows the pre-multiplied energy $k_x\phi_{uu}/U_\tau^2$ at $z^+ \approx (15Re_\tau)^{1/2} \approx 160$. This figure shows that the peak energy in the geometric centre of the log region occurs at smaller wavelengths as $\beta$ increases. Note that for the ZPG case, the outer peak occurs at $\lambda_x/\delta \approx 6$, in agreement with Hutchins and Marusic (2007a) and Mathis et al. (2009). This is shown by the solid line (the outer peak occurs at slightly shorter than $\lambda_x/\delta = 6$ here is due to the low Reynolds number). However, the peak seems to concentrate at $\lambda_x/\delta \approx 2$ in the case of $\beta = 4.54$, shown by the dashed-dotted line. This behaviour supports the findings in Lee and Sung (2009) that large-scale features break up, creating shorter structures.

At $z/\delta \approx 0.3$ shown in Figure 4.13($d$), $k_x\phi_{uu}/U_\tau^2$ concentrates at $\lambda_x/\delta \approx 2$. This is similar with the most energetic length scales in the varying pressure gradient shown in Figures 4.3($d$). With this set of data, it can be observed that the rise of the large-scale energy systematically increases with $\beta$. The gradual change that is observed in the outer region (in Figures 4.13($b$)-($d$)) suggests that $\beta$ is an important parameter in characterising the behaviour of the large-scale features.

The $3\delta$ energy or LSM observed at large $\beta$ values is a very important feature in APG. These structures seem to have swamped the $6\delta$ energy. To confirm the prominence of the $3\delta$ energy in the log region, the difference in energy could be calculated by subtracting the energy in the ZPG case from the APG cases. The energy difference is shown by the following equation

$$\frac{\psi_{uu}|_n}{U_\tau^2} = \frac{k_x[(\phi_{uu})|_{\beta=n} - (\phi_{uu})|_{\beta=0}]}{U_\tau^2}. \tag{4.3}$$

Figures 4.14($a$) - ($e$) show the pre-multiplied energy spectra, $k_x\phi_{uu}/U_\tau^2$ maps for constant $Re_\tau \approx 1900$ data. In the ZPG case, (4.14($a$)), the inner peak can be observed very clearly to occur at $z^+ \approx 15$ with wavelength $\lambda_x^+ \approx 1000$. The outer peak could not be observed clearly due to the low Reynolds number. In the APG cases, the inner peaks also occur at $z^+ \approx 15$ with wavelength $\lambda_x^+ \approx 1000$.

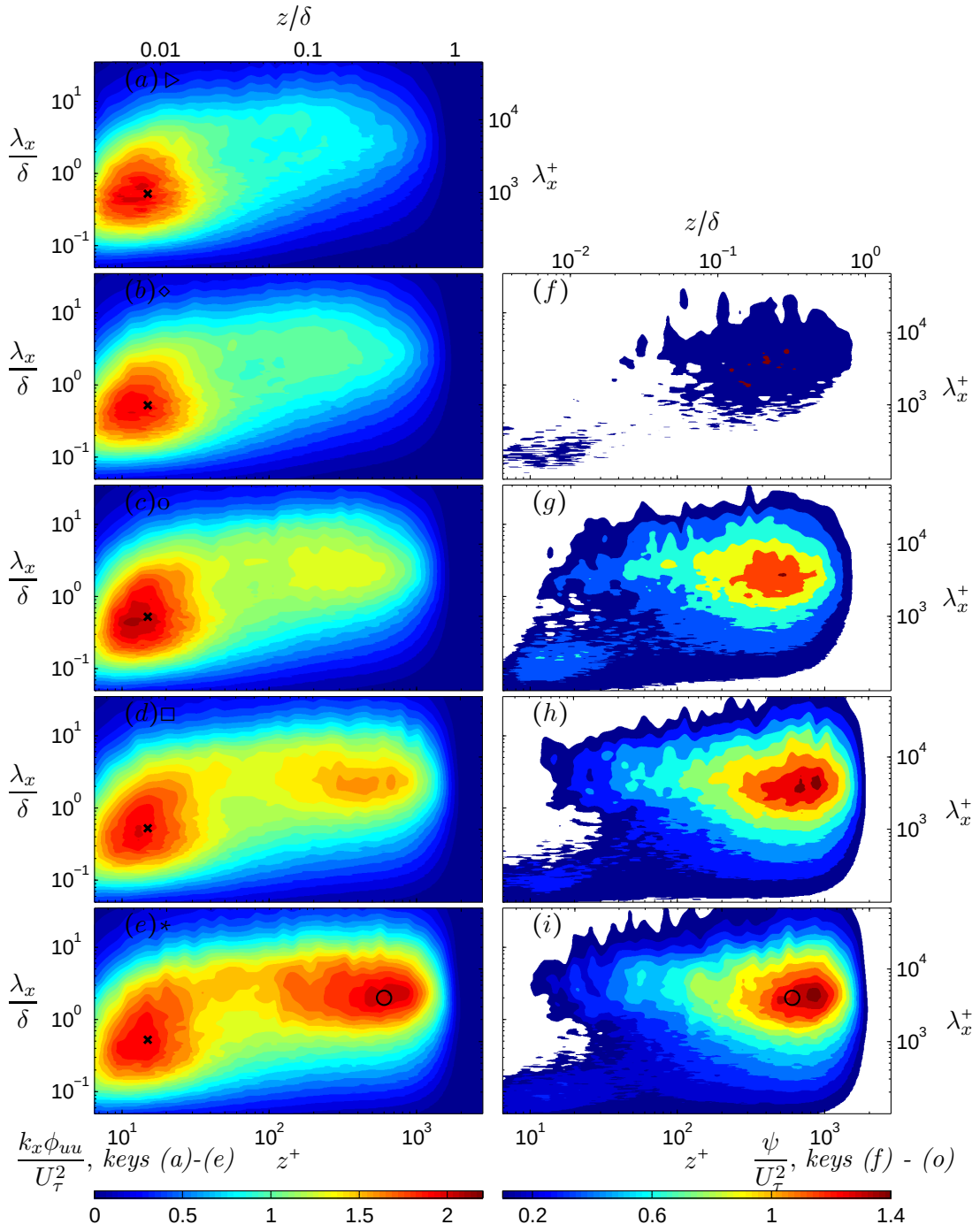


FIGURE 4.14: Pre-multiplied energy spectra of streamwise velocity fluctuation $k_x\phi_{uu}/U_\tau^2$ ($a$ - $d$) and energy difference ($f$ - $i$) for constant $Re_\tau \approx 1900$. Symbols: (▷) ZPG, (◇) $\beta$ = 0.91, (○) $\beta$ = 1.67, (□) $\beta$ = 2.81, (∗) $\beta$ = 4.54. The signs '×' denote near-wall peaks $z^+ \approx 15$, $\lambda_x^+ \approx 1000$ and '○' denote $z/\delta = 0.4$, $\lambda_x/\delta = 2$.

The occurrence of the outer peak is becoming clear with increasing $\beta$. This trend can be observed when comparing Figure 4.14($b$) downwards until Figure 4.14($e$). In the case of largest $\beta$, the outer peak seems to occur at $z/\delta$ = 0.3, $\lambda_x/\delta$ = 2.

The energy difference, $\psi_{uu}/U_\tau^2$ is shown on the right hand side of Figure 4.14. Figure 4.14($f$) shows that at small pressure gradient ($\beta$ = 0.91), $\psi_{uu}/U_\tau^2$ is only slightly different in the outer region. Note that the color key for $k_x\phi_{uu}/U_\tau^2$ is different from that for $\psi_{uu}/U_\tau^2$. The energy difference, $\psi_{uu}/U_\tau^2$ is markedly increased in Figure 4.14($g$), the same trend continues until Figure 4.14($i$) where the pressure gradient, $\beta$ = 4.54. The signs '○' in Figure 4.14($e$) and ($i$) denote $z/\delta$ = 0.3, $\lambda_x/\delta$ = 2, this is approximately the location for outer peak in the APG cases. However, the wall-normal location where energy difference is maximum ($\psi_{uu}/U_\tau^2|_{max}$), is shifted slightly further away from the wall. It can be shown that $\psi_{uu}/U_\tau^2|_{max}$ occurs at $z/\delta$ = 0.4. It is likely that the wall-normal location where $\psi_{uu}/U_\tau^2|_{max}$ occurs, increases with pressure gradient. The occurrence of $\psi_{uu}/U_\tau^2|_{max}$ at higher wall-normal location can be generally related to the rise of turbulence intensities as observed in Figures 3.9($b$) or 3.12($b$) (turbulence intensity profiles for APG, ZPG and FPG flows at constant $Re_\tau \approx 3000$ and turbulence intensity profiles for increasing $\beta$ flows at constant $Re_\tau \approx 1900$). In the near-wall region, there is no drastic change for the $\lambda_x^+ \approx 1000$ structures. There is however an increased energy for structures with wavelengths of $100 < \lambda_x^+ < 300$.

The main conclusions resulting from energy spectra and scale decomposition analyses are:

1. Despite recent findings that pressure gradient causes structural changes in the near-wall region, for example Nagano et al. (1998) and Lee and Sung (2009) in APG and Bourassa and Thomas (2009) in FPG, the energy spectral density study shows that there is only insignificant structural change. It is reminded that the pressure gradients are mild (-0.4< $\beta$ <1.6) and performed in the intermediate range of Reynolds number ($Re_\tau \approx$ 1900 and 3000). In APG however, these are about the range of the pressure gradient parameters used in Nagano et al. (1998) and Lee and Sung (2009) studies (refer to Table 1.1).

2. APG causes 3$\delta$ energy to emerge as the most dominant structures, swamping the 6$\delta$ energy. The 3$\delta$ energy also appears in other wall-bounded flows i.e. channel and pipe flows (Balakumar and Adrian, 2007, Guala et al., 2006, Monty et al., 2009). These structures however are so energised in APG as compared with other flows

that they are responsible for the rise in the outer region in the mean velocities and turbulence intensities.

3. The outer peak in APG no longer occurs in the approximate centre of the log region $z^+ \approx (15Re_\tau)^{1/2}$ or $z/\delta \approx 0.06$, instead it occurs further away from the wall, $z/\delta \approx 0.3$. The large scale structures are energised for the entire log region (starting from $z^+ \approx 100$) towards a great percentage of the outer region ($z/\delta \approx 0.8$), before they rapidly decay towards the edge of the boundary layer.

4. When a longer sensor length, e.g. $l^+ \approx 40$ is used in an APG flow, the near-wall peak appears to occur with superficially longer wavelength, e.g. $\lambda_x^+ \approx 1500$ in the spectral density analysis. This is the immediate result from the combination of the small-scale attenuations and the rise of the large-scale in the near-wall region due to APG introduction. Therefore, it is suggested that the sensor length should be small e.g. $l^+ \lesssim 20$ in APG. Since $\beta$ is an important factor in determining the magnitude of the near-wall peak in turbulence intensities, the empirical formulation by Hutchins et al. (2009) will not be able to predict such magnitude in APG flows. It would be interesting if a study similar to Hutchins *et al.* were repeated in boundary layers with pressure gradients.

# Chapter 5

# Streamwise velocity correlation

Two-point hotwire measurements have been performed at various wall-normal locations with one sensor stationary and the other travelling in the wall-normal or spanwise direction. Throughout this thesis the stationary sensor is referred to as sensor 1 and the travelling sensor is referred to as sensor 2. A typical set-up for a two-sensor measurement is shown in Figure 5.1. In this figure, the left hand-side is called sensor 1 and the right hand-side, sensor 2.

FIGURE 5.1: Typical hotwire sensors at the start of an experiment with sensor 1 on the left and sensor 2 on the right. The smooth and shiny floor reflects the image and is captured in the photograph.

The two-point correlation equation is

$$R_{uu}(\Delta x, \Delta y) = \frac{< u(x,y)u(x+\Delta x, y+\Delta y) >}{\sigma_u(x,y)\sigma_u(x+\Delta x, y+\Delta y)}, \tag{5.1}$$

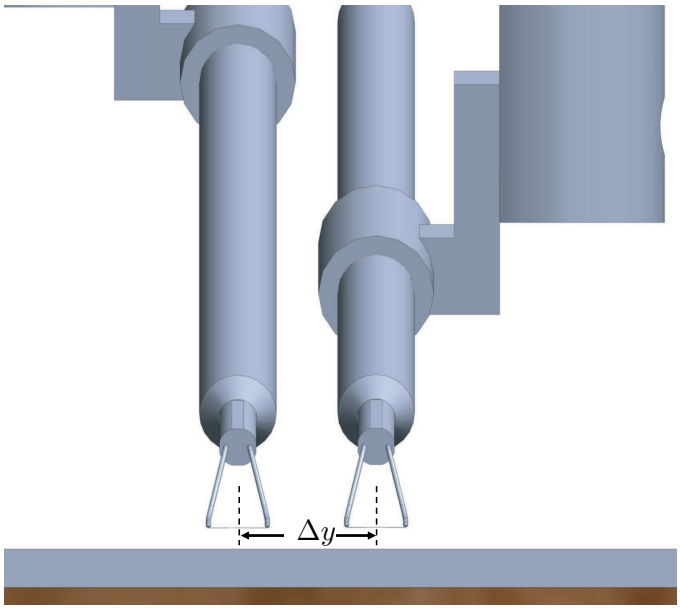


FIGURE 5.2: Hotwire diagram.

where $u$ is the fluctuating velocity, $\Delta x$ and $\Delta y$ are the separations between the two sensors in the streamwise and spanwise directions respectively and $\sigma$ is the standard deviation. The requirement of fixed $l^+ \approx 16$ is maintained for both sensors. There are two types of two-point hotwire measurements for the correlation conducted:

($a$). Wall-normal - sensor 1 is stationary and sensor 2 travels in the wall-normal direction and

($b$). Spanwise - sensor 1 is stationary and sensor 2 travels is the spanwise direction.

An elevation, front-view drawing of the hotwire sensors, with their holders are shown in Figure 5.2. In this figure, the sensors' centre-to-centre distance $\Delta y$ is indicated.

Some settings and results of the two experiments are discussed in Section 5.1 and Section 5.2. For brevity, one case each of zero, favourable and adverse pressure gradients was used as an example to characterize the effect of the pressure gradient on boundary layers. In order to isolate the Reynolds number effect, the chosen boundary layer cases are approximately at $Re_\tau = 1900$. The ZPG and APG cases are from the constant $Re_\tau \approx 1900$ experiments (from Station 1 and 3 respectively), while the FPG case is from the constant $U_{inlet}$ =15 m/s experiment (Station 3). The Reynolds number for the FPG

case is slightly higher than the target $Re_\tau \approx 1900$, however the difference in the Reynolds number here is too small to cause any significant Reynolds number effect. Refer to Table 2.1 for details.

## 5.1 Structure inclination angle

The hotwire and the hotfilm measurements and analysis of Brown and Thomas (1977) have shown that organised structures exist in a boundary layer and these structures have an inclination angle of nominally 15° from the wall at $Re_\theta \approx 10000$. An array of four hotwire sensors located at different wall-normal locations and a hotfilm sensor on the wall for wall-shear stress signature were used. For each hotwire sensor (at different wall normal locations), there is a peak value of the cross-correlation coefficient. Assuming the Taylor hypothesis of frozen turbulence, the distance at which this peak occurs can be found and, from this, an inclination angle can be calculated.

A V-shaped array of hotwire sensors were used by Wark and Nagib (1991) to measure the streamwise and spanwise stresses on the wall of ZPG boundary layers. A similar correlation method as that used by Brown and Thomas (1977) for obtaining the inclination angle was employed, but at a lower Reynolds number ($3000 < Re_\theta < 9000$). The cross-correlation analysis yields an average inclination angle of greater than 20° in APG flows (Krogstad and Skåre, 1995) and smaller than 10° in FPG flows[1]. From these results, Krogstad and Skåre (1995) suggested that APG causes the structures in the outer region to rise and breakup, while Dixit and Ramesh (2010) explained that FPG stretches and flattens the structures.

Adrian et al. (2000) presented PIV measurements and analysis of vortex structure of ZPG boundary layers. It is shown that hairpin vortices self-organize to form coherent vortex packets of different sizes. Close to the wall, the hairpins in a packet appear to have a mild inclination angle of 12°. It was also observed that the inclination angle grows with distance from the wall. Marusic and Heuer (2007) showed that the inclination angle of the structure is invariant with Reynolds numbers (13° to 15°), extending over almost three decades of Reynolds numbers ($10^3 < Re_\tau < 10^6$). Thus, there should not be any concern of Reynolds number effect as discussed at the start of this chapter.

[1] In ZPG flow, the nominal structural inclination angle is 13 - 18° (Adrian et al., 2000, Brown and Thomas, 1977, Ganapathisubramani et al., 2003, Marusic and Heuer, 2007, Robinson, 1991)

Ganapathisubramani et al. (2003) noted that the large-scale features sometimes extend up to $2\delta$ in streamwise length with an angle of $10^o$ to $20^o$ by using a feature extraction method on their PIV data. Also using PIV, Hutchins et al. (2005) observed that the inclination angle is on the larger end ($20^o$). It was also observed that the inclination angle increased with distance from the wall.

For boundary layer flows in adverse pressure gradients, there have been studies which elaborate the effect of the pressure gradient on the inclination angle. Krogstad and Skåre (1995) found that the inclination angle is $45^o$ for almost all through the boundary layer at large adverse pressure gradient ($\beta \approx 20$). Note that in ZPG boundary layers, the inclination angles are shallower in the near-wall region and grow with distance from the wall up until the log region where it maintains approximately constant. The steep angle in the near-wall region may be explained by the following: the pressure gradient parameter was large ($\beta = 20$). In this condition, the boundary layer is thickened and the coefficient of friction is close to zero (near separation from the wall). The active structures are shifted further away from the wall when compared with the ZPG case. This causes the inclination angle to be greater.

The correlation analysis in the near-wall region could have been affected by the modulating large-scale features in the log and outer regions. Considering that the experiment was performed at large Reynolds numbers ($40000 \lesssim Re_\theta \lesssim 50000$), the modulating effect was stronger. This is demonstrated at the end of the chapter, where it is found that the small-scale velocity fluctuations are enveloped by the large-scale fluctuations. Two-point correlation in the near-wall region largely picks up the enveloping movements, resulting in the coefficient of correlation to scale with the outer variable. This result has been published in Harun et al. (2011).

Lee and Sung (2009) found that the vortex packets in the outer region have an inclination angle of $18^o$ in DNS data of $1200 < Re_\theta < 1400$, in APG flow where $\beta = 1.68$. They used Galilean decomposition to detect swirling motions. The same method yields an inclination angle of $13^o$ for their ZPG case. Both Krogstad and Skåre (1995) and Lee and Sung (2009) APG found that the spanwise and vertical extents in $R_{uu}$ are larger than those of the ZPG flow. In ZPG flow (e.g., Head and Bandyopadhyay, 1981) indicated that the dominant structures consist of vortex loops or the swirling motions. Lee and Sung (2009) indicate that the swirling motions in the streamwise direction for APG flows are stronger than in the ZPG flows.

In FPG flows, Dixit and Ramesh (2010) have reported a structural inclination angle that decreases with acceleration parameter $K$. The (favourable) pressure gradient is large (in reverse-transitional sink flow boundary layers). The inclination angle decreases systematically from 14° at $K = 0.77 \times 10^{-6}$ to 5° at $K = 4.5 \times 10^{-6}$. For measuring the wall-shear stress, the surface hotwire (SHW) sensor was used. It consisted of a hotwire sensing element soldered to the tips of two sharp needles protruding out from the surface of a Teflon plug, which was flush-mounted with the test surface. Interestingly, the wall-normal extent of the correlation coefficient was found to be invariant with the pressure gradient, though the streamwise extent was remarkably stretched.

Table 5.1 summarizes these studies; the Reynolds numbers, pressure gradients and the structural inclination angles, $\theta_{struc}$, are shown. There are numerous studies in ZPG boundary layers however only two studies are listed in the table. There are somewhat limited studies that focus on the structural inclination angle in pressure gradient TBL flows. A general trend can be deduced from the existing studies: $\theta_{struc} \approx 15°$ in ZPG, grows to as much as 45° in strong APG and in contrast flattens to as shallow as 5° in strong FPG. While the general trend of the structural inclination angle is quite obvious from the table, the extent to which the turbulent features behave in the wall-normal direction in the presence of pressure gradients remains in question. This section systematically analyses the effect of pressure gradient on turbulent structures by the correlation method, and subsequently calculates the inclination angle.

The structure inclination angle can be calculated by

$$\theta_{struc} = tan^{-1} \frac{z}{\Delta x_{peak}}, \tag{5.2}$$

where $z$ refers to the wall-normal height at which the correlation is calculated and $\Delta x_{peak}$ is the spatial difference where the maximum correlation occurs. Assuming Taylor's hypothesis of frozen turbulence, the time series data is converted into space via $\Delta x_{peak} = U_c \Delta t$, where $U_c$ is the convection velocity or local mean for sensor 2. The structure inclination angles for FPG, ZPG and APG in the current experiments (inclusive but not limited to data used for in Figure 5.3) range from 11° to 18° with a tendency of a milder slope for the FPG case and a steeper slope for the APG case. The ZPG boundary layers have nominal values of $12° < \theta_{struc} < 16°$.

To highlight the wall-normal extent of the features in the boundary layer, a contour map reconstructed from individual wall-normal $R_{uu}$ is plotted and shown in Figure 5.3. In the figure, sensor 1 is stationary at $\Delta t U_c/\delta = 0$ in the streamwise direction and $z/\delta \approx 0.004$

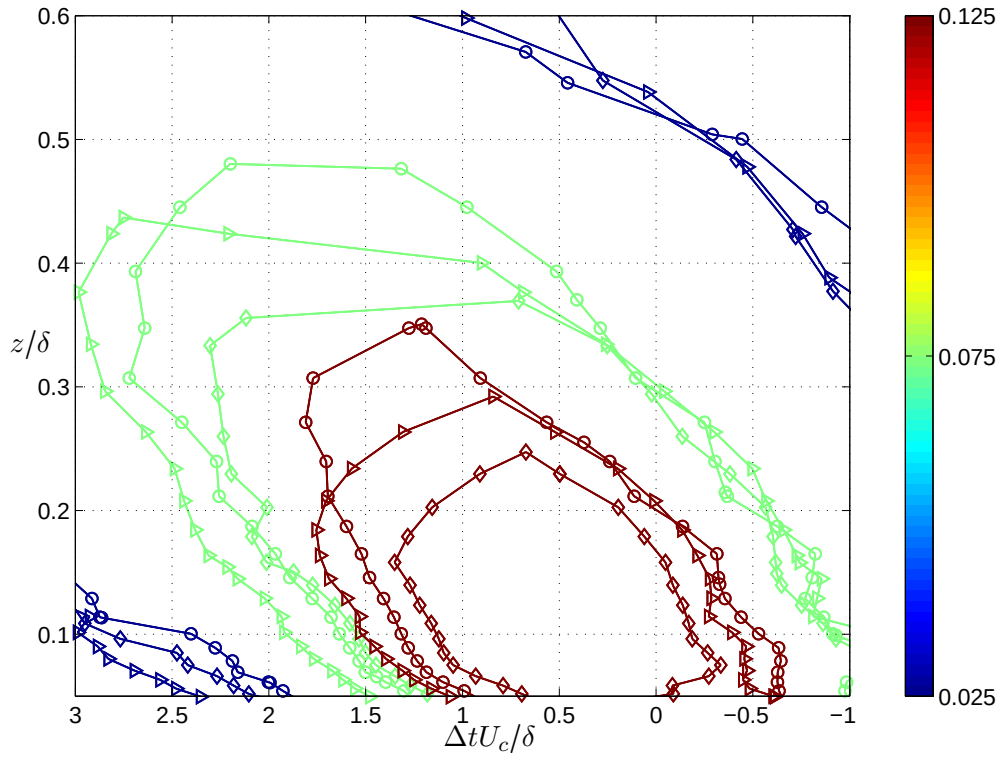


FIGURE 5.3: Two-point wall-normal correlation $R_{uu}$ for ZPG ($\triangleright$), APG (o) and FPG ($\diamond$) flows at $Re_\tau \approx 1900$. Contour levels are from $R_{uu} = 0.025$ in increments of 0.05 starting with thick blue colour contour line in the outside. For details, refer to Table 2.1.

($z^+ \approx 7$), while sensor 2 moves from $z/\delta \approx 0.016$ ($z^+ \approx 30$) in the wall-normal direction along $\Delta t U_c/\delta = 0$. All three pressure gradient cases are shown here. The $R_{uu}$ coefficient changes are indicated by the colour: red for the high correlation region and blue for the low correlation region (refer to key). It can be observed that the region with highly correlated activity in the FPG is closer to the wall and in contrast, extends further from the wall in the APG. These observations are especially significant in the log region. In a physical sense, on average, the FPG suppresses the features while the APG extends the features outward. This finding is in agreement with Krogstad and Skåre (1995), who then attributed this effect to 'inrushing fluid which is squeezed out laterally near the wall and to some degree reflected back to the flow'.

| Workers | $Re_\theta$ | Pressure Gradient | Inclination angle, $\theta_{struc}$ |
|---|---|---|---|
| Dixit and Ramesh (2010) | 220 – 1300 | FPG, $K = 4.5 \times 10^{-6}$ - $0.77 \times 10^{-6}$ | 5 – 14$^o$ |
| Wark and Nagib (1991) | 3000 – 9000. | ZPG | 15$^o$ |
| Adrian et al. (2000) | 930-6845 | ZPG | 12$^o$ close to wall<br>15-70$^o$, typically 45$^o$ in outer layer |
| Marusic and Heuer (2007) | $1 \times 10^2 - 1 \times 10^5$ | ZPG | 15 |
| Krogstad and Skåre (1995) | 39100 – 51000 | APG $\beta \approx 20$ | 45$^o$ throughout boundary layer |
| Lee and Sung (2009) | 1200-1400 | APG, $\beta = 1.68$ | 18$^o$ |

TABLE 5.1: A review of structural inclination angles in FPG, ZPG and APG boundary layers.

## 5.2 Streamwise and spanwise correlation

Streamwise auto-correlation and two-point correlation in the spanwise direction can be used to analyse the effect of pressure gradients in the near-wall and outer regions. The streamwise auto-correlation gives the streamwise extent of the structure, as shown by Krogstad and Skåre (1995) and Ganapathisubramani et al. (2005). The instantaneous multi-point spanwise correlation from a rake-like hotwire sensor set up by Hutchins and Marusic (2007a) reveals long and meandering features in the log region. Two-point spanwise correlation gives statistical information about the width and spacing of coherent structures in ZPG boundary layers, (Blackwelder and Kaplan, 1976, Hutchins et al., 2005, Monty et al., 2007). A number of papers where two-point spanwise correlation is employed in the boundary layers subjected to pressure gradient have also been published (Dixit and Ramesh, 2010, Krogstad and Skåre, 1995, Lee and Sung, 2009). In this section, from the two-point sensor experiment and correlation analysis, pressure gradient effects on the structure in the near-wall and outer regions will be shown.

Streak spacing is one of the turbulent flow properties that could be identified from correlation analysis. It has been found that the streak spacing is affected by pressure gradient. Streaks are defined by Kline et al. (1967) as well-organised spatially and temporally dependent motions within the laminar sub-layer. The streak spacing in ZPG was found by Kline to be approximately 100 viscous wall units. Lee and Sung (2009) found that the near-wall streaks are weakened and the spanwise spacing is 400 viscous wall units in APG flow. Streak spacing in FPG is also found to be above the nominal ZPG value of 100 viscous wall units (Bourassa and Thomas, 2009). A review of streak spacing for boundary layer flows is shown in Table 5.2. From this table, it seems to be evident (by the change in streak spacing) that a pressure gradient actually causes the structure in the near-wall to change.

All these studies have been performed at different Reynolds numbers, as shown in Table 5.2. The streak spacing in Table 5.2 is shown in non-dimensionalised length scaled with $U_\tau$, $\lambda_y^+$, where $y$ denotes the spanwise direction. In order to perform the correlation analysis properly, certain important parameters have to be made constant. These parameters are the sensor length, $l^+$, and the Reynolds number. The reasons for keeping $l^+$ small and constant are discussed in Chapter 4. The Reynolds number effect is known to alter certain turbulence statistics in the outer region, e.g. turbulence intensities, turbulence production and more importantly the emergence of footprint in high Reynolds number

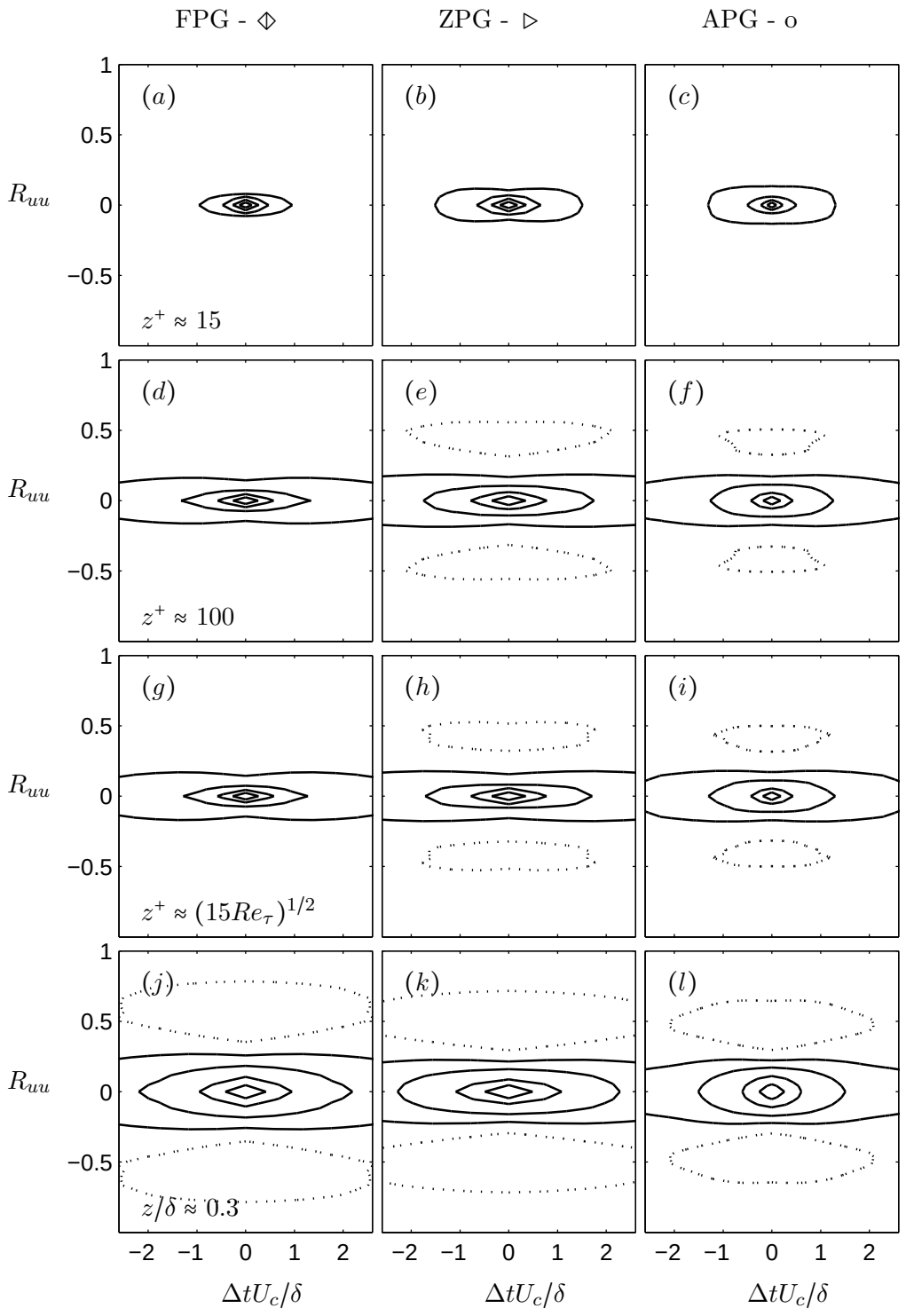


FIGURE 5.4: Two point velocity correlations $R_{uu}$ in the $(x, y)$ plane at $Re_\tau \approx 1900$ for FPG ($\diamondsuit$), ZPG ($\triangleright$) and APG (o) flows at $Re_\tau \approx 1900$ at $z^+ \approx 15$ ($a$,$b$,$c$), $z^+ \approx 100$ ($d$,$e$,$f$), $z^+ \approx (15Re_\tau)^{1/2}$ ($g$,$h$,$i$) and at $z/\delta \approx 0.3$ ($j$,$k$,$l$)

.

flows (Hutchins and Marusic, 2007a, Marusic et al., 2010a). To isolate any Reynolds number effect, the Reynolds number has been maintained at $Re_\tau \approx 1900$.

Due to time constraints, the two-point spanwise measurements were performed at four selected wall-normal locations only. These particular wall-normal locations are selected because of the following: $z^+ = 15$ is obviously the location where energy is maximum in the near-wall region (Hutchins and Marusic, 2007a), $z^+ = 100$ is approximately the start of the log region, $z^+ = (15Re_\tau)^{1/2}$ is the geometric centre of the log region (Mathis et al., 2009) where outer peak occurs in ZPG, and $z/\delta = 0.3$ is the location where the same occurs for APG (Harun et al., 2010a).

Figure 5.4 shows the outer scale two-point correlation for the streamwise velocity fluctuation $R_{uu}(\Delta x, \Delta y)$ correlation map at four wall-normal locations. The columns show flows in different pressure gradients (FPG - left column, ZPG - middle column and APG - right column). The rows show the wall-normal locations at which measurements were performed ($z^+ \approx 15$ - first row, $z^+ \approx 100$ - second row $z^+ \approx (15Re_\tau)^{1/2}$ - third row and $z/\delta \approx 0.3$ - last row). Contour levels are -0.08, 0.08, 0.25, 0.5 and 0.75 with the dashed lines showing negative contours and solid lines showing positive contours. The general trend that can be observed in these plots is that the negative-positive-negative correlations are more obvious in the outer region than in the near-wall region. The FPG case does not show any negative correlation except at $z/\delta \approx 0.3$. Therefore, at first look, the FPG case has the weakest negative-positive-negative correlation in the near-wall and log regions.

It is a little bit difficult to gauge the effect of pressure gradient when the contour maps are not shown on a common axis. Thus it is helpful to view the contour with the three pressure gradient cases on one plot. A slice of $R_{uu}$ at $\Delta y = 0$ or auto-correlation of each pressure gradient case and each wall-normal height is shown on the left-hand side of Figure 5.5, while the spanwise correlations ($\Delta x = 0$) are shown on the right-hand side.

Comparing the plots on the left-hand side of Figure 5.5 from top to bottom reveals the streamwise length of the correlation collapse in the near-wall region. The streamwise length of the APG case appears to be shorter than that of the ZPG and FPG cases in the log region ($z^+ \approx 100$ and $z^+ \approx (15Re_\tau)^{1/2}$. In the outer region $z/\delta \approx 0.3$, the shorter streamwise length of the APG case is much more pronounced. This effect has been observed in a much stronger adverse pressure gradient by Krogstad and Skåre (1995).

The latter attributed this affect to a much less efficient streamwise vortex stretching when a boundary layer is subjected to an APG. The long tails in streamwise correlations

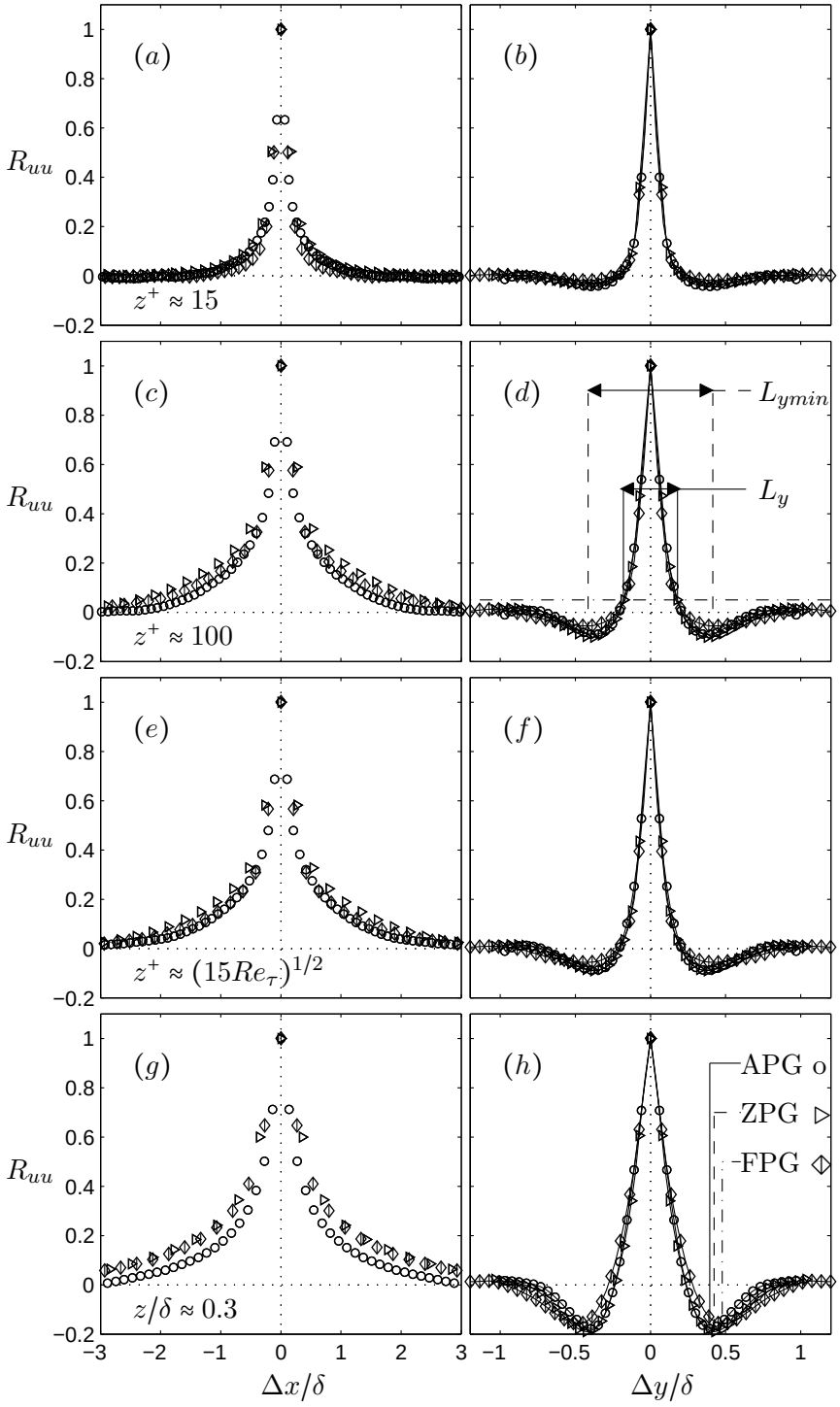


FIGURE 5.5: Streamwise (left) and spanwise (right) two-point correlation $R_{uu}$ for FPG (◇), ZPG (▷) and APG (o) flows at $Re_\tau \approx 1900$ at $z^+ \approx 15$ $(a, b)$, $z^+ \approx 100$ $(c, d)$, $z^+ \approx (15Re_\tau)^{1/2}$ $(e, f)$ and at $z/\delta \approx 0.3$ $(g, h)$. In $(d)$, the vertical dashed lines indicate the $L_{ymin}$ and the vertical dashed-dotted lines indicate $L_y$ for the APG case. In $(h)$, the vertical solid, dashed and dashed-dotted lines indicate occurrences of minima $R_{uu}$ for APG, ZPG and FPG respectively.

| Workers | $Re_\theta$ | Pressure Gradient | Streak spacing, $\lambda_y^+$ |
|---|---|---|---|
| Bourassa and Thomas (2009) | 4590 | FPG, $K \approx 4.4 \times 10^{-6}$ | > 100 |
| Finnicum and Hanratty (1988) | - | FPG, $K \approx 2 \times 10^{-6}$ | 105-110 |
| Robinson (1991) review paper | $Re_\theta \leq 6000$ | ZPG | 100 |
| Adrian et al. (2000) | 930-6845 | ZPG | 100 |
| Skote and Henningson (2002) | 300-700 | ZPG to strong APG (separated) | 100 (ZPG) - 130 |
| Lee and Sung (2009) | 1200-1400 | APG, $\beta = 1.68$ | 400 |

TABLE 5.2: A review of streak spacing in FPG, ZPG and APG boundary layers.

in the ZPG case have been observed by Kovasznay et al. (1970) and more recently by Ganapathisubramani et al. (2005). Ganapathisubramani et al. (2005) attributed the long tails in streamwise correlation to the existence of vortices organised within packets. The coherent structures of hairpins in packets are in agreement with Adrian et al. (2000). The shorter structures in the APG case suggest that an APG causes the steamwise structures to break up and get shorter. This result is in agreement with the finding from energy spectra analysis where the most energetic wavelength has been reduced by half (from $6\delta$ in ZPG to 2 - $3\delta$ in APG, shown in Section 4.4). This effect is more prominently observed in the outer layer ($z/\delta \approx 0.3$), both in spectra and correlation analyses.

Though the APG case shows shorter structures in the log and outer regions compared to the ZPG case, $R_{uu}$ for the FPG case collapses well with the ZPG case, indicating that the streamwise length scale does not change going from ZPG to FPG. This is in contrast with the recent finding of Dixit and Ramesh (2010) where structures get elongated with FPG. The contrast is explained by the strength of the acceleration parameter $K$; the current FPG case is exposed to only approximately one-tenth of the acceleration parameter strength in Dixit and Ramesh (2010).

All of the spanwise two-point correlations, $R_{uu}$, are scaled with $\delta$, shown on the right-hand side of Figure 5.5. Again, going down the column shows spanwise $R_{uu}$ with increasing wall-normal location. The first thing to note is the negative-positive-negative correlation trend that gets amplified with the distance from the wall. The correlation in the near-wall and log regions appears to collapse well for $z^+ \leqslant (15Re_\tau)^{1/2}$. However, there is a slight deviation in the outer region, where the minimum-to-minimum distance changes with pressure gradients as shown in Figure 5.5($h$).

Note that there are 40 spanwise measurements which span over $1.2\delta$ with equal space (except between the first and second measurement). The markers in the spanwise plots

5.5($b$) and subsequently 5.5($d$) ,($f$) and ($h$) have been reduced, leaving only solid lines. The solid lines are spline-fit from the data. This is done to facilitate visualisation, especially at locations where $R_{uu}$ reaches its minimum. Scaling with outer variable $\delta$ is chosen following the findings by Hutchins and Marusic (2007a), Hutchins et al. (2005).

The most interesting point of the spanwise $R_{uu}$ result would be if there is an indication of a change in the near-wall structures due to pressure gradient. A change in either the streak spacing or the streak width would indicate a structural change. In Table 5.2, the wide range of Reynolds number data shows that streak spacing concentrates in the order of $y^+ \approx 100$, therefore, the correlation coefficients should have minima in the region of $y^+ \approx 50$ for the near-wall region. The separation at which this minimum occurs provides an estimate of the mean separation between the high- and low-speed fluid, i.e. the streak spacing is approximately twice the distance Kim et al. (1987). Figure 5.5($b$) shows that the minima are approximately $0.5\delta$ suggesting the structure's spacing is $1\delta$ for all pressure gradient cases. This is obviously not in agreement with existing data as shown in Table 5.2. We shall come back to this after going through the entire spanwise $R_{uu}$.

Before going deeper into the analysis, a few more parameters are defined. The first is $L_y$, the characteristic spanwise length scale determined on the intercept with a given threshold, $th$ in $R_{uu}$ plot ($th = 0.05$ in the thesis). The definition here is the same as in Ganapathisubramani et al. (2005), Hutchins et al. (2005) and Monty et al. (2009). The definition of $L_y$ is shown in Figure 5.5($d$); $L_y$ is the width indicated by the vertical solid lines, intercepting with $th = 0.05$ . The second parameter is the introduction of $L_{ymin}$, the characteristic spanwise length scale when minima in $R_{uu}$ occur. These definitions are shown in Figure 5.5($h$).

Figure 5.5($d$) and ($f$) show spanwise $R_{uu}$ collapse for all three pressure gradient cases in the log region. The stronger negative-positive-negative correlation trend with wall distance is indicative of alternating regions of low- and high-speed regions (Ganapathisubramani et al., 2005, Hutchins et al., 2005, Monty et al., 2009) in the outer regions, despite pressure gradients.

Figure 5.5($h$) shows spanwise $R_{uu}$ collapse only for $\Delta y/\delta < 0.2\delta$ for all three pressure gradient cases in the outer region, however $R_{uu}$ does not collapse for the FPG case beyond $0.2\delta$. In ZPG boundary layers, Hutchins et al. (2005) noted that the spanwise correlations scale with outer variables and that the growth of the spanwise length scale is approximately linear with distance from the wall.

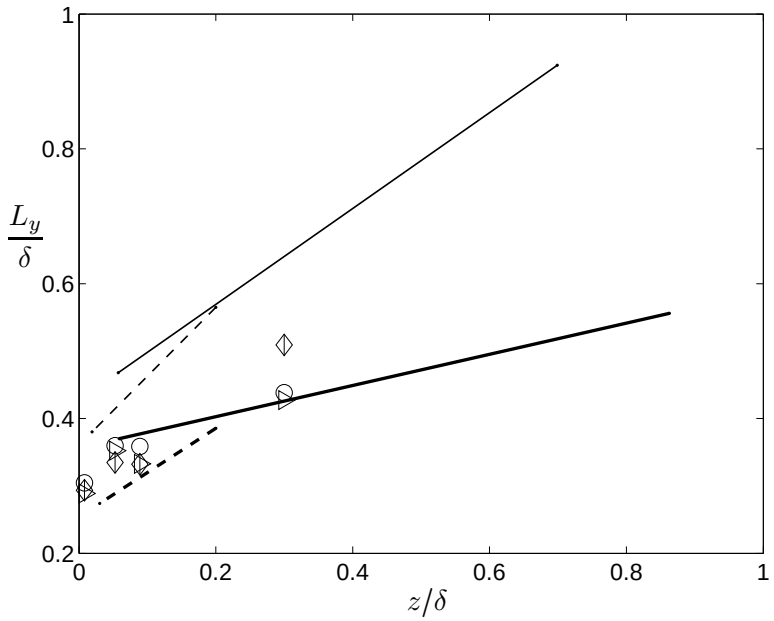


FIGURE 5.6: The characteristic spanwise length scale, $L_y/\delta$. Symbols: ($\diamondsuit$) FPG, ($\triangleright$) ZPG and (o) APG. The thick lines show fitted data from ZPG data from Hutchins et al. (2005). The thin lines show channel flow data compiled by Monty et al. (2007). Dashed-lines indicate curve-fit of existing data for $z/\delta < 0.15$ while solid lines indicate curve-fit of existing data beyond $z/\delta > 0.4$.

The characteristic spanwise length scale, $L_y/\delta$, of the three pressure gradient cases is shown in Figure 5.6. To compare this with other boundary layer data, results from Hutchins et al. (2005) are inserted. These are denoted by the thick solid line (for $z/\delta < 0.15$) and thick dashed line ($z/\delta > 0.4$). For the region $z/\delta < 0.15$, $L_y/\delta$ for the current experiment is slightly greater than the ZPG data of Hutchins et al. (2005), indicating wider turbulent structure in the current experiments. However, $L_y/\delta$ for current ZPG and APG data collapse well with Hutchins et al. (2005) (shown by the collapse with the solid thick line for $z/\delta > 0.4$). $L_y/\delta$ for the current FPG data is slightly wider. The channel flow data from Monty et al. (2007) is also shown in this figure. The thin solid and thin dashed line denote $L_y/\delta$ from Monty et al. (2007) (thin dashed line for $y/\delta < 0.15$ and thin solid line for $z/\delta > 0.4$). In general $L_y/\delta$ for FPG data for $z/\delta > 0.4$ lies *between* existing ZPG data and channel flow data.

Further to the characteristic spanwise length scale analysis, the occurrence of a minimum in spanwise $R_{uu}$, $L_{ymin}$, for the right hand side of Figure 5.4 is also calculated, shown in Figure 5.7. It can be seen that the FPG case has slightly wider structures at all wall-normal positions considered, compared with the ZPG and APG cases. The difference is

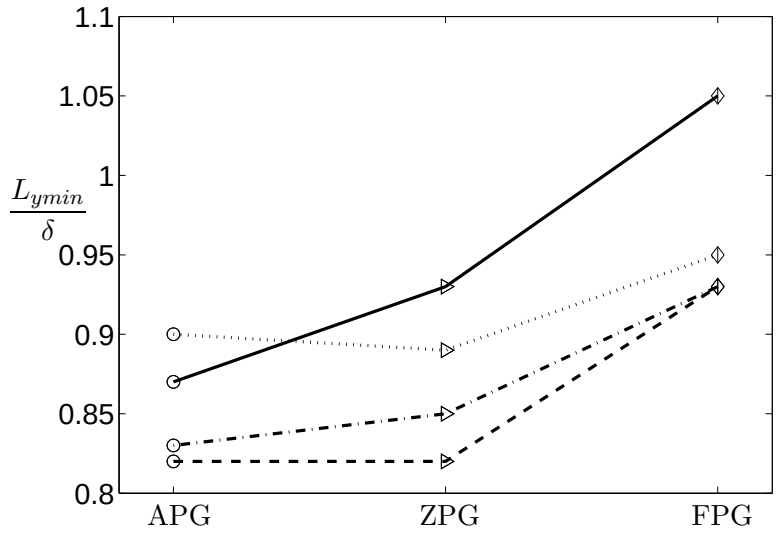


FIGURE 5.7: The occurrence of minima $L_{ymin}$ in $R_{uu}$ for FPG ($\diamond$), ZPG ($\triangleright$) and APG (o) flows at $Re_\tau \approx 1900$ at $z^+ \approx 15$ (dotted line), $z^+ \approx 100$ (dashed-dotted line), $z^+ \approx (15Re)^{1/2}$ (dashed line) and at $z/\delta \approx 0.3$ (solid line).

greatest at $z/\delta = 0.3$, where $L_{ymin}$ for the FPG case is wider by approximately 10% than in the ZPG/APG cases. If this figure is compared with Figure 5.6, we can clearly see the effect of pressure gradient on the width of the structures in the flow. Considering $L_y$ and $L_{ymin}$ at $z/\delta = 0.3$, the large-scale structures which dominate the log and outer region for the FPG case have a width that is on average between that of ZPG/APG and channel flows.

## 5.3 The large scale effect

Thus far, it has been shown that the spanwise $R_{uu}$ on the right hand side of Figure 5.5 collapses well for the APG and ZPG cases from the near-wall to the outer regions. The FPG case has on average approximately 10% wider structures. While in the log and outer regions, the observed spanwise width in the $R_{uu}$ can be associated with the large-scale structures; the same cannot be applied to the near-wall region. The trend to note is that the widths from the outer towards the near-wall regions scale with $\delta$. Returning to the near-wall $R_{uu}$ in Figure 5.5($b$), it is immediately clear that the correlation analysis is giving a misleading description of the turbulent structures, i.e. the correlation analysis in the near-wall region has picked up the pattern of the large-scale events in the log

and outer regions. Without this precaution, one would infer that the most significant structures in the near-wall have a length scale of $\delta$. This effect grows with Reynolds number. The large-scale structures cause a foot-print in the near-wall region (Hutchins and Marusic, 2007a).

Therefore a tool to separate the large- and small-scale structures, or to extract only the small-scale features is needed. A spatial-filter is one of the ways to filter out the enveloping large-scale effect. This study adapts the filtering method by Hutchins and Marusic (2007a) and Mathis et al. (2009), where the cut-off length scale $\lambda_x/\delta$ = 1 is chosen (refer to Chapter 4). For smaller Reynolds numbers such as in this experiment ($Re_\tau$ = 1900), there could be an insufficient of scale separation. With an insufficient of scale separation, the large- and small-scales features cannot be completely filtered out, and this may affect subsequent correlation operations for the filtered signals. The original signal from sensor 1 shown in Figure 5.8($a$) (top) is filtered into large-scale fluctuation ($u^+_{1l}$); $\lambda_x/\delta \geq 1$ (the thick line in the middle) and small-scale fluctuations ($u^+_{1s}$); $\lambda_x/\delta < 1$ (the thin line at the bottom). The mean local velocity $U^+_c$ is subtracted for the original fluctuating velocities and filtered signals. The procedures are repeated for sensor 2. Note how the large-scale structures signal ($u^+_{1l}$) acts like an envelope which modulates the small-scale fluctuations, ($u^+_{1s}$). Since only the small-scale fluctuations are needed, $u^+_{1s}$ and $u^+_{2s}$ are extracted for correlation analysis.

Figure 5.9 shows spanwise correlation for the small-scale velocity fluctuations $u^+_{1s}$ and $u^+_{2s}$. This is later called $R_{uuss}$. The lines indicated in this figure are spline-fit from the data. $R_{uu}$ collapses for the FPG and ZPG cases however the APG case seems to have a thinner average turbulent structure width (smaller spanwise spacing between the alternating high- and low-speed regions). This still does not follow the trend shown in Table 5.2, which is explained by the fact that there is not enough resolution in the spanwise spacing of the sensors, as sensor 2 is located at $y^+ \approx$ 90 - 100 from sensor 1 (at initial position). This is towards the experimental limit of the facilities used. Figure 5.2 (front view of hotwire diagram) at the start of this chapter shows this limitation. In Figure 5.2, both sensor 1 and two as well as their holders are obstacles in reaching a small enough initial spanwise spacing between the two sensors, $\Delta y$.

Nevertheless Figure 5.9 shows that the correlation's negative-to-negative distance to be $y^+ \approx 160-200$. This is very different to when unfiltered data was used, as shown in Figure 5.5($b$) i.e. $y^+ \approx 1900$ (negative-to-negative distance scales with $\delta$). The effect of high-pass filtering of the fluctuating data is to reduce the minimum-to-minimum distance. Now this phenomenon explains the reason why 5.5($b$) shows negative-to-negative distance

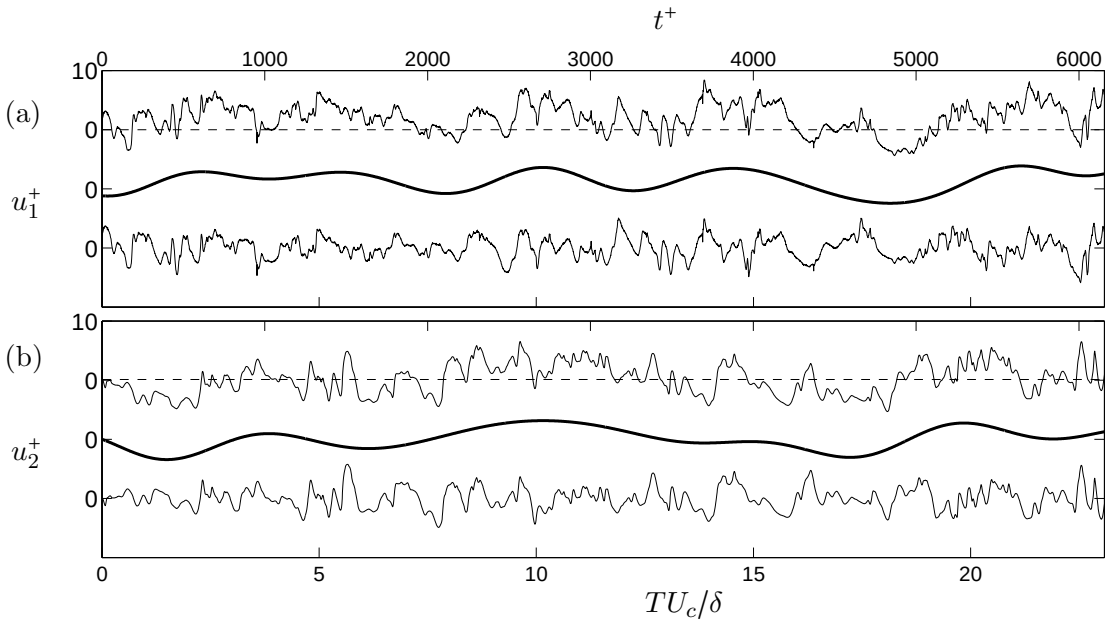


FIGURE 5.8: Sample of fluctuating velocity $u$ signal in the near-wall region at $z^+ \approx 15$ at $Re_\tau \approx 1900$ for ZPG data. $(a)$ Shows $u$ for the first sensor, $u_1^+$. The raw data at the top is filtered into large-scale fluctuations ($u_{1l}^+$); $\lambda_x/\delta \geq 1$ (the thick line in the middle) and small-scale fluctuations ($u_{1s}^+$); $\lambda_x/\delta < 1$ (the thin line at the bottom). Dashed-lines show local mean velocity $U_c^+$. $U_c^+$ is subtracted for original fluctuating velocities and filtered signals. $(b)$ Shows $u$ for the second sensor, $u_2^+$.

of $1\delta$; this is simply due to the influences of the large-scale structures on the small-scales fluctuations in the near-wall region. The conclusion above explains the reason for 'increased' streak spacing in Lee and Sung (2009)'s analysis. The correlations of unfiltered data in Lee and Sung (2009) which was performed at relatively low Reynolds number has yielded minimum-to-minimum correlations distance that scales with $\delta$. This information should not have been taken as the streak spacing.

The choice of $\lambda_x/\delta = 1$ is indeed a good start when trying to filter out the large-scale fluctuations. Trials with a fraction of, or greater than $\delta$ as filter cut-off yield less negative correlation, but this procedure does not change the shape of $R_{uu}$. The conclusion from the near-wall spanwise $R_{uuss}$ is that the FPG and ZPG cases have a similar spanwise streak spacing and, the APG case has a shorter spanwise streak spacing.

Previous studies show that these three cases have different turbulent structures in the near-wall and the outer regions. The energy spectra analysis indicates that the near-wall structures have a similar streamwise length scale of $\lambda_x^+ \approx 1000$ in all pressure gradient

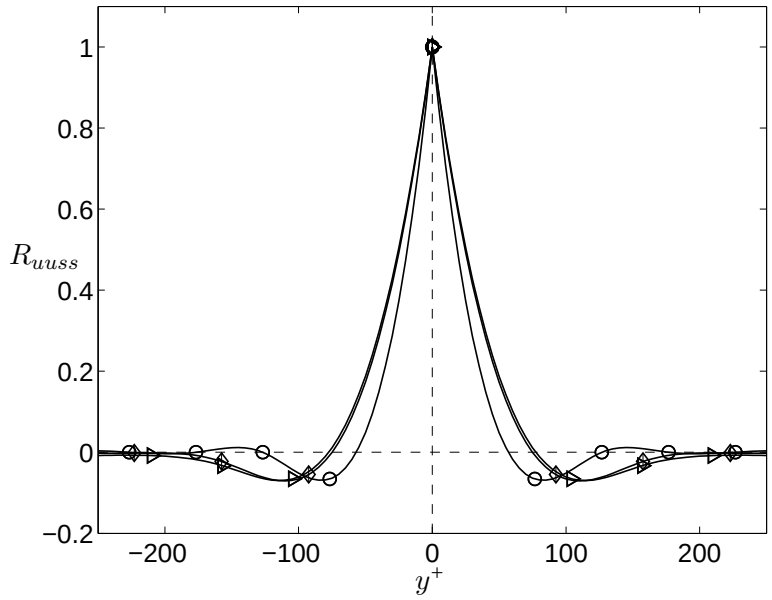


FIGURE 5.9: $R_{uuss}$ for small-scale fluctuations $u^+_{1s}$ and $u^+_{2s}$ in the near-wall region at $z^+ \approx 15$ at $Re_\tau \approx 1900$ for three pressure gradient cases. Symbols: (⟡) FPG, (▷) ZPG and (o) APG.

cases. The streak spacings are in the same order for the APG, ZPG and FPG cases (even though the APG case might have slightly thinner streak width).

A few important features are established in the streamwise velocity fluctuations analysis. In APG, the large-scales are broken-up and become approximately shorter by half their average streamwise length in the ZPG boundary layer. In FPG, the large-scale structures' width grow by 10%, though the length stays the same. The big differences in the three boundary layer cases are especially evident in the outer region. The differences get smaller in the log region and even smaller in the near-wall region. Correlation of small-scale velocity fluctuations reveals that the streak spacing does not significantly change across the pressure gradient cases, in contrast to several recent reports.

# Chapter 6

# History effect

This chapter discusses the effect of the streamwise distance for which the boundary layer is exposed to pressure gradient. This term is simply called the 'history effect'. An example is presented to discuss the statistics from APG flows at matched conditions. The only one variable in these two flows is that one flow is exposed to APG for a much longer streamwise distance than the other. The distances for which these boundary layers are exposed to APG are $9.8\delta$ and $20.2\delta$ respectively. The analysis shows that the mean velocity, skewness and flatness profiles collapse, however, there are more large-scales when the boundary layer is exposed for longer distance to APG, leading to higher turbulence intensity profile in the outer region.

One way to evaluate the extent of the history effect is to compare turbulent statistics from flow with the same pressure gradient parameter, $\beta$ however with different streamwise distance, therefore the history that these two flows have experienced at the measurement points are different. The other variables concerning the state of the flows proposed by Perry et al. (2002) shown in (3.31) i.e. $\Pi$, $S = U_1/U_\tau$, $\beta$, $\zeta = S\delta_c \mathrm{d}\Pi/\mathrm{d}x$ shall be constant. Furthermore, any other variables that affect the measurement such as $l^+$, should also be fixed.

The current experimental set up is based on a linearly increasing coefficient of pressure, $C_P$ arising from constant $\mathrm{d}P_1/\mathrm{d}x$ and at the same time a moderate pressure gradient. In order to obtain another measurement with the same pressure gradient parameter, $\beta$ but with a longer exposure to APG, a milder roof gradient is necessary. Therefore, the author has set-up the wind tunnel ceiling to achieve a milder $\mathrm{d}P_1/\mathrm{d}x$. The resulting $C_P$ is shown by the symbol '□' in Figure 2.5 (Chapter 2). In order to achieve a comparable

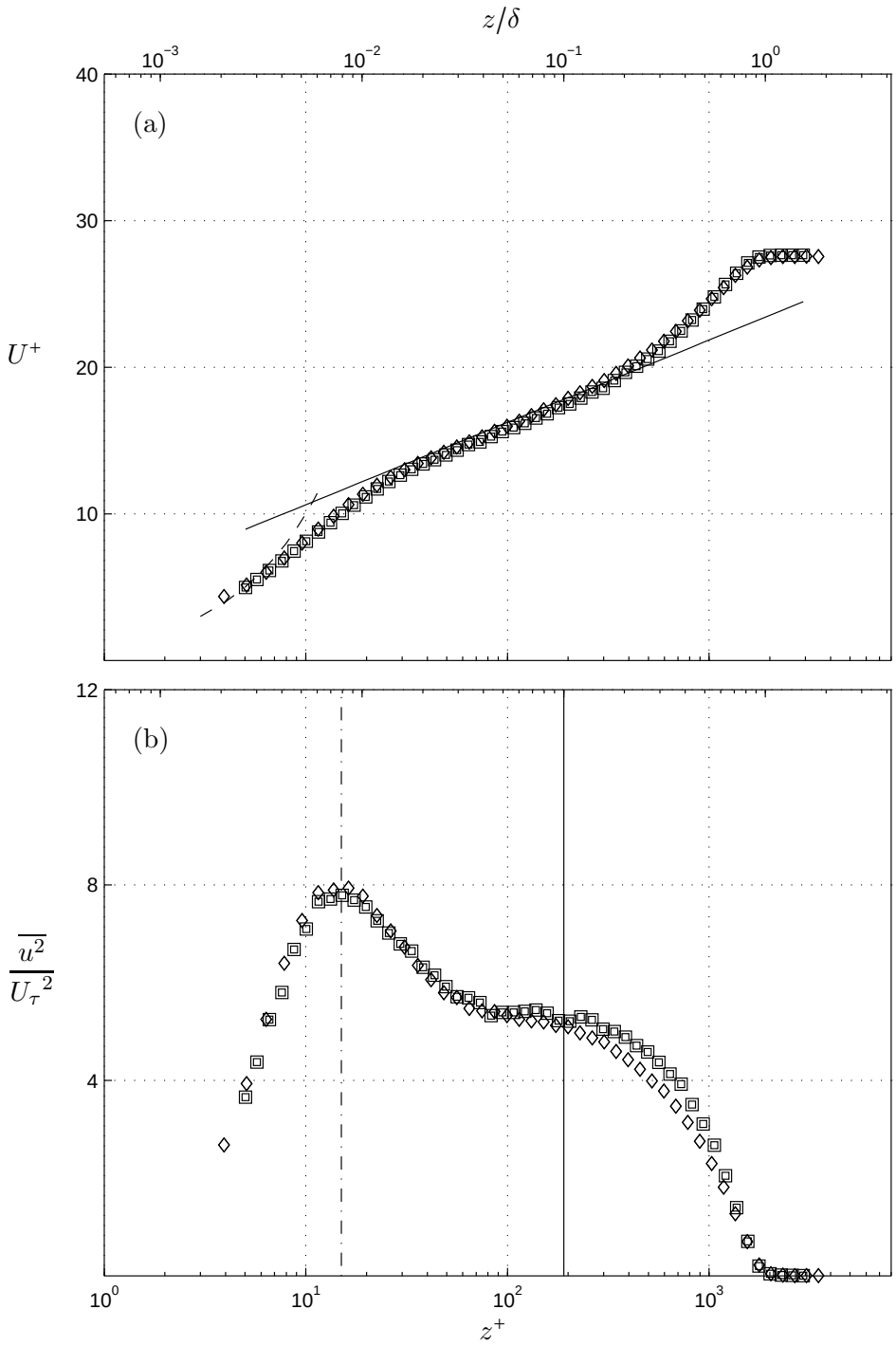


FIGURE 6.1: Comparison of the mean statistics for APG boundary layers with constant $Re_\tau \approx 1900$, but at milder coefficient of pressure gradient, $\mathrm{d}C_p\mathrm{d}x = 0.1144$ identified as *Case 1* (⧈) *versus* $\mathrm{d}C_p\mathrm{d}x = 0.2185$ identified as *Case 2* (⋄). (*a*) Mean velocity and, (*b*) turbulence intensity profiles. For other parameters, refer to table 2.1. In (*a*), the solid line shows equation 3.6 with $\kappa = 0.41$, $A = 5.0$, the dashed line shows $U^+ = z^+$. In (*b*), the dashed-dot line indicates $z^+ = 15$ and the solid line indicates $z/\delta = 0.1$.

| | Name | Exposure | Stn, $x$ (m) | $C_p$ | $\frac{dC_P}{dx}$ | $\Pi$ | $S = \frac{U_1}{U_\tau}$ | $\beta$ | $\zeta = S\delta_p\frac{d\Pi}{dx}$ |
|---|---|---|---|---|---|---|---|---|---|
| ⧈ | *Case 1* | $20.2\delta$ | 5, 4.78 | 0.1941 | 0.2185 | **0.91** | **27.58** | **0.81** | **$\approx$ 0.5** |
| ◇ | *Case 2* | $9.8\delta$ | 2, 3.50 | 0.1904 | 0.1144 | **0.95** | **27.55** | **0.91** | **1.45** |

TABLE 6.1: Parameters for comparison of APG flows with a shorter and a longer streamwise exposure to APG at $Re_\tau \approx 1850$ and $l^+ = 16$.

Reynolds number, different inlet velocities were used. The flow that is exposed to a longer streamwise distance with a milder $dP_1/dx$ from the new wind tunnel set-up is identified as *Case 1* and shown along with existing flow with a shorter streamwise APG exposure, identified as *Case 2*. The distance for which these boundary layers are exposed to APG is taken from the start of the APG section, i.e. $x$ = 2.9m. The non-dimensionalised exposure lengths are $9.8\delta$ and $20.2\delta$ respectively. The other parameters are shown in Table 6.1. As shown in the table, *Case 1* is from Station 5. *Case 2* is from the constant Reynolds number $Re_\tau \approx 1900$ data set shown earlier in Table 2.1. As mentioned earlier, the Reynolds number and sensor length are constant: $Re_\tau \approx 1850$ and $l^+ \approx 16$. The parameters in Perry et al. (2002) are also shown in the table (in bold); these parameters are constant except for $\zeta$. Note that the calculations for $\zeta = S\delta_p d\Pi/dx$ for *Case 2* is an approximation because the measurements with the new ceiling only included station 4 and station 5. Initially, the term $dP_1/dx$ was calculated based on two measurement points only (the value for the $d\Pi/dx$ is based on a smaller streamwise span, i.e. $dx$ = 4.78 - 4.46 = 0.32 m), this may not yield an accurate result. Since $\Pi$ for ZPG is known to be in the region $0.5 < \Pi < 0.6$ (e.g. Monkewitz et al., 2008, Nagib and Chauhan, 2008), therefore this approximation is now extended over a longer distance, $x$, i.e. it includes the ZPG point at station 1 ($x$ = 2.90 with assumed $\Pi$ = 0.6).

Figure 6.1($a$) shows the comparison of mean velocity profiles for *Case 1* and *Case 2*. The mean velocity profiles scaled with inner variables collapse well for the entire boundary layer. As friction velocity, $U_\tau$ from both flows were obtained from oil-film interferometry, (OFI), both profiles show deviations from the log law of the wall.

Figure 6.1($b$) displays the turbulence intensities profiles, $\overline{u^2}/{U_\tau}^2$. In the near-wall region, $\overline{u^2}/{U_\tau}^2$ collapse well when scaled with inner variables. However, in the outer region, $z/\delta \gtrsim 0.1$, $\overline{u^2}/{U_\tau}^2$ for *Case 1* is slightly higher. This suggest that there is more energy

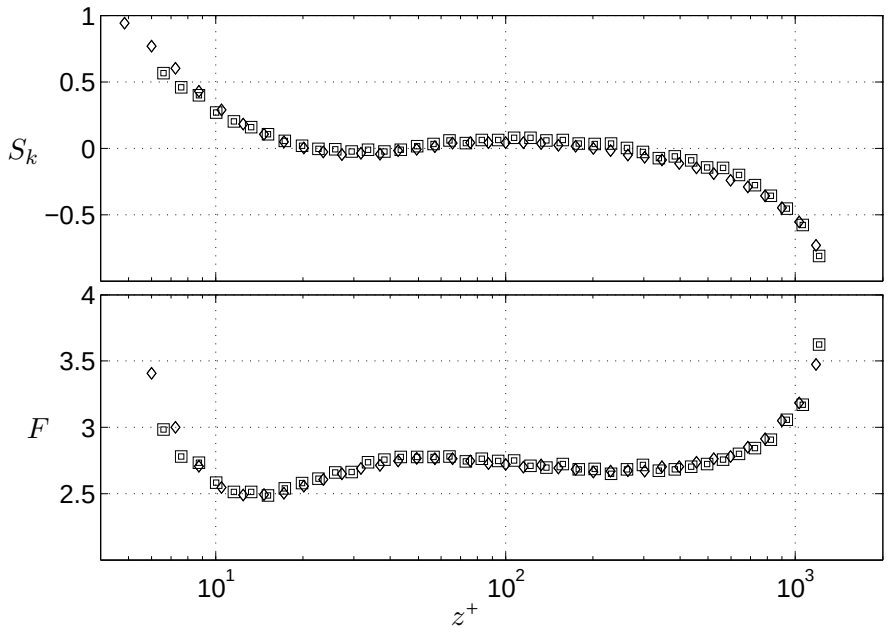


FIGURE 6.2: (a) Skewness $S$ and (b) flatness $F$ for adverse, zero and favourable pressure gradients at $Re_\tau \approx 1900$ and $\beta \approx 0.9$ for *Case 1* (⧈), and *Case 2* (⋄). For other parameters, refer to Table 6.1.

for the flow exposed longer in APG, therefore energy spectra analysis is required to further understand the energy distribution.

Figure 6.2($a$) shows the comparison of the skewness, $S_k$ for *Case 1* and *Case 2*. $S_k$ profiles for both cases collapse with inner variables. It can also be shown that $S_k$ also collapses if scaled with outer variable, $\delta$ (not shown). Figure 6.2($b$) shows the flatness, $F$ for both cases, again $F$ collapses well. $F$ also collapses if scaled with outer variable, $\delta$ (not shown).

The pre-multiplied spectra scaled with friction velocity, $k_x\phi_{uu}/U_\tau^2$ for *Case 1* and *Case 2* at each wall-normal location are shown in Figure 6.3($a$) to ($d$). In the near wall region, in Figure ($a$), the inner peak occurs at $\lambda_x^+ \approx 1000$. There is no particular deviation in the energy distribution at $z^+ \approx 100$ in Figure ($b$). In the geometric centre of the log region, $z^+ \approx (15Re_\tau)^{1/2}$ in Figure ($c$), the most energetic wavelength occurs at $\lambda_x/\delta \approx 6$ as in ZPG cases. The $\lambda_x/\delta = 6$ is shown by the solid vertical line. Note that in Chapter 4, in the strong APG parameter, $\beta$ cases, the most energetic wavelength occurs at $\lambda_x/\delta \approx 2$, however, for these very weak cases ($\beta \approx 0.9$), no substantial difference from the ZPG cases is observed, as expected. In the outer region, $z/\delta \approx 0.3$ shown in Figure ($d$), *Case 1* has more energy than *Case 2*. The most energetic structures are still at $\lambda_x/\delta \approx 3$,

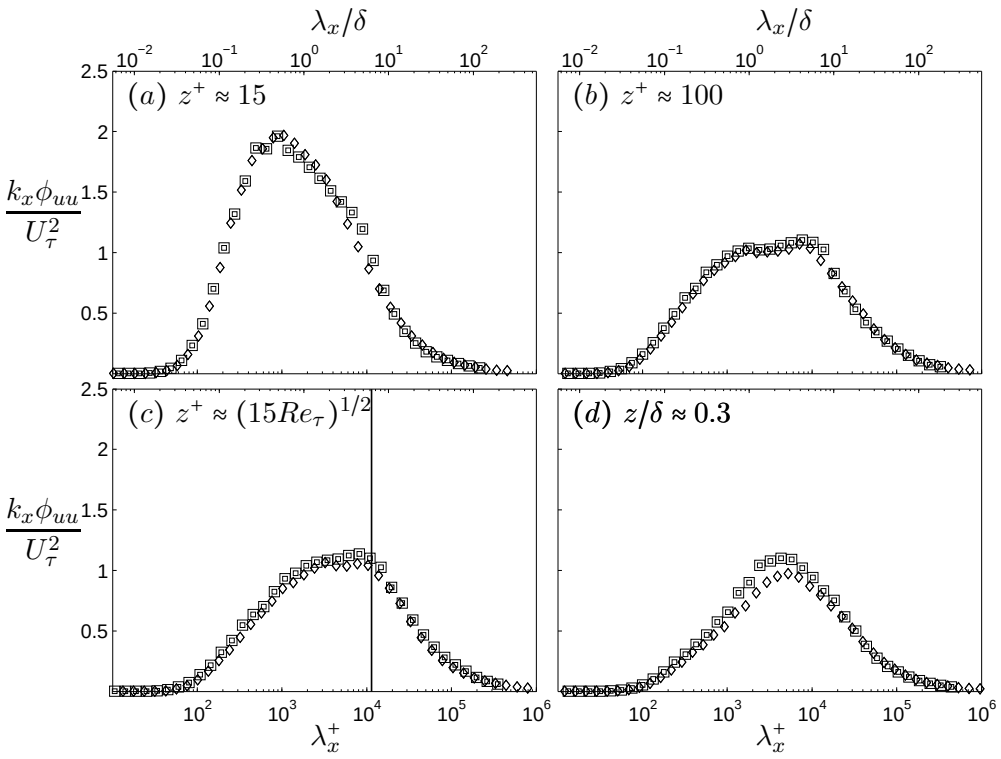


FIGURE 6.3: Pre-multiplied energy spectra, $k_x\phi_{uu}/U_\tau^2$ at constant $Re_\tau \approx 1900$ for *Case 1* (▣), and *Case 2* (◇), at four selected wall-normal locations, (*a*) $z^+ \approx 15$, (*b*) $z^+ \approx 100$, (*c*) $z^+ \approx (15Re_\tau)^{1/2}$, and (*d*) $z/\delta \approx 0.3$. Solid line indicates $\lambda_x/\delta = 6$. For other parameters, refer to Table 6.1.

this could be shown when energy in the outer region is scaled with its maximum value, $k_x\phi_{uu}/k_x\phi_{uu}|_{max}$ as in Chapter 4 (not shown).

For brevity, the pre-multiplied spectra scaled with local free stream velocity, $k_x\phi_{uu}/U_1^2$ are not shown. However, it can be shown that $k_x\phi_{uu}/U_1^2$ for both cases collapse at $z^+ \approx 15$, $z^+ \approx 100$ and $z^+ \approx (15Re_\tau)^{1/2}$. However, $k_x\phi_{uu}/U_1^2$ for *Case 1* is higher than *Case 2*, similar to the trend in Figure 6.3(*d*). This suggests that the flow with a longer exposure to APG does have a higher energy in the outer region, as any discrepancies due to the scaling employed are ruled out.

The higher energy shown in Figure 6.3(*d*) is related to the higher turbulence intensities seen in Figure 6.1(*b*). At this juncture, the reason for the higher energy in *Case 1* is not known. Therefore it is helpful to decompose the energy in to a small– and a large-scale component as in Chapter 4. Figure 6.4 shows the decomposed turbulence intensity profiles for *Case 1* and *Case 2*. The vertical line is $z/\delta = 0.1$, where turbulence intensities between the two flows start to show differences. The difference is caused by

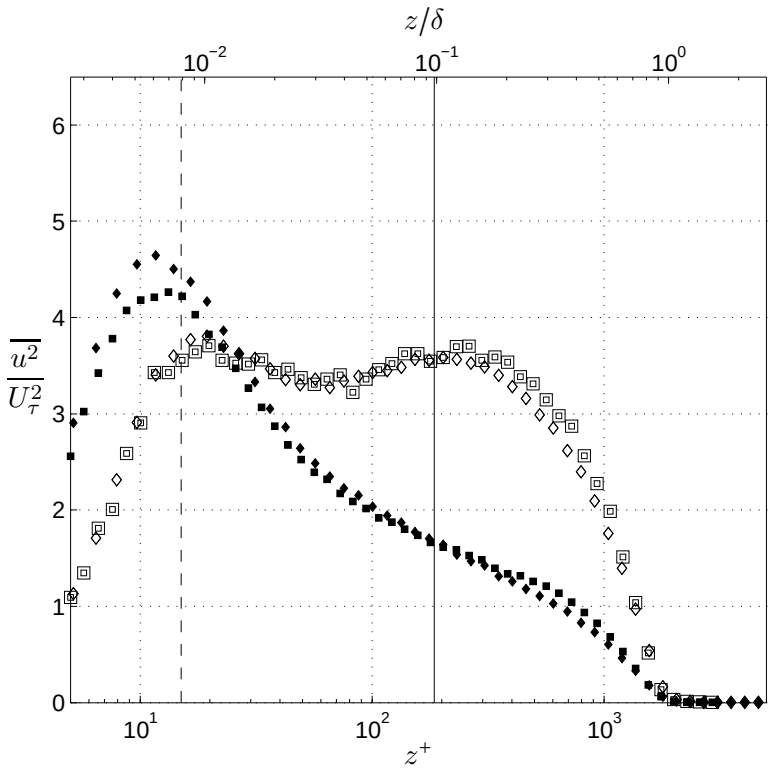


FIGURE 6.4: Decomposition of the broadband turbulence intensity profiles $\overline{u^2}/{U_\tau}^2$ into a small- and a large-scale components at constant $Re_\tau \approx 1900$ for *Case 1* and *Case 2*. Small-scale components ($\lambda_x/\delta < 1$) symbols: (▪) *Case 1* and (◆) *Case 2*. Large-scale components ($\lambda_x/\delta \geq 1$) symbols: (▣) *Case 1* and (◇) *Case 2*. Dashed line denotes $z^+ = 15$ and solid line denotes $z/\delta = 0.1$.

more large-scale contribution in *Case 1*. Further away from the wall at $z/\delta \approx 0.4$, there is also increased contribution from the small-scales in *Case 1*.

Even though most of the turbulence statistics (mean velocity, skewness and flatness profiles) collapse when two APG boundary layers with a similar APG parameter $\beta$ are compared, the turbulence intensities are higher in the outer region if the boundary layer is exposed to APG spatially long enough. In this case, the difference in exposure distance is approximately twice ($20.2\delta$ for *Case 1* and $9.8\delta$ for *Case 2*). It is proposed that as the exposure distance increases, both small– and large-scale features increase in the outer region - the reason for the increased turbulence intensities here. These differences may be associated with $\zeta$, refer to Table 6.1. Nevertheless, the changes observed in the turbulence intensities and spectra are small and it is felt that the effect of history does not give significant change to the analysis in the Chapters 3 and 4.

# Chapter 7

# Concluding remarks and outlook

The overall goal of the project is to determine the effect of pressure gradient on the structure of boundary layers. Several experiments were performed, the most important ones being the constant inlet velocities both in APG and FPG flows. Furthermore, in order to isolate the Reynolds number effect, constant $Re_\tau$ experiments were performed. As spatial resolution is getting more important, these measurements were performed complying with the generally accepted sensor length (Hutchins et al., 2009). In fact, the effect of the sensor length, $l^+$, is studied by varying $l^+$ in pressure gradient flows. Other requirements to ensure resolved measurements, such as the boundary layer turnover times and sampling frequency, are adhered to.

The main conclusions of these studies are as follows:

1. The oil-film interferometry method was used to determine the wall shear stress and it was shown that results obtained were different from those of the Clauser chart method, for stronger pressure gradients ($\beta \gtrsim 2$). These deviations however are quite small in FPG flows.

2. In the traditionally accepted logarithmic region of the flow, there is a systematic decrease in mean velocity below the log law with increasing APG strength. Further inspection of this region via the diagnostic function revealed that the wake of the mean velocity profile begins much closer to the wall in APG than in the ZPG flows. This leads to the conclusion that, for mild to strong adverse pressure gradients, there is no identifiable logarithmic region (within the Reynolds number range of the study, $1500 \lesssim Re_\tau \lesssim 4000$). In contrast, when subjected to stronger FPG, the log region extends further towards the edge of the boundary layer.

3. Reynolds number similarity is observed in the mean velocity profiles when $\beta$ is held constant and the shape factor formulation of Monkewitz et al. (2008), developed for ZPG flows, appears to follow the data closely. There are two set of experiments to demonstrate this which are the constant $\beta \approx 1.6$ and the constant $\beta \approx 4.3$. This evidence is further confirmation towards Reynolds number similarity in constant APG parameter $\beta$, as the mean velocity profiles of these data also show a constant deviation from the log law.

4. Skewness profiles show that increasing APG strength causes a rise in the skewness and in contrast, FPG reduces skewness. A high-pass filter reduces the skewness profile in all pressure gradient cases in the near-wall region, confirming the results of Metzger and Klewicki (2001). In the outer region, a high-pass filter brings the skewness close to Gaussian distribution from large negative values. The skewness relationship with amplitude modulation (AM) in ZPG (Mathis et al., 2011) is repeated in pressure gradient flows. It is shown here that the cross product term $\overbrace{3u_L^+u_S^{+2}}$ of the expanded skewness (into large– and small-scale components, $S_k(u_L^+ + u_S^+)$ resembles the AM profiles proposed by Mathis et al. (2009). This is especially apparent when a multiplier of 2 is introduced to the cross product term i.e. $\overbrace{6u_L^+u_S^{+2}}$ is similar to the AM profiles proposed by Mathis et al. (2009).

5. From energy spectra considerations, the large-scale structures in the turbulent boundary layer are clearly energised more strongly than the small-scale structures by the presence of the adverse pressure gradient. The increased energy of these large motions is felt throughout the layer, which can also be observed from the decomposition of the turbulence intensities into small- and large-scale contributions. The rise of the large-scale energy due to pressure gradient is observed to be much more substantial than that due to Reynolds number. The large-scale structures are broken down (in the streamwise direction) due to APG, the most energised structures in the outer region occur at $\lambda_x/\delta \approx 3$ and the outer peak occurs at a much further wall-normal distance, $z/\delta \approx 0.3$. This is in contrast with ZPG flow, where the most energetic structures have a wavelength of $\lambda_x/\delta \approx 6$ and they reside in the log region, $z/\delta \approx 0.06$ or $z^+ \approx (15Re_\tau)^{1/2}$ (Hutchins and Marusic, 2007a, Mathis et al., 2009).

   Scaling the energy spectra results with local free stream velocities, or simply with the maximum value of the energy spectra magnitude itself, revealed that the shorter structures are not due to the scaling used. This agrees with Skåre and

Krogstad (1994), however there is no clear evidence from the energy spectra results that there is a stretching of the structures in FPG, as was reported by Dixit and Ramesh (2010).

6. The spatial resolution of hot-wires for boundary layers exposed to pressure gradient is also analysed in the thesis. In general, small-scale attenuations occur in pressure gradient boundary layers similar to the ZPG boundary layers, as described in Hutchins et al. (2009). However, as one of the effects of APG is to increase the presence of large-scale structures in the near-wall region, measurement with large enough $l^+$ will misleadingly indicate the most active structure in the near-wall region to be longer than the nominal $\lambda_x^+ \approx 1000$ on the one-dimensional energy spectra map. At $l^+ \approx 40$, the most energised structures were detected to occur at $\lambda_x^+ \approx 1500$, therefore it is recommended that studies in APG be performed at $l^+ \lesssim 20$. Varying $l^+$ in FPG does not change the detected wavelength of the most active structures i.e. $\lambda_x^+ \approx 1000$.

7. Two-point correlation shows that APG increases the structural inclination angle to $\theta_{struc} \approx 20^o$ (nominal values of $12^o < \theta_{struc} < 18^o$ in ZPG). FPG suppresses the structural inclination to $\theta_{struc} \approx 11^o$. The difference in the structural inclination angle between the three pressure gradients cases are however small because of the mild pressure gradients.

   The streamwise slice of the correlation maps shows that streamwise length of the correlation is less for the APG than for the ZPG and FPG cases. This result, together with the energy spectra results, confirms that APG breaks the structures (they are shorter in the streamwise direction).

8. Energy spectra, turbulence production and two-point correlation analysis have shown that the near-wall region is not disturbed by pressure gradient. Given a similar adverse pressure gradient parameter $\beta$ as in Lee and Sung (2009), the streak spacing remains similar as compared with Lee and Sung (2009). However, with a high-pass filter applied to the fluctuating velocities $u$, the near-wall streak spacing seems to be $y^+ \approx 150 - 180$ regardless of pressure gradients. This indicates that the streak spacing is insensitive[1] to pressure gradients and the changes reported by Lee and Sung (2009) i.e. increasing streak spacing with APG, is only due to the footprint effect of the large-scale features in the outer region.

[1]There may be some changes in the near wall motion as discussed in Section 3.15 (Turbulence production) and Chapter 4 (Energy distribution), however these changes do not cause the streak spacing increase or decrease by the magnitude shown in Lee and Sung (2009) i.e. three to four times

## 7.1 Recommendations for futures work

A few settings could be improved in the current experimental set-up. In the two-point correlation, the closest distance between two sensors is only $y^+ \approx 80$. This is towards the experimental capability of the current set up, however the laboratory is actively testing much smaller sensor sizes. This would enable measurement of, for example streak spacing, to be performed more accurately.

The Reynolds numbers of the current experiment is in the range $1500 \lesssim Re_\tau \lesssim 4000$. More points in the high Reynolds numbers are needed to confirm some of the analysis. For example, in the energy spectra analysis, at $Re_\tau \approx 3000$, there may be an insufficient scale separation. In another example, the analysis of the shape factor similar to Monkewitz et al. (2008), was performed at relatively low Reynolds numbers.

The entire experiment was performed with normal hotwires, therefore spanwise and wall-normal velocity fluctuations $v$ and $w$ were not measured. Thus, statistics concerning $v$ and $w$ could not be analysed and when necessary, as in the case of turbulence production, were approximated.

# Appendix A

# Equipment

## A.1 List of equipment

The following equipment was used for hotwire and OFI measurements:

| | Equipment | Makes/Model |
|---|---|---|
| | Hotwire equipment | |
| 1 | Anemometer | DISA /AA LAB/ Melbourne Uni. Constant Temperature Anemometer (MUCTA) |
| 2 | Pressure sensor | Sensor Technique |
| 3 | Encoder | Renishaw RGH24H |
| 4 | Temperature sensor | Termistor Omega Engrg |
| 5 | Data Acquisition System | Data Translation |
| 6 | Pressure Transducer | MKS Baratron 10Torr |
| 7 | Signal conditioner | MKS Type 670 |
| 8 | Scanivalve | 69 Channel |
| 9 | Laptop | Dell Latitute 6400 with Matlab |

continue on next page

from previous page

| | OFI equipment | |
|---|---|---|
| 1 | Lamp | OSRAM Vialox SON-E 70 or 90 watt |
| 2 | Camera | Nikon D90 |
| 3 | Lense | 105 mm micro Nikkor |
| 5 | Another laptop | Dell Latitute 6400 with Matlab |
| 6 | A tripod | |
| 7 | Syringes | |

The pressure sensor, pressure transducer, signal conditioner and temperature sensor from hotwire equipment were utililised.

TABLE A.1: List of equipment

## A.2 Oil-Film Interferometry (OFI) Silicone Oil Calibration

Oil-Film Interferometry (OFI) measurements were performed for the particular hotwire measurements in ZPG, APG and FPG. The locations where OFI measurements were to be carried out, were first identified with very high accuracy. The wind tunnel floor was drilled with a special drill to avoid chipping of the round edge. Eight sets of aluminium plugs and frames were constructed. Five of these plugs were installed on the wall, while the remaining three, were retained as spares. The frames were installed in stages to ensure that the epoxy applied around the aluminium frame (and the non-metal edge of the wind tunnel) did not create dips or bulges. During the installation, good care was taken not to scratch the floor of the wind tunnel and to avoid any of the pressure taps getting stuck.

Calibrations were performed for the used silicone oils by Jean-Daniel Ruedi and given to the author via private communications. The calibration details are given in tables A.2 and A.3.

The calibration used here has been used in Chauhan et al. (2010). An in-house calibration has also been carried out and internally and the calibration curve and equation is shown in Figure A.1. Since the oil has been used within the calibrated temperature limits, there should not be any issue with viscousity. It is noted that since the temperature sensor is located slightly away from the viewing window/glass plug (where oil is dropped), it is possible that sometimes, the temperature of the glass plug is slightly higher than the sampled temperature (used for calculation). However, it has been in

| | | |
|---|---|---|
| Silicon oil | | |
| Date | : | 25 Apr. 2008 |
| Silicon oil 20 cst | : | from EPFL-LMF (Lion d'or) |
| Refraction index | : | 1.4 |
| Oil density | : | 951 kg/m$^3$ |
| | | |
| Equipment | | |
| Thermo-regulated Lauda bath E200 | | |
| Capilary viscometer | : | Schott 50120 II, k: 0.1022 |
| type 28540061 | | App 1036705, Tcorr = 0 for t > 80 |
| Handheld thermometer | : | Flucke 52II SN: 74690102 |
| | | |
| Coefficients for 20 cst oil | | |
| General model | : | a$e^{bx}$, 95% confidence bounds |
| a | : | 5.015e-05 (4.913e-05, 5.116e-05) |
| b | : | -0.01896 (-0.01976, -0.01816) |
| sse | : | 3.7074e-15 |
| rsquare | : | 0.9998 |
| dfe | : | 2 |
| adjrsquare | : | 0.9997 |
| rmse | : | 4.3055e-08 |

TABLE A.2: Silicone oil 20 cst Calibration

practice that whenever illumination is not required, the bulb is covered with a piece of paper to prevent it from heating the glass plug.

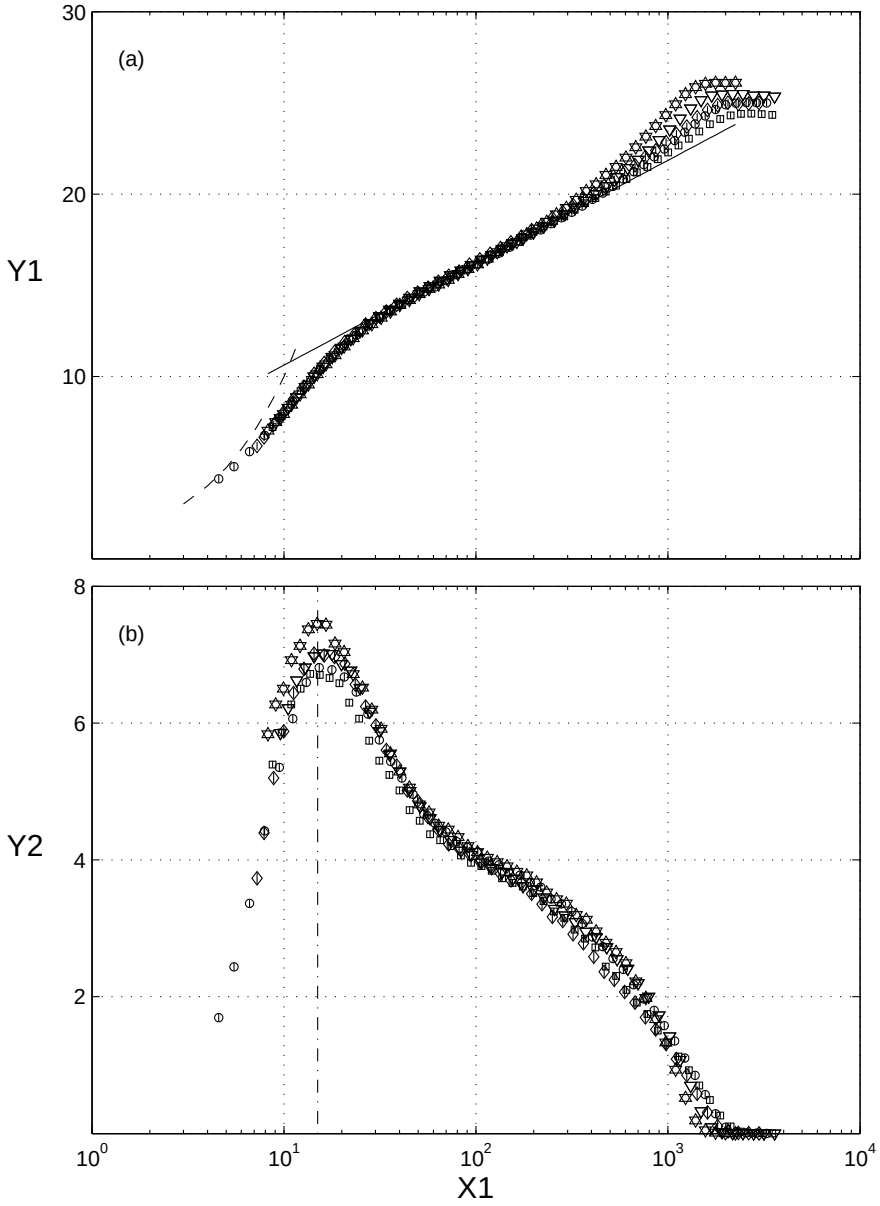


FIGURE A.1: Calibration of 20 cSt oil performed at the University of Melbourne.

| | | |
|---|---|---|
| Silicon oil | | |
| Date | : | 2 June 2008 |
| Silicon oil 200 cst | : | from EPFL-LMF (Lion d'or) |
| Refraction index | : | 1.4 |
| Oil density | : | 968 kg/m$^3$ |
| | | |
| Equipment | | |
| Thermo-regulated Lauda bath E200 | | |
| Capilary viscometer | : | Schott 53223 IIc, k: 0.3129 |
| No 73835 | | |
| Handheld thermometer | : | Flucke 52II SN: 74690102 |
| | | |
| Coefficients for 200 cst oil | | |
| General model | : | a$e^{bx}$, 95% confidence bounds |
| a | : | 3.320e-04 (3.287e-04, 3.353e-04) |
| b | : | -1.918e-02 (-1.957e-02, -1.878e-02) |
| sse | : | 1.6106e-13 |
| rsquare | : | 0.9999 |
| dfe | : | 3 |
| adjrsquare | : | 0.9998 |
| rmse | : | 2.3170e-07 |

TABLE A.3: Silicone oil 200 cSt Calibration

# Appendix B

# Additional discussions

## B.1 Skewness

The analysis and results in this section highlight the differences between the external geometry-flows (APG, ZPG and FPG TBL flows) with the internal geometry-flows (pipe and channel flows) obtained from Monty et al. (2009) and Mathis et al. (2009). These comparisons are not the main focus of the thesis, however they provide insightful knowledge into these two types of flows. Understanding the internal and external geometry-flows at a certain point helps explain the differences between the three TBL flow cases better. To ensure that spatial resolution issues are accounted for, the Reynolds number and the sensor length are constant, $Re_\tau \approx 3000$ and $l^+ \approx 30$[1]. It is important to have a constant sensor length parameter, $l^+$, as the attenuations to the small-scale features in the near-wall region is known to change the skewness (Section 3.13, Johansson and Alfredsson (1983)).

Figure B.1($a$) shows the skewness of streamwise velocity fluctuations for APG, ZPG, FPG TBL flows as well as for pipe and channel flows at $Re_\tau \approx 3000$. In the near-wall region, $z/\delta < 0.01$, the skewness collapse ($S_k \approx 0$) for the internal geometry-flows and the FPG flow. The skewness is slightly higher for the ZPG, however it is evident that the skewness is much higher ($S_k \approx 0.2$) for the APG flow. Analysis from Section 3.13 has shown that the large-scale features are responsible for the increase in the skewness. In the outer region ($z/\delta \approx 0.3$), the same trend is observed.

[1]It is noted that for the APG case, the attenuations of the small-scale structures are significant. These attenuations cause much lower $\overline{u^2}/{U_\tau}^2$ in the near-wall region and analysis of energy spectra for such spatially-unresolved data yields an inner peak that occurs at superficially longer wavelengths (Section 4.3).

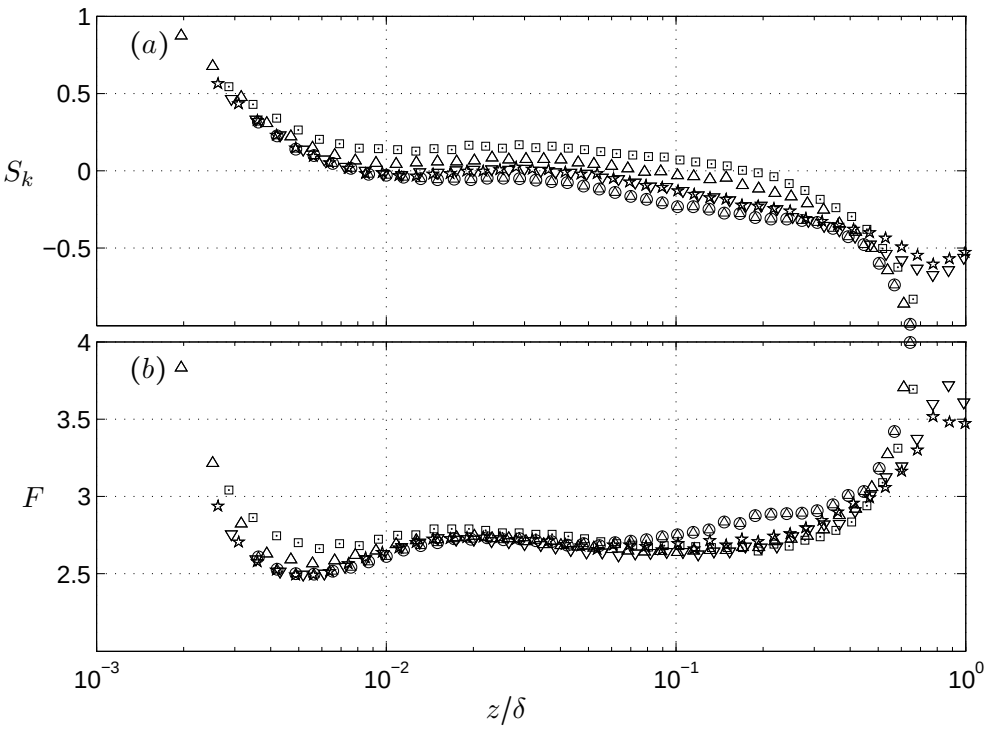


FIGURE B.1: $(a)$ Skewness $S_k$ and $(b)$ flatness $F$ for adverse, zero, favourable pressure gradients, pipe and channel flows at $Re_\tau \approx 3000$. Symbols: (⊡) APG, (△) ZPG, (⏢) FPG, (☆) pipe and (▽) channel flows. For other details, refer to Table 2.1.

The flatness shown in Figure B.1$(b)$ collapses for the internal geometry-flows and the FPG flow in the near wall region, $z/\delta < 0.02$. The minima in the flatness profiles occur at $z/\delta \approx 0.005$. Here, the flatness is lowest ($F \approx 2.5$) for the internal geometry-flows and the FPG flow. The flatness is higher for the ZPG flow, and highest ($F \approx 2.7$) for the APG flow. At $z/\delta \approx 0.3$, the flatness almost collapses for the internal geometry-flows, together with the APG and ZPG flows, however interestingly, the flatness for FPG deviates from this trend.

Figures B.2$(a)$ and $(b)$ compare probability density function (PDF) for the internal geometry and external geometry-flows at $Re_\tau \approx 3000$. The large negative skewness for the internal geometry-flows in Figure B.1$(a)$ is shown more clearly by the larger negative deviation from $(u - \overline{U})/U_\tau = 0$ in Figure B.2$(a)$. There appear to be two collapses, one for the internal geometry-flows and the other (near-collapse) for the external geometry-flows. In the outer region, only the internal geometry-flows collapse. The range for velocity fluctuations is largest in the APG case and smallest in the FPG case.

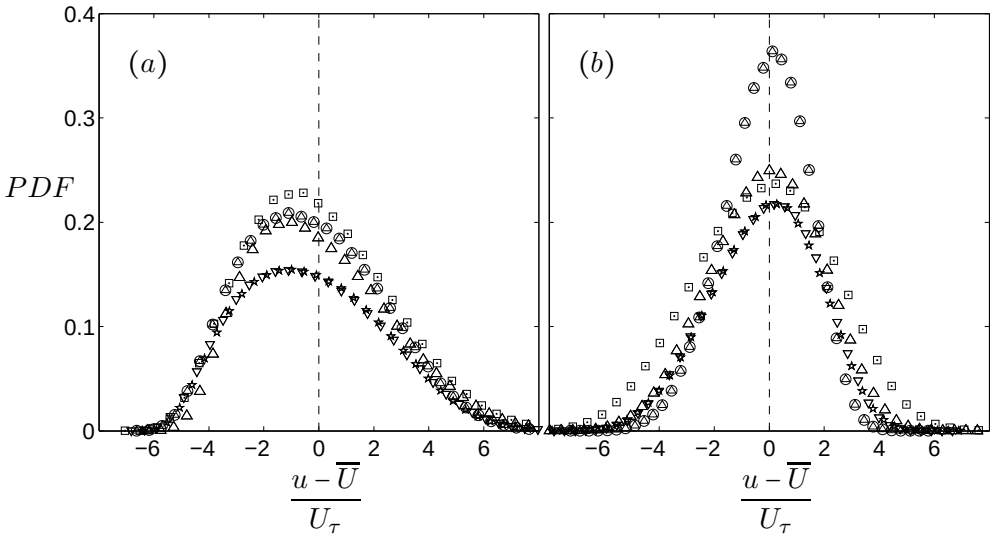


FIGURE B.2: Probability density function (PDF) at $(a)$ $z^+ \approx 15$ and, $(b)$ $z/\delta \approx 0.3$ for adverse, zero, favourable pressure gradients, pipe and channel flows at $Re_\tau \approx 3000$. (⊡) APG, (△) ZPG, (◬) FPG, (☆) pipe and (▽) channel flows.

In order to understand the effect of the larger-scale features in the internal geometry-flows on the skewness, it is useful to analyse the fluctuating velocities when the larger-scale features are removed. In Section 3.13, it was shown that APG causes the larger-scales to be more energised in the near-wall region. Consequently, the skewness also

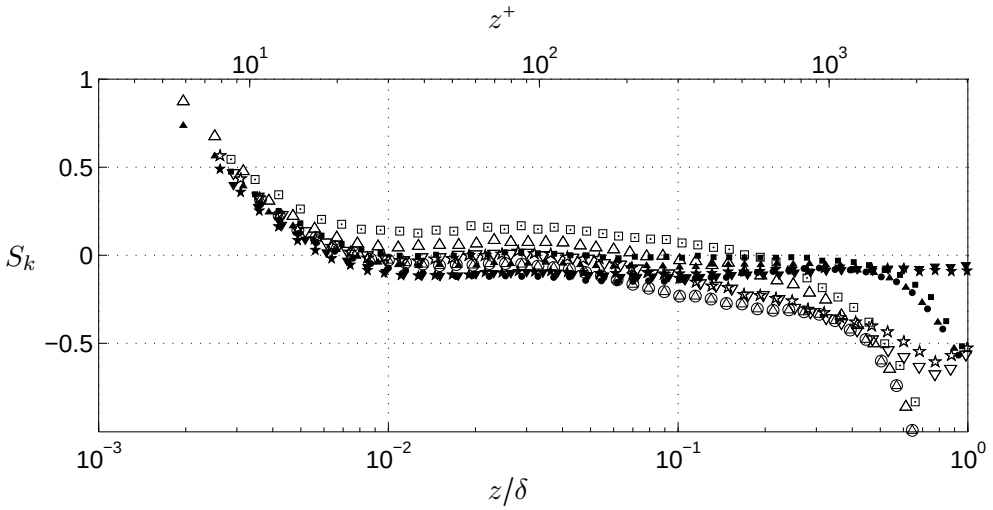


FIGURE B.3: Skewness $S_k$ for adverse, zero, favourable pressure gradients, pipe and channel flows at $Re_\tau \approx 3000$. Symbols: (⊡) APG, (△) ZPG, (◬) FPG, (☆) pipe and (▽) channel flows. Filtered data ($\lambda_x/\delta < 1$) symbols: (■) APG, ZPG (▲), FPG (●), pipe (⋆) and channel flow (▼).

increases[2]. A high-pass filter with a cut-off wavelength of $\lambda_{xc} = \delta$ was employed and the corresponding skewness profiles are shown in Figures B.3. Generally, a high-pass filter causes the skewness to decrease in the near-wall region. The shift-downs in the values of the skewness coefficients for the internal geometry, ZPG and FPG flows are $\Delta S_k \approx 0.1$, however for the APG flow the value is double, $\Delta S_k \approx 0.2$. This indicates that in this region, the large-scale features have more significant roles in the APG flow than in any other flows considered here. The trend observed in the near-wall region persists until the log region. At $z/\delta = 0.3$, the high pass brings the distribution of the skewness closer to the Gaussian distribution.

## B.2 Spectra

Similar analysis as in Section B.1 is provided here for energy spectra to compare the internal and external geometry-flows. Figures B.4($a$) to ($d$) show pre-multiplied spectra scaled with friction velocity, $k_x\phi_{uu}/U_\tau^2$ at four selected wall-normal locations similar to Figures 4.3($a$) - ($d$). However in these figures, the energy spectra for pipe and channel flows discussed in Monty et al. (2009) and Mathis et al. (2009) are added. Figure B.4($a$) shows that energy distribution in the near-wall ($z^+ \approx 15$) is similar for ZPG, FPG, pipe and channel flows, however, there is more large-scale contribution for the APG flow. The energetic peaks for all flows occur at $\lambda_x^+ \approx 1000$, as shown by Monty et al. (2009) and in Section 4.1. This suggests that the near-wall cycles of streaks are similar for all except for the APG case where it is slightly different.

At the approximate start of the log region, at $z^+ \approx 100$, Figure B.4($b$) reveals that the energy distributions for the pipe and channel flows are similar to that of the FPG flow, however, there is slightly more contribution from the larger-scale features. The 2-6$\delta$ features are most significantly energised in the APG case, followed by the ZPG, pipe & channel and the FPG flows.

At the approximate start of the log region, $z^+ \approx (15Re_\tau)^{1/2}$, the structures break down in the APG case, creating shorter structures with the most energetic structures at wavelengths of $2\delta$. This is in agreement with the correlation experiment and analysis in Section 5.2 and in Lee and Sung (2009), Skåre and Krogstad (1994). The most energetic

[2]The increased large-scale features in APG flow causes the skewness to increase as shown in Section 3.13 similar to the effect of increased large-scale features when the Reynolds number is increased shown in Metzger and Klewicki (2001).

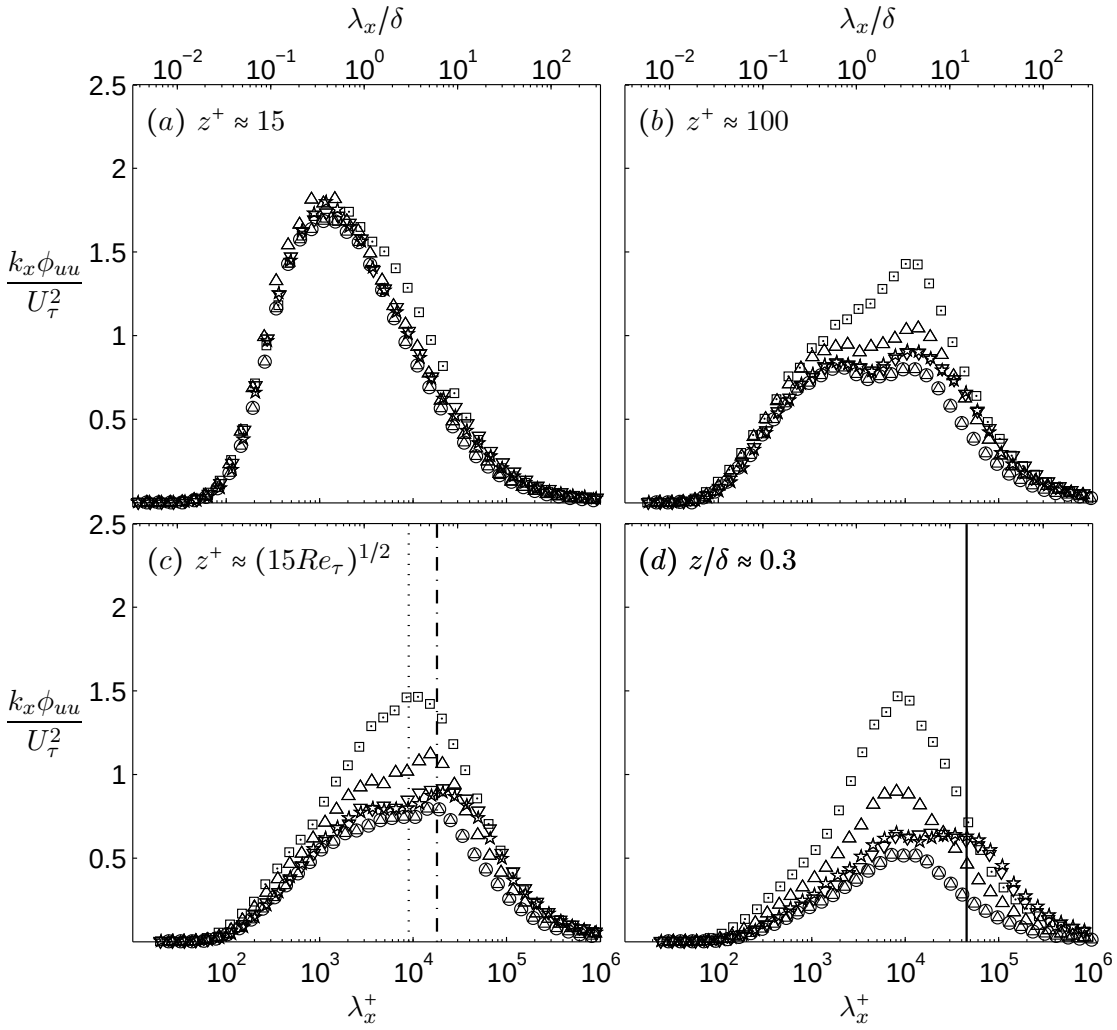


FIGURE B.4: Pre-multiplied energy spectra, $k_x\phi_{uu}/U_\tau^2$ at constant $Re_\tau \approx 3000$ and $l^+ \approx 30$ at four selected wall-normal locations, $(a)$ $z^+ \approx 15$, $(b)$ $z^+ \approx 100$, $(c)$ $z^+ \approx (15Re_\tau)^{1/2}$, and $(d)$ $z/\delta \approx 0.3$. (⊡) APG, (△) ZPG, (⟁) FPG, (☆) pipe and (▽) channel flows. Dotted line indicates $\lambda_x/\delta = 3$, dashed-dotted line indicates $\lambda_x/\delta = 6$ and solid line indicates $\lambda_x/\delta = 15$.

structures here observed in the pipe and channel flows occur at a wavelength of $10\delta$, longer than that for the ZPG and FPG flows, which is at $6\delta$.

Although there is a slight difference in the APG case in the near-wall region, as well as some differences in the log region, it is the outer region that distinguishes these flows the most. At $z/\delta \approx 0.3$ shown in Figure B.4$(d)$, the differences for the internal and external geometry-flows are very significant. For the external geometry-flows, there is one energetic, dominant mode at $\lambda_x/\delta \approx 3$. However, for the internal geometry-flows,

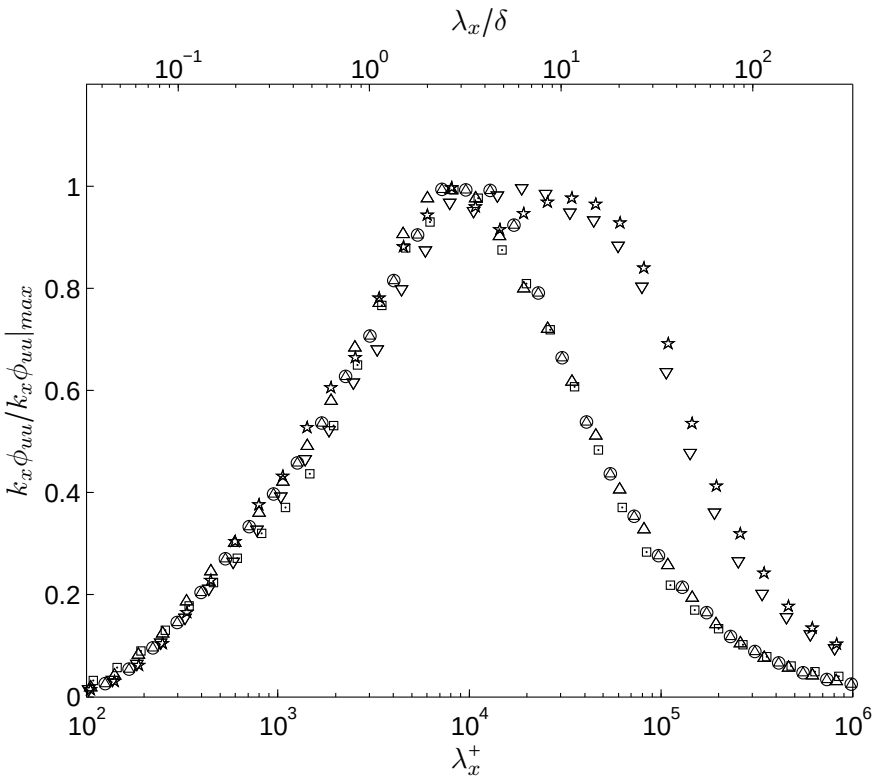


FIGURE B.5: Pre-multiplied energy spectra of streamwise velocity fluctuation $k_x\phi_{uu}/k_x\phi_{uu}|_{max}$ at constant $Re_\tau \approx 3000$ and $l^+ \approx 30$ at $z/\delta \approx 0.3$. (⊡) APG, (△) ZPG, (⏢) FPG, (☆) pipe and (▽) channel flows.

there is also another energetic mode at $\lambda_x/\delta \approx 15$. This is shown by the solid line in this figure. The energy scaled with $U_\tau$ shows that the APG case has significantly more $3\delta$ energy, followed by the ZPG case. The FPG case and the internal geometry flows has approximately similar $k_x\phi_{uu}/U_\tau^2$ magnitudes at this wavelength ($\lambda_x/\delta \approx 3$).

To ensure that the conclusions based on the inner scaling in Figure B.4($d$) are not affected by the scaling used, the energy is now scaled with its maximum value , $k_x\phi_{uu}/k_x\phi_{uu}|_{max}$ as shown in Figure B.5. This figure reveals the second mode in the internal geometry-flows clearly. The energy for internal flows collapse well at all wavelengths. However, $k_x\phi_{uu}/k_x\phi_{uu}|_{max}$ for the internal geometry-flows only collapses with the external geometry-flows at shorter wavelengths ($\lambda_x/\delta \lesssim 3$). There is a slight dip in the energy before $k_x\phi_{uu}/k_x\phi_{uu}|_{max}$ matches that of channel flow at $\lambda_x/\delta \approx 3$.

The energy spectra analysis for the internal and external geometry-flows indicates that all wall-bounded flows share similar structures in the near-wall region except in the

APG case. This may explain similar turbulence intensities for all of this flow except for the APG case (the turbulence intensities for the pipe, channel and ZPG flows almost collapse in the near wall region in Monty et al. (2009)). The skewness and flatness also are almost similar for all flows except for the APG flow. As shown in Figure B.3, the large-scale features are responsible for these differences.

The outer regions contain the most distinguishing features for every flow. The characteristics of the most energetic scales differ from one flow to another. These large-scale features are responsible for the differences in the mean velocities, turbulence intensities, turbulence production, skewness, flatness and etc. In Appendix B.1, it was shown that if the large-scale features were removed, the skewness profiles in the outer region ($z/\delta \approx 0.3$) share similar properties. The point is that the large-scales in the outer region are responsible for the differences between the different types of flows.

## B.3 Dissipation

It was shown in Section 3.15 that the turbulence production $Prod$ at $Re_\tau \approx 3000$ increases with the pressure gradient in the outer region. This observation extends results from previous studies, for example by Skåre and Krogstad (1994) in APG and by Fernholz and Warnack (1998) in FPG. It is also concluded in Section 3.15 that the pressure gradient does not cause a significant impact on the production of turbulence in the near-wall region. In this section, both turbulence production and dissipation are analysed, with the addition of data from the pipe and channel flows. Firstly, the turbulence production analysis is revisited. Turbulence production is given by

$$Prod = -\overline{uw}\frac{\partial \overline{u}}{\partial z} - \overline{u^2}\frac{\partial U_1}{\partial x} + \overline{w^2}\frac{\partial U_1}{\partial x}. \tag{B.1}$$

Figure B.6($a$) shows turbulence production scaled with $\delta/U_\tau^3$. The outer region shows that the pressure gradient causes the APG case to have higher turbulence production. This effect can be shown clearly with the pre-multiplied turbulence production $Prod\ z$ as shown in Section 3.15. The magnitude of $Prod$ observed in the current APG data is however remarkably lower than the one observed in Skåre and Krogstad (1994) because of the mild pressure gradient. The ZPG, FPG and the internal flow cases have similar turbulence production in this region.

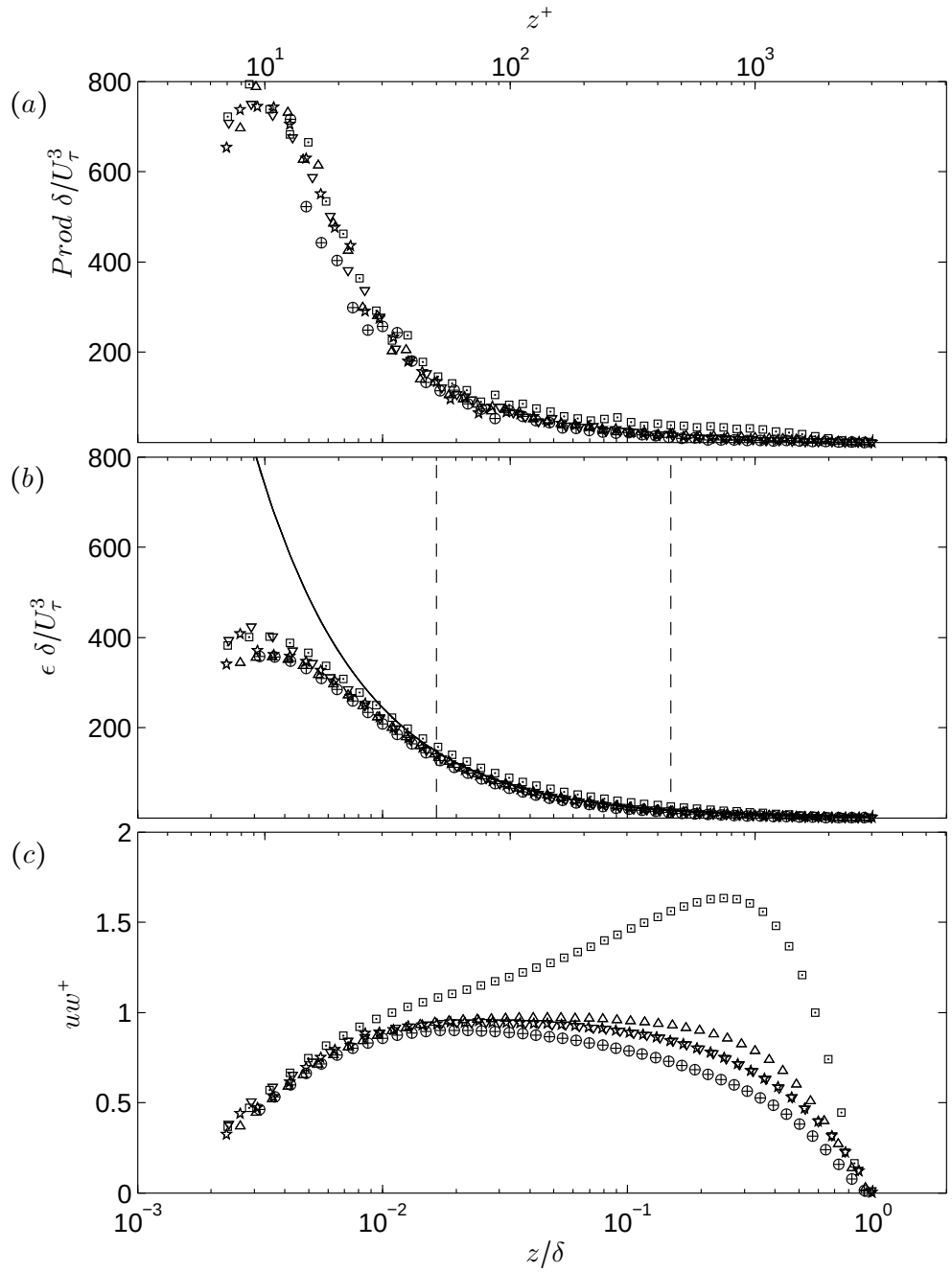


FIGURE B.6: (*a*) Turbulence production, (*b*) dissipation rate, $\epsilon = -\overline{uw}^+ U_\tau^3/(\kappa z)$ and (*c*) Reynolds shear-stress at $Re_\tau \approx 3000$ for internal and external-geometry flows at $Re_\tau \approx 3000$ and $l^+ \approx 30$. Symbols: (⊡) APG, (△) ZPG, (⊕) FPG, (☆) pipe and (▽) channel flows. The curve denotes dissipation rate approximation obtained from $\epsilon \approx U_\tau^3/(\kappa z)$. Dashed lines denote $z^+ = 50$ and $z/\delta = 0.15$.

In ZPG flows, turbulence production and dissipation are the main contributors to the *turbulence budget* except near the edge of the layer (e.g. Bradshaw, 1967a, Spalart, 1988). However, with increasing pressure gradient, the advection and and diffusion terms become significant, these are shown by Skåre and Krogstad (1994) experimentally. This section attempts to highlight the pressure gradient's effect on the energy dissipation rate.

Figure B.6($b$) shows dissipation rate $\epsilon$ distribution for the internal and external flows. The dissipation rate calculation is given by 'local equilibrium' approximation (e.g. McKeon and Morrison, 2007)

$$\epsilon \;=\; -\overline{uw}^{+}\frac{U_\tau^3}{\kappa z} \;=\; -\overline{uw}\frac{\partial U}{\partial z}, \tag{B.2}$$

where the rate of production is balanced by the energy dissipation rate. Such approximation where energy is dissipated close to where it is produced in the log region becomes more accurate as the Reynolds number increases, so that the net spatial transport becomes negligible (McKeon and Morrison, 2007). The approximate log region is shown in this figure by the region contained by the two dashed lines which are $z^+ = 50$ and $z/\delta = 0.15$. For the entire log region, Figure B.6($b$) shows that $\epsilon$ for the APG case is higher than any other flows considered.

Note that Tennekes and Lumley (1972) showed that $\epsilon$ in the log region can also be approximated by $\epsilon = U_\tau^3/\kappa z$ (by assuming that the Reynolds shear stress in this region is equal to $\rho U_\tau^2$, mean velocity gradient is given by $U_\tau/(\kappa z)$, therefore turbulence production rate $-\overline{uw}\partial U/\partial z$ is equal to $U_\tau^3/(\kappa z)$. It was shown that turbulence is balanced by the dissipation rate). However, in the favourable and adverse pressure gradient cases, errors due to this approximation become large. Figure B.6($c$) demonstrates that Reynolds shear stress increases remarkably in the log region for the APG case. By omitting the Reynolds shear stress term, the rise of the $\overline{uw}$ in the APG case in Figure B.6($c$) is underestimated, resulting in lower dissipation rate magnitude shown by the curve in Figure B.6($b$). A similar effect can also be observed in the FPG case, however in the opposite direction. The omission of the Reynolds shear stress term cannot be observed in the ZPG and internal geometry-flows. Therefore, analysis using this approximation e.g. in Balint et al. (1991) where the $uw$ term is omitted, is accurate. However, such approximation is not valid in the near-wall region.

As shown in Section 3.15, the Reynolds shear stresses $\overline{uw}$ for the boundary layer cases are approximated by formulations given in Perry et al. (2002) and Kunkel and Marusic (2006). The Reynolds shear stresses in the pipe and channel flows are approximated by the momentum equation (Sreenivasan and Sahay, 1997, Tennekes and Lumley, 1972)

$$\frac{\mathrm{d}U^+}{\mathrm{d}z^+} = 1 + \overline{uw}^+ - \frac{z}{H}, \tag{B.3}$$

where $H$ is the channel's half-width or pipe's radius.

The turbulence dissipation rate for the current data could also be calculated by assuming the local isotropy theory. The average turbulent energy dissipation rate $\epsilon$ is given by (e.g. Hinze, 1975)

$$\epsilon = \nu\overline{\left(\frac{\partial u_i}{\partial x_j} + \frac{\partial u_j}{\partial x_i}\right)\frac{\partial u_j}{\partial x_i}}. \tag{B.4}$$

Local isotropy theory has been assumed to simplify the dissipation rate calculation. The local isotropy hypothesis states that at sufficiently high Reynolds numbers, the small-scale structures of turbulent motions are independent of large-scale structures (Kolmogorov, 1941). If the dissipating range of eddy sizes is statistically isotropic, equation (B.4) can be reduced to

$$\epsilon \approx 15\nu\overline{\left(\frac{\partial u}{\partial x}\right)^2}. \tag{B.5}$$

Assuming the Taylor hypothesis, the dissipation energy rate can be approximated by (Taylor, 1935, Townsend, 1976)

$$\epsilon \approx 15\nu\overline{\left(\frac{1}{U}\frac{\partial u}{\partial t}\right)^2}. \tag{B.6}$$

Equivalently, the dissipation rate may be obtained from the one-dimensional spectral density (Batchelor, 1953, Townsend, 1976)

$$\epsilon = 15\nu \int_0^\infty k_x^2 \phi(k_x)\, \mathrm{d}k_x. \tag{B.7}$$

The dissipation rates calculated by both fluctuating velocities (B.6) and energy spectrum integration (B.7) result in variations of ±5% within these two methods. In the log region, $z/\delta = 0.15$, the dissipation rate calculated by the local equilibrium approximation, (B.2) is always at least 10% higher than the isotropic relations (B.6) and (B.7). The approximation using the isotropic relations is subjected to the spatial resolution issues. Hutchins et al. (2009) demonstrated that the longer hotwire probe is unable to resolve the high wave number features shown in the Kolmogorov-scaled energy plots. This effect is not only present in the inner region, but extends well into the log region, $z/\delta = 0.15$ (Hutchins et al., 2009).

### B.3.1 Kolmogorov-scaled energy

The different calculations for energy dissipation make it difficult to draw any conclusion regarding the pressure gradient effect. Therefore, it is important to employ the right method. Spatial resolutions issues seem to be the main problem, resulting in inaccuracies in $\epsilon$ from the isotropic relations (B.6) and (B.7). To highlight the spatial resolution effect, it is useful to discuss the unresolved Kolmogorov-scaled energy in Hutchins et al. (2009). The Kolmogorov-scaled energy is given by

$$E_K = \epsilon^{-2/3} k_x^{5/3} \phi_{uu}. \tag{B.8}$$

Figures B.7 show Kolmogorov scaled energy at $Re_\tau \approx 3000$ for APG, ZPG, FPG, pipe and channel flows at constant $Re_\tau \approx 3000$ and $l^+ \approx 30$ at four selected wall-normal locations. It is easy to observe that the longer wire $l^+ \approx 40$ for the APG flow detects less energy in the range of $0.01 \lesssim k_x\eta_K \lesssim 1$. Here $\eta_K$ is the Kolmogorov length scales, given by

$$\eta_K = \frac{\nu^{3/4}}{\epsilon^{1/4}}, \quad \eta_K^+ = \frac{\eta_K U_\tau}{\nu}. \tag{B.9}$$

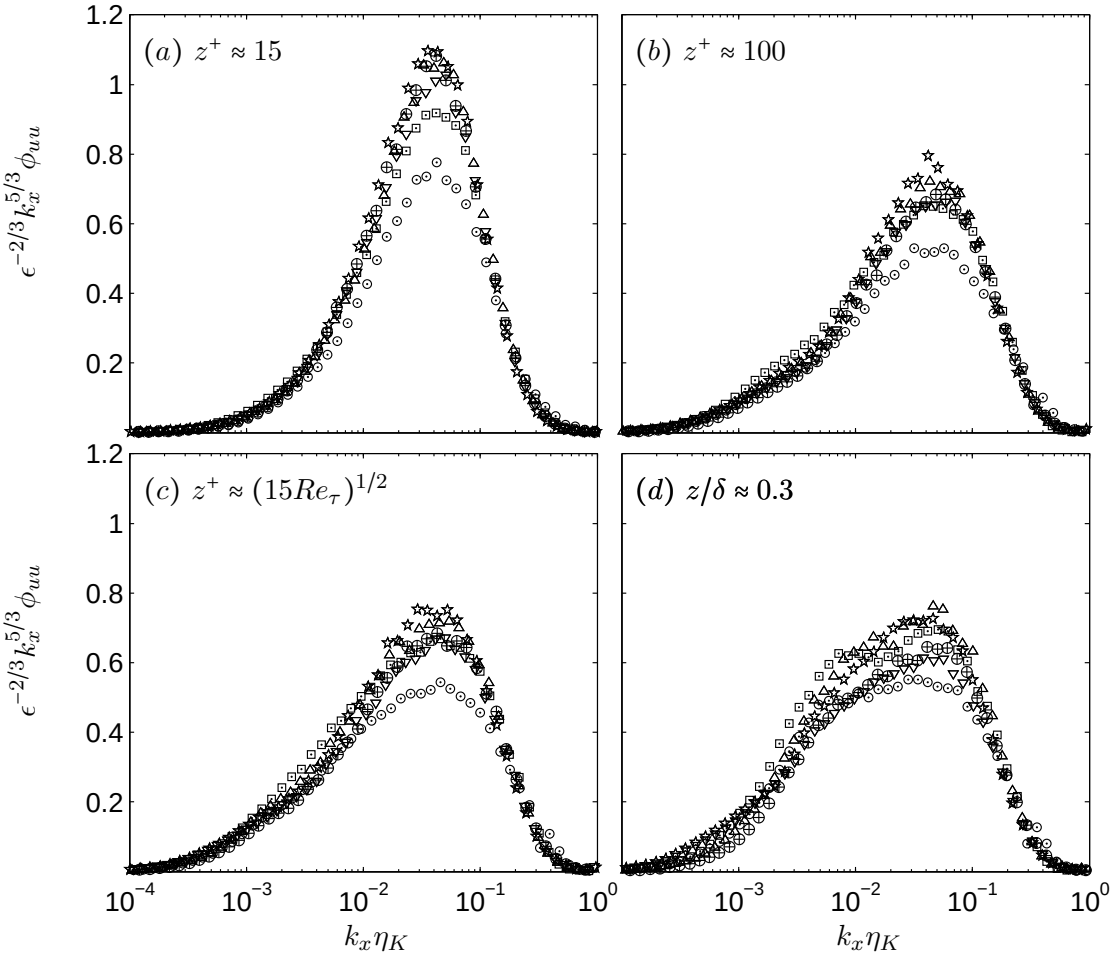


FIGURE B.7: Kolmogorov scaled energy at $Re_\tau \approx 3000$ for APG, ZPG, FPG, pipe and channel flows at constant $Re_\tau \approx 3000$ and $l^+ \approx 30$. Symbols: (⊡) APG, (△) ZPG, (⊕) FPG, (☆) pipe and (▽) channel flows. An APG flow at larger $l^+ \approx 40$: (⊙).

and $\epsilon$ is approximated using the energy spectrum method equation (B.7). Figures B.7($a$) -($c$) continuously show that the Kolmogorov scaled energy almost collapses in the near-wall and log regions for all flows considered at $l^+ \approx 30$ (note symbol ⊙ represents an APG flow at larger $l^+ \approx 40$). The only difference is observed in the outer region, where the smaller wave number structures seem to be more energised for the APG and ZPG cases than for the other flows. However, the magnitudes of Kolmogorov-scaled energy $\epsilon^{-2/3}k_x^{5/3}\phi_{uu}$ do not agree with existing results. The discrepancies can be explained by the following: consider a sufficiently large Reynolds number flow, with viscous dissipation negligible over a large range of wave numbers and viscous forces have no direct

influence on the motions by these components. In such an *inertial subrange* of the equilibrium spectrum, the spectrum function should be independent of fluid viscosity and (Kolmogorov, 1941, Townsend, 1976)

$$\phi_{uu}(k_x) = C_K \epsilon^{2/3} k_x^{-5/3}, \tag{B.10}$$

where $C_K$ is the Kolmogorov constant. A lot of experimental evidence has been shown in support of this expression, for example by Falkovich (1994), Ferchichi and Tavoularis (2000). Saddoughi and Veeravalli (1994) and McKeon and Morrison (2007) supported that $C_K$ is a function of the Kolmogorov-scaled wave number i.e. $C_K = f(k_x\eta_K)$. In Sreenivasan and Antonia (2007b)'s review paper, it is proposed that $C_K \approx 0.5 \pm 0.05$ over a wide range of Reynolds numbers. It is now obvious that the results shown in Figures B.7 suggests a $C_K$ value that is approximately equal to 0.7 (30-40% larger than the proposed value). The errors could be attributed to the approximation of $\epsilon$, as discussed previously, and the spatial resolution issues. Assuming that the spatial resolution only causes much smaller effects in the magnitude of $\epsilon^{-2/3}k_x^{5/3}\phi_{uu}$ (probe length variations need to be $l^+ \approx 80 \pm 60$ to cause 10% in $\epsilon^{-2/3}k_x^{5/3}\phi_{uu}$ in Hutchins et al. (2009)). Therefore, a larger error must be due to the calculation of $\epsilon$.

Figure B.8($a$) at $z^+ \approx (15Re_\tau)^{1/2}$ and B.8($b$) at $z/\delta \approx 0.15$ show $\epsilon^{-2/3}k_x^{5/3}\phi_{uu}$ using the dissipation rate calculated by the local equilibrium approximation $\epsilon = -\overline{uw}^+ U_\tau^3/(\kappa z)$. It is clear now that the external and internal geometry-flows, with the exception of the APG flow, support (B.10) with $C_K$ approximately within the limits in Sreenivasan and Antonia (2007b). At $z/\delta \approx 0.15$ in Figure B.8($b$) , the largest magnitude of the Kolmogorov-scaled energy for the APG flow is approximately 0.6, larger than any of the peaks for the other flows considered. Furthermore, the features in the APG appear to be more energetic in the region of $0.01 \lesssim k_x\eta_K \lesssim 1$. The spectral bump in Figure B.8($b$) (Falkovich, 1994, McKeon and Morrison, 2007, Saddoughi and Veeravalli, 1994) approximately located by the dashed lines, $k_x\eta_K = 0.05$, can clearly be observed for the APG and ZPG flows, but not for the others.

### B.3.2 Distribution of dissipation

Figure B.9 shows the distribution of Kolmogorov normalised length scale $\eta_K^+$ (B.9) for turbulent boundary layers, channel and pipe flows at $Re_\tau \approx 3000$ and $l^+ \approx 30$. Yakhot

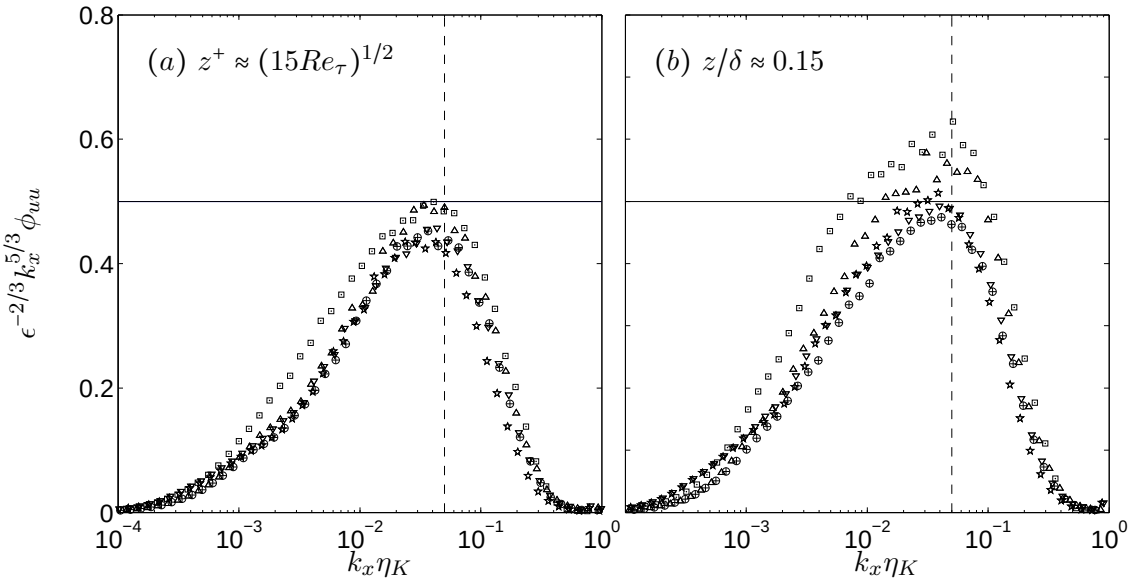


FIGURE B.8: Kolmogorov scaled energy $\epsilon^{-2/3}k_x^{5/3}\phi_{uu}$ at $Re_\tau \approx 3000$ for APG, ZPG, FPG, pipe and channel flows at constant $Re_\tau \approx 3000$ and $l^+ \approx 30$. Symbols: (⊡) APG, (△) ZPG, (⊕) FPG, (☆) pipe and (▽) channel flows. Solid lines denote $\epsilon^{-2/3}k_x^{5/3}\phi_{uu} = 0.5$. Dashed lines denote $k_x\eta_K = 0.05$ (Falkovich, 1994, McKeon and Morrison, 2007, Saddoughi and Veeravalli, 1994)

et al. (2010) showed that $\eta_K^+$ shall collapse in the region $z \lesssim 50$ for $25 \times 10^3 \lesssim Re_D \lesssim 150 \times 10^3$. The dissipation rate is approximated by integrating dissipation spectrum (B.7), the same way as in Yakhot et al. (2010). It is proposed here that $\eta_K^+$ collapse for all internal and external geometry-flows in the region $z \lesssim 50$ as long as the probe length is constant. It can also be shown that the collapse in $\eta_K^+$ extends further, until the approximate start of the log region ($z^+ = 100$) when the local equilibrium calculation (B.2) is used. However, $\eta_K^+$ for the APG case starts to deviate in the middle of the log region.

Table B.1 shows the value of $\eta_K^+$ at $z/\delta = 0.15$, $\epsilon$ is calculated using the equilibrium calculation (B.2). $\eta_K^+ \approx 3.8$ in this region is however slightly smaller for the APG flow. The data in the table shows that $\eta_K^+$ collapses for the region much further up than described in Yakhot et al. (2010). In the table, the Taylor microscale Reynolds number is

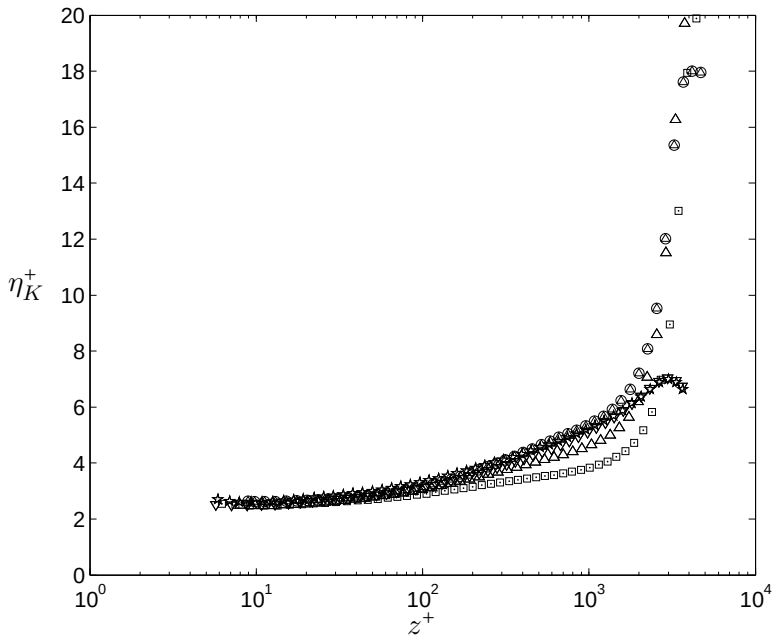


FIGURE B.9: Distribution of dissipation for APG, ZPG, FPG, pipe and channel flows at constant $Re_\tau \approx 3000$ and $l^+ \approx 30$. Symbols: (⊡) APG, (△) ZPG, (⊕) FPG, (☆) pipe and (▽) channel flows. An APG flow at smaller $l^+ \approx 20$: (⊙).

| Flow | Symbol | $Re_{\lambda T}$ | $\eta_K^+$ | $Prod\ \delta/U_\tau^3$ eq. (B.1) | $\epsilon\ \delta/U_\tau^3$ eq. (B.2) |
|---|---|---|---|---|---|
| APG | ⊡ | 315 | **3.35** | **38** | **25** |
| ZPG | △ | 250 | 3.77 | 19 | 15 |
| ZPG | ⊕ | 246 | 4.00 | 11 | 12 |
| Pipe | ☆ | 326 | 3.84 | 11 | 12 |
| Channel | ▽ | 290 | 3.88 | 15 | 13 |

TABLE B.1: Normalised Kolmogorov length-scale $\eta_K^+$ for APG, ZPG, FPG, pipe and channel flows at constant $Re_\tau \approx 3000$ and $l^+ \approx 30$ at $z/\delta = 0.15$.

$$Re_{\lambda T} = \lambda_T \frac{\sqrt{\overline{u^2}}}{\nu}, \quad \lambda_T = \frac{\sqrt{\overline{u^2}}}{\overline{(\partial u/\partial x)^2}} \tag{B.11}$$

where $\lambda_T$ is known as the Taylor microscale. $Re_{\lambda T}$ number needs to be large, i.e. $Re_{\lambda T} > 150$ to observe a plateau in (B.8) (e.g. Ferchichi and Tavoularis, 2000, Saddoughi and Veeravalli, 1994).

The magnitudes for turbulence production and dissipation rate scaled with $\delta/U_\tau^3$ at $z/\delta$ = 0.15 are shown in Table B.1. The values consistently show $Prod\ \delta/U_\tau^3 \approx 3.8$ and $\epsilon\ \delta/U_\tau^3 \approx 13$ except for the APG case, where turbulence production and dissipation rate are larger by 100% and 50% respectively. Here, $\epsilon$ is approximated using the local equilibrium relationship (B.2), therefore the values shown here do not correspond to Figure B.9 (where $\epsilon$ is calculated using the energy spectrum method (B.7)). The larger energy dissipation rate for the APG flow in the log region is expected because the dissipation rate is similar to the turbulence production, which is known to increase in APG flows (Nagano et al., 1998, Skåre and Krogstad, 1994).

The smaller non-dimensionalised Kolmogorov length scale for the APG case ($\eta_K^+ \approx 3.4$ instead of $\eta_K^+ \approx 3.9$ for the rest) suggests that the APG has also caused these small structures to change. Furthermore, the value of the Kolmogorov constant $C_K$ remains approximately 0.5 for the considered ZPG, FPG and the internal geometry-flows data, the APG flow appears to deviate from this relationship by overestimating $C_K$ by 10%. In summary, this section concludes that the activated log region brought by APG has energised the smaller-scale structures. While there may be some changes between the internal and external geometry-flows, the differences caused in the APG flow are significantly larger than those in the other flows.

# Bibliography


H. Abe, H. Kawamura, and H. Choi. Very large-scale structures and their effects on the wall shear-stress fluctuations in a turbulent channel flow up to $Re_\tau = 640$. *J. Fluid J. Fluids Engng.*, 126:835–843, 2004.

R. J. Adrian, C. D. Meinhart, and C. D. Tomkins. Vortex organization in the outer region of a turbulent boundary layer. *J. Fluid Mech.*, 422:1–53, 2000.

J. Andreopoulos, F. Durst, and Z. Zaric Javanović. Influence of Reynolds number on characteristics of turbulent wall boundary layers. *Exp. Fluids*, 2:7–16, 1984.

R.A. Antonia, M. Teitel, J. Kim, and L. W. B. Browne. Low-Reynolds number effects in a fully developed turbulent channel flow. *J. Fluid Mech.*, 236:579–605, 1994.

C. D. Aubertine and J. K. Eaton. Turbulence development in a non-equilibrium turbulent boundary layer with mild adverse pressure gradient. *J. Fluid Mech.*, 532:345–364, 2005.

B.J. Balakumar and R. J. Adrian. Large- and very-large-scale motions in channel and boundary-layer flows. *Phil. Trans. R. Soc. A*, 365:665–681, 2007.

J-L Balint, J. M. Wallace, and Petar Vukoslavačević. The velocity and vorticity vector fields of a turbulent boundary layer. Part 2. Statistical properties. *J. Fluid Mech.*, 228:53–86, 1991.

G. I. Barenblatt. Scaling laws for fully developed turbulent shear flows. Part 1. Basic hypotheses and analysis. *J. Fluid Mech.*, 248:513–520, 1993.

G. K. Batchelor. *The theory of homogeneous turbulence.* Cambridge University Press, 1953.

R. F. Blackwelder and R. E. Kaplan. On the wall structure of the turbulent boundary layer. *J. Fluid Mech.*, 76:89–112, 1976.

C. Bourassa and F. O. Thomas. An experimental investigation of a highly accelerated turbulent boundary layer. *J. Fluid Mech.*, 634:359–404, 2009.

P. Bradshaw. The turbulence structure of equilibrium boundary layers. *J. Fluid Mech.*, 29:625–645, 1967a.

P. Bradshaw. 'Inactive' motion and pressure fluctuations in turbulent boundary layers. *J. Fluid Mech.*, 30:241–258, 1967b.

G. L. Brown and S. W. Thomas. Large structure in turbulent boundary layer. *Phys. Fluids*, 20:S243–S252, 1977.

H. H. Bruun. *Hot wire anemometry*. Oxford University Press, 1995.

L. Castillo and W. K. George. Similarity analysis for turbulent boundary layer with pressure gradient: Outer flow. *AIAA Journal*, 39(1):41–47, 2001.

K. Chauhan, H. Ng, and I. Marusic. Empirical mode decomposition and Hilbert transforms for analysis of oil-film interferograms. *Meas. Sci. Technol.*, 21:105405, 1–13, 2010.

K. A. Chauhan, P. A. Monkewitz, and H. M. Nagib. Criteria for assessing experiments in zero pressure gradient boundary layers. *Fluid Dyn. Res.*, 41:021404, 1–23, 2009.

C. Chin, N. Hutchins, A. Ooi, and I. Marusic. Spatial resolution correction for hot-wire anemometry in wall turbulence. *Exp. Fluids*, 50:1443–1453, 2011.

C. Y. Ching, L. Djenidi, and R. A. Antonia. Low-Reynolds-number effects in a turbulent boundary layer. *Exp. Fluids*, 19:61–68, 1995.

K. T. Christensen and R. J. Adrian. Statistical evidence of hairpin vortex packets in wall turbulence. *J. Fluid Mech.*, 431:433–443, 2001.

F. H. Clauser. Turbulent boundary layers in adverse pressure gradients. *J. Aero. Sci.*, 21:91–108, 1954.

D. E. Coles. The law of the wake in the turbulent boundary layer. *J. Fluid Mech.*, 1: 191–226, 1956.

D. E. Coles. The turbulent boundary layer in a compressible fluid. Technical Report R-403-PR, United States Air Force Project RAND, R-403-PR, 1962.

A. D. Cutler and J. P. Johnston. The relaxation of a turbulent boundary layer in an adverse pressure gradient. *J. Fluid Mech.*, 200:367–387, 1989.

D. E. DeGraaff and J. K. Eaton. Reynolds-number scaling of the flat-plate turbulent boundary layer. *J. Fluid Mech.*, 422:319–346, 2000.

J. C. del Álamo and J. Jiménez. Spectra of the very large anisotropic scales in turbulent channels. *Phys. Fluids*, 15(6):L41–L44, 2003.

J. C. del Álamo, J. Jiménez, P. Zandonade, and R. D. Moser. Scaling of the energy spectra of turbulent channels. *J. Fluid Mech.*, 500:135–144, 2004.

J. M. J. den Toonder and F. T. M. Nieuwstadt. Reynolds number effects in a turbulent pipe flow for low to moderate Re. *Phys. Fluids*, 9:11, 3398–3409, 1997.

P. Dengel and H. H. Fernholz. An experimental investigation of an incompressible turbulent boundary layer in the vicinity of separation. *J. Fluid Mech.*, 212:615–636, 1990.

D. J. C. Dennis and T. B. Nickels. On the limitations of Taylor's hypothesis in constructing long structures in a turbulent boundary layer. *J. Fluid Mech.*, 614:197–206, 2008.

S.A. Dixit and O.N. Ramesh. Large-scale structures in turbulent and reverse-transitional sink flow boundary layers. *J. Fluid Mech.*, 649:233–273, 2010.

F. Durst, M. Fischer, J. Jovanović, and H. Kikura. Methods to set up and investigate low Reynolds nuymber, fully developed turbulent plane channel flows. *J. Fluids Engng.*, 120:496–503, 1998.

G. Falkovich. Bottleneck phenomenon in developed turbulence. *Phys. Fluids*, 6:4, 1411–1414, 1994.

M. Ferchichi and S. Tavoularis. Reynolds number effects on the fine structure of uniformly sheared turbulence. *Phys. Fluids*, 12:2942–2953, 2000.

H. H. Fernholz and P. J. Finley. The incompressible zero-pressure-gradient turbulent boundary layer: An assessment of the data. *Prog. Aero. Sci.*, 32:245–311, 1996.

H. H. Fernholz and D. Warnack. The effects of a favourable pressure gradient and of the reynolds number on an incompressible axisymmetric turbulent boundary layer. Part 1. The turbulent boundary layer. *J. Fluid Mech.*, 359:329–356, 1998.

D. S. Finnicum and T. J. Hanratty. Effect of favorable pressure gradients on turbulent boundary layers. *AIChe. J.*, 34:529–540, 1988.

M. Gad-el-Hak and P.R. Bandyopadahyay. Reynolds number effects in wall-bounded turbulent flows. *Appl. Mech. Rev.*, 47:307–365, 1994.

B. Ganapathisubramani, E. K. Longmire, and I. Marusic. Characteristics of vortex packets in turbulent boundary layers. *J. Fluid Mech.*, 478:35–46, 2003.

B. Ganapathisubramani, E. K. Longmire, and I. Marusic. Investigation of large-scale coherence in a turbulent boundary layer using two-point correlations. *J. Fluid Mech.*, 524:57–80, 2005.

W. K. George and L. Castillo. Zero-pressure gradient turbulent boundary layer. *Appl. Mech. Rev.*, 50(11):689–729, 1997.

M. Guala, S. E. Hommema, and R. J. Adrian. Large-scale and very-large-scale motions in turbulent pipe flow. *J. Fluid Mech.*, 554:521–542, 2006.

K. J. Harder and W. G. Tiederman. Drag reduction and turbulent structure in two-dimensional channel flows. *Phil. Trans. R. Soc. A*, 336:19–34, 1991.

Z. Harun, V. Kulandaivelu, B. Nugroho, M. Khashehchi, J.P. Monty, and I. Marusic. Large scale structures in an adverse pressure gradient turbulent boundary layer. *In Proc. $8^{th}$ Intern.ERCOFTAC Symp. Engineering Turbulence, Modelling and Measurements. Marseille, France*, pages 183–188, 2010a.

Z. Harun, J.P. Monty, and I. Marusic. Constant adverse pressure gradient turbulent boundary layers. *In Proc. $17^{th}$ Australasian Fluid Mechanics Conference. Auckland, New Zealand*, 2010b.

Z. Harun, J.P. Monty, and I. Marusic. The structure of zero, favorable and adverse pressure gradient turbulent boundary layers. *In Proc. $7^{th}$ Turbulence and Shear Flow Phenomena, (TSFP). Ottawa, Canada*, 2011.

M. R. Head and P. Bandyopadhyay. New aspects of turbulent boundary-layer structure. *J. Fluid Mech.*, 107:297–338, 1981.

J. O. Hinze. *Turbulence*. $2^{nd}$ Edn. McGraw-Hill, 1975.

M. Hultmark, S. C. C. Bailey, and A. J. Smits. Scaling of near-wall turbulence in pipe flow. *J. Fluid Mech.*, 649:103–113, 2010.

N. Hutchins and I. Marusic. Evidence of very long meandering features in the logarithmic region of turbulent boundary layers. *J. Fluid Mech.*, 579:1–28, 2007a.

N. Hutchins and I. Marusic. Large-scale influences in near-wall turbulence. *Phil. Trans. R. Soc. A*, 365:647–664, 2007b.

N. Hutchins, W.T. Hambleton, and I. Marusic. Inclined cross-stream stereo particle image velocimetry measurements in turbulent boundary layers. *J. Fluid Mech.*, 541: 21–54, 2005.

N. Hutchins, T. B. Nickels, I. Marusic, and M. S. Chong. Hot-wire spatial resolution issues in wall-bounded turbulence. *J. Fluid Mech.*, 635:103–136, 2009.

J. Jeong, F. Hussain, W. Schoppa, and J. Kim. Coherent structures near the wall in a turbulent channel flow. *J. Fluid Mech.*, 332:185–214, 1997.

A. V. Johansson and P. H. Alfredsson. On the structure of turbulent channel flow. *J. Fluid Mech.*, 122:295–314, 1982.

A. V. Johansson and P. H. Alfredsson. Effects of imperfect spatial resolution on measurements of wall-bounded turbulent shear flows. *J. Fluid Mech.*, 137:409–421, 1983.

M. B. Jones, I. Marusic, and A. E. Perry. Evolution and structure of sink flow turbulent boundary layers. *J. Fluid Mech.*, 428:1–27, 2001.

J. Kim, P. Moin, and R. Moser. Turbulence statistics in fully developed channel flow at low reynolds number. *J. Fluid Mech.*, 177:133–166, 1987.

K. C. Kim and R. J. Adrian. Very large-scale motion in the outer layer. *Phys. Fluids*, 11(2):417–422, 1999.

J. C. Klewicki and R. E. Falco. On accurately measuring statistics associated with small-scale structure in turbulent boundary layers using hot-wire probes. *J. Fluid Mech.*, 219:119–142, 1990.

S. J. Kline and F. A. McClintock. Describing uncertainties in single sample experiments. *Mech. Eng.*, 75(1):3–8, 1953.

S. J. Kline, W. C. Reynolds, F. A. Schraub, and P. W. Runstadler. The structure of turbulent boundary layers. *J. Fluid Mech.*, 30:741–773, 1967.

A. N. Kolmogorov. The local structure of turbulence in incompressible viscous fluid for very large Reynolds numbers. *C. R. Acad. Sci URSS*, 30:301, 1941.

L. S. G. Kovasznay, V. Kibens, and R. F. Blackwelder. Large-scale motion in the intermittent region of a turbulent boundary layer. *J. Fluid Mech.*, 41:283–325, 1970.

P.-Å. Krogstad and P. E. Skåre. Influence of a strong adverse pressure gradient on the turbulent structure in a boundary layer. *Phys. Fluids*, 7:2014–2024, 1995.

G. Kunkel and I. Marusic. Study of the near-wall-turbulent region of the high-reynolds-number boundary layer using an atmospheric flow. *J. Fluid Mech.*, 548:375–402, 2006.

J. H. Lee and H. J. Sung. Effects of an adverse pressure gradient on a turbulent boundary layer. *Intl. J. Heat Fluid Flow*, 29:568–578, 2008.

J. H. Lee and H. J. Sung. Structures in turbulent boundary layers subjected to adverse pressure gradients. *J. Fluid Mech.*, 639:101–131, 2009.

P. M. Ligrani and P. Bradshaw. Spatial resolution and measurement of turbulence in the viscous sublayer using subminiature hot-wire probes. *Exp. Fluids*, 5:407–417, 1987.

S. S. Lu and W. W. Willmarth. Measurements of the structure of the reynolds stress in a turbulent boundary layer. *J. Fluid Mech.*, 60:481–417, 1973.

Y. Maciel, K-S Rossignol, and J Lemay. Self-similarity in the outer region of adverse-pressure-gradient turbulent boundary layers. *AIAA Journal*, 44(11):2450–2464, 2006.

R. Madad, Z. Harun, K. Chauhan, J.P. Monty, and I. Marusic. Skin Friction Measurement in Zero and Adverse Pressure Gradient Boundary Layers Using Oil Film Interferometry. *In Proc. 17$^{th}$ Australasian Fluid Mechanics Conference. Auckland, New Zealand*, 2010.

I. Marusic and W. D. C Heuer. Reynolds number invariance of the structure inclination angle in wall turbulence. *Phys. Review Letter*, 99:41–45, 2007.

I. Marusic and A. E. Perry. A wall-wake model for the turbulence structure of boundary layers. Part 2. Further experimental support. *J. Fluid Mech.*, 298:389–407, 1995.

I. Marusic, R. Mathis, and N. Hutchins. High Reynolds number effects in wall turbulence. *Int. J. Heat Fluid Flow*, 31:418–428, 2010a.

I. Marusic, R. Mathis, and N. Hutchins. Predictive model for wall-bounded turbulent flow. *Science*, 329(5988):193–196, 2010b.

I. Marusic, B. J. McKeon, P. A. Monkewitz, H. M. Nagib, Smits A. J., and K. R. Sreenivasan. Wall-bounded turbulent flows at high reynolds number: Recent advances and key issues. *Phys. Fluids*, 22:065103, 1–24, 2010c.

R. Mathis, N. Hutchins, and I. Marusic. Large-scale amplitude modulation of the small-scale structures in turbulent boudary layers. *J. Fluid Mech.*, 628:311–337, 2009.

R. Mathis, N. Hutchins, and I. Marusic. Relationship between turbulence modulation and skewness in wall bounded flows. *In Proc. $7^{th}$ Turbulence and Shear Flow Phenomena, (TSFP). Ottawa, Canada*, 2011.

B. J. McKeon and J. F. Morrison. Asymptotic scaling in turbulent pipe flow. *Phil. Trans. R. Soc. A*, 365:771–787, 2007.

G. L. Mellor and D. M. Gibson. Equilibrium turbulent boundary layers. *J. Fluid Mech.*, 24:(2), 225–253, 1966.

M. Metzger, J. Klewicki, K. Bradshaw, and R. Sadr. Scaling the near-wall axial turbulent stress in the zero pressure gradient boundary layer. *Phys. Fluids*, 13:6, 1819–1821, 2001.

M. M. Metzger and J. C. Klewicki. A comparative study of near-wall turbulence in high and low Reynolds number boundary layers. *Phys. Fluids*, 13:3, 692–701, 2001.

C. B. Millikan. A critical discussion of turbulent flows in channels and circular tubes. *In Proc. $5^th$ Intl. Congress for App. Mech., Cambridge, Massachusetts*, pages 386–392, 1938.

S. Mochizuki and F. T. M. Nieuwstadt. Reynolds-number-dependence of the maximum in the streamwise velocity fluctuations in wall turbulence. *Exp. Fluids*, 21:218–226, 1996.

P. A. Monkewitz, K. A. Chauhan, and H. M Nagib. Comparison of mean flow similarity laws in zero pressure gradient turbulent boundary layers. *Phys. Fluids*, 20:105102, 1–16, 2008.

D. J. Monson. A nonintrusive laser interferometer methodfor measurement of skin friction. *Exp. Fluids*, 1:15–22, 1983.

D. J. Monson and H Higuchi. Skin friction measurements by a dual-laser-beam interferometer technique. *AIAA J.*, 19:739–744, 1981.

J. P. Monty, J. A. Stewart, R. C. Williams, and M. S. Chong. Large-scale features in turbulent pipe and channel flows. *J. Fluid Mech.*, 589:147–156, 2007.

J. P. Monty, N. Hutchins, H .C. H. Ng, and M. S. Chong. A comparison of turbulent pipe, channel and boundary layer flows. *J. Fluid Mech.*, 632:431–442, 2009.

J. P. Monty, Z. Harun, and I. Marusic. A parametric study of adverse pressure gradient turbulent boundary layers. *Int. J. Heat Fluid Flow*, 32:575–585, 2011.

Y. Nagano and T. Houra. Higher-order moments and spectra of velocity fluctuations in adverse-pressure-gradient turbulent boundary layer. *Exp. Fluids*, 33:22–30, 2002.

Y. Nagano, M. Tagawa, and T. Tsuji. Effects of adverse pressure gradients on mean flows and turbulence statistics in a boundary layer. *Turbulent Shear Flows 8, Springer, Berlin*, 8:7–21, 1992.

Y. Nagano, T. Tsuji, and T. Houra. Structure of turbulent boundary layer subjected to adverse pressure gradient. *Int. J. Heat Fluid Flow*, 19:563–572, 1998.

H. M. Nagib and K. A. Chauhan. Variations of von Kármán coefficient in canonical flows. *Phys. Fluids*, 20:101518, 1–10, 2008.

H. M. Nagib, C. Christophorou, J. Rüedi, P. A. Monkewitz, J. M. Österlund, and S. Gravante. Can we ever rely on results from wall-bounded flows without direct measurements of wall shear stress? *In Proc. AIAA Aerodynamic Measurement Technology and Ground Testing Conference, Portland*, pages 2004–2392, 2004.

H. M. Nagib, K. A. Chauhan, and P. A. Monkewitz. Approach to an asymptotic state of zero pressure gradient turbulent boundary layers. *Phil. Trans. R. Soc. A*, 365: 755–770, 2007.

J. W. Naughton and M. Sheplak. Modern developments in shear-stress measurement. *Prog. Aerosp. Sci.*, 38:515–570, 2003.

H. C. H. Ng, I. Marusic, J. P. Monty, N. Hutchins, and M. s. Chong. Oil film interferometry in high Reynolds number turbulent boundary layers. *In Proc. $16^{th}$ Australasian Fluid Mechanics Conference. Gold Coast, Australia*, pages 807–814, 2007.

H .C. H. Ng, J. P. Monty, , M. S. Chong, and I Marusic. Comparison of turbulent channel and pipe flows with varying Reynolds number. *Exp. Fluids*, In press., 2011.

T. B. Nickels. Inner scaling for wall-bounded flows subject to large pressure gradients. *J. Fluid Mech.*, 521:217–239, 2004.

T. B. Nickels, I. Marusic, S. Hafez, and M. S. Chong. Evidence of the $k_1^{-1}$ law in a high-Reynolds-number turbulent boundary layer. *Phys. Rev. Lett.*, 95:074501, 1–4, 2005.

J. M. Österlund. *Experimental studies of zero pressure-gradient turbulentboundary layer flow*. PhD thesis, Royal Institute of Technology, Sweden, 1999.

J. M. Österlund and A V. Johansson. A note on the overlap region in turbulent boundary layers. *Phys. Fluids*, 12:1–4, 2000.

R. L Panton. *Self-Sustaining Mechanisms of Wall Turbulence*. Comp. Mech. Publ., 1997.

A. E. Perry and M. S. Chong. On the mechanism of wall turbulence. *J. Fluid Mech.*, 119:173–217, 1982.

A. E. Perry and J. D. Li. Experimental support for the attached-eddy hypothesis in zero-pressure-gradient turbulent boundary layers. *J. Fluid Mech.*, 218:405–438, 1990.

A. E. Perry and I. Marusic. A wall-wake model for the turbulence structure of boundary layers. Part 1. Extension of the attached eddy hypothesis. *J. Fluid Mech.*, 298:361–388, 1995.

A. E. Perry and W. H. Schofield. Mean velocity and shear stress distributions in turbulent boundary layers. *Phys. Fluids*, 16:12, 2068–2074, 1973.

A. E. Perry, J. B. Bell, and P. N. Joubert. Velocity and temperature profiles in adverse pressure gradient turbulent boundary layers. *J. Fluid Mech.*, 25:299–320, 1966.

A. E. Perry, I. Marusic, and J. D. Li. Wall turbulence closure based on classical similarity laws and the attached eddy hypothesis. *Phys. Fluids*, 6:2, 1024–1035, 1994.

A. E. Perry, I. Marusic, and M. B Jones. On the streamwise evolution of turbulent boundary layers in arbitrary pressure gradients. *J. Fluid Mech.*, 461:61–91, 2002.

S. B. Pope. *Turbulent flows*. Cambridge University Press, 2000.

J. H. Preston. Determination of turbulent skin friction by means of pitot tubes. *J. Royal Aero. Soc.*, 58:109–121, 1954.

S. Rahgozar and Y. Maciel. Large and very large scale structures in the outer region of an adverse pressure gradient turbulent boundary layer. *In Proc. $7^{th}$ Turbulence and shear flow phenomena, Ottawa*, pages 1–6, 2011a.

S. Rahgozar and Y. Maciel. Low- and high-speed structures in the outer region of an adverse-pressure-gradient turbulent boundary layer. *Exp. Thermal and Fluid Sci.*, 35: 1575–1587, 2011b.

S. K. Robinson. Coherent motions in the turbulent boundary layer. *Annu. Rev. Fluid Mech.*, 23:601–639, 1991.

J. C. Rotta. Turbulent boundary layers in incompressible flow. *Prog. Aero. Sci.*, 2: 1–219, 1962.

S. G. Saddoughi and S. V. Veeravalli. Local isotropy in turbulent boundary layers at high Reynolds number. *J. Fluid Mech.*, 268:333–372, 1994.

A. E. Samuel and P. N. Joubert. A boundary layer developing in an increasingly adverse pressure gradient. *J. Fluid Mech.*, 66:481–505, 1974.

P. Schlatter and R. Örlü. Quantifying the interaction between large and small scales in wall-bounded turbulent flows: A note of caution. *Phys. Fluids*, 22:051704, 1–4, 2010.

W. H. Schofield. Equilibrium boundary layers in moderate to strong adverse pressure gradients. *J. Fluid Mech.*, 113:91–122, 1981.

W. H. Schofield and A. E. Perry. The turbulent boundary layer as a wall confined wake. Technical Report 134, Australian Defence Scientific Service, Dept. of Supply, Australia, 1973.

M. Skote and D. S. Henningson. Direct numerical simulation of a seperated turbulent boundary layer. *J. Fluid Mech.*, 471:107–136, 2002.

M. Skote, D. S. Henningson, and R. A. W. M. Henkes. Direct numerical simulation of self-similar turbulent boundary layers in adverse pressure gradients. *Flow, Turbulence and Combustion*, 60:47–85, 1998.

P. E. Skåre and P.-A. Krogstad. A turbulent equilibrium boundary layer near separation. *J. Fluid Mech.*, 272:319–348, 1994.

C. R. Smith and S. P. Metzler. The characteristics of low-speed streaks in the near-wall region of a turbulent boundary layer. *J. Fluid Mech.*, 129:27–54, 1983.

Alexander J. Smits, Beverley J. McKeon, and Ivan Marusic. High Reynolds number wall turbulence. *Annu. Rev. of Fluid Mech.*, 43:353–375, 2011.

P. R. Spalart. Numerical study of sink-flow boundary layers. *J. Fluid Mech.*, 172: 307–328, 1986.

P. R. Spalart. Direct simulation of a turbulent boundary layer up to $R_\theta$=1410. *J. Fluid Mech.*, 187:61–98, 1988.

P. R. Spalart and J. H. Watmuff. Experimental and numerical study of a turbulent boundary layer with pressure gradients. *J. Fluid Mech.*, 249:337–371, 1993.

L. C. Squire. The motion of a thin oil sheet under the steady boundary layer on a body. *J. Fluid Mech.*, 11:161–179, 1961.

K. R. Sreenivasan. The turbulent boundary layer. *In Frontiers in Experimental Fluid Mechanics, ed M Gad-el-Hak, Springer-Verlag*, pages 159–209, 1989.

K. R. Sreenivasan and R. A. Antonia. The phenomenology of small-scale turbulence. *Annu. Rev. of Fluid Mech.*, 29:435–472, 2007b.

K. R. Sreenivasan and Anupam Sahay. The persistence of viscous effects in the overlap region, and the mean velocity in turbulent pipe and channel flows. *Advances in Fluid Mechanics*, pages 253–272, 1997.

V. Stenzel, Y. Wilke, and W Hage. Drag-reducing paints for the reduction of fuel consumption in aviation and shipping. *Prog. Organic Coatings*, 70:224–229, 2011.

B. S . Stratford. The prediction of separation of the turbulent boundary layer. *J. Fluid Mech.*, 5:1–16, 1959.

L. H. Tanner. A comparison of the viscosity balance and Preston tube methods of skin friction measurement. *J. Phys. E: Sci. Instrum.*, 10:627–632, 1977a.

L. H. Tanner. A skin friction meter, using the viscosity balance principle, suitable for use with flat or curved metal surfaces (based on thickness measurement). *J. Phys. E: Sci. Instrum.*, 10:278–284, 1977b.

L. H. Tanner and L. G. Blows. A study of the motion of oil films on surfaces in air flow, with application to the measurement of skin friction. *J. Phys. E: Sci. Instrum.*, 9: 194–202, 1976.

G. I. Taylor. Distribution of dissipation of energy in a pipe over its cross-section. *Proc. R. Soc.. lond. A*, 151:455–464, 1935.

H. Tennekes and J. L. Lumley. *A first course in turbulence.* MIT Press, 1972.

C. D. Tomkins and R. J. Adrian. Spanwise structure and scale growth in turbulent boundary layers. *J. Fluid Mech.*, 490:37–74, 2003.

A. A. Townsend. Equilibrium layers and wall turbulence. *J. Fluid Mech.*, 11:97–120, 1961.

A. A. Townsend. *The structure of turbulent shear flow.* $2^{nd}$ Edn. Cambridge University Press, 1976.

F. Walleffe. On a self-sustaining process in shear flows. *Phys. Fluids*, 99:4, 883–900, 1997.

C.E Wark and H. M. Nagib. Experimental investigation of coherent structures in turbulent boundary layers. *J. Fluid Mech.*, 230:183–208, 1991.

D. Warnack and H. H. Fernholz. The effects of a favourable pressure gradient and of the Reynolds number on an incompressible axisymmetric turbulent boundary layer. Part 2. The boundary layer with relaminarization. *J. Fluid Mech.*, 359:357–381, 1998.

T. Wei and W. W. Wilmarth. Reynolds number effects on the structure of a turbulent channel flow. *J. Fluid Mech.*, 204:57–95, 1989.

F. M. White. *Viscous fluid flow.* $2^{nd}$ Edn. McGwaw Hill, 1991.

V. Yakhot, S.C.C. Bailey, and A.J. Smits. Scaling of global properties of turbulence and skin friction in pipe and channel flows. *J. Fluid Mech.*, 652:65–73, 2010.

M. V. Zagarola and A. J. Smits. Mean-flow scaling of turbulent pipe flow. *J. Fluid Mech.*, 373:33–79, 1998.

E. S. Zanoun, F. Durst, and H. Nagib. Evaluating the law of the wall in two-dimensional fully developed turbulent channel flows. *Phys. Fluids*, 15:3079–3089, 2003.